Incremental Forming of Light Weight Sheet Materials at Elevated Temperature: An Investigation of Formability, Failure, and Output Quality of the Process

by

Hosein Khalatbari

A Dissertation Submitted to the
Graduate School of Sciences and Engineering
in Partial Fulfillment of the Requirements for
the Degree of
Doctor of Philosophy
in
Mechanical Engineering

KOÇ ÜNİVERSİTESİ

August 2021

Incremental Forming of Light Weight Sheet Materials at Elevated Temperature: An Investigation of Formability, Failure, and Output Quality of the Process

Koc University
Graduate School of Sciences and Engineering
This is to certify that I have examined this copy of a doctoral dissertation by

Hosein Khalatbari

and have found that it is complete and satisfactory in all respects,
and that any and all revisions required by the final
examining committee have been made.

Committee Members:

Prof. Ismail Lazoglu (Advisor, Koc University)

Prof. Demircan Canadinç (Koc University)

Assoc. Prof. Uğur Ünal (Koc University)

Prof. Haydar Livatyali (Yildiz Technical University)

Prof. Mustafa Bakkal (Istanbul Technical University)

Date: 8.9.2021

Dedicated

To

My Family

ABSTRACT

Incremental Forming of Light Weight Sheet Materials at Elevated Temperature: An Investigation of Formability, Failure, and Output Quality of the Process
Hosein Khalatbari
Doctor of Philosophy in Mechanical Engineering
August 2021

Abstract: Sheet metal forming is an integral part of the manufacturing field that is widely used in the aerospace and automotive industries. Today, the highly competitive field of manufacturing demands a higher level of product customization, a shorter design-to-release time cycle, and higher productivity. A novel sheet forming technology to cope with the requirements of agile manufacturing is deemed to have a flexible and highly capable tooling system. By employing the computer numerical control (CNC) technology and relatively simple tooling, Incremental Sheet Forming (ISF) offers a die-less forming possibility. More specifically, heat-assisted ISF has been appeared promising in terms of sheet formability and dimensional accuracy of the final sheet component. Due to the global warming concerns, aerospace and automotive industries are urged to implement lightweight materials and design principles. This has led to continuous growth in the consumption of thermoplastics, for example, in the automotive sector. During the last decade, a great deal of effort has been devoted by scholars to understand the mechanism and the governing rules of the ISF process. These studies have mostly targeted metallic alloys namely aluminum, steel, titanium, and magnesium. Polyoxymethylene (POM) is the least investigated thermoplastic among the engineering polymers employed for ISF, possibly due to its low formability at ambient temperature. However, POM is known as a semicrystalline thermoplastic of good creep and fatigue durability. POM also offers high resistance against chemicals, oil, and fuel corrosion. In addition, POM provides a good surface finish and friction resistance quality. This thesis aims to investigate Friction Stir Incremental Sheet Forming (FSISF) of Polyoxymethylene. Therefore, a comprehensive experimental, analytical and numerical (FEA) study is conducted. The proposed analytical and FEA frameworks are tuned to provide fairly accurate predictions with an affordable simulation cost in terms of the computation time and the required hardware.

A comprehensive experimental campaign is conducted by adopting Design of Experiment (DOE) and response surface methods. Individual and interactive effects of the process parameters, namely tool size, step size, feed rate, and spindle speed on the

process outputs are discussed in terms of forming force, contact temperature, heating rate, and deformation rate. An empirical model is provided to predict the total forming force as a function of the process parameters and time. Also, similar models are developed for the maximum force and the tool-tip temperature. Relatively high sheet formability is achieved, whereas heat-induced defects are avoided. The effects of geometrical parameters on sheet formability are briefly discussed and a new formability criterion is proposed for ISF. Friction in FSISF of POM is experimentally evaluated. Dimensional integrity, thickness distribution, surface quality, the evolution of the material crystallinity, surface hardness, and elastic modulus of POM under specific forming conditions are measured and discussed. A discussion is also provided on fracture in FSISF of POM based on the morphology of the cracks acquired by Scanning Electron Microscopy (SEM).

A joint numerical-analytical method is proposed to efficiently predict force and contact temperature in the FSISF of POM. For this purpose, the mechanism of deformation and stress-strain state is defined based on a membrane analytical framework including the stretch-bending effect. Also, the pronounced bending effect in the initial stage of the forming process is investigated by extending an available analytical framework for deflection of a circular sheet under a lateral concentrated load. The friction-induced heat and temperature distribution in tool and sheet are derived by adopting the Finite Difference Method (FDM). The area of the tool-sheet contact interface is estimated by proposing two geometrical approaches. Predicted forming force and contact temperature are validated by experimental measurements. Friction-induced heat rate and meridional stress component are presented as a function of the equivalent plastic strain for some FSISF benchmarks. The ratio of the plastic strain energy density to the triaxiality is also presented as a function of the final equivalent plastic strain. Accordingly, a brief discussion is provided on the sheet failure in the FSISF process.

It is aimed to establish a framework for a fairly accurate FEA of the FSISF process with an affordable simulation cost. For this purpose, the material constitutive models namely Two-Layer Viscoplastic (TLV), Parallel Rheological Framework (PRF), Three Network (TN), and Johnson-Cook (JC) are discussed and calibrated. A series of comparative FEAs is conducted to identify the best meshing strategies, FSISF tool definition, element type, element size, and mass scaling. Heat partitioning between tool and sheet is discussed in detail by conducting a precise review on the available approximate analytical methods in the literature. Benchmark FSISF tests are considered for simulation. To demonstrate the capability of the proposed FEA methodology, the simulation case studies reflect a broad range of sheet formability, temperature, and stress triaxiality. The simulation results are validated by experimental measurements. A brief discussion and numerical investigation are provided on damage evolution and failure in FSISF of POM.

ÖZETÇE

Özetçe: Sac metal şekillendirme, havacılık ve otomotiv endüstrilerinde yaygın olarak kullanılmakta ve üretim alanının ayrılmaz bir parçasıdır. Günümüzde, son derece rekabetçi olan üretim alanı, daha yüksek düzeyde ürün özelleştirmesi, daha kısa tasarımdan piyasaya sürülme süresi ve daha yüksek üretkenlik talep etmektedir. Çevik imalatın gereksinimleriyle başa çıkmak için yeni sac şekillendirme teknolojisi esnek ve elverişli bir takımlama sistemine sahip olmalıdır. Kademeli Sac Şekillendirme (ISF) yöntemi bilgisayarlı sayısal kontrol (CNC) teknolojisini ve nispeten basit takımlama kullanarak, kalıpsız bir şekillendirme imkanı sunar. Isı destekli ISF, son sac bileşeninin sac şekillendirilebilirliği ve boyutsal doğruluğu açısından umut vaad etmektedir. Küresel ısınma endişeleri nedeniyle, havacılık ve otomotiv endüstrileri artık hafif malzeme ve tasarım ilkelerini uygulamaya teşvik etmektedir. Bu durumda, örneğin otomotiv sektöründe, termoplastik tüketiminde sürekli bir büyümeye yol açmıştır. Son on yılda, araştırmacılar ISF sürecinin mekanizmasını ve çalışma kurallarını anlamak için büyük çaba sarf etmişlerdir. Bu çalışmalar çoğunlukla alüminyum, çelik, titanyum ve magnezyum gibi metalik alaşımları hedef almıştır. Polioksimetilen (POM), ortam sıcaklığında düşük şekillendirilebilirliği nedeniyle, ISF için kullanılan mühendislik polimerleri arasında en az araştırılan termoplastiktir. Bununla birlikte, POM, iyi sürünme ve yorulma dayanıklılığına sahip yarı kristal bir termoplastik olarak bilinir. POM ayrıca kimyasallara, yağa ve yakıt korozyonuna karşı yüksek direnç sunar. Ayrıca POM, iyi bir yüzey kalitesi ve sürtünme direnci kalitesi de sağlamaktadır. Bu tez, Polioksimetilenin Sürtünme Karıştırma Kademeli Levha Şekillendirmesini (FSISF) araştırmaktadır. Bu nedenle kapsamlı deneysel, analitik ve sayısal (FEA) çalışması yapılmştır. Önerilen analitik ve FEA çerçeveleri, hesaplama süresi ve gerekli donanım açısından uygun bir simülasyon maliyeti ile oldukça doğru tahminler sağlayacak şekilde ayarlanmıştır.

Deney tasarım (DOE) ve yanıt yüzeyi yöntemleri benimsenerek kapsamlı bir deneysel çalışma yürütülmüştür. Takım boyu, adım boyu, ilerleme hızı ve iş mili hızı gibi proses parametrelerinin proses çıktıları üzerindeki bireysel ve etkileşimli etkileri, şekillendirme kuvveti, temas sıcaklığı, ısıtma hızı ve deformasyon oranı üzerinden tartışılmıştır. Proses parametrelerinin ve zamanın bir fonksiyonu olarak toplam şekillendirme kuvvetini tahmin etmek için ampirik bir model oluşturulmuştur. Ayrıca maksimum kuvvet ve takım ucu sıcaklığı için benzer modeller geliştirilmiştir. Nispeten yüksek sac şekillendirilebilirliği elde edilirken, ısı kaynaklı kusurlardan kaçınılır. Geometrik parametrelerin sac şekillendirilebilirliği üzerindeki etkileri kısaca tartışılmış ve ISF için yeni bir şekillendirilebilirlik kriteri önerilmiştir. POM'un FSISF'sindeki sürtünme deneysel olarak değerlendirilmiştir. Boyutsal bütünlük, kalınlık dağılımı, yüzey kalitesi,

malzeme kristalliğinin evrimi, yüzey sertliği ve belirli şekillendirme koşulları altında POM'un elastik modülü ölçülmüş ve tartışılmıştır. Taramalı Elektron Mikroskobu (SEM) ile elde edilen çatlakların morfolojisine dayalı olarak POM'un FSISF'sindeki kırılma hakkında da bir tartışma sunulmaktadır.

POM'un FSISF'sinde kuvvet ve temas sıcaklığını verimli bir şekilde tahmin etmek için ortak bir sayısal-analitik yöntem önerilmiştir. Bu amaçla, deformasyon mekanizması ve gerilme-gerinim durumu, esneme-bükülme etkisini içeren bir membran analitik çerçevesine dayalı olarak tanımlanmıştır. Ayrıca, şekillendirme işleminin ilk aşamasında belirgin eğilme etkisi, dairesel bir sacın yanal konsantre yük altında bükülmesi için mevcut bir analitik çerçeve genişletilerek araştırılmıştır. Takım ve sacdaki sürtünme kaynaklı ısı ve sıcaklık dağılımı, Sonlu Fark Metodu (FDM) benimsenerek elde edilmiştir. Takım sayfası temas arayüzünün alanı, iki geometrik yaklaşım önerilerek tahmin edilmiştir. Öngörülen şekillendirme kuvveti ve temas sıcaklığı deneysel ölçümlerle doğrulanmıştır. Sürtünme kaynaklı ısı katsayısı ve meridyonel stres bileşeni, bazı FSISF karşılaştırma ölçütleri için eşdeğer plastik gerinimin bir fonksiyonu olarak sunulmuştur. Plastik şekil değiştirme enerji yoğunluğunun üç eksenliliğe oranı da nihai eşdeğer plastik şekil değiştirmenin bir fonksiyonu olarak sunulmuştur. Buna göre, FSISF sürecindeki sac hatası hakkında kısa bir tartışma da sunulmuştur.

Bu tezde uygun bir simülasyon maliyeti ile FSISF sürecinin doğru sonlu eleman analizi modeli oluşturulması amaçlanmaktadır. Bu amaçla, İki Katmanlı Viskoplastik (TLV), Paralel Reolojik Çerçeve (PRF), Üç Ağ (TN) ve Johnson-Cook (JC) gibi malzeme modelleri tartışılmış ve kalibre edilmiştir. En iyi yüzey oluşturma stratejilerini, FSISF araç tanımını, eleman tipini, eleman boyutunu ve kütle ölçeklemeyi belirlemek için bir dizi karşılaştırmalı FEA yürütülmüştür. Takım ve sac arasındaki ısı dağılımı, literatürde mevcut yaklaşık analitik yöntemler üzerinde bir inceleme yapılarak ayrıntılı olarak tartışılmıştır. Kıstas FSISF testleri simülasyon için kabul edilmiştir. Simülasyon vaka çalışmaları, önerilen FEA metodolojisinin kapasitesini göstermek için çok çeşitli sac şekillendirilebilirliği, sıcaklık ve gerilim üç eksenliliğini yansıtmaktadır. Simülasyon sonuçları deneysel ölçümlerle doğrulanır. POM'un FSISF'sindeki hasar gelişimi ve hatası hakkında kısa bir tartışma sunulmuştur.

ACKNOWLEDGEMENT

While challenging at every turn, it has been enormously rewarding having the opportunity to study at Koc University. This work, and the amazing experience I had during my Ph.D. journey, was possible only through the help and support of many people.

First, I would like to thank my thesis advisor Professor. Dr. Ismail Lazoglu for providing me this opportunity, and for his continued support throughout my research period in Manufacturing and Automation Research Center (MARC).

I would also like to thank my fellow MARC colleagues for their support and friendship. I am also thankful to all the university staff, specifically the members of the GSSE for their professional and friendly attitude. I would also like to thank the respected thesis committee members for their valuable time and comments.

I am most thankful to my wife, parents, and parents-in-law for their unconditional love and continuous support. I am eternally grateful for their patience and prayers through all those years. Last but not least, I am grateful to my dear grandmother, Shahrbanoo, who passed away during my study period, but her memory stays alive in my heart.

TABLE OF CONTENTS

LIST OF TABLES

LIST OF FIGURES

ABBREVIATIONS

Alternative Toolpath	ATP
Asymmetric Incremental Sheet Forming	AISF
Central Composite Design of Experiment	CCD-DOE
Computer Numerical Control	CNC
Continuous Stiffness Measurement	CSM
Design of Experiment	DOE
Ductility Factor	DF
Electric Hot Double-Sided Incremental Forming	EDISF
Field of View	FOV
Finite Difference Analysis	FDA
Finite Difference Method	FDM
Finite Element Analysis	FEA
Flexible Manufacturing Systems	FMS
Forming Limit Diagram	FLD
Forming Rate Indicator	FRI
Friction Stir Incremental Sheet Forming	FSISF
Heat Partitioning Factor	HPF
High Development	HD
High-Density Polyethylene	HDPE
Incremental Sheet Forming	ISF
Johnson-Cook	JC
Linear Heating Rate Index	LHRI
Low Development	LD
Mass Scaling Factor	MSF
Modified Mohr–Coulomb	MMC3
Parallel Rheological Framework	PRF

Partial Differential Equations	PDEs
Polyamide	PA
Polycarbonate	PC
Polyethylene	PE
Polyethylene Terephthalate	PET
Polylactic Acid	PLA
Polyoxymethylene	POM
Polypropylene Random Copolymer	PPRC
Polyvinyl Chloride	PVC
Quasi-Linear Viscoelastic	QLV
Quick Response Manufacturing	QRM
Rapid Freeform Sheet Metal Forming Technology	RAFFT
Rolling Direction	RD
Root Mean Square Error	RMSE
Rotating-Tool ISF	RISF
Scanning Electron Microscopy	SEM
Shape Inclusive Formability	SIF
Single Point Incremental Sheet Forming	SPISF
Strain-Induced Crystallization	SIC
Three Network	TN
Double Tool ISF	DISF
Transverse Direction	TD
Tungsten Carbide	WC
Two-Layer Viscoplastic	TLV
Two Point Incremental Sheet Forming	TPISF
Unidirectional Toolpath	UTP
Vertical Scanning Interferometry	VSI
White Lite Interferometry	WLI
X-Ray Diffraction	XRD

Chapter 1

INTRODUCTION AND LITERATURE REVIEW

1.1 Introduction and overview

Sheet metal forming is an integral part of the manufacturing sector that is vastly used in aerospace, and more extensively, in automotive industries. The highly competitive field of car manufacturing demands more diversity in design, shorter design-to-release time-cycle, and higher productivity. Due to the globally growing environmental concerns, aerospace and automotive industries are urged to implement lightweight design principles. Therefore, new materials, forming technologies, and design principles are required to fulfill such ever-growing needs [1]. Conventional sheet forming technologies namely, bending [2, 3], deep drawing [4, 5], spinning [6–8], stamping [9–11], and stretch forming [12] are comprehensively studied, and widely industrialized. However, the conventional sheet forming processes are largely dependent on punches and dies to provide the required load for bending, shearing, stretching, and generally forming the sheet blank to the desired shape [13]. In many cases, punches and dies are part-specific or dedicated to a single sheet component. Therefore, conventional forming technologies are mainly suitable for mass and large-batch productions. However, the growing demand for tailored products is reinforcing a new trend that is customized manufacturing [14–16]. The rapidly growing market of additive manufacturing exemplifies such a new trend [17]. A novel sheet forming technology to cope with the requirements of customized manufacturing is deemed to have a flexible and highly capable tooling system. By employing the computer numerical control (CNC) technology and simple tooling, Incremental Sheet Forming (ISF) offers a die-less forming possibility. In ISF, localized plastic deformation is incrementally developed by navigating a stylus tool (equipped with a round rigid tip or a roller head) along a prescribed toolpath. Therefore, ISF promises more flexibility in the process, lower production cost, and shorter lead time, in addition to improved formability of material as compared to the conventional sheet forming processes [18–20]. These characteristics outfit ISF for prototyping, rapid production, and low-batch production [21, 22].

As stated before, there has been also an increasing tendency in automotive and aerospace sectors for lightweight design to minimize fuel consumption, and reduce CO_2 emissions. By employing new materials, adopting innovative design principles, and developing novel manufacturing techniques, the weight of the products can be reduced without compromising performance, safety, and cost [23]. As for the application of lightweight materials by transportation industries, consumption of thermoplastics and thermoplastic-matrix composites shows a constantly increasing trend [24]. The polymer processing technologies can be divided into two major categories, namely cold and hot. The conventional cold processing techniques applicable to the production of relatively complex sheet components are stamping, hydroforming, and stretch forming [25]. Cold forming of thermoplastics of low formability at room temperature is troublesome. The conventional hot polymer forming technologies are extrusion, compression molding, injection molding, blow molding, rotational molding, transfer molding, and thermoforming [26]. Since polymers in molten or rubbery states are processed by using the aforesaid hot forming technologies, the heating costs and environmental pollutions are matters of concern [27]. In addition, both hot and cold conventional polymer processing technologies mainly require part-specific punch and dies. This is in contrast to the agility, flexibility, and product customization demands in today's manufacturing sector as discussed before.

Friction Stir Incremental Sheet Forming (FSISF) of thermoplastics is deemed promising to fill the gap. Therefore, tailored production of geometrically complex and lightweight thermoplastic sheet components at elevated temperatures is expected at relatively lower costs, and with a relatively lower CO_2 footprint. This thesis aims at experimental, analytical, and numerical investigation of FSISF of Polyoxymethylene (POM), which is a less-studied engineering semicrystalline thermoplastic of outstanding mechanical, physical and chemical characteristics. This chapter continues with a brief literature review on ISF in general, followed by a detailed review on ISF at elevated temperatures. Afterward, the application of thermoplastics in automotive industries is discussed, followed by a critical review of the ISF of polymers. At the end of this chapter, the thesis outline is pointed out.

1.2 Incremental sheet forming: an overview

Historically, the modern ISF process is originated from the spin and shear forming processes. Mason in 1978 [28], discussed the best sheet forming processes for low batch production, where he outlined the concept of ISF as well. However, Japanese scholars initiated the practical development of the ISF process as known today. Iseki et al. published their research work titled "flexible and incremental sheet metal forming using a spherical roller" in 1989 [29]. Kitazawa's research group also published several works on CNC incremental sheet stretch-expanding of aluminum alloys [30–33]. Moreover, Japanese car manufacturing companies filed several patents on ISF during the last decade of the twenty century. For instance, Matsubara filed two patents on ISF with partial dies in the same period [34]. By the beginning of the twenty-first century, ISF attracted the attention of scholars from South Korea, North America and Canada, Europe, and elsewhere. Kim and Yang (South Korea; 2000) [35] studied the thickness distribution and improvement of the formability of annealed aluminum sheet in the ISF process. Hagan and Jeswiet (Canada; 2003) [36] published the first comparative review on traditional and modern incremental forming technologies, where they discussed incremental forming of non-symmetrical sheet components by using CNC technology.

The incremental sheet forming (ISF) technology offers the great possibility of die-less sheet forming. Such an opportunity is created by making use of a simple tooling system that is made of a rigid shank equipped with a hemispherical tip or a rolling-ball-head. The sheet is fully clamped at the periphery by using a clamping system. The ISF forming tool delicately presses the sheet down by a specific step size. At the same time, the tool is guided along a predefined path by implementing CNC technology. Taking this approach, the sheet is incrementally formed to the desired shape through the accumulation of localized plastic deformations applied by the forming tool. Figure 1.1 provides a schematic view of the basic die-less arrangement of the ISF that is single point incremental forming (SPISF). Apart from the basic die-less arrangement of the ISF

(SPISF) as shown by Figure 1.1, three Two-Point variants of ISF (TPISF), namely TPISF with full die, TPISF with partial die, and TPISF with a counter tool are developed as presented by Figure 1.2.

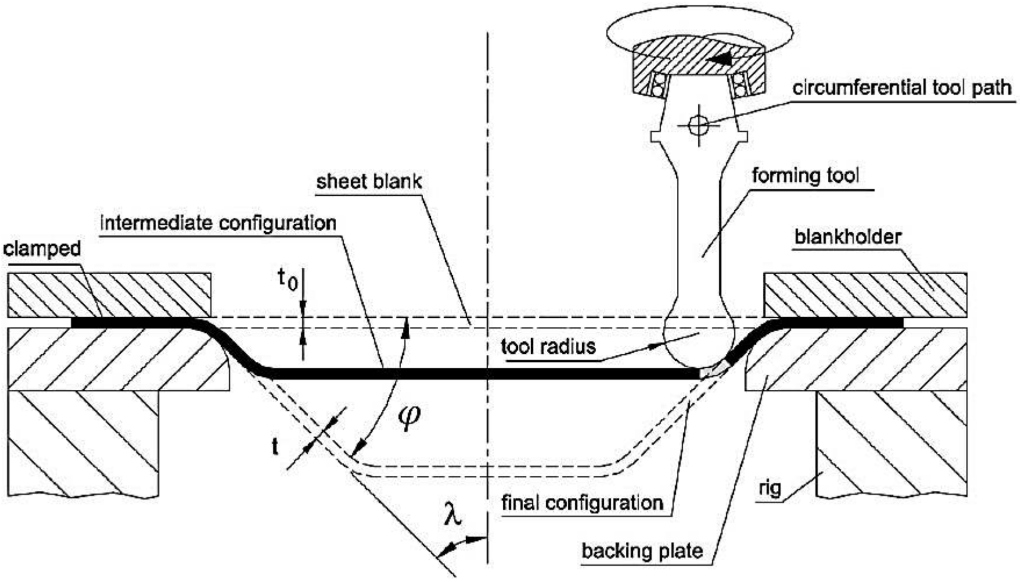

Figure 1.1: A schematic view of the basic arrangement of ISF (SPISF) and some process parameters [37].

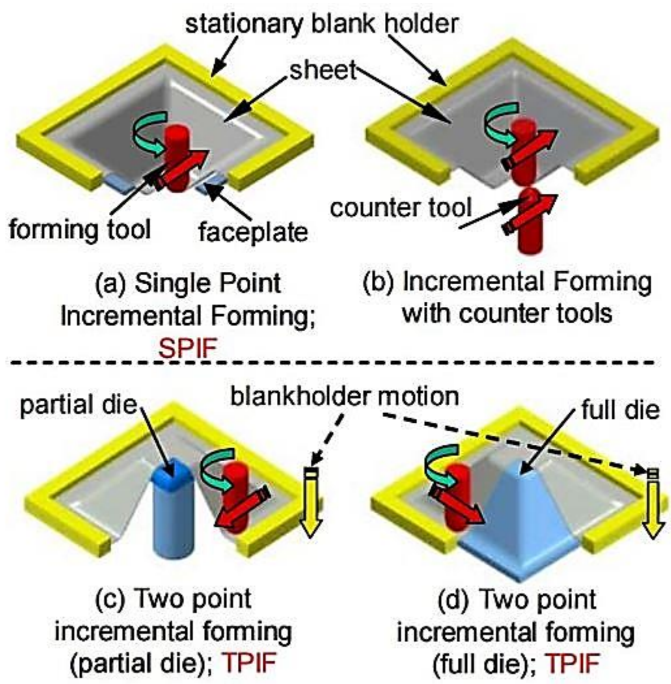

Figure 1.2: Schematic view of single-point incremental forming (SPISF) and variants of two-point incremental forming (TPISF) [38].

The basic die-less SPISF process offers advantages over the TPISF, namely relatively simpler tooling, clamping and control system, lower cost, and higher flexibility. In contrast, TPISF provides more controllability over the geometry of the sheet component as compared to SPISF. Due to the localized nature of deformation in ISF, this process provides better sheet-formability, higher flexibility in processing, lower capital tooling cost, and shorter lead time as compared to conventional sheet forming processes [39]. In contrast, relatively longer processing time and lower dimensional accuracy are the main drawbacks of the ISF process as compared to conventional technologies [18]. Figure 1.3 presents sample sheet components produced by using the basic die-less ISF process [40, 41]. Some of the presented sheet components are hard to be produced by using conventional sheet forming technologies.

(a) (b)

Figure 1.3: Sample sheet components produced by using ISF (a) [40], and (b) [41].

Figure 1.4 presents a 1/8 scale model of the nose section of a Shinkansen (Bullet Train) made by Amino (using SPISF) in Japan [42]. Figure 1.5 present a photo of the Rapid Freeform Sheet Metal Forming Technology (RAFFT) Machine, which is in fact, a TPISF machine developed by a joint contribution of Ford Motor Company, The Boeing Company, Massachusetts Institute of Technology (MIT), and Penn State Erie, The

Behrend College. The sheet component presented in the figure is a 0.4 scale Mustang hood outer made out of an aluminum alloy.

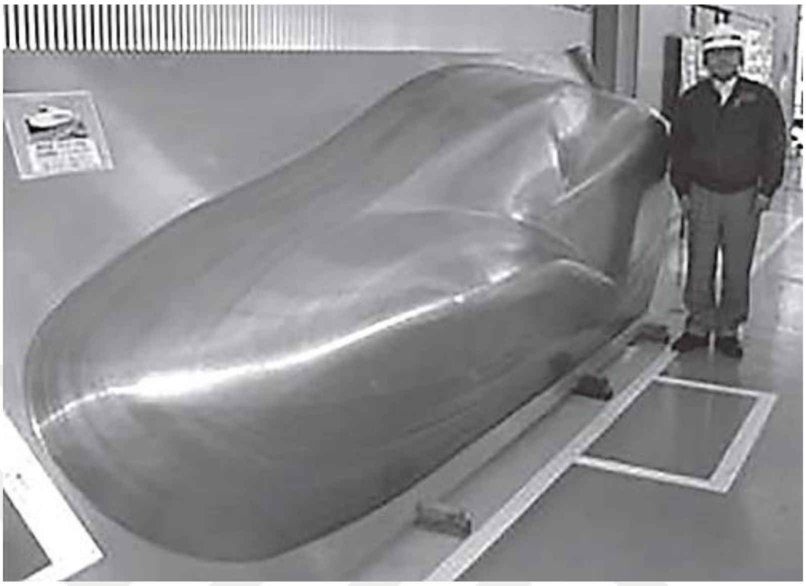

Figure 1.4: A 1/8 scale model of the nose section of a Shinkansen (Bullet Train) made by Amino in Japan [42].

Figure 1.5: Rapid Freeform Sheet Metal Forming Technology (RAFFT) Machine producing a 0.4 scale Mustang hood in Ford Motor Co [43].

The incremental Sheet Forming process has attracted considerable attention from the manufacturing research community during the first decade of the 21st century. A tremendous amount of research work has been devoted to investigating all variant categories of ISF during this period. Therefore, several review papers are published focusing on different aspects of the ISF process. In this section, the major review papers on ISF are briefly discussed based on a chronicle order to provide a systematic overview of the field. Jeswiet et al. [39] discussed the development of the traditional sheet forming technologies involved with localized plastic deformation (such as spinning and shear forming) towards the novel CNC asymmetric incremental sheet forming. They concluded with the effects of process parameters namely, sheet thickness, tool size, step size, forming speed, and wall angle of the sheet component on process outputs namely, sheet formability, surface roughness, forming force, and elastic spring-back effect. They also added that there is a need for further investigations to develop forming strategies leading to the higher dimensional accuracy of the final sheet component. Emmens and Boogaard [44] discussed the mechanism behind the relatively better formability of the sheet in ISF as compared to the conventional forming technologies. They attributed this quality to the localized nature of deformation in ISF. They discussed six stabilizing mechanisms namely contact stress, bending-under-tension, shear, cyclic straining, geometrical inability to grow and hydrostatic stress. They concluded that all the aforesaid mechanisms could postpone the development of necking except the last one, which affects the rupture, but not the forming limit. Emmens et al. [45] provided an overview of the technological development of the ISF process by reviewing the relevant patents filed (1987-2010). They stated that the process gained significant attention, especially from automotive industries, mainly focusing on the high level of flexibility provided by the process (specifically TPISF variants). Echrif and Hrairi [20] reviewed the recent development in ISF at the time (2011) and maintained that further investigation is required in terms of spring back effect and dimensional accuracy, timely-efficient simulation of the process, materials rather than aluminum. They also stated that no numerical simulation is available for ISF of polymers. Taleb Araghi et al. [46] argued that Asymmetric Incremental Sheet Forming (AISF) had not been much industrialized to the date (2011). They maintained that the reason is the strategies proposed to improve the dimensional accuracy, process speed and the scale of feasible geometries had not been enough effective. Therefore, they studied the three hybrid variants of AISF developed at RWTH Aachen University namely, stretch forming combined with ISF, laser-assisted AISF, and hybrid aluminum-steel sheet forming. They concluded that the first hybrid technology could improve the sheet thickness distribution, dimensional accuracy, and processing speed. They also stated that laser-assisted AISF provides a unique possibility for forming hard-to-form sheet alloys such as magnesium and titanium. Reddy et al. [47] wrote a book chapter on toolpath generation and experimental and numerical investigation of formability and dimensional accuracy in different variants of the ISF process. They concluded that the dimensional accuracy is affected by bending at the initial stages of deformation, continuous elastic spring back during the forming process, and global spring back after the tool retraction and unclamping. They stated that predicting the spring back and adopting a compensation strategy with the toolpath is time-consuming. In contrast, TPISF by employing a counter tool was suggested to provide higher dimensional accuracy in complex geometries along with shorter design-to-reals time. Gatea et al. [48] reviewed the ISF literature in terms of the effects of the process parameters on formability, failure, dimensional accuracy, and surface quality of the sheet component. The concluded with several remarks regarding the aforesaid process outputs. They stated that step size and feed rate have a very small effect on sheet formability. They added that a large-size tool used with spiral tool path, and high spindle speed accompanied with low feed rate result in better formability and thickness distribution. In contrast, they concluded that a larger tool increases the chance of fracture. Also, they maintained that cracks develop along the circumferential direction under the effect of tensile stress along the meridional direction. They also stated that spring back could be reduced by increasing the tensile load along the meridional direction. In other words, increasing the sheet thickness, tool size, spindle speed, and feed rate as well as decreasing the step size alleviated the spring back. McAnulty et al. [49] conducted a quantitative and comparative review on 35 papers published on the effects of the process parameters on sheet formability in ISF and concluded with a general statement that the interactive effects of process parameters are less studied in the literature. Due to the same fact, they concluded that the process parameters should be optimized based on the sheet material to achieve the best formability. In other words, conceiving a linear relation between the process outputs and each process parameter is counterproductive. Li et al. [50], first, reviewed deformation mechanisms affecting formability in ISF. Then a critical review of the analytical and numerical simulation of the process was conducted with a special focus on force prediction. Also, hybrid ISF arrangements were discussed. They maintained that contribution of a complex mechanism consisting of bending, stretching and shearing is discussed in the literature. They stated that no agreement is yet reached in the research community on the deriving deformation mechanism in ISF, and a contradiction is evident among the findings of different studies. They also reported that the geometrical models of ISF provide fairly acceptable results, but the effect of the material is neglected by this method. In that sense, Finite Element Analysis (FEA) provides a more comprehensive solution, but the simulation is very expensive in terms of the required time and hardware. They concluded that a timely efficient and fairly accurate simulation approach is still lacking in the literature. Regarding the force prediction, they maintained that several experimental studies are available (mostly on metals), but they lack the physical justification behind the observations, therefore, a need for analytical models is evident. The same conclusion was made regarding the effects of the process parameters on the process outputs such as formability. Behera et al. [51] reviewed ISF literature in terms of the hardware arrangements, deformation and failure mechanisms, process simulation and force prediction methods, toolpath strategies, and sustainability of the process during the 2005-2015 period. They stated that the sheet formability could be improved by the optimization of the process parameters, and by using multi-stage forming and heat-assisted forming. Better prediction of force and failure is expected in the future by the implementation of advanced material models. In addition, fast simulation skims are expected to be implemented for real-time process control in the future. They maintained that ISF would be used as a part of flexible manufacturing systems (FMS) and complex hybrid processes. They also stated that multi-axis tooling, part orientation, and advanced control systems equipped with toolpath optimization skim could provide a better thickness distribution in geometrically complex sheet components made by ISF. Afonso et al. [52] aimed at providing guidelines for integrated design and process skims, including part configuration and design orientation in customized manufacturing of sheet components by using SPISF. Duflou et al. [53] provided a relatively inclusive literature review (2003-2017 period) on several aspects of the SPISF process. They discussed hardware and positioning system, tool, lubrication, clamping fixture and support, forming mechanism and formability, failure mechanism, fracture prediction, process insatiability, several heat-assisted SPISF arrangements, toolpath strategies, part orientation skims, toolpath compensation skims for accuracy improvement, FEA and material models, force and thickness prediction methods, applications of the process, and expected future trend. They maintained that though the geometrical accuracy is still considered as a bottleneck for industrialization of the process, sub-millimeter tolerances is achievable today by adopting optimized multistage toolpath strategies. In addition, heat-assisted SPISF provides the possibility of forming very complex shapes by using verity of materials including hard-to-form alloys. They stated that high speed forming is an available option in terms of hardware, but it depends on strain-rate property of materials as well. They also maintained that SPISF outfits Quick Response Manufacturing (QRM) approach, thus, the process is economically feasible for production of up to few hundreds components depending on part complexity (with relatively low environmental impact). Peng et al. [54] provided a comparative literature review on TPISF with a counter tool (DISF) and SPISF. They stated that the former variant is supposed to provide lower geometrical tolerances, and enhanced material forming stability as compared to the generic variant. They maintained that the application of closed-loop control systems based on the data acquired from the implemented sensors on the tools provide the possibility of toolpath adjustment with the objectives of formability enhancement, accuracy improvement, or a combined objective. They also stated that FEA provides a powerful tool for investigation of deformation in DISF, though the simulation cost and reliable fracture prediction still require further attention from the research community. The concluded that the effects of the relative position of the counter tools, sheet squeezing, tool deflection, the stiffness of the machine, process and toolpath optimization require further investigations. They also added that heat assisted DSIF appears to be promising. Ai et al. [55] reviewed the sheet formability and fracture mechanism in ISF of metallic alloys. Dewang et al. [56] reviewed experimental studies and FEA of hole flanging by using ISF. They concluded that multistage flange forming by ISF offers better sheet formability as compared to conventional press forming methods due to necking stabilization in ISF. Vignesh et al.

[57] also reviewed the literature on multistage ISF for creating components of vertical walls. They concluded that a major drawback of the process is relatively long processing time, along with tool footprint and step formation on the sheet, and sinking defect. Optimization of the process parameters and multi-stage toolpath generation along with fracture analysis are recommended as future works. Lu et al. [58] provided a literature review on strategies to improve dimensional accuracy of sheet components created by ISF. They categorized five enhancement strategies, namely hybrid ISF or TPSPIF, multi-stage ISF, toolpath compensation or toolpath optimization, feedback control and alternative methods (included multi-objective process optimization). The two most investigated strategies are toolpath compensation or toolpath optimization, and feedback control. Multi-stages ISF benefits both formability and dimensional accuracy, but the process is more time-consuming, and it requires rigorous optimization to be effective. Cheng et al. [59] presented an extensive literature review on production of biomedical implants by using ISF, discussing both feasibility of technology and performance of the process (formability, surface quality, and dimensional accuracy). Therefore, tolerances of 1-2 mm in implant products were reported from the literature, and tighter tolerance was recommended by implementing toolpath optimization skims. Physical and chemical surface modification methods were suggested to enhance the biocompatibility of the ISF-made implants. A micro-macro hybrid ISF variant was also proposed for production of biomedical implants.

As pointed out here, heat-assisted ISF is strongly advocated by scholars [51, 53, 54] due to the expected positive effects on both sheet formability and dimensional accuracy of the final sheet component. Such advantages are more pronounced in the case of sheet materials with poor formability at room temperature. Therefore, a detailed literature review on heat-assisted ISF is provided in the next section.

1.3 Heat-assisted incremental sheet forming

Varieties of heating methods have been employed for ISF at elevated temperatures so far. Heat sources in hot ISF include laser, electrical resistive heat, halogen lamp, inductive heating, hot air, hot oil, and friction heating. Duflou et al. [60, 61] reported 50% forming force reduction in robotic dynamic-local hot ISF of Al5182 and 65Cr2 by using a 500W

Nd-YAG laser with a glass fiber beam. This hot ISF resulted in better formability of the sheets as well as an improvement in the dimensional accuracy of the final part. Go¨ttmann et al. [62] designed a coaxial rotating optic system by using a10 kW fiber-coupled diode laser, which was integrated into a CNC forming machine for hot ISF of Ti Grade 2 and Ti Grade 5 (TiAl6V4) sheets. However, the complicated system did not enhance the formality and a premature sheet failure was reported as a result of excessive frictional effects. Mohammadi et al. [63] investigated the effect of different laser spot positioning strategies on forming of bulge in hot ISF forming of AA5182-O sheets. Performing thermal finite element simulations accompanied with experimental validations, they could adopt an optimum laser spot positioning strategy leading to approximately 40% reduction in bulge height (dimensional error). Mohammadi et al. [64] experimentally studied the effect of different heat treatment conditions on the formability of AA2024-T3 in pre-heated sheet incremental forming and laser-assisted ISF. They achieved a 41% increase in formability of sheets with T-temper condition under both preheated and laser-assisted incremental forming conditions, whereas post-forming hardness of the sheet formed by laser-assisted ISF was preserved after natural aging. Mohammadi et al. [65] studied the effect of laser-assisted band hardening on the dimensional accuracy of AISI 5155 steel sheet components formed by laser-assisted ISF. Go¨ttmann et al. [66] developed a closed-loop PID control system by embedding a thermocouple inside the ISF forming tool and close to the tooltip. They investigated the applicability of the control system in laser-assisted and resistance-heating ISF of DC04 sheet and concluded with some remarks to enhance the functionality of the system.

Ambrogio et al. [67] investigated the formability of magnesium alloy AZ31 in electrical-heat-assisted ISF and concluded that an improvement in the formability of the sheet was possible as a result of heating up to 250 °C. In the DC-electrical-heat-assisted ISF method introduced by Ambrogio et al. [68], electrical current (0–1000 A) is supplied to the tool-sheet interface by making a close loop. In their setup, the tool is connected to the power supply by a graphite connector from one side, and the sheet is directly connected to the power supply from the other side. The tool-holder and the base of the sheet clamping device are electrically insulated. The authors drew the workability window of the system for lightweight alloys, namely AA2024-T3, AZ31B-O, and

Ti6Al4V. Fan et al. [69] studied the effects of process parameters, namely tool size, step size, feed rate, and electrical current on the formability of AZ31 magnesium sheet and dimensional errors in $TiAl_2Mn_{1.5}$ titanium sheet components formed by ISF with Joule heating. They concluded that increased electric current could result in improved sheet formability, while increased tool and step size, and higher feed rate could reduce temperature and formability. Fan et al. [70] adopted the same technique to explore a proper temperature range and lubrication method to acquire Ti-6Al-4V titanium sheet components with acceptable formability and surface quality. Therefore, a lubricant film of nickel matrix with MoS2 self-lubricating material and temperature range of 500–600°C were reported to serve the purpose. Fan et al. [71] studied the microstructure, hardness, and tensile strength of the Ti-6Al-4V titanium sheet formed by a similar hot ISF setup. They concluded that a composite with enhanced properties could be achieved, which contained elongated α-phase grains and basketweave structure. They added that single-phase formed sheets require special post-heat-treatments. Fan et al. [72] numerically simulated electric hot ISF of Ti-6Al-4V titanium sheet by using the MSC commercial FEA package (hexahedral elemental dimension: 2.5×2.5×0.5 mm, i.e. two elements along the sheet thickness). The paper does not discuss important simulation details such as loading, boundary conditions, and heat partitioning between tool and sheet. Moreover, simulation outcomes are not validated against experimental results. The authors stated that by controlling the bending in the initial forming stage, the overall dimensional accuracy could be improved. Le Van and Nguyen Thanh [73] developed a hot ISF setup based on Joule heating, in which the close electrical loop is merely created in the sheet so that the temperature of the whole sheet could be increased uniformly. They reported that the formability of both AA5055 aluminum and AZ31 magnesium alloys could be improved by adopting this method. They also concluded that the interactive effects of step size and feed rate played a significant role in the formability of AZ31 alloy, while such an interactive effect was negligible in the case of AA5055 alloy. Shi et al. [74] developed a new algorithm to generate a helical toolpath for electric hot ISF of low carbon steel DC04. Therefore, an excessive electrical discharge was avoided. Such an electrical discharge occurs when employing high current values, high forming speeds, and a traditional contour toolpath. By taking this approach, a better formability and surface quality of the sheet with less tool wearing and less dimensional errors were reported to be achievable (with electrical current range of 300 to 400 A). David and Jeswiet [75] studied the effect of current density in electric hot ISF of AA6061-T6 alloy and concluded that a significant improvement in formability was possible by employing a proper current density range. Bao et al. [76] developed an electropulse-assisted ISF technique and investigated the formability of AZ31B alloy under the effect of electro-plasticity. They concluded that the formability of the sheet could be significantly improved (from a final angle of 39.6° in traditional ISF to 70°) under the effect of root mean square of peak current density. Moreover, they explored that electropulse could decrease the dynamic recrystallization temperature of the alloy. Thus, the recrystallization process was accelerated, in turn, the cracks could be confined. Honarpisheh et al. [77] conducted experimental and numerical investigations on the effects of forming angle, tool size and step size in electric hot ISF of Ti-6Al-4V alloy (current: 400 A – temperature: 400 to 500 °C). They used the commercial FEA package Abaqus, Johnson-Cook (JC) material model, and C3D8RT solid element. However, important simulation details such as thermal loading and boundary conditions, and heat partitioning between tool and sheet are not discussed in the paper. Khazaali and Fereshteh-Saniee [78] experimentally studied the effects of tool and step size and forming temperature on the formability and elastic spring-back of Ti-6Al-4V sheet in electric hot ISF (simple groove forming). They concluded that forming temperature had a major effect so that increasing the temperature resulted in improving the formability and decreasing the elastic spring back. To address the severe tool-sheet wear in electric hot ISF, Liu et al. [79] developed a new tooling system by adopting different rolling tool-heads and water cooling channels inside the tool shanks. Therefore, they reported less tool wear and better surface roughness in electric hot ISF of Ti6Al4V (T3 and T4) sheets by employing the new tooling system. Amini Najafabady and Ghaei [80] developed an electric hot ISF device working with alternative current (previous setups work with DC). Using this device, they formed Ti-6Al-4V alloy sheets and concluded that dimensional accuracy could be improved due to the heat; the dimensional error was maximum near the flange; surface roughness increased by increasing the step size, and hardness increased in the forming area from the flange to the apex. Xu et al. [81] developed an electric hot double-sided incremental forming (EDISF) device with a force-controlled slave tool. They formed AZ31B magnesium alloy sheets and concluded that the EDISF was more advantageous as compared to traditional single sided technology (ESISF); the solid tool had a better performance as compared to the rolling tool, and the hybrid DSIF toolpath strategy adopted in the study improved the dimensional accuracy of the final sheet component. Li et al. [82] experimentally investigated the effects of tool size, step size, feed rate, and current on temperature (max., avg., and max. deference) in electric hot ISF of AA1060 sheet by adopting Box–Behnken response surface method. They concluded that the tool size had the most significant effect on the forming temperature, and the heat could generally improve the dimensional accuracy of the final part. Magnus [83, 84], in the first part, provides a critical brief literature review on ISF at elevated temperatures, then a simplified analytical framework is developed to explain the effects of the major influencing parameters on the forming zone temperature due to Joule heating. In the second part, the architecture of a novel EDISF setup with two industrial six-axis robots programmed with KRL, and equipped with force-torque sensors is presented. The electric power supply was a mid-frequency welding inverter (1 kHz) with a two-stage mid-frequency transformer that could alternatively provide a voltage of 6.3 or 13.2 V and output current of 3000 A (using a Siemens S7 PLC). Also, a long-wave IR camera from Optris GmbH was used for temperature measurement. An advanced tooling system with internal channels for cooling liquid and removable tooltips of variant shapes was also designed and presented. Therefore, the author reported reduced forming forces, reduced spring-back and dimensional errors, reduced tool and sheet wears and increased formability of Ti6Al4V sheet formed by the presented EDISF system. Min et al. [85] developed an analytical model to predict the local forming temperature as a function of geometric and process parameters in an electric hot ISF system. The model was validated by isothermally forming two high strength steels (CP-K 60/78 and a DP1000) at 873 K and measuring the maximum temperature by an IR camera. It was also explored that the tool size and the forming angle had the most significant effects on the forming temperature under Joule heating. Pacheco and Silveira [86] conducted a numerical investigation by using RADIOSS FEA package to study the stress-strain states in hot ISF of 1050 aluminum sheet with and without pre-heating (using shell elements). Details on thermal boundary conditions and heat partitioning between tool and sheet are not discussed, and the FEA outcomes are not experimentally validated. They concluded that heat could result in more dimensional error due to the residual stresses during cooling, and the larger the tool size the worse could be such an effect.

Al-Obaidi et al. [87] developed an induction hot ISF system that the inductor moves synchronized with the tool and beneath the sheet. Using this system, they incrementally formed high-strength steel alloys, namely 22MnB5, DP 980, and DC04, and concluded that the induction heating could result in lower forming force (up to ~60%), lower residual stresses, lower spring-back, and higher dimensional accuracy. Al-Obaidi et al. [88] used the same apparatus to incrementally form the high-strength steel alloys HCT980C. They reported that the forming force was decreased by 66.63%, the geometrical accuracy was improved at 15 kW induction power, and formability was improved (forming angle of 70° was reached). Ambrogio et al. [89] used an inductive hot ISF system equipped with a moving cryogenic cooling system to incrementally form a Ti-6Al-4V alloy sheet at 700°C. They stated that the meta-dynamic and static recrystallization could be suppressed through this process.

Kim et al. [90] used halogen lamps to incrementally form magnesium AZ31 alloy sheets at 100, 200, 250, and 300 °C. They concluded that by increase in temperature, formability increased. Ji and Park [91] used hot air to incrementally form magnesium AZ31 alloy sheets at temperatures 20, 100, 150, 200, and 250 °C. They concluded that the formability of the sheet increased by an increase in temperature. The same authors [92] employed the same method to incrementally form AZ31 alloy sheets. They concluded that a significant increase in formability of sheets at 150 °C was due to the sudden decrease in the grain size. Galdos et al. [93] used hot oil to incrementally form the magnesium AZ31 alloy sheet. They concluded that the best formability was achieved at 250 °C due to full recrystallization of the microstructure.

Durante et al. [94] investigated the effect of the rotational speed of the forming tool on forming force, friction coefficient, temperature, and surface roughness in the ISF of AA7075-T0 alloy sheet. They concluded that as the rotational speed increases, the temperature increases, the forming force decreases, and the surface roughness does not show a significant change. Duc-Toan et al. [95] intended to investigate (experimentally and numerically) the ductile fracture in ISF of magnesium alloy sheet, when employing a rotating tool (RISF). By using the JC model and ductile fracture criteria in Abaqus, they claimed that the fracture could be enough accurately predicted. Details on thermal boundary conditions and heat partitioning between tool and sheet are not discussed. Same authors [96] extended the FEA in the previous study and concluded that by slope angles smaller than 60°, the ductile fracture integral was less than 1 (no fracture). Also increasing the tool size and step size, formability was decreased. Park et al. [97] studied the strain distribution (including sheet thickness distribution) and the forming limit diagram (FLD) in the RISF of magnesium alloy sheets. They concluded that a smaller tool size and higher temperature moved the forming limit upwards (improved formability). Xu et al. [98] investigated the effect of rotational speed (0 to 7000 rpm) of the forming tool on temperature, formability, and force in the ISF of AA5052-H32. They reported that at very low rotational speed (0-500 rpm), formability increased under the effect of reduced friction; at low rotational speed (500-1000 rpm) formability reduced due to reduction in through-thickness-shear; at high rotational speed (1000-3000 rpm) friction-induced-heat resulted in better formability and very high rotational speed (3000-7000 rpm) triggered recrystallization of the microstructure, so formability was further improved. Buffa et al. [99] experimentally investigated the effect of the rotational speed of the tool (100-10000 rpm) on formability of AA1050-O, AA1050-H24, and AA6082-T6. Therefore, the maximum forming angle was increased by 7.5°, 10°, and 12.5°; the average grain size was reduced by approximately 70%, and the micro hardness was decreased by 45%. Khalatbari et al. [100] employed DOE to extensively investigate the effect of the process parameters namely sheet thickness, tool size, step size, spindle rotational speed, and linear forming speed on formability of AA3003-H12 sheet in ISF process. Adopting response surface method and optimization, they showed that high-speed ISF of the aluminum sheet was possible (at least 5000 mm/min), whereas 90% of the maximum achievable formability was preserved. They also highlighted the significant contribution of the rotational speed of the tool (3000 rpm) to maximizing the formability. Davarpanah et al. [101] experimentally investigated the effects of the rotational speed of tool and pitch size on failure mode (tearing or wrinkling), forming force, crystallinity, and void density in ISF of polylactic acid (PLA) and polyvinyl chloride (PVC). They concluded that a larger pitch size could lead to better formability, but more wrinkling was observed and the void density increased as well. They also maintained that by increasing the rotational spindle speed, the chance of wrinkling also increased, whereas, force components decreased. Wang et al. [102] investigated the effects of sheet thickness, slope angle, spindle speed, step size, tool size, and feed rate on forming temperature in the ISF of AZ31B magnesium alloy. For this purpose, sheet thickness varied over two levels, and other parameters varied over three levels. They concluded that the temperature significantly increased by an increase in spindle speed, sheet thickness, step size, but it reduced by the increase in feed rate. Baharudin et al. [103], by adopting a Taguchi DOE, investigated the effects of spindle speed, step size, tool size, and feed rate on forming force in the ISF of AA6061-T6 aluminum alloy. They concluded that the spindle speed had the most significant effect on forming force, followed by feed rate, step size, and tool size. Liy [104] investigated formability, surface roughness, tensile strength, and micro-hardness of incrementally formed 7075 aluminum alloy sheets under the effect of several spindle speeds. They stated that by an increase in spindle speed; formability generally improved; the surface roughness decreased (specifically above 2000 rpm); tensile strength and micro-hardness decreased (for 4000-7000 rpm). Uheida et al. [105] investigated the effect of the direction of the spindle speed (1940 rpm) on temperature, formability, force, dimensional accuracy, and surface quality in ISF of CP titanium sheet. They maintained that when rotational spindle speed and feed (linear forming speed) were in the same direction, better formability and dimensional accuracy were achievable as compared to the case that the previously mentioned velocities were in the opposite directions. However, surface quality was poorer when velocities were in the same direction.

As indicated by reviewing the literature on heat-assisted ISF, the majority of studies are performed on metallic alloys, namely magnesium, titanium, aluminum, low carbon steel, and high-strength steel. The most popular method in the literature is electric hot ISF. This method is capable of elevating temperature up to 600°C, which is quite enough for forming the aforesaid alloys. The required apparatus is less complicated and more cost-effective as compared to laser-assisted ISF. This method also provides more controllability over the produced heat and temperature (independent of ISF process parameters) specifically as compared to friction-assisted hot ISF. The main drawback of this technique is poor surface quality and significant tool-sheet wearing (due to electric sparks). Moreover, electric hot ISF does not apply to polymeric sheets. Considering the literature on heat-assisted ISF, a very limited number of studies are performed on heat-assisted ISF of polymers (4% of the reviewed literature). However, as stated in the first section of the current chapter, there has been an increasing tendency in automotive and aerospace sectors for lightweight design by application of thermoplastics. Therefore, the next section is devoted to a discussion on the consumption of thermoplastics by manufacturing sectors, specifically automotive industries. The next section is in turn, followed by a literature review on the ISF of polymers.

1.4 Consumption of thermoplastics for lightweight manufacturing

The application of plastics (thermoplastics and thermosets) in various industries including car manufacturing has been showing continuous and considerable growth during the last 50 years. In contrast, the consumption of different metallic alloys by the automotive sector renders a decreasing weight percentage in the same period. Such a trend is reflected by a report presented by Weill et al. (Kearney Insitute) [24] that estimates the average weight percentage of metals and plastics consumed in the production of vehicles from 1970 to 2020 (Figure 1.6).

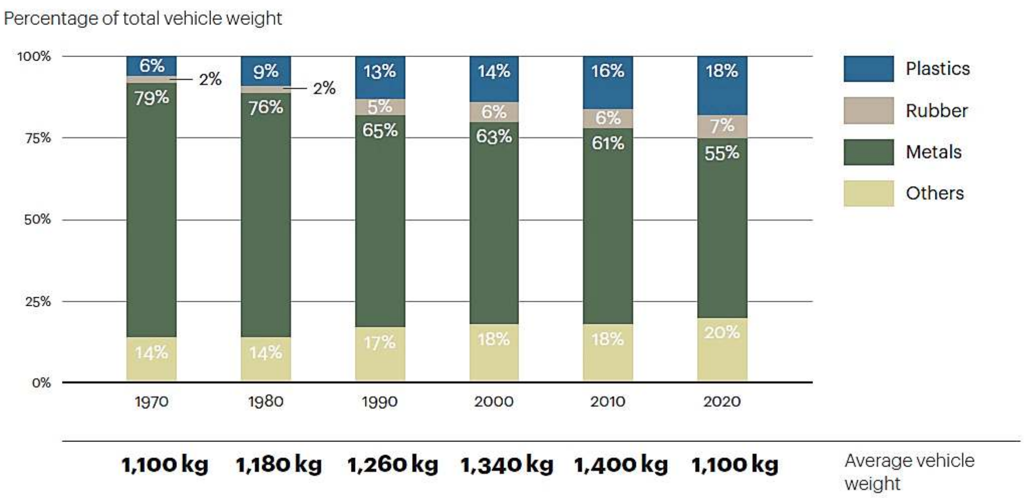

Figure 1.6: Average weight percentage of plastics usage in automobiles from 1970 to 2020 [24].

Plastics have much less density and melting temperature as compared to widely used metals such as steel and aluminum (e.g. aluminum is over twice as heavy as the majority of plastics). Such a growing trend in the application of plastics in automotive industries is partially motivated by increasing demand for low-weight cars, which translates to a reduction in fuel consumption. This is favorable not only because of the cost directly linked to reducing the fuel consumption, but also it is crucial to address the globally increasing concerns about CO_2 emission.

Research conducted by Lotus Engineering Inc. [106] for The International Council on Clean Transportation can provide a practical example for an industrial light-weight vehicle design. As a part of this research work, potential materials and methods for weight reduction in a base-design automobile, Toyota Venza (2009), were investigated. For this purpose, two different vehicle designs were studied. The first concept, so-called "Low Development" (LD), targeted a weight reduction of 20% as compared to the base design by employing available technologies between 2014 and 2017. The second concept, so-called "High Development" (HD), aimed at weight reduction of 40% as compared to the base design by using the available technologies between 2017 and 2020. Both redesign processes encompassed all non-powertrain subsystems, namely body structure, closures, front and rear bumpers, glazing, interior, chassis, air conditioning, and electrical components. Figure 1.7 represents the result of the research in terms of the contribution of different materials including plastics, conventional and non-conventional metallic alloys to each particular lightweight designed car. It is worth mentioning that the cost factors for LD and HD approaches are respectively 97.9% and 103.0% with respect to the base design. The cost factors confirm the cost-effectiveness of the High Weight-Reduction Design in the short time and long time (considering the fuel consumption).

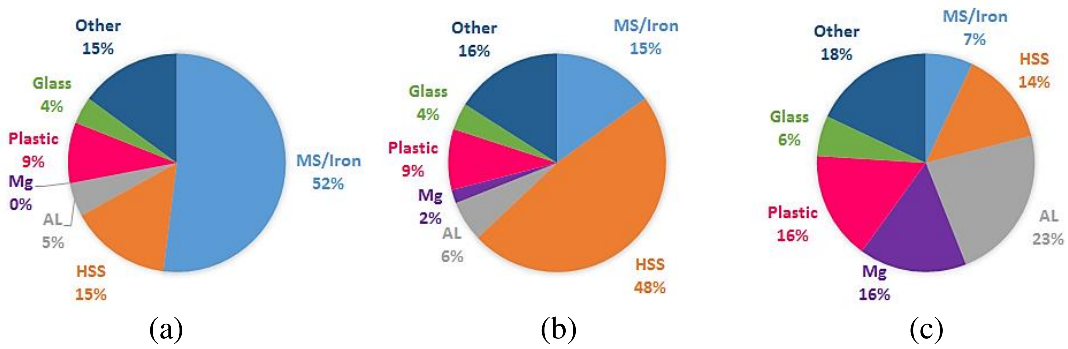

Figure 1.7: Contribution of different materials in (a) Base design Toyota Venza (2009); (b) Low Weight-Reduction Design with 21.5% mass reduction (2014-2017); (c) High Weight-Reduction Design with 38.5% mass reduction (2017-2020) [106].

As it is evident from this figure, the application of plastics for light-weight car design increases from 9% for the base design in 2009 to 16% for a high weight-reduction design in 2020. The increasing trend of plastics usage in car manufacturing as inferred by this specific case study is in agreement with the growing trend of average weight percentage of plastics usage in cars from 1970 to 2020 as represented by the former study (Figure 1.6).

Due to the lower density and melting temperature of thermoplastics as compared to conventional metallic alloys, they can be easily formed into geometrically complex components. By producing more complex parts, the need for assembly and the relevant costs can be also diminished. Some attractive features of thermoplastics are related to their cosmetic properties, for instance, good surface finish, and availability of different colors, which eliminates the need for painting. Durability and resistance to corrosion and scratch, good noise and damping properties, and impact strength are also among the advantages of thermoplastics. However, the application of thermoplastics in car manufacturing requires some challenges to be faced. From the cost perspective, steel (similar to the most conventionally used metals in the automotive sector), has a lower price as compared to most of the thermoplastics. Moreover, the price of the thermoplastics is dependent on the oil price, which is fluctuating and unstable. Another issue is that a limited number of plastics suppliers are available worldwide being capable of producing a variety of thermoplastics. Steel also represents more flexibility when it comes to processing and joining technologies. Though production of environment-friendly bioplastics is steadily growing and the majority of thermoplastics are recyclable, debris lasts long in the environment. Various polymers, namely PP, PUR, ABS, PVC, PE, PA, POM, PC, LCP, PBT, PPS, SMA, UP, and ASA have applications in car manufacturing. However, the first four thermoplastics as mentioned above are expected to form 70% of polymers usage in auto industries [24, 107]. Table 1.1 provides a brief overview of the application of thermoplastics in automobiles. Figure 1.8 provides information regarding the application of thermoplastics, specifically Polyoxymethylene (POM) in car manufacturing.

Table 1.1: An overview of the application of thermoplastics in a typical car [107].

Components	Main Types of Plastics	Avg. Weight in Cars (kg)
Bumpers	PS, ABS, PC/PBT	10.0
Seating	PUR, PP, PVC, ABS, PA	13.0
Dashboard	PP, ABS, SMA, PPE, PC	7.0
Fuel systems	HDPE, POM, PA, PP, PBT	6.0
Body (including panels)	PP, PPE, UP	6.0
Under-bonnet components	PA, PP, PBT	9.0
Interior trim	PP, ABS, PET, POM, PVC	20.0
Electrical components	PP, PE, PBT, PA, PVC	7.0
Exterior trim	ABS, PA, PBT, POM, ASA, PP	4.0
Lighting	PC, PBT, ABS, PMMA, UP	5.0
Upholstery	PVC, PUR, PP, PE	8.0
Liquid reservoirs	PP, PE, PA	1.0

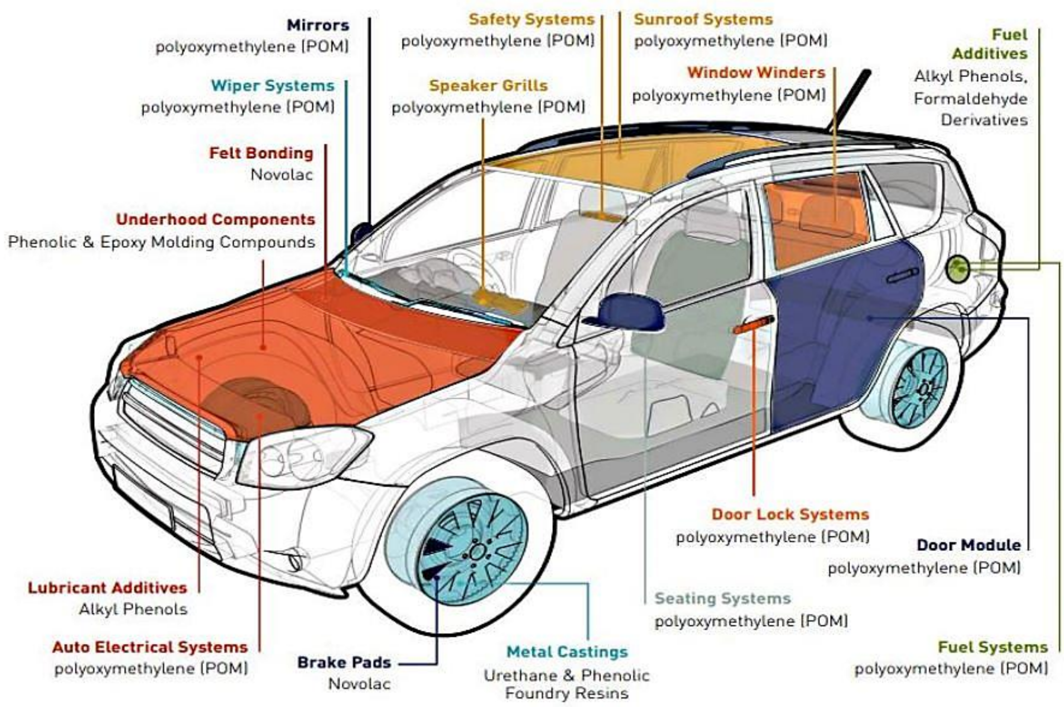

Figure 1.8: Application of thermoplastics, specifically Polyoxymethylene (POM) in car manufacturing [108].

1.5 Incremental sheet forming of thermoplastics

During the last decade, a great deal of effort has been devoted by scholars to understand the mechanism and governing rules of the ISF process. Several attempts have been also made to investigate the effect of different process parameters on the formability of sheet as well as dimensional accuracy and surface quality of finish part in this process. These studies have mostly targeted sheet metals namely aluminum, steel, titanium, and magnesium. For example, in the literature review conducted by Liu [109] on heat-assisted incremental forming strategies, only 3% of the research work was related to polymers.

As discussed in the previous section, thermoplastics represent a significant fraction of the raw materials currently used by manufacturing companies including automotive industries [106], and it still shows a growing trend [24]. While conventional forming processes are mainly appropriate for mass production, increasing demand for tailored-customized products suggests the need for developing new polymer processing techniques. Such technologies should perfectly outfit low batch-size production in a short lead-time. The incremental Sheet Forming (ISF) process appears to provide the required agility, flexibility, and cost-effectiveness for this purpose.

Franzen et al. [37] investigated the effect of blank thickness and tool size on the formability of commercial PVC sheet based on the maximum achievable forming angle. They recognized three different modes of failure in ISF of PVC induced by pure meridional tensile stress, wrinkling of sheet material near apex, and the combination of bending and shear stress. Figure 1.9 demonstrates the three aforesaid modes of failure. The same authors extended the mentioned study by including the effect of feed rate and the initial forming angle to investigate formability and dimensional accuracy of several polymers, namely PVC, Polyoxymethylene (POM), Polyethylene (PE), Polyamide (PA), and Polycarbonate (PC) under ISF [110]. The increase in initial forming angle was found to induce a reduction in formability of all investigated thermoplastics except for POM. However, the overall formability of POM was reported to be considerably lower than other polymers. In that study, PVC and PE exhibited the minimum and the maximum dimensional error, respectively. Figure 1.10 shows the truncated hyperboloid ISF specimens formed throughout this study and the formability of each thermoplastic sheet.

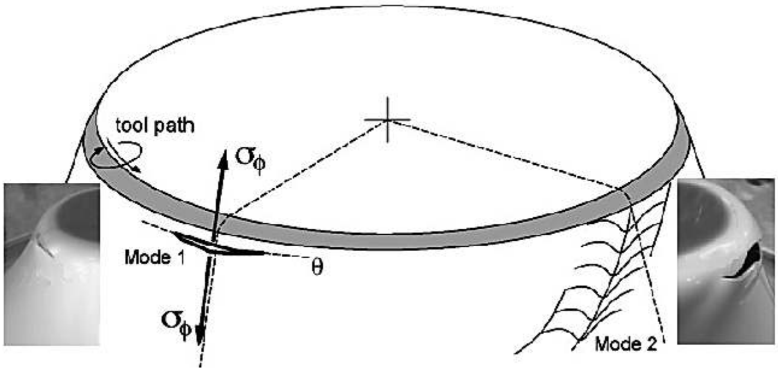

(a)

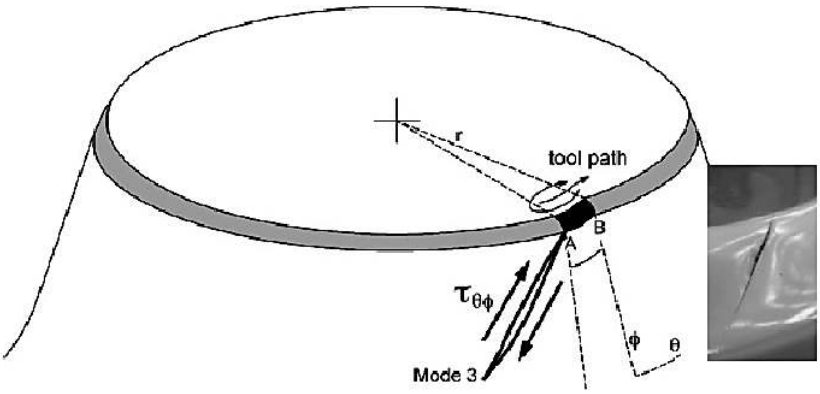

(b)

Figure 1.9: Fracture modes one and two (a), and three (b) in a truncated hyper-bolide ISF specimens as described by Franzen et al. [37].

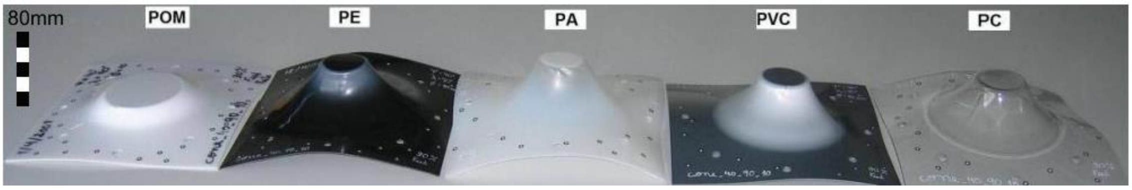

Figure 1.10: The truncated hyperboloid ISF benchmarks formed by Franzen et al. [110] demonstrating the formability of each thermoplastic sheet.

The same three modes of failure were observed in this study as well. A so-called "Ductility Factor" (DF), defined as the square of the ratio of fracture toughness to the yield strength of the material, was identified to significantly contribute towards the formability of polymeric material. An increase in initial wall angle generally resulted in a decrease in the maximum achievable forming angle, except for POM. Failure of POM and PC occurred according to mode 1. In the case of PA and PE, failure mode 2 was observed when the initial forming angle was set to 40°, 50°, and 60°. However, in the case of a small initial wall angle (30°), failure mode 1 was observed for PA and PE. PVC was reported to show controversial failure including all the three modes, based on the process parameters and the sheet surface quality (scratches, etc.). Stress whitening in PVC specimens was attributed to the crazing mechanism. Regarding the dimensional accuracy of the final parts, the spring back effect was attributed to the ratio of the yield stress over multiplication of the elastic modulus and sheet thickness.

By taking a similar approach, Martins et al. [111] maintained that increase in initial wall angle from 40° to 60°, and the tool-tip diameter from 5 to 7.5 mm led to a decrease in the formability of polymeric sheets. They also pointed out that an increase in sheet thickness from 2 mm to 3 mm improved the formability. Although PA and PVC rendered formability of about average value (75.4 °), PE reached the largest value of 81°, and POM failed at the initial stages of forming. As evident from Figure 1.11a, deformation in ISF of PVC occurred under plane strain condition without a significant necking before fracture. Figure 1.11b represents the stress whitening in the studied thermoplastics; therefore, PVC and POM rendered the maximum and the minimum color change, respectively. This observation could imply that the volume strain in POM is relatively insignificant. The authors dismissed POM for ISF, due to its inferior formability as compared to the other polymers.

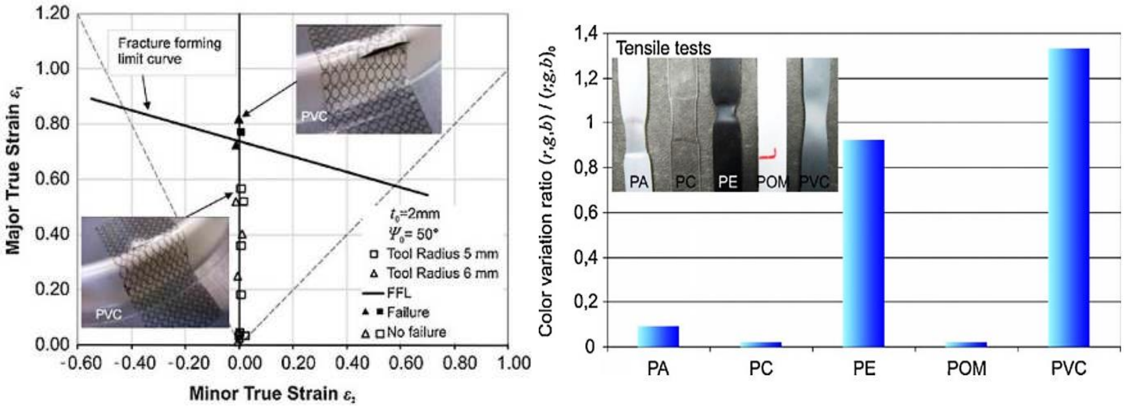

(a) (b)

Figure 1.11: Experimental principal strains in ISF of PVC (a); and stress-induced color change in PA, PC, PE, POM, and PVC [111].

Silva et al. [112] attempted to provide an insight into the mechanism of incremental forming of PVC sheets. For this purpose, they extended the membrane analysis approach proposed by Silva et al. [113] for the ISF of metals. They employed a pressure-sensitive version of von Mises yield function and the associated flow rule, which are conventionally applied to the cold forming of polymers. This method was based on some simplifying assumptions such as neglecting the effects of strain hardening, strain rate, the anisotropy of material properties, bending, and friction in the circumferential direction. They argued for the positive effect of the thicker sheet, larger tool diameter, smaller initial wall angle, and crazing phenomenon on improving the formability of PVC sheet in the ISF process. Marques et al. [114] followed a very similar approach to investigate the formability of thermoplastic sheets, namely polyethylene terephthalate (PET), PA, PVC, and PC in the ISF process. In their ISF experiments, they varied the diameter of the tools and the initial forming angles over three different magnitudes while letting the forming tool freely rotate (spin) along its longitudinal axis. Adopting an initial forming angle of 30°, they reported a maximum achievable forming angle of 90° for PA and PET. They observed a negligible change in density of PET, PA, and PC after forming, as compared to a significant deformation-induced change in the density of PVC (Figure 1.12). Therefore, they concluded that the effect of crazing on the formability of the three previously mentioned polymers was negligible as compared to PVC. Figure 1.13 demonstrates the principal strains at the external surface of the ISF truncated conical specimens made of PC and PET. Though different initial sheet thicknesses (Figure 1.13a) and several wall angles (Figure 1.13b) are adopted, forming limit diagrams represent a plane strain condition in the ISF of thermoplastics (for conical specimens).

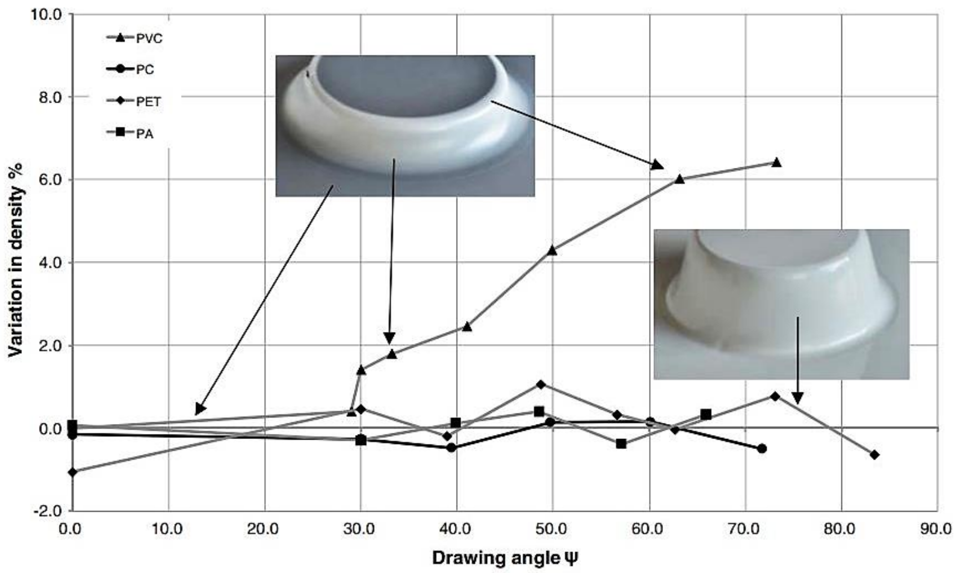

Figure 1.12: Variation of density as a function of slope angle in conical ISF specimens made of PVC, PC, PET, and PA [114].

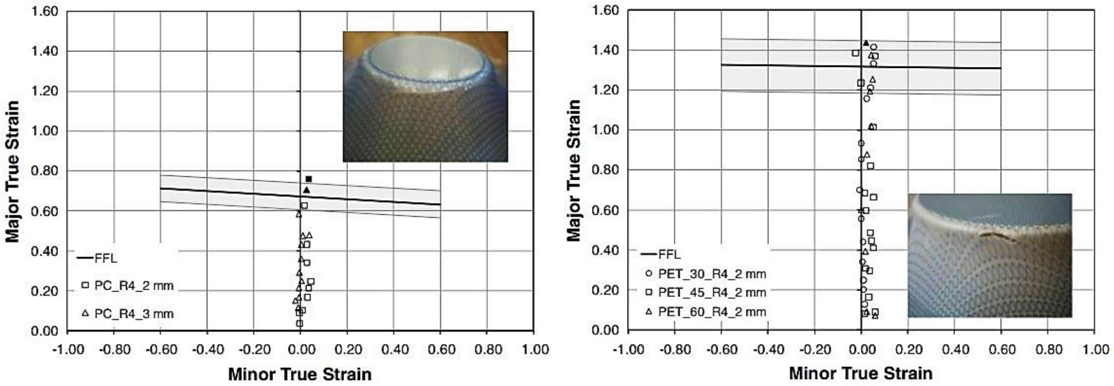

(a) (b)

Figure 1.13: Experimental principal strains in truncated conical ISF specimens made of PC (a), and PET (b) [114].

Silva et al. [115] investigated the possibility of incremental multi-stage hole-flange forming of PET and PC sheets. By experimentally drawing the forming limit diagram, they concluded that plane strain stretching accompanied by bending is the driving mechanism of deformation in the process. They also reported that PC sheets failed at the second stage (70°), while PET sheets could be perfectly formed to flanges of vertical walls, thanks to the relatively high fracture toughness and semicrystalline structure of the material. A schematic view of the process setup is shown in Figure 1.14.

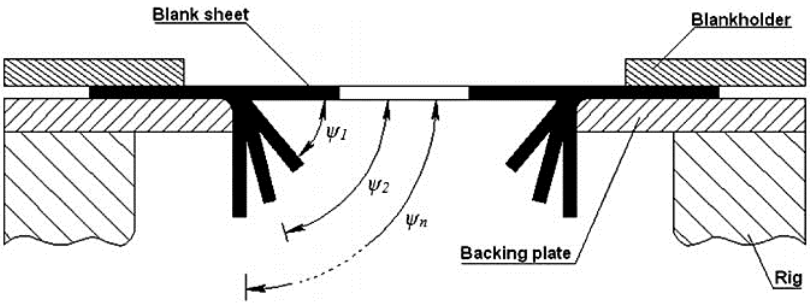

Figure 1.14: An schematic view of the multistage SPISF hole flanging process [115].

As stated before, the analytical models proposed by Silva et al. [112] and Marques et al. [114] involve several simplifying assumptions. Yonan et al. [116] aimed to propose a proper constitutive model for Finite Element Analysis (FEA) of incremental forming of thermoplastic sheets, namely PC, PVC, and high-density polyethylene (HDPE). However, the effects of temperature and strain hardening are neglected in their model. Yonan et al. [117] developed a finite strain extension of the nonlinear viscoplastic material model proposed by Yonan et al. [118]. Despite the simplifying assumptions made for post-uniform deformation and the relevant hardening-softening effects, the model was reported to reasonably predict forces in cold forming of PVC (Figure 1.15). Nonetheless, by increasing the sheet thickness, planar forces were overestimated by FEA, which could be due to an increase in the bending effect.

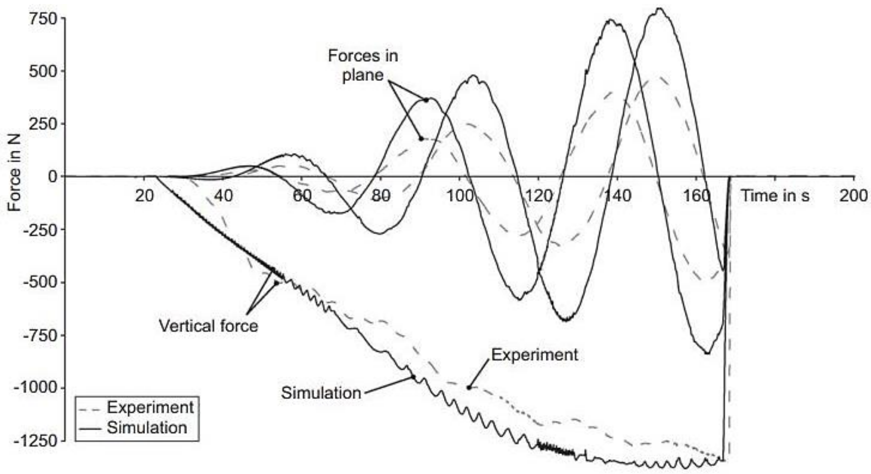

Figure 1.15: Force predicted by FEA in ISF of PVC [117].

Davarpanah et al. [101] experimentally investigated the effect of step size and the rotational speed of tool on forming forces, failure modes, void content, and crystallinity of PVC and bio-based polylactic acid (PLA) of thicknesses 1.5 mm and 0.7 mm, respectively. They maintained that increase in spindle speed had no significant positive effect on formability, but it could lead to wrinkling or galling defects, specifically in PVC specimens. They did not derive any meaningful relation between void volume density and the formability of PVC sheets. However, failure mode 1 was delayed by observing an increase of void volume density in PLA specimens. The higher crystallinity of the formed polymers as compared to that of as-received material was linked to strain-induced crystallization (SIC). Bagudanch et al. [119] employed two levels of step size, tool diameter, feed rate, sheet thickness, and spindle speed in an experimental investigation of PVC in the ISF process. They concluded that the larger the tool diameter and the sheet thickness, the higher the force magnitude along the tool direction. However, the larger step size created a minor increase in the force magnitude. They also reported a decrease in the forming force by altering the rotational speed of the tool from free-to-rotate to 1000 and 2000 rpm. Increasing tool diameter, step size, and forming speed from 6 to 10 mm, 0.2 to 0.5 mm, and 1500 to 3000 mm/min, respectively, resulted in better formability.

Experimentally drawing the forming limit diagram (FLD), they concluded that deformation mode in pyramid specimens' wall was a plane strain, while it was bi-axial stretching at corners. They also reported that an increase in step size and spindle speed resulted in larger R_a values on the surface. Durante et al. [120] studied the effect of two toolpath strategies namely Unidirectional Toolpath (UTP) and an Alternative Toolpath (ATP) along with two types of tools with rigid and roller heads on formability and twisting defect in SPISF of polycarbonate (PC) sheet. They concluded that the ATP strategy adopted with a tool of rolling head improved sheet formability and significantly reduced the angle of twisting. Figure 1.16 shows their approach and results.

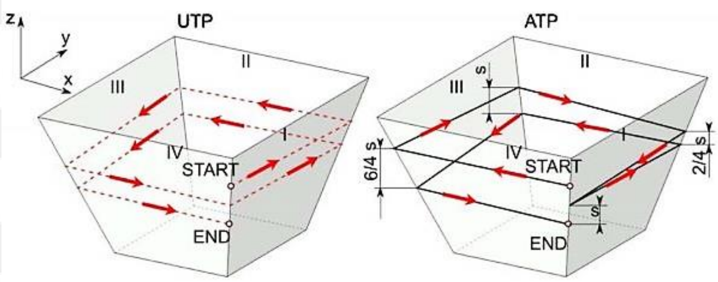

(a)

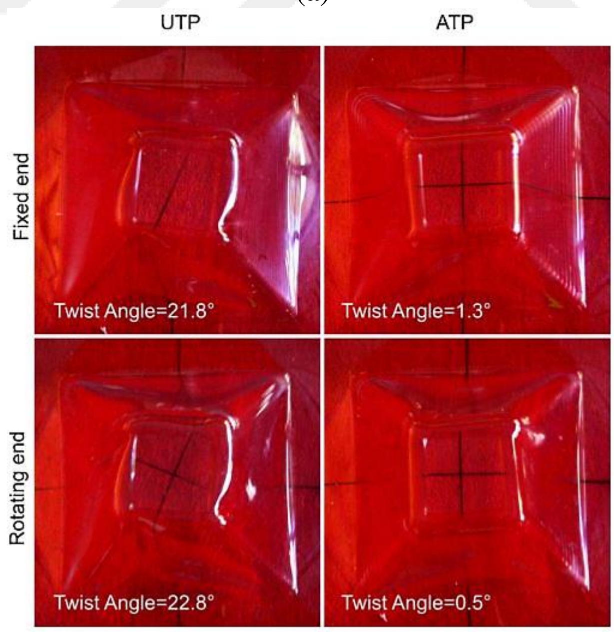

(b)

Figure 1.16:The toolpath strategies UTP and ATP (a), and the twisting angles in the PC pyramid specimens made by adopting the toolpath strategies and ISF tools of rigid and rolling heads [120].

Hassan et al. [26] conducted an extensive and inclusive literature review on the incremental forming of polymers. Different aspects of the process including formability, failure, deformation mechanism, forming force, spring back effect, and post-forming properties of sheet are discussed. Therefore, they concluded that thinner sheets, larger pitch size, and a larger radius of curvature stimulate fracture mode 2, whereas larger initial slope angle and smaller pitch size stimulate the other two fracture modes. They stated that the effects of the other major process parameters, namely feed rate, spindle speed, and tool size on the promotion of the fracture modes require further investigations. The effects of process parameters on sheet formability are expected to vary with the sheet material. A consensus among researchers was reported regarding independency of forming force from feed rate. However, no agreement exists in the research community on the effects of step size and spindle speed on forming force. Possibly such effects are material dependent too, therefore, further investigation is recommended. They also maintained that the spring back as the major concern in ISF of polymers could be enhanced by process parameters optimization, toolpath optimization, or by adopting heat-assisted forming strategies. They maintained that to remedy the relatively long processing time, high-speed ISF remains for further studies. As evident from this review, POM is the least investigated thermoplastic among the engineering polymers used for ISF, possibly due to its low formability at ambient temperature. Zhu et al. [121] published a similar review on incremental sheet forming of thermoplastics. They summarized the research challenges, namely the lack of proper constitutive material models and fracture models to simulate ISF of thermoplastics, the complexity of the process for analytical simulation by considering the stretch-bending and shear effects, the complexity of fracture modes 2 and 3 to be analytically modeled, and a proper arrangement for heat-assisted ISF of thermoplastics. Moreover, they pointed out the current research gaps and the major future research directions, namely Finite Element Analysis (FEA) of the ISF of thermoplastics, and prediction of failure by adopting numerical or analytical methods. Such models should be capable of simulating the effects of temperature, strain rate, and strain softening/hardening on process outputs in heat-assisted ISF of thermoplastics. In addition, they maintained that a balance must be achieved between advantages (enhanced formability and accuracy) and disadvantages (rough surface) in hot ISF of thermoplastics.

1.6 Objective and overview of the thesis

As detailed in this chapter, there has been a growing demand for lightweight and customized products in the manufacturing sector. Such a tendency has led to continuous growth in the consumption of thermoplastics, for example, in the automotive sector. The new trend also reinforces the need for a novel sheet forming technology to cope with the requirements of customized manufacturing. Such a forming process is deemed to provide a flexible and highly capable tooling system. By employing the computer numerical control (CNC) technology and simple tooling, Incremental Sheet Forming (ISF) offers a die-less forming possibility. Therefore, ISF promises more flexibility in the process, lower production cost, and shorter lead-time, in addition to improved formability of material as compared to the conventional sheet forming processes.

During the last decade, a great deal of effort has been devoted by scholars to understand the mechanism and the governing rules of the ISF process. Several attempts have been also made to investigate the effects of the process parameters on the process outputs. These studies have mostly targeted sheet metals namely aluminum, steel, titanium, and magnesium. As pointed out by the literature review provided in this chapter, heat-assisted ISF appears very promising in terms of improving the sheet formability, enhancing the dimensional accuracy, and reducing the ISF processing time. However, as stated in the section on heat-assisted ISF, only 4% of the research work in the field has been related to heat-assisted ISF of polymers. In addition, Polyoxymethylene (POM) is the least investigated thermoplastic among the engineering polymers used for ISF. In a very few research works conducted by using POM, it has been dismissed for ISF, mainly due to its low formability at room temperature. However, POM is known as a semicrystalline thermoplastic of good creep and fatigue durability, high resistance against chemicals, oil, and fuel corrosion, accompanied by a good surface finish and friction resistance quality.

Considering the above discussion and the literature reviews cited in the previous section, the research gap is identified as a comprehensive experimental, analytical and numerical (FEA) investigation of Friction Stir Incremental Sheet Forming (FSISF) of Polyoxymethylene. The analytical and FEA frameworks are expected to provide fairly accurate predictions with an affordable simulation cost in terms of the computation time and the required hardware.

In this thesis, the first chapter starts with a brief discussion on the current and future trends in sheet forming technology. This introduction is followed by a literature review on incremental sheet forming (ISF) in general. Afterward, a detailed review of ISF at elevated temperatures is conducted. The next section provides a brief but detailed discussion on the application of thermoplastics in the automotive industry. This section is brought to the end by a critical review of the ISF of polymers.

The second chapter starts with an introduction, and the objective of the chapter that is an experimental investigation of Friction Stir Incremental Sheet Forming (FSISF) of Polyoxymethylene (POM). More specifically, the objective is to achieve maximum formability while heat-induced defects are avoided. First, the experimental design and setup are elaborated in detail. Then by adopting proper DOE and response surface methods, the individual and interactive effects of the process parameters are discussed in terms of the physical counterparts, namely force, temperature, heating rate, deformation rate, and stress triaxiality. This approach was adopted to better understand and explain the material behavior under different ISF forming conditions. The effect of specimen geometry on formability is discussed and a new formability criterion is proposed based on the geometry of the benchmarks. Forming force in FSISF of POM is investigated experimentally and physical justifications are provided. Also, an empirical model is developed to predict the total forming force as a function of the process parameters and time. Friction in FSISF of POM is experimentally evaluated and briefly discussed. The temperature at the tool-sheet contact interface, at the center, and the base of the specimens is measured. A response surface is provided to demonstrate the interface temperature as a function of the process parameters. Interdependent effects of force, forming angle, and temperature are discussed by providing physical explanations. In addition, dimensional integrity, thickness distribution, surface quality as well as the evolution of crystallinity, surface hardness, and elastic modulus of POM under specific forming conditions are discussed in this chapter. At the end of the chapter, a discussion is provided on fracture in FSISF of POM based on the morphology of the cracks acquired by Scanning Electron Microscopy (SEM).

The third chapter starts with an introduction, and the objective of the chapter that is proposing a combined numerical-analytical discipline to efficiently predict force and temperature at the tool-sheet contact interface in FSISF of POM. First, the mechanism of deformation and stress-strain state is defined based on a membrane analytical framework. A brief discussion is also provided on strain calculation considering the stretch-bending in the sheet. The area of the tool-sheet contact interface is estimated by proposing two geometrical approaches. Then, the pronounced bending effect in the initial stage of the forming process is investigated by extending an available analytical framework for deflection of a circular sheet under lateral concentrated load. Calculation of the friction-induced heat and heat partitioning is briefly discussed. Temperature distribution in tool and sheet is calculated by adopting the Finite Difference Method (FDM). At the end of the chapter, analytical results are validated by the experimental results. More specifically, analytically predicted contact area for some benchmark cases is compared against validated FEA results. The predicted total force for five major FSISF benchmarks is compared against the experimental results. Tooltip temperature estimated by using the analytical framework is compared against the temperature experimentally recorded by using a pyrometer. Friction-induced heat rate and meridional stress component are presented as a function of the equivalent plastic strain in the five major FSISF benchmarks. The ratio of the plastic strain energy density to the triaxiality is also presented as a function of the final equivalent plastic strain for the FSISF benchmarks. Accordingly, a brief discussion is provided on the sheet failure in the FSISF process.

The fourth chapter starts with an introduction, and the objective of the chapter that is fairly accurate and timely efficient FEA of FSISF of POM. The chapter continues with a brief discussion on Implicit and Explicit solutions. Afterward, a detailed discussion is provided on the selection of a proper material model for the FEA of FSISF of POM. More specifically, the material constitutive models namely Two-Layer Viscoplastic (TLV), Parallel Rheological Framework (PRF), Three Network (TN), and Johnson-Cook (JC) are discussed and calibrated. Also, a nonlinear elastic model with acceptable accuracy is proposed and calibrated. Then, detailed and comparative discussions are provided on meshing strategies, FSISF tool definition, element type, element size, and mass scaling to achieve the objective of fairly accurate and timely efficient FEA of FSISF of POM.

Following these sections, heat partitioning between tool and sheet is discussed in detail. For this purpose, also a precise review is provided on heat partitioning in problems involving friction-induced heat such as pin-on-disk, disk-brake, and rail-wheel contact problems. Next, the friction coefficient is briefly discussed, and a numerical investigation is presented. Following the explanatory sections on the proper methodology for FEA of FSISF of POM, benchmark FSISF tests are considered for simulation. To demonstrate the capability of the proposed FEA methodology, the simulation case studies reflect a broad range of sheet formability, temperature, and stress triaxiality (as a measure of ductile fracture). The simulation results are validated against experimental results (mainly in terms of forming force). In addition, a brief discussion and numerical investigation are provided on damage evolution and failure in FSISF of POM. Finally, a brief conclusion is provided including a direction for future research.

Chapter 2

EXPERIMENTAL INVESTIGATION

2.1 Introduction and overview

As detailed in the first chapter, despite the considerable effort concentrated on investigating the ISF process parameters individually, the interactive effects on the outputs of the process have been less studied. Also, reviewing the literature on the ISF process, POM has been far less investigated as compared to other thermoplastics of vast application in manufacturing industries, namely PP, PVC, PE, and PA. In a very few research works conducted by using POM, it has been disqualified for ISF, mainly due to its very low formability at room temperature. However, POM is known as a semicrystalline thermoplastic of good creep and fatigue durability, high resistance against chemicals, oil, and fuel corrosion accompanied by a good surface finish, and friction resistance quality [122]. This study aims to address the problem by adopting friction-induced heat to form POM sheets by employing the friction stir incremental sheet forming (FSISF) process. The objective is to achieve maximum formability while heat-induced defects are avoided. Employing the Design of Experiment (DOE) method, this chapter is set out with the aim of experimentally investigating the formability and failure of POM sheets in ISF at elevated temperatures. For this purpose, interactive and interdependent effects of the process parameters are discussed in terms of the physical counterparts, namely force, temperature, heating rate, deformation rate, and stress triaxiality. This approach was adopted to better understand and explain the material behavior under different ISF forming conditions. Tools of different diameters were employed with several pitch sizes, translational speeds, and rotational speeds to experimentally evaluate the friction coefficient at several temperatures and under different normal force magnitudes. A new criterion for formability is also introduced to account for the effects of geometrical factors on formability. Dimensional integrity, thickness distribution, surface quality as well as the evolution of crystallinity, surface hardness, and elastic modulus of POM under specific forming conditions are discussed in this chapter. In the end, a discussion is provided on fracture in FSISF of POM based on the morphology of the cracks acquired by Scanning Electron Microscopy (SEM).

2.2 Experimental design and set-up

To investigate the effects of the major ISF process parameters on the resultant heat, force, and sheet formability, a Central Composite Design of Experiment (CCD-DOE) was adopted. It must be emphasized here that it is not intended to treat the process as a black box by employing DOE. However, the objective is to provide a broader perspective of the interactive and interdependent effects of the process parameters on the outputs of the process. It is also aimed to explain the physical reasons behind observations. For this purpose, four major process parameters, namely tool size, step size (pitch size), translational speed of tool (forming speed), and spindle rotational speed (spindle speed) were considered. Each ISF parameter varied over five different levels to form an experimental campaign of 28 tests; each test was replicated once. As mentioned before (in the first chapter), the positive effect of sheet thickness on sheet formability and dimensional integrity of ISF-made thermoplastic components is well established in the literature. This is partially due to a remarkable decrease in triaxiality ratio, as a measure of accumulation of ductile damage, by an increase in sheet thickness [112, 123, 124]. To keep the size of the experimental campaign feasible, the thickness of POM sheets was kept constant at 2 mm. Table 2.1 presents the variation of the ISF process parameters in the adopted DOE. Eight screaming experiments were also performed to ensure the proper range of ISF process parameters as reported in Table 2.1.

Table 2.1: Variation of the ISF process parameters in CCD experimental campaign.

ISF Process Parameters	Unit	Levels				
		1	2	3	4	5
Tool Tip Diameter (T)	mm	4	6	8	10	12
Pitch Size (P)	mm	0.4	0.8	1.2	1.6	2
Forming Speed (F)	mm/min	500	1400	2300	3200	4100
Spindle Rotational Speed (S)	rpm	0	1400	2800	4200	5600

The results of those screening test by using a non-rotational forming tool (cold ISF) was in complete agreement with what Franzen et al. [110] and Martins et al. [111] reported, which is an early failure of the POM sheet. POM sheets of 240×240×2 mm size were used to form ISF specimens. Conical frustum specimen of the equal base radius and depth of 40 mm, with an increasing wall angle from 45° to 90° along a circular generatrix of 56.57 mm in radius was designed using the commercial CAD-CAM package NX. Due to the curvatures of the specimens, generating spiral toolpaths of constant pitch size was hard to manage in NX (UG), which is dedicated to machining. Therefore, a proper algorithm was developed in MATLAB to produce the relevant NC codes for such ISF toolpath. It is possible with this algorithm to animate the motion of ISF tool in 3D and verify the tool path as shown in Figure 2.1. Forming tools are made of Tungsten Carbide (WC) styluses of hemispherical heads. Because of inherent self-lubricity of POM sheet (due to very fine surface quality) and to account for environmental concerns, no lubrication was employed.

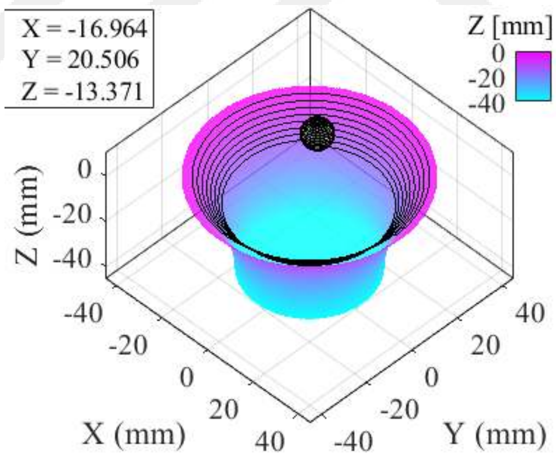

Figure 2.1: Generation, simulation, and verification of spiral tool path of constant pitch size in MATLAB.

During the forming process, the temperature was measured by using thermocouples attached to two stationary spots. One spot was located at the center (apex) and the other was 5 mm away from the periphery (base circle) of the frustum specimens. Ambient temperature was also measured separately for each test. For temperature measurement, an NI 9213 NATIONAL INSTRUMENT thermocouple input (±78 mV, 75 S/s, 16 Chanel Module) was used along with RS Pro Type J thermocouples (-50 °C to 350 °C). ARCTIC MX-2 thermal paste was also used in the contact interface to safeguard proper thermal conductivity. In addition, the tool-tip temperature was measured by using a handy clamp multimeter (Fluke 325 True-RMS) immediately after stopping the forming process and raising the tool. The temperature at the tool-sheet interface was also measured for benchmark specimens by using a MicroEpsilon LT-CF1-CB3 pyrometer. Further details regarding the pyrometer setup are provided in the section of friction measurement. A table-type dynamometer (KISTLER-Type 9257B) was embedded under the ISF sheet-clamping device for force measurement. Figure 2.2 provides a detailed view of the experimental setup used for this study.

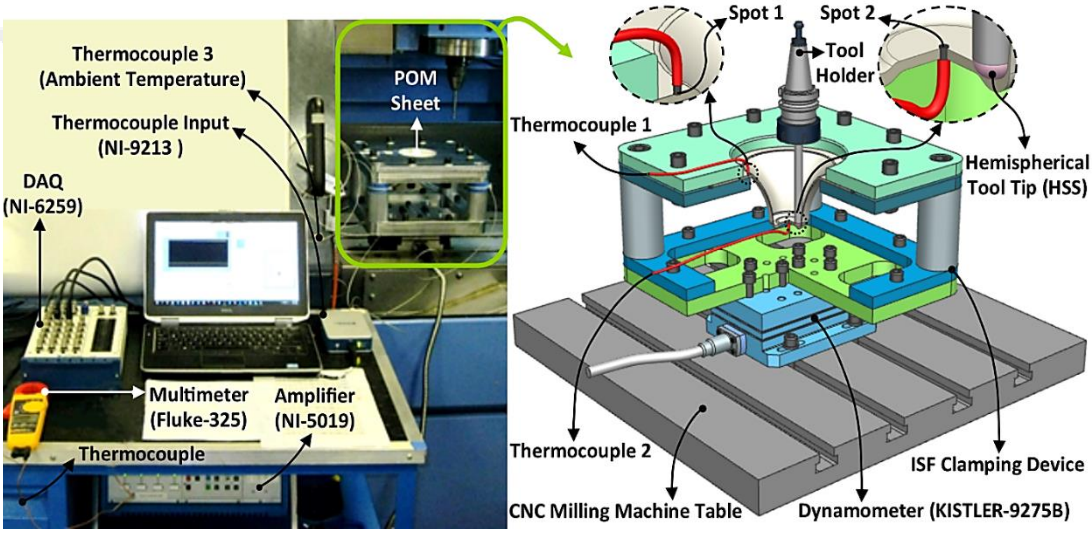

Figure 2.2: ISF experimental setup.

2.3 *Experimental results and observations*

In this section, experimental observations on POM sheet formability and failure, forming forces, friction-induced heat, and temperature in incrementally formed specimens are discussed. In addition, dimensional integrity and thickness distribution, surface quality, crystallinity, and mechanical properties in some benchmark specimens are elaborated. To comprehend the geometrical effects on sheet formability, a new formability criterion is proposed by using standard conical frustum specimens.

2.3.1 Formability and failure

Each specimen was continuously formed until any sign of failure including crack or wrinkling appeared, when the machine was immediately stopped. At this time, the relevant depth of failure along the tool direction (Z-axis) was recorded for the calculation of the maximum achievable forming angle, ϕ, as the measure of sheet formability in ISF. Notably, no significant wrinkling was observed during the experiments. The onset of a crack in the ISF of polymers does not necessarily create an audible sound as it does in the case of metal forming. Therefore, the acquired force data was later employed to detect the instant of failure from a significant drop in the magnitude of force at the onset of the crack. By using the code developed for toolpath generation, failure time instant was used for the calculation of the depth of fracture and the corresponding failure wall angle for each test. Considering the results, the highly interactive effects of the process parameters along with the complex rate-dependent and temperature-dependent behavior of material cause highly nonlinear outcomes in terms of formability. Therefore, no response surface of a reasonably low number of constants could be fitted to data. The maximum forming depths acquired in replicated tests were averaged and reported in Table 2.2.

For example, the application of tool diameters of 6 mm and 10 mm, pitch size of 0.8 mm, forming speed of 1400 mm/min, and spindle speed of 1400 rpm resulted in the maximum formability (ϕ_{max}=90°). Considering the very poor formability of POM sheets as reported in the literature, achieving a maximum wall angle of 90° represents an accomplishment. The average measure of formability (ϕ_{avg} = 66.9°) can be roughly regarded as 50% of the height (or depth) of the designed geometry. Interestingly, ϕ_{avg} was very close to the maximum forming angle achieved by setting all the FSISF process parameters at moderate values, which translates to the center point of CCD-DOE ($\phi_{T8P1.2F2300S2800}$=66.5°). Surprisingly, the minimum formality was achieved not by applying a condition of cold forming (spindle speed of 0 rpm). A small tool size (6 mm), relatively low forming speed (1400 mm/min), the maximum pitch size (1.6 mm), and a relatively high spindle speed (4200 rpm) resulted in the minimum formability. This could be due to some heat-induced defects probably augmented with some initial material flaw such as production-induced voids. Generally, a combination of large step size and a high spindle speed may lead to penetration of the tool to the sheet, stimulation of large stress concentration around a material defect, and propagation of a crack before the material can deform. A combination of zero spindle speed and moderate values of tool size, pitch size, and forming speed led to a maximum wall angle of 60.7°. The physical causes attributed to these observations are further discussed by elaborating the acquired force and temperature data in the coming sections.

Table 2.2: FSISF test parameters and final fracture depth (formability) of specimens.

Test No.	Tool Diameter [mm]	Pitch Size [mm]	Feed Rate [mm/min]	Spindle Speed [rpm]	Fracture Depth [mm]
1	6	1.6	1400	1400	19.9
2	6	0.8	1400	4200	10.3
3	10	1.6	1400	4200	15.9
4	8	2	2300	2800	21.4
5	6	1.6	3200	1400	15.5
6	10	1.6	3200	4200	17.0
7	10	1.6	3200	1400	9.5
8	8	0.4	2300	2800	7.6
9	8	0.4	2300	2800	16.4
10	10	1.6	1400	1400	34.8
11	8	1.2	2300	2800	17.6
12	6	0.8	1400	1400	40.0*
13	10	0.8	3200	4200	12.2
14	10	0.8	3200	1400	10.0
15	6	1.6	1400	4200	7.2
16	12	1.2	2300	2800	14.8
17	6	1.6	3200	4200	8.9
18	10	0.8	1400	4200	10.8
19	8	1.2	2300	0	12.3
20	8	1.2	4100	2800	14.7
21	10	0.8	1400	1400	40.0*
22	8	1.2	500	2800	11.5
23	8	0.4	2300	2800	19.2
24	4	1.2	2300	2800	35.4
25	8	0.4	2300	2800	17.2
26	6	0.8	3200	1400	23.2
27	8	1.2	2300	5600	24.7
28	6	0.8	3200	4200	18.1

Figure 2.3 represents the ISF specimen being formed by employing zero spindle speed and those specimens corresponding to the minimum, average, and maximum formability. These benchmark specimens can be used to concisely portray the whole spectrum of the experimental campaign. By inspecting all the specimens, it was noticed that cracks propagate along the circumferential direction at the boundary region between the inclined

wall of the specimen and the upper side of the tool-sheet contact interface. Therefore, formability in FSISF of POM is limited by failure mode 1 according to Franzen et al. [37].

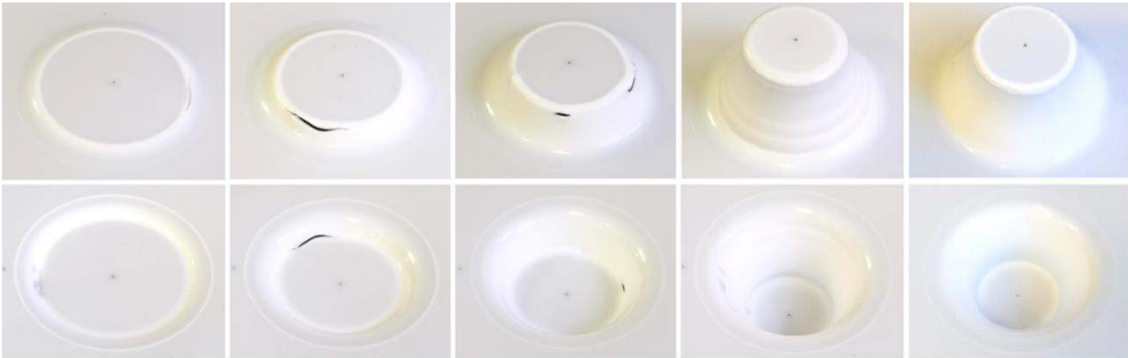

Figure 2.3: Outside and inside view of FSISF specimens corresponding to the minimum formability (a - Test 15), zero spindle speed (b - Test 19), the average formability (c - Test 11), and the maximum formability (d - Test 21; e - Test 12).

Similar to the incremental forming of metallic sheets to conical frustums, the forming mechanism corresponding to the aforesaid failure mode is largely derived by the meridional tensile stresses [112, 113]. It is worth mentioning that no significant wrinkling was observed on any of the specimens throughout the experimental campaign. To explain the formability of POM under different ISF forming conditions, deformation mechanisms, namely crazing, cavitation, and slip are to be considered. The effects of temperature and strain rate on these mechanisms are discussed in the coming sections.

2.3.2 The effect of specimen geometry on formability: a new formability criterion

The effect of specimen geometry on the formability of sheet material has been discussed in a few studies. Hussain et al. [125] investigated the formability of aluminum sheets being formed to conical and pyramid shapes of different uniform wall angles and funnels of different generatrix arcs. All the specimens had an equal initial angle, the same final slope angle, and an identical base radius. Adopting the maximum achievable wall angle as the formability criterion, they listed the specimens from the best to the least formability according to the following order: funnels of exponential, parabolic, elliptical, and circular generatrix followed by conical and pyramid frustums. Davarpanah et al. [126] investigated conical and funnel specimens of PLA with different uniform slope angles and radiuses of curvature. By increasing the wall angle or radius of curvature, the maximum achievable forming angle decreased, meanwhile wrinkling gradually replaced tearing as the dominant mode of failure. Khalatbari et al. [18], by investigating the formability of AA3003-H12 aluminum, argued that merely considering the maximum achievable forming angle is insufficient for a comprehensive measure of formability. They maintained that the history of slope angles leading to a specific failure angle in ISF specimens must be also taken into account. Marques et al. [114] drew the Fracture Limit Diagrams (FLD) corresponding to incrementally formed specimens of PC, PVC, PA, and PET. They showed that the plane strain stretching is the dominant mechanism of deformation in the conical, funnel, and non-corner areas of pyramid specimens. The meridional stress, σ_{φ}, as the major cause for the circumferential crack under plane strain stretching condition can be developed based on the research work presented by Silva et al. [112]:

$$\sigma_{\varphi} = \frac{\sqrt{\sigma_{YC}\sigma_{YT} - (\sigma_{YC} - \sigma_{YT})(3\sigma_h)}}{\left(1 + \frac{t_0 \sin(\pi/_2 - \varphi)}{r_{tool}}\right)} \tag{2.1}$$

Where, σ_{YC} and σ_{YT} are compressive and tensile yield strength of the material and σ_h represents the hydrostatic stress. By increasing the forming angle (φ) in equation 1, the instantaneous sheet thickness derived from the sine law decreases, and the normal meridional stress (σ_{φ}) increases. An increase in the radius of a circular generatrix, when the depth of the specimen is constant may lead to a larger average-wall-angle (φ_{avg}). This, in turn, results in larger meridional stress and earlier failure. Merely increasing the base radius of the axisymmetric ISF specimen, the forming tool travels over a longer path to reach a unit length along the depth. As a result, friction-induced heat considerably increases when a rotating tool is being used. Depending on the material and the level of heat, the formability can be affected either negatively or positively.

Based on the above discussion, though the maximum achievable wall angle provides a convenient measure of formability, it does not inclusively account for all the geometrical factors. This section aims to address the problem by proposing a new convenient criterion to experimentally evaluate the formability of sheet material in the ISF process. The shape-inclusive-formability (SIF) is defined as the ratio of the area of the sheet that underwent deformation before the onset of failure to the area created by projecting that deformed surface to the initial blank plane. Figure 2.4 portraits a schematic view of the problem.

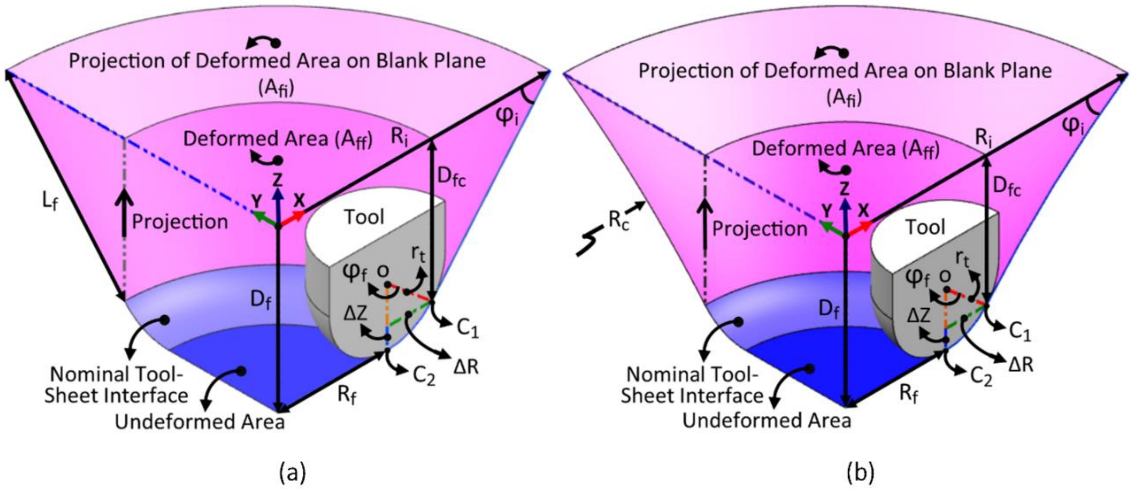

Figure 2.4: A schematic view of ISF conical (a) and funnel (b) frustum specimen and the relevant geometrical measures used to derive the new formability criterion (SIF).

For both the conical frustum of uniform slope angle and the funnel frustum of circular generatrix, which are extensively used to examine sheet formability under specific forming conditions in the ISF literature, SIF is defined as follows:

$$SIF = \frac{A_{ff}}{A_{fi}} \tag{2.2}$$

Where, A_{ff} and A_{fi} represent the area of the sheet that underwent deformation, and the area of the projection of this region to the blank (horizontal) plane, respectively.

$$A_{fi} = \pi\left[R_i^2 - \left(R_f + \Delta R\right)^2\right] \tag{2.3}$$

$$\Delta R = r_t \sin(\varphi_f) \tag{2.4}$$

Where, R_i, R_f, stand for the radius of the base circle and the radius of the circle on top of the apex (undeformed area) as represented in Figure 2.4. Symbols r_t and ΔR represent the forming tool radius and the radial (horizontal) distance between the two nominal contact points C_1 and C_2 in conical and funnel frustums, respectively. For any ISF specimen of conical frustum shape with constant wall angle:

$$A_{ff} = \pi L_f \left[R_i + R_f + \Delta R\right] \tag{2.5}$$

$$L_f = D_{fc}/\sin(\varphi_i) \tag{2.6}$$

$$D_{fc} = D_f - \Delta Z \tag{2.7}$$

$$\Delta Z = r_t\left(1 - \cos\left(\varphi_f\right)\right) \tag{2.8}$$

$$SIF_{Cone} = \frac{\left[D_f - r_t\left(1 - \cos\left(\varphi_f\right)\right)\right]\left[R_i + R_f + r_t \sin\left(\varphi_f\right)\right]}{\sin(\varphi_i)\left[R_i^2 - \left(R_f + r_t \sin\left(\varphi_f\right)\right)^2\right]} \tag{2.9}$$

In the case of frustum shape with constant wall angle: $\varphi_f = \varphi_i$. As represented in Figure 2.4, L_f, D_f, D_{fc}, ΔZ stand for the length of the inclined wall (deformed area), final depth of the specimen from apex to the base, the axial distance from the contact point C_1 to the base, and the axial distance between the two nominal contact points C_1 and C_2 (along Z direction), respectively. For any ISF specimen of funnel shape with circular generatrix and varying wall angle:

$$A_{ff} = \int_{x_1 = R_f + \Delta R}^{x_2 = R_i} 2\pi x \sqrt{1 + \left(\frac{dz}{dx}\right)^2}\, dx \tag{2.10}$$

$$[z - z_{max}]^2 + [x - (R_i + z_{max}\tan\varphi_i)]^2 = {R_c}^2 \tag{2.11}$$

$$A_{ff} = \int_{x_1 = R_f + \Delta R}^{x_2 = R_i} 2\pi x \sqrt{\frac{R_c}{R_c^2 - \left(x - (R_i + z_{max}\tan\varphi_i)\right)^2}}\, dx \tag{2.12}$$

$$SIF_{Funnel} = \frac{2R_c \left| \frac{\left[R_i + z_{max}\tan\varphi_i\right]\sin^{-1}\left(\frac{x - \left(R_i + z_{max}\tan\varphi_i\right)}{R_c}\right) - }{\sqrt{R_c^2 - \left(x - \left(R_i + z_{max}\tan\varphi_i\right)\right)^2}} \right|_{x_1 = R_f + r_t\sin\left(\varphi_f\right)}^{x_2 = R_i}}{\left[R_i^2 - \left(R_f + r_t\sin\left(\varphi_f\right)\right)^2\right]} \tag{2.13}$$

$$z_{max} = R_c \cos\varphi_i \tag{2.14}$$

$$\varphi_f = \sin^{-1}\left(\frac{R_i - R_f + R_c\sin\varphi_i}{R_c + r_t}\right) \tag{2.15}$$

Where, φ_i, φ_f, represent the initial and the maximum-achievable (final) wall angles, respectively. As represented in Figure 2.4, R_c stands for the radius of curvature in funnel specimens of circular generatrix. Points C_1 and C_2 represent the two nominal contact points in the tool-sheet contact interface in a cross-section as shown in Figure 2.4. During the ISF experiments, it was noticed that cracks normally initiate somewhere around the point C_1 at the boundary of the nominal tool-sheet contact interface and the inclined wall of the specimen. These observations are consistent with the analytical framework provided by Silva et al. [113] for incremental forming of metallic frustums. One may notice that variable R_f can be also mathematically calculated based on the three independent variables r_t, D_f and φ_i. In fact, such relations between the aforesaid parameters are embedded in the algorithm developed here to generate the NC-Codes, therefore, R_f was readily available. The maximum achievable depth of the funnel specimen, which corresponds to its depth at $\varphi = 90°$, was represented as z_{max}. This variable can be calculated by using R_c and φ_i as represented in Equation 2.14. The same approach as taken in the calculation of SIF for conical frustums of constant angle can be applied to funnels of variant slope angle. For this purpose, the funnel can be discretized to enough small strips around its axis of symmetry. Therefore, each band can be assumed as an infinitesimal cone of constant slope. By integrating the area of infinitesimal conical surface elements over the proper radial range, A_{ff} for a funnel specimen of a circular generatrix can be derived as provided in the Equations 2.10 to 2.15. Similar to the normal strain, SIF has no dimension and might be regarded as a 2D planar strain.

To investigate the shape-inclusive-formability (SIF) experimentally, six FSISF tests were designed and performed as reported in Figure 2.5. This figure shows the toolpath, geometrical parameters, forming forces, and the final shape of POM sheets incrementally formed to six conical frustums of different geometries. A similar forming condition to that of the FSISF test 11 (T8P1.2F2300S2800) that corresponds to average formability in the main experimental campaign was adopted for all the tests. Figure 2.6 provides the possibility to compare the ISF output variables namely, φ_f, D_f, SIF, F_{max} and F_{avg}. This figure also provides the possibility to judge the consistency of the formability measures as geometrical factors change in the above-mentioned six FSISF tests.

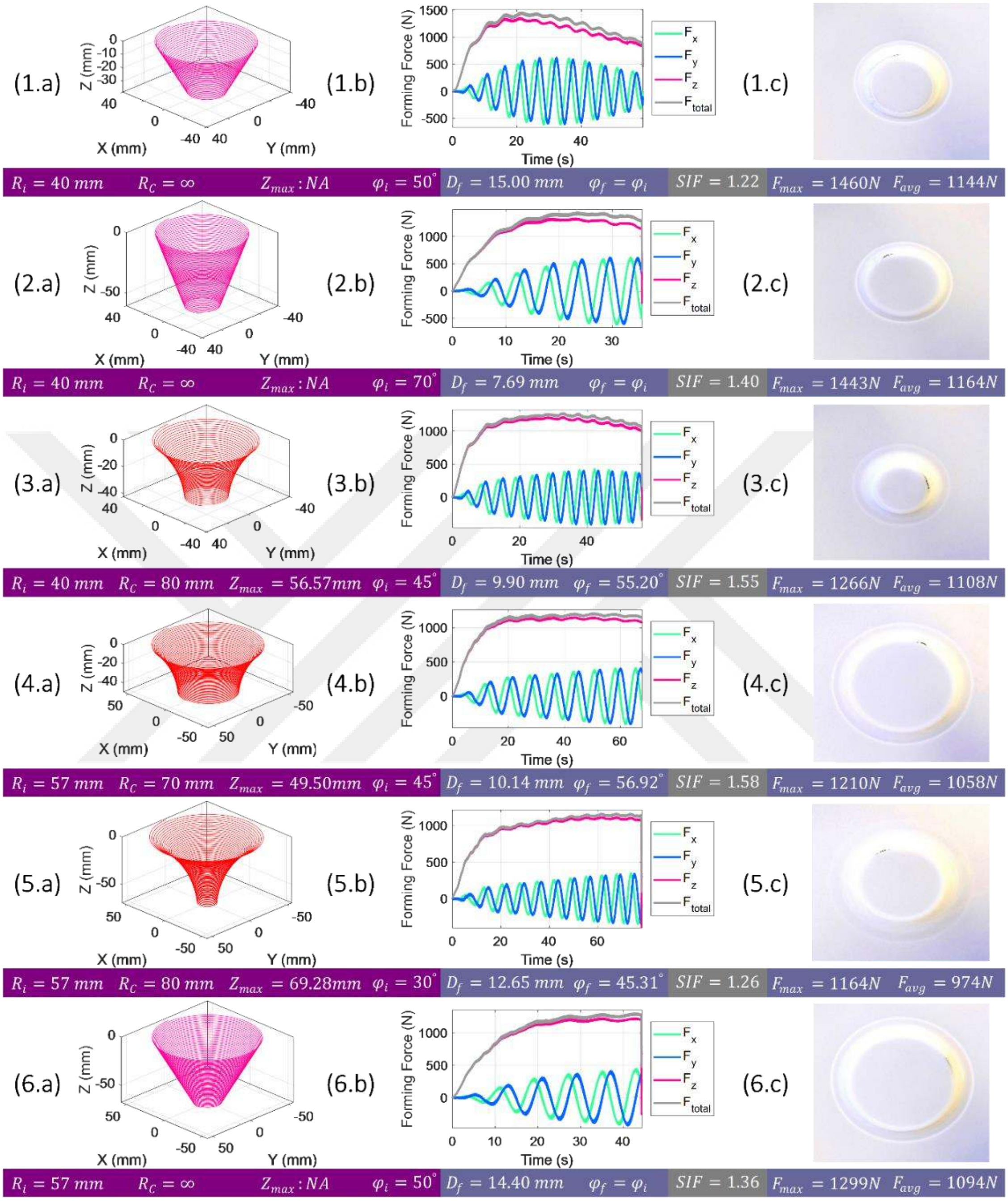

Figure 2.5: Formability and forming force in FSISF of POM under the effects of different geometrical variables.

To provide a standard measure for the deviation of the ISF output variables namely, φ_f, D_f, SIF, F_{max} and F_{avg}, under the effect of shape factors represented in Figure 2.5, the normalized root-mean-square deviation, $NRMSD = \sqrt{(\sum_{i=1}^{n}(\bar{y} - y_i)^2)/n}/\bar{y}$, was calculated for each variable. Therefore, NRMSD values of 13.7%, 22.4%, 9.7%, 40.2%

and 8.5% were derived for φ_f, D_f, SIF, F_{max} and F_{avg}, respectively. As it is evident from NRMSD values, SIF provides the minimum normalized standard deviation among formability criteria. As it is evident from Figure 2.6 (a) and (b), taking either φ_f or D_f as the measure of formability creates ambiguity in comparison of formability, while SIF allows for a conclusive comparison. Performing a Finite Element Analysis on the presented FSISF tests helps to better understand the underlying forming and failure mechanism by taking into account factors namely, strain rate, temperature, and stress triaxiality.

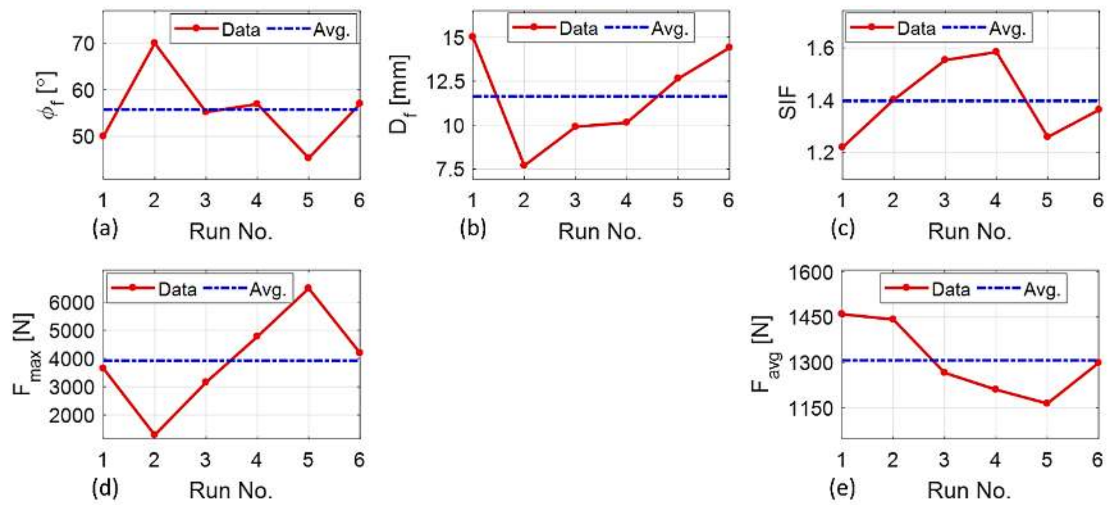

Figure 2.6: Variation of φ_f (a), D_f (b), SIF (c), F_{max} (d), F_{avg} (e) in the ISF specimens of different geometries.

2.3.3 Forming force

Force measurement in FSISF of POM was aimed for a two-fold objective. First, to provide empirical models useful to both the research communities and industries for process and machine design. Second, to elaborate the forming forces under interactive effects of the process parameters and realize the overall effect on the process outcomes such as the sheet formability. Time-dependent total forming force data were used for regression analysis by implementing the nonlinear least square method in MATLAB by adopting a function of the following form:

$$F_{total} = at^{\alpha} - bt^{\beta} \tag{2.16}$$

The regression coefficients a, b, α, and β were employed for the subsequent polynomial regressions using the FSISF process parameters. Therefore, the forming force was derived as a function of time and forming conditions in a broad range of FSISF parameters as investigated in this study and reported in Table 2.2. Equations 2.17 to 2.20 define the coefficients a, b, α and β from Equation 2.16, as functions of the FSISF process parameters. The good-of-fitness measures corresponding to the coefficients in the empirical force model (Equations 2.17 to 2.20) are provided in Table 2.3.

$$\begin{aligned} a = {} & 14.17T + 476.55P + 0.53F + 0.02S + 1.92TP - 0.03TF - 0.02TS \\ & + 0.05PF - (4.98e-3)PS + (2.47e-5)FS + 0.57T^2 \\ & - 221.82P^2 - (9.22e-5)F^2 + (9.74e-6)S^2 - 2.24 \end{aligned} \tag{2.17}$$

$$\begin{aligned} \alpha = {} & -0.26T - 0.18P - (5.07e-5)F + (2.29e-4)S - 0.02TP \\ & + (8.87e-7)TF + (7.92e-6)TS - (2.30e-5)PF \\ & - (3.07e-5)PS - (4.33e-8)FS + 0.02T^2 + 0.21P^2 \\ & + (3.74e-8)F^2 - (1.84e-8)S^2 + 1.17 \end{aligned} \tag{2.18}$$

$$\begin{aligned} b = {} & -30.04T + 248.54P + 0.42F + 0.07S - 2.83TP - 0.03TF - 0.02TS \\ & + 0.03PF - 0.01PS + (1.16e-5)FS + 4.55T^2 - 97.77P^2 \\ & - (6.75e-5)F^2 + (7.62e-6)S^2 + 90.94 \end{aligned} \tag{2.19}$$

$$\begin{aligned} \beta = {} & -0.24T - 0.32P - (2.60e-4)F + (8.82e-5)S - (9.26e-3)TP \\ & + (1.41e-5)TF + (1.54e-5)TS - (2.62e-6)PF \\ & + (6.00e-6)PS - (2.77e-8)FS + 0.02T^2 + 0.20P^2 \\ & + (5.68e-8)F^2 - (1.79e-8)S^2 + 1.57 \end{aligned} \tag{2.20}$$

Table 2.3: Good-of-fitness measures corresponding to the coefficients in the empirical force model.

Parameters	R^2	R^2_{Adj}	$R_{Signal/Noise}$
a	0.97	0.92	14.46
α	0.94	0.88	12.02
b	0.97	0.91	12.64
β	0.97	0.90	14.12

Figure 2.7 shows the forming forces experimentally acquired for the five major forming conditions (as shown in Figure 2.3). This figure also illustrates the empirical model's fitness to the experimental data.

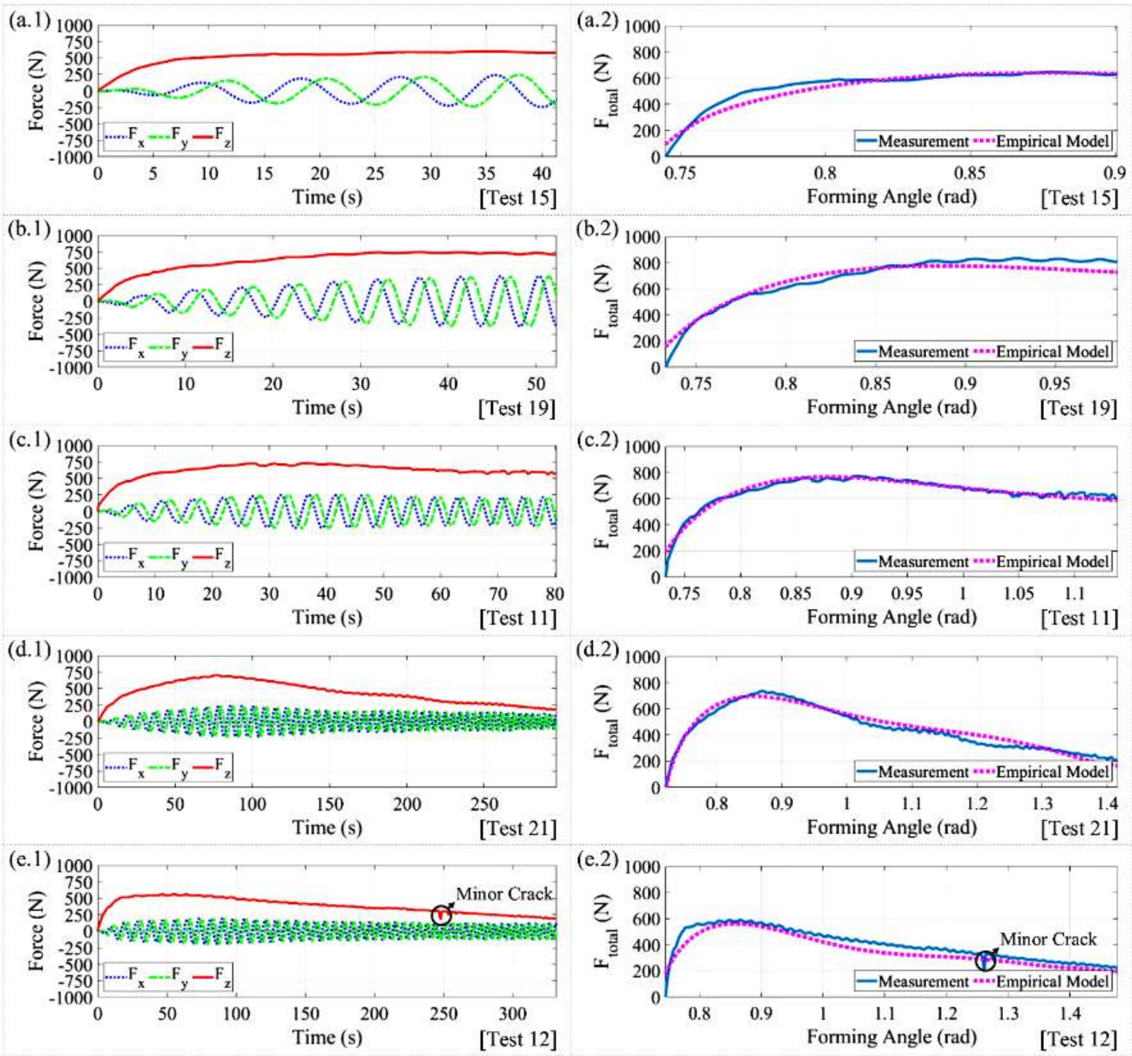

Figure 2.7: Forming forces acquired for the five major FSISF conditions by experiments (a1 to e1) and by using the empirical model (a2 to e2).

By further investigation of the experimental force components, specifically for the five major FSISF conditions as presented by figure 2.7, it was found that the ratio of the planar to normal force components increases by time through the course of forming up to sheet failure. This could imply a steady increase in friction coefficient over time as a result of the increase in temperature. The research outcomes on frictional and thermal effects in sliding contact between steel plates and POM bars support this assumption [127].

Magnitudes of the maximum total forming forces corresponding to each forming condition are provided in Table 2.4.

Table 2.4: Magnitudes of the maximum total forming forces corresponding to each forming condition.

Test No.	Tool Diameter [mm]	Pitch Size [mm]	Feed Rate [mm/min]	Spindle Speed [rpm]	Max. Force [N]
1	6	1.6	1400	1400	698
2	6	0.8	1400	4200	577
3	10	1.6	1400	4200	863
4	8	2	2300	2800	897
5	6	1.6	3200	1400	737
6	10	1.6	3200	4200	964
7	10	1.6	3200	1400	983
8	8	0.4	2300	2800	594
9	8	0.4	2300	2800	811
10	10	1.6	1400	1400	917
11	8	1.2	2300	2800	779
12	6	0.8	1400	1400	596
13	10	0.8	3200	4200	824
14	10	0.8	3200	1400	852
15	6	1.6	1400	4200	655
16	12	1.2	2300	2800	948
17	6	1.6	3200	4200	717
18	10	0.8	1400	4200	718
19	8	1.2	2300	0	839
20	8	1.2	4100	2800	811
21	10	0.8	1400	1400	745
22	8	1.2	500	2800	617
23	8	0.4	2300	2800	769
24	4	1.2	2300	2800	477
25	8	0.4	2300	2800	757
26	6	0.8	3200	1400	606
27	8	1.2	2300	5600	771
28	6	0.8	3200	4200	619

No relation between the maximum forming force and formability can be established by using the available experimental data. For example, there is a difference of about 40% between the maximum total forming forces acquired for the two forming conditions leading to the maximum formability ($\varphi_f = 90°$). The maximum forming force magnitudes corresponding to the best-case formability (Test 12) and that of the least formability are almost equal. The maximum total forming force corresponding to each forming condition is still quite informative when process and machine design are concerned. By using the experimental data provided in Table 2.4, nonlinear regression was performed to a function of the following form:

$$F_{max} = 118.97T^{0.54}P^{0.25}F^{0.12}S^{-0.03} \tag{2.21}$$

Where, T, P, F, and S, as stated before, stand for tool diameter, pitch size, linear forming speed, and spindle speed, respectively. The application of empirical models at the boundaries of the response surface requires careful attention. Specifically, the forming condition of zero spindle speed can be considered as a singularity point in the above reported empirical model. As being reported in the literature and here, POM provides very poor formability at room temperature, which means such singularities (forming condition with zero spindle speed) are trivial. This empirical model rendered good-of-fitness measures of R^2, R^2_{Adj} and an average value of residuals equal to 0.99, 0.98, and 1.91%, respectively. The empirical model proposed by Aerens et al. [128] for predicting axial force in ISF of metals can be mentioned for the sake of comparison. This model was later adjusted by Bagudanch et al. [119] for predicting force in ISF of PVC, and resulted in overestimations up to 41%. Equation 2.21 represents a response surface by which the interactive effects of tool diameter, pitch size, linear forming speed, and spindle speed on the maximum total forming force can be portrayed as indicated by Figure 2.8. ANOVA reveals that all the ISF process parameters are individually significant in terms of their effect on the measure of the maximum total forming force.

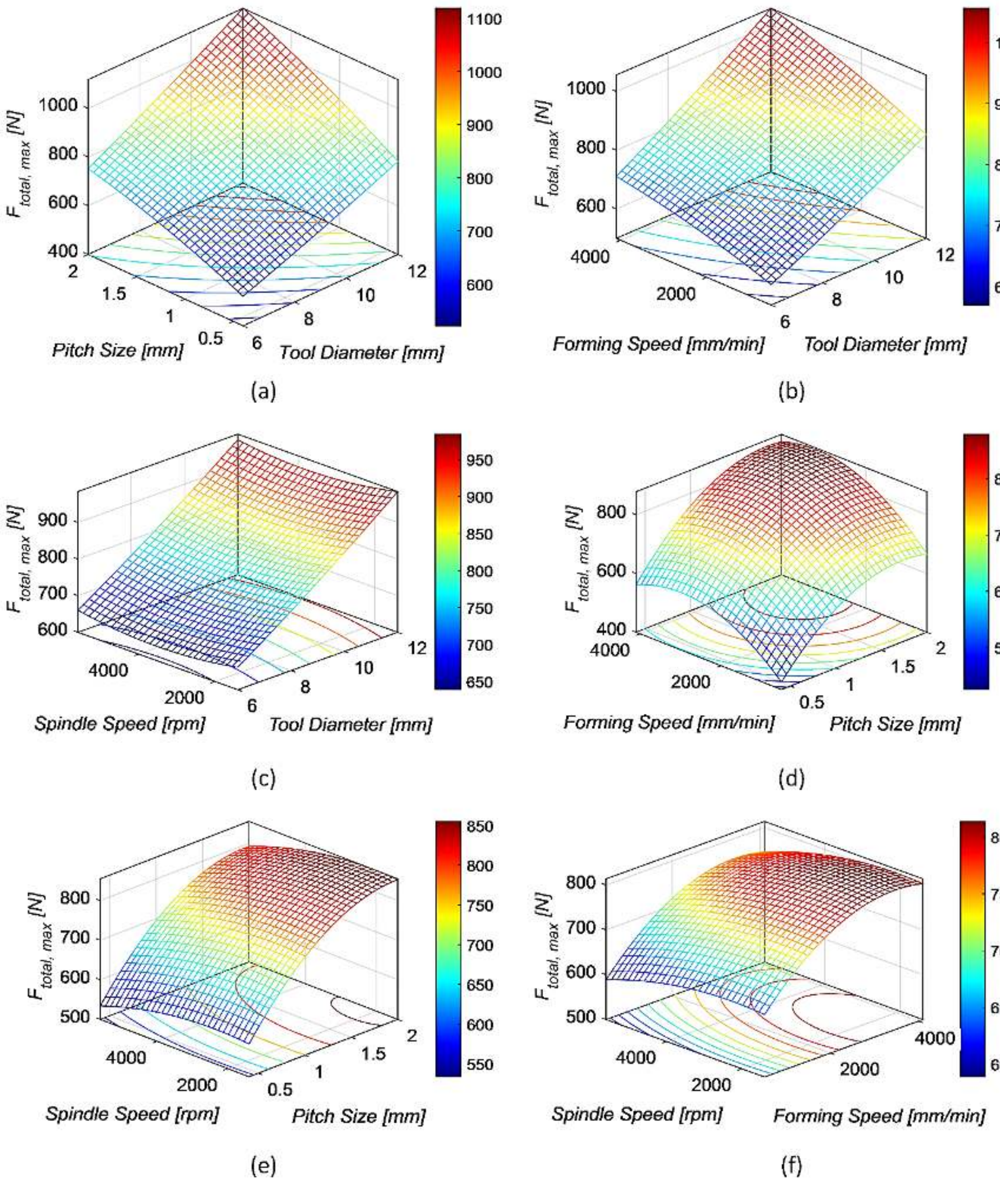

Figure 2.8: 3D contour plots showing the maximum total forming forces under interactive effects of ISF process parameters.

2.3.4 Friction

The friction coefficient was estimated by using the force data experimentally acquired, while the ISF tools sweeping along a nonintersecting reciprocal path over horizontally leveled POM sheets being clamped on the table type dynamometer. Different tool and pitch sizes were adopted along with several translational and rotational spindle speeds to evaluate the friction coefficient at different temperatures and normal force magnitudes. To measure the temperature, a Micro-Epsilon LT-CF1-CB3 pyrometer was mounted on the spindle of the CNC machine. The friction measurement setup is presented in figure 2.9.

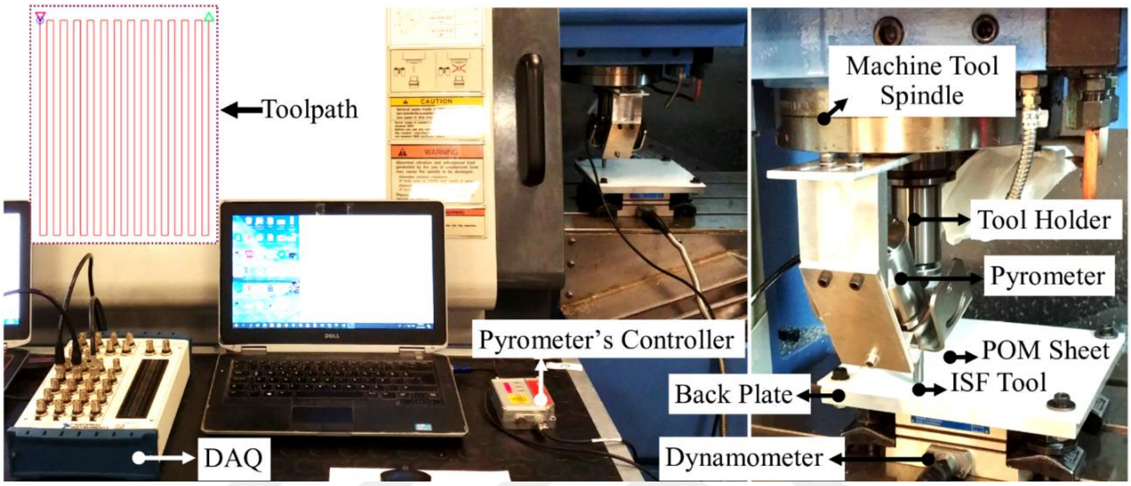

Figure 2.9: Friction measurement setup including the pyrometer mounted on the machine tool spindle.

This pyrometer is equipped with a double laser pointer, which ensures precise targeting of the measurement spot, which is right behind the tool at its footprint on the sheet. The pyrometer also provides the possibility of measuring the emissivity of a target material, e.g. POM, at any known temperature. A table of temperature-dependent emissivity measures can be set into the real-time data acquisition software, CompactConnect, working with the pyrometer. To measure the emissivity of POM at different temperatures, a stationary setup was designed, in which a piece of POM sheet is attached to a cartridge heater. The temperature of the heater-sheet was controlled by using an Arduino MEGA card, a thermistor, J-Type thermocouples, and a PID controller in MATLAB (Figure 2.10). Figure 2.11 shows the emissivity of POM as a function of temperature. It is noteworthy that the measurement of emissivity at each temperature level was repeated 20 times and the average value was considered. Figure 2.12 shows the results of temperature measurements in two friction tests at relatively low and high temperatures. Figure 2.13 shows the corresponding force components measured for the two friction tests. Therefore, it could be concluded that the friction coefficient varies between 0.04 and 0.14 for the range of the normal force as presented in Figure 2.13.

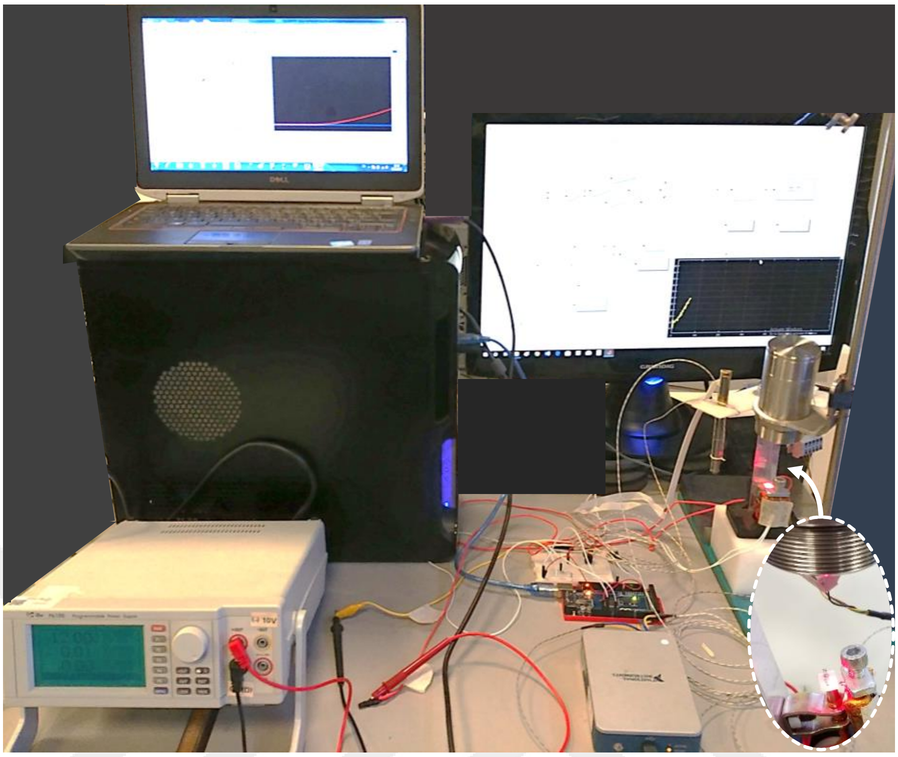

Figure 2.10: The setup for measurement of emissivity of POM as a function of temperature.

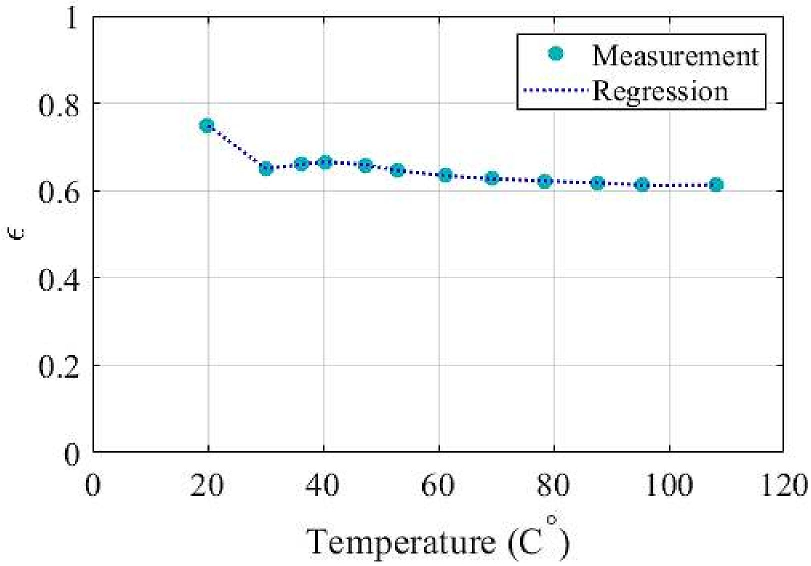

Figure 2.11: Emissivity of POM as a function of temperature.

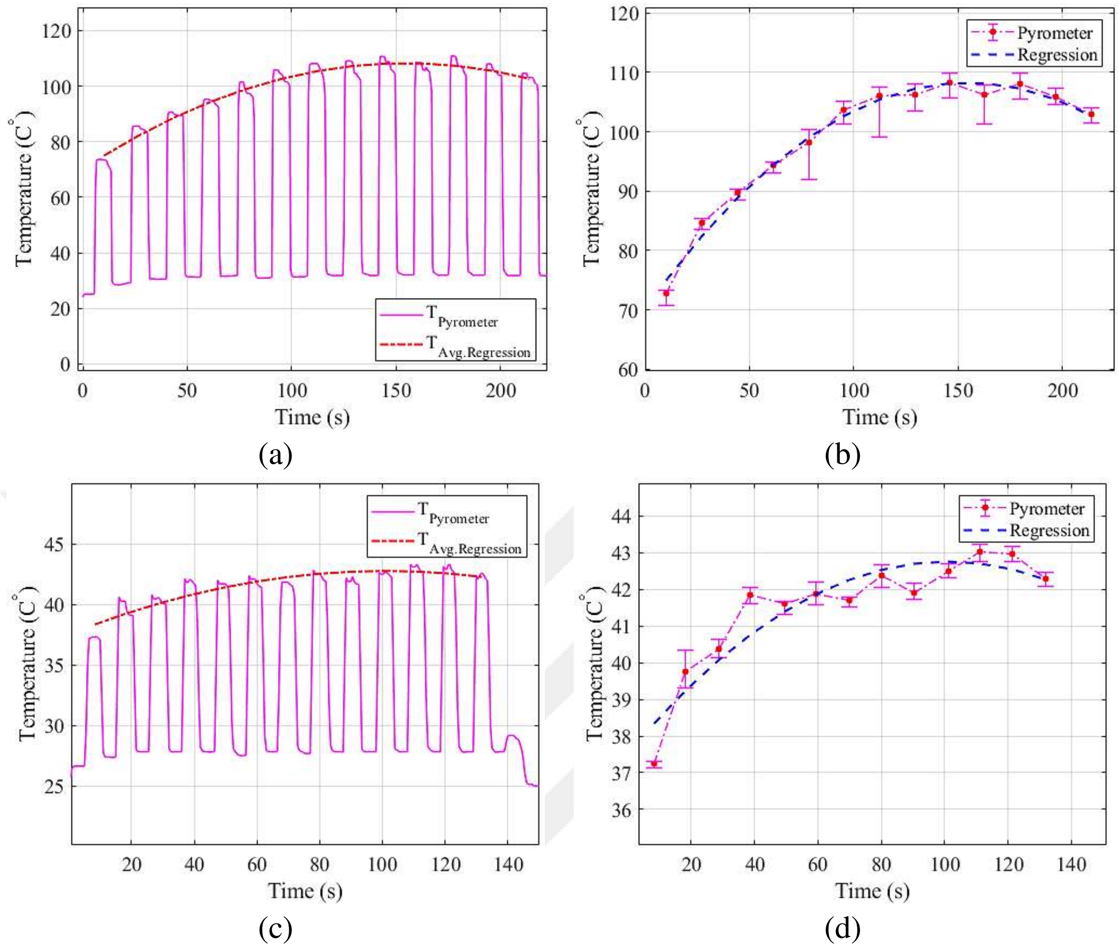

Figure 2.12: Raw temperature data (a-c), and the temperature at tool-sheet contact interface (b-d) in friction tests under conditions T10P0.4F1400S4200 (a-b), and T9P0.4F2300S0 (c-d).

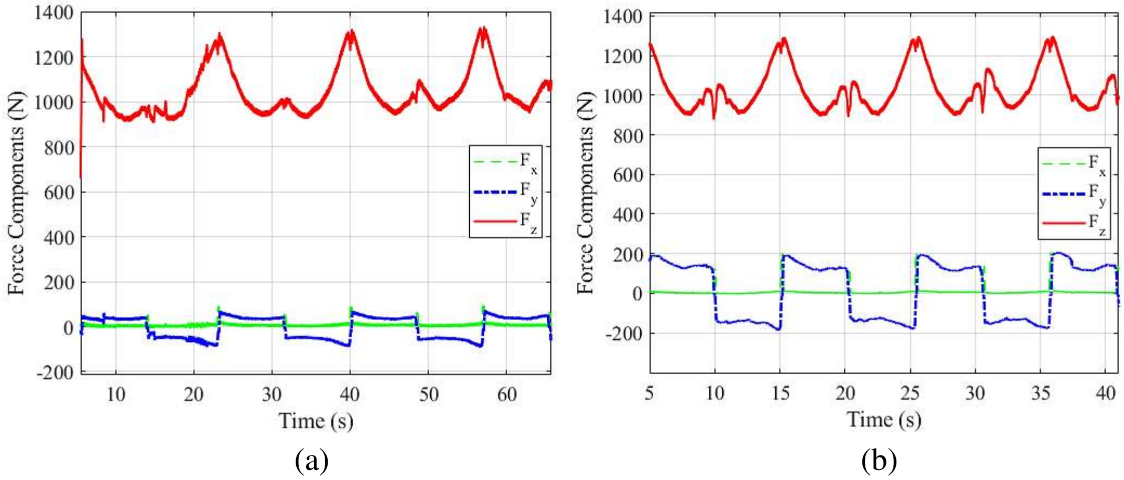

Figure 2.13: Force components in friction tests under conditions T10P0.4F1400S4200 (a), and T9P0.4F2300S0 (b).

2.3.5 Temperature

The glass transition and melting temperatures of the POM copolymer employed for this study are -60°C and 165-167°C, as provided by the material supplier and reported in the literature [129]. Section 2.2 describes the apparatus and set-up used for the measurement of temperature. As stated before, the deformation zone in the FSISF process is more localized around the tool-sheet interface. Therefore, the temperature data acquired from measurement spots 1 and 2 (Figure 2.2) is insufficient to explain the deformation of the material under the heat effects. This data still provides useful information regarding the gradient of temperature over the sheet. Therefore, the focus here is on the tool-tip temperature recorded immediately after the onset of failure, T_f, as provided in Table 2.5. Since the rise in temperature is due to the friction-induced heat, it is partially dependent on how long the forming tool moves by sliding over the sheet. Therefore, better formability implies the possibility for a further increase in the temperature. The acquired data were employed for a regression analysis to generate an empirical model of the following form:

$$\begin{aligned} T_f = 25.69T - 66.06P + 0.03F - 0.03S + 3.25TP - (4.36e-3)TF \\ + (1.82e-3)TS - (4.45e-3)PF + (4.64e-3)PS \\ + (5.13e-7)FS - 1.22T^2 + 9.98P^2 + (5.83e-7)F^2 \\ + (2.16e-6)S^2 + 1.51 \end{aligned} \tag{2.22}$$

In the model, the good-of-fitness measures, namely R^2, R^2_{Adj}, $R_{Signal/Noise}$ and the average residuals are equal to 0.98, 0.94, 12.27, and 2.67%, respectively. ANOVA showed that T, P, F, S, TF, TS, and T^2 are the significant terms as far as T_f is concerned. Figure 2.14 shows the response surfaces portraying the interactive effects of the process parameters on T_f. As stated before, the application of empirical models at the boundaries of DOE requires careful attention. The tool diameter of 4 mm and the spindle speed of 0 rpm in tests 19 and 24, exemplify such boundary forming conditions, respectively. The temperatures measured for such tests appear as the outliers to the above-presented response surface. The forming time, t_f, from the instant of the tool-sheet engagement to the onset of failure (or the end of the process without failure e.g. in tests 12 and 21) was derived from the experimental force data corresponding to each forming condition. Therefore, the linear heating rate index (LHRI [$°Cs^{-1}$]) was calculated as follows:

$$\text{LHRI} = \frac{T_f - T_{amb}}{t_f} \tag{2.23}$$

Where, T_{amb} represents the average ambient temperature measured for each test. Table 2.5 also presents the resultant LHRI magnitudes for each forming condition.

Table 2.5: Magnitudes of the final tool tip temperature and the linear heating rate index (LHRI) for FSISF tests.

Test No.	Tool Diameter [mm]	Pitch Size [mm]	Feed Rate [mm/min]	Spindle Speed [rpm]	Final Tooltip Temperature [°C]	LHRI [$°Cs^{-1}$]
1	6	1.6	1400	1400	48	0.24
2	6	0.8	1400	4200	55	0.27
3	10	1.6	1400	4200	99	0.97
4	8	2	2300	2800	58	0.69
5	6	1.6	3200	1400	44	0.56
6	10	1.6	3200	4200	65	1.15
7	10	1.6	3200	1400	44	0.90
8	8	0.4	2300	2800	80	0.60
9	8	0.4	2300	2800	59	0.52
10	10	1.6	1400	1400	74	0.37
11	8	1.2	2300	2800	62	0.55
12	6	0.8	1400	1400	65	0.11
13	10	0.8	3200	4200	70	0.84
14	10	0.8	3200	1400	55	0.67
15	6	1.6	1400	4200	44	0.47
16	12	1.2	2300	2800	64	0.69
17	6	1.6	3200	4200	45	0.94
18	10	0.8	1400	4200	90	0.58
19	8	1.2	2300	0	34	0.18
20	8	1.2	4100	2800	55	0.90
21	10	0.8	1400	1400	91	0.21
22	8	1.2	500	2800	74	0.22
23	8	0.4	2300	2800	65	0.57
24	4	1.2	2300	2800	54	0.23
25	8	0.4	2300	2800	62	0.56
26	6	0.8	3200	1400	45	0.21
27	8	1.2	2300	5600	86	0.68
28	6	0.8	3200	4200	59	0.43

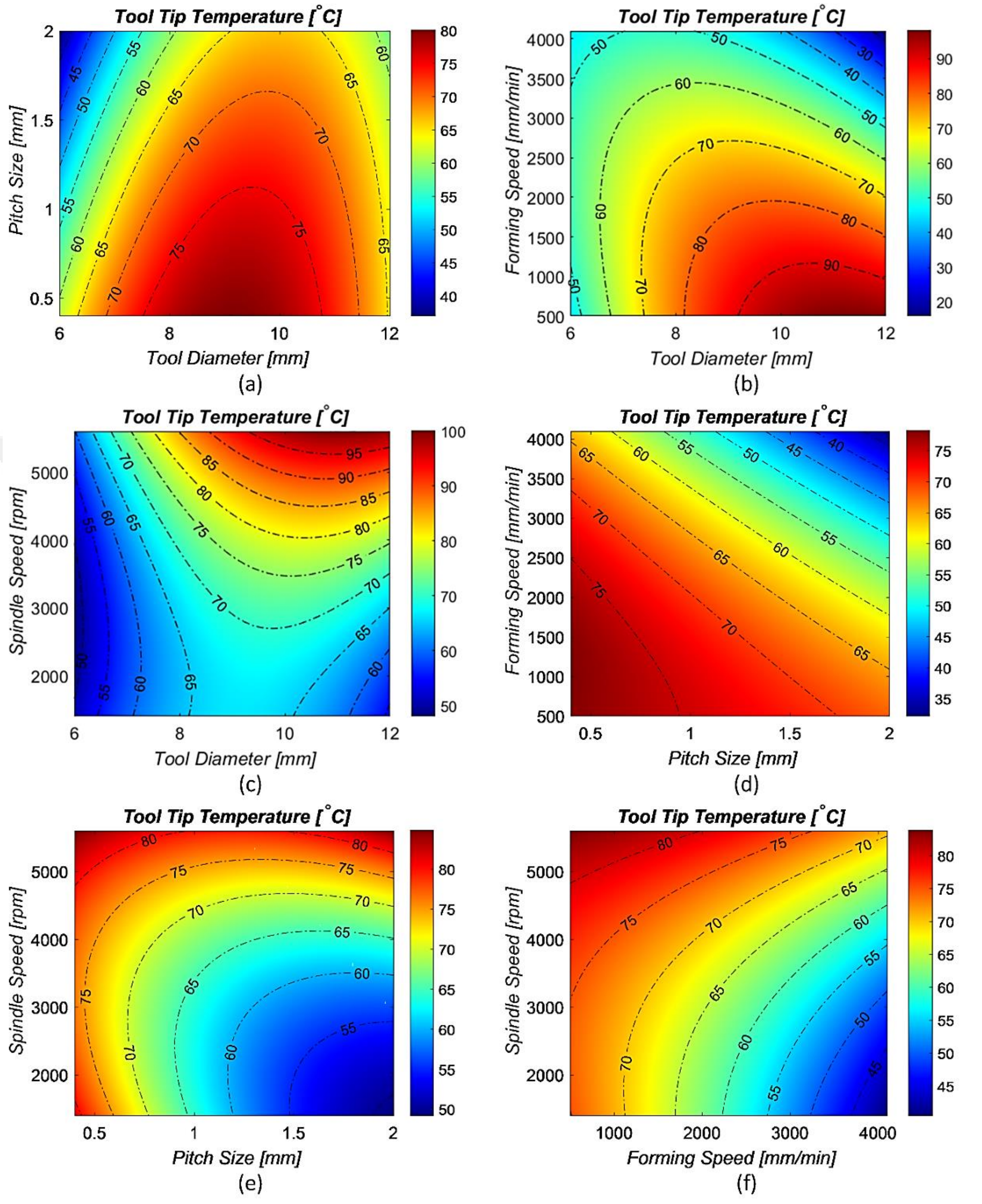

Figure 2.14: Contour plots showing the interactive effects of FSISF process parameters on the tool-tip temperature measured immediately after the end of the process.

Interestingly, the minimum heating rate (LHRI), 0.11 °Cs^{-1}, was derived for the optimal forming condition leading to the best formability. In this case, the tool-tip temperature reached approximately 65°C at the onset of failure, which is very close to the average value among all the tests. Considering the two forming conditions leading to the best formability, only a change in tool diameter from 6 mm in test 12 to 10 mm in test 21, resulted in a 44% increase in the temperature. This observation is in complete agreement with the ANOVA results stating that individual and interactive effects of tool size (T, TF, TS, and T^2) are significant as the final tool temperature is concerned. The larger tool size in test 21 leads to a shorter forming time as compared to test 12. It also results in a wider area of sliding contact between the tool and the sheet in addition to a larger magnitude of the forming force as presented in Figure 2.7, and Table 2.4. These conditions translated to a relatively low LHRI value of 0.21°Cs^{-1} and a high T_f value of 91°C in test 21. Under such conditions, the galling effect was visible on the internal surface of specimen 21. Figure 2.15 shows SEM images of the internal surface of specimens 21 and 8, and galling effects near to the specimens' apex. The internal surface of the specimens 3, 18, 27, 8, 22 and 10 corresponding to the failure temperatures of 99°C, 90°C, 86°C, 80°C, 74°C, and 74°C respectively, show galling effects to different extents.

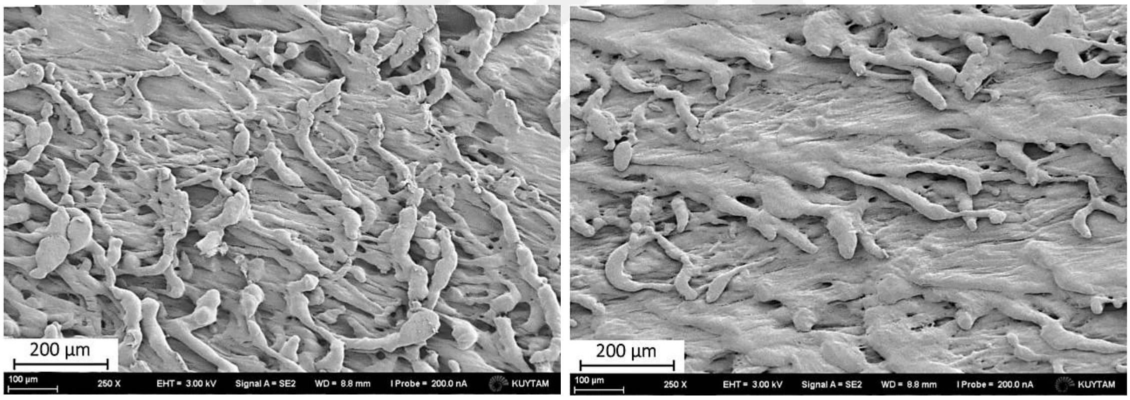

(a) (b)

Figure 2.15: SEM images showing the heat-induced galling effect on the internal surface of specimens 21 (a) and 8 (b)

The second least formability case (test 8) highlights the significant effect of the heating rate on sheet formability. In this case, the failure temperature was 80°C, which is close to that of the second-best formability case (91°C). However, the heating rate in test 8 was 0.60°Cs^{-1}, which is above that of test 21 and the overall average value (0.55°Cs-1). Taking into account the outputs of the study in terms of the sheet formability, surface quality, and geometrical integrity of the specimens, a threshold band was set for the maximum allowable tool-tip temperature. The temperature range of 70°C to 75°C can be regarded as a threshold band not to be exceeded to avoid significant damage. Considering Figure 2.14, adopting any combination of the FSISF process parameters leading to exceeding the isothermal contour lines corresponding to the aforesaid threshold band, translates to some heat-induced damages.

2.3.6 Dimensional integrity and thickness distribution

In the literature, low dimensional accuracy has been frequently underlined as a drawback in die-less ISF, which hinders a wider industrial application of the process [39]. The two major sources of dimensional inaccuracy in the process are the local elastic spring back effect during the forming process and the overall spring back effect after unclamping the sheet. Wrinkling, twisting, and heat-related distortions fall in another category of dimensional distortions. The significant viscoelasticity of thermoplastics intensifies the problem as compared to metals. Realizing the optimum forming conditions leading to the best formability in the FSISF experimental campaign, dimensional integrity of such POM specimens is a matter of concern. Evaluation of the thickness distribution is also necessary, since excessive thinning limits the application of incrementally formed sheet components.

Visually inspecting the specimens of the best formability, some heat-related distortions are evident on specimen 21 as shown in Figure 2.3d. Such heat-induced effects are also reflected in the corresponding forming force curve as presented in Figure 2.7d. On the other side, specimen 12 appears to maintain high geometrical integrity, as shown in Figure 2.3e. Therefore, this specimen was examined for dimensional error and sheet thickness distribution by using a DEA Coordinate Measuring Machine (CMM) working with PC-DIMS CAD++ software. The CMM probe scanned the specimen from both sides separately, by adopting an incremental distance of 200 μm. During the scanning process, the specimen was still clamped between the two holding plates. Considering the axisymmetric geometry of the specimen, two different scanning modes were adopted, namely linear and surface scanning. The line of scanning started from the symmetry axis at the apex of the frustum continuing along the Y-axis as illustrated in Figure 2.4. Surface scanning covered a one-eighth section of the frustum including the line of scanning. Later, the point clouds corresponding to the internal and the external scans were implemented in a single coordinate system to calculate the sheet thickness distribution in MATLAB. As it is evident from Figure 2.16, the sheet thickness varies from 0.43 mm to 2.00 mm. The latter is the average initial thickness of POM blanks as measured by using a Mitutoyo micrometer of 1 µm accuracy. The minimum sheet thickness translates to a maximum thinning of 78.5% and a true plastic strain of -1.54 along the sheet thickness. The thickness distribution was also calculated by using "sine law" as depicted by Figure 2.16.a. Adopting the CAD profile data (ideal part profile) for calculation of sheet thickness by using "sine law" results in a significant error specifically around the base of the funnel that is more under the effect of bending. However, by using the CMM profile data (internal profile of the specimen) and sine law, the predicted thickness closely follows the experimental data. By scrutinizing the 3D view of the sheet thickness distribution in Figure 2.16b, a surface defect is visible. This defect has been probably initiated from a material flaw, and later has been developed to surface delamination due to the effect of heat and strain. It is noteworthy that such surface defects did not appear on the replicated specimen.

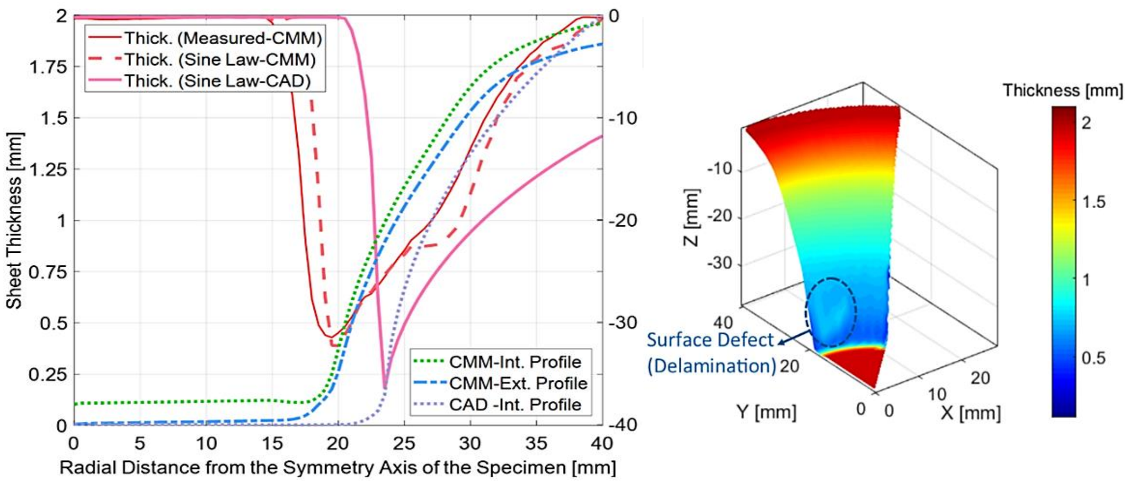

(a) (b)

Figure 2.16: 2D internal and external profiles of the specimen 12 and a 2D representation of the sheet thickness distribution (a); 3D representation of the sheet thickness distribution (b).

To derive the dimensional error in the formed specimen, the MATLAB code was extended so that the internal CAD and CMM data points could be compared. As reflected in Figure 2.17, a maximum dimensional error of 4.5 mm was detected. By comparing the apex of CAD and CMM profiles, an overall spring back effect of approximately 2 mm is evident along the vertical direction, which translates to 5% of the pre-designed depth of the specimen. By further inspections, a minor wrinkling effect is evident near to the apex of the specimen in the 3D representation of the dimensional error in Figure 2.17b.

Recalling from Figure 2.16, the sheet thickness is approximately 0.45 mm in this region. Also, the temperature was ~65°C, and the axial load was ~200 N in the same region. These numbers properly explain the presence of such a minor wrinkling effect. As measured by thermocouple 2 (Figure 2.2), the temperature was ~40°C at the center of the apex at the end of the forming process. Such a temperature gradient also partially implies why the wrinkling is restricted to a narrow region near the apex. It is worth mentioning that the wrinkling was not noticeable by naked eyes.

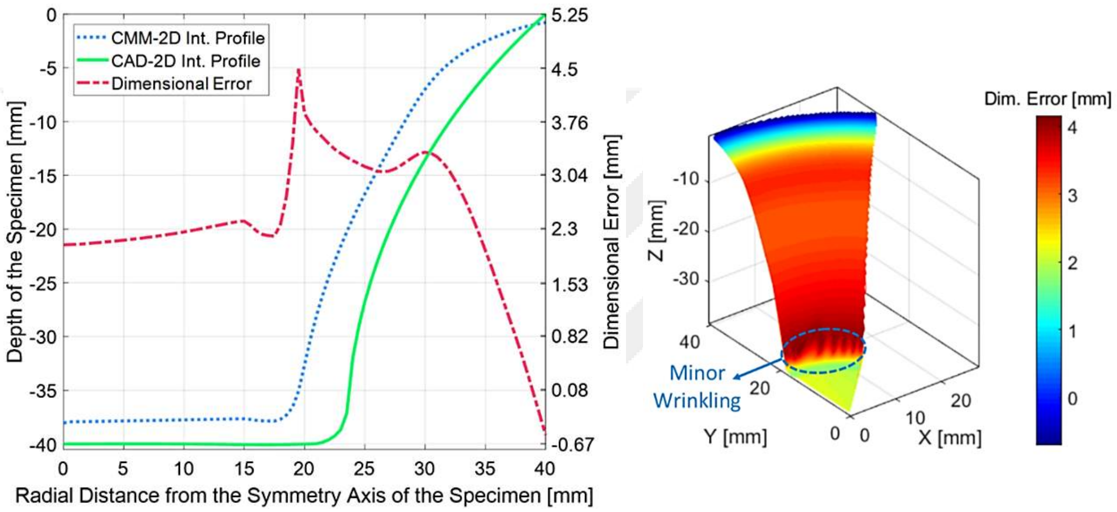

(a) (b)

Figure 2.17: 2D internal CAD-CMM profiles of the specimen No.12 and a 2D representation of dimensional error (a) A 3D representation of dimensional error (b).

2.3.7 *Surface quality*

The surface quality of FSISF-made thermoplastic components has been rarely discussed in the literature. Franzen et al. [37] showed that the surface quality of PVC conical frustums can be improved by decreasing the forming tool diameter from 15 mm to 10 mm. Therefore, a reduction in the measure of R_a, from 2.65 µm to 0.67 µm, was reported. Bagudanch et al. [119] investigated individual and interactive effects of the process parameters on the surface quality of PVC specimens, by performing ANOVA on the R_a data acquired from 16 ISF tests. The average $R_a$values of 0.42 µm and 0.62 µm were reported for the two completely formed specimens. In both studies, 2D surface texture profilers with contact stylus were used without discussing any measure of surface waviness. This study seeks to move beyond the literature by discussing surface roughness and waviness. Due to the circular generatrix of the specimens in this study, the application of 2D texture profilers renders erroneous results. Another drawback of 2D texture profilers is that the perpendicular measurement range can be only increased by defining a skid plate and using larger steps. However, such rectification would act as a mechanical filter for surface waviness. Moreover, stylus tips are made of very hard materials to decrease the wearing in the probe. Therefore, the stylus tip may create scratches while it is sweeping over the surface of soft materials such as thermoplastics, which leads to inaccurate results.

For all these reasons, White Lite Interferometry (WLI) and Vertical Scanning Interferometry (VSI) methods were employed in this study. For this purpose, a Bruker Contour Elite 3D optical profiler for a 3D surface visualization was used. First, a strip of approximately 12 mm in width was cut from specimen 12 (with the best formability). This strip was later cut to seven pieces of equal size, starting from the undeformed area of the blank (No. 0) down towards the apex of the frustum (No. 6) as represented in Figure 2.18. A measurement spot of rectangular shape (2×0.5 mm^2) was assigned at the center of each sample (Figure 2.18). A magnification of 50x, a field of view (FOV) of 0.126×0.095 mm^2 with full resolution, and a back-front scan range of 220 μm were adopted in WLI 3D profiler software (Vision). A stitching algorithm of proper overlap (40%) was also used. Considering the curvature of the specimens, such settings guarantee nanometer accuracy along the perpendicular direction to the surface. It also allows for scanning over enough large surfaces to account for the waviness of the surface.

The raw data acquired from the 3D microscope (real surface), was first filtered by using low-pass filters (S-filter) of proper window size. Consequently, data were fitted to polynomial surfaces of proper orders by performing regression so that the tilt and the form of the surface were removed (F-operators). Afterward, a high-pass robust Gaussian filter being capable of end-effect management with a cut-off wavelength (nesting index) of 0.08 mm was adopted for filtering the waviness and providing the surface roughness. To realize a proper cut-off for the high-pass filter (L-filter), some 2D primary profiles of each measurement spot were initially filtered by adopting various standard nesting indexes. The resultant waviness profiles were visually checked by comparing them with the relevant primary and roughness profiles so that the best cut-off value was derived. Whenever noise filtering was required, the histograms of the data were also used for threshold filtering. Filtering tasks and presentation of the results were managed in MATLAB and Vision 64 Map (MountainsMap®) software.

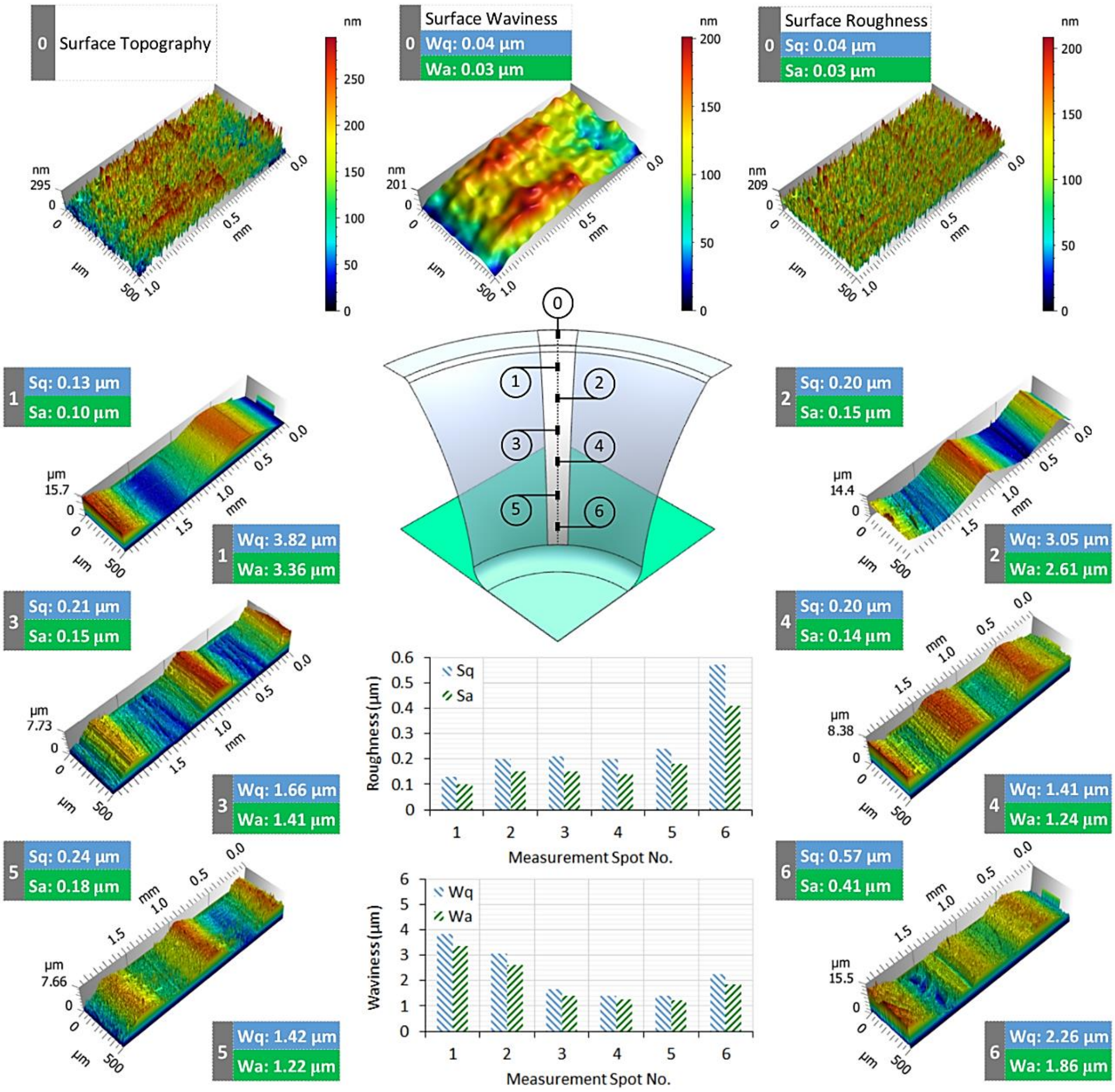

Figure 2.18: Roughness and waviness of the internal surface of specimen 12 (T6P0.8F1400S1400).

Figure 2.18 shows the resultant surface topography after removing shape and tilt, roughness and waviness in seven measurement spots at specimen 12 (the case of the best formability). The resultant roughness (S_a and S_q) and waviness (W_a and W_q) measures are also compared in this figure. The roughness and waviness of the POM blank show very small values in the range of 30 nm to 40 nm, which translates to a very fine initial surface. Considering the bar charts in this figure, surface roughness increases by approximately 400% by moving downwards from the base of the frustum towards the apex. Meanwhile, the forming force decreases after reaching its maximum at the initials stages of deformation as presented in Figure 2.7e. Therefore, the significant increase in surface roughness is mainly attributed to the rise of temperature. As stated before, the ratio of planar to axial force also continuously increases throughout the course of forming. This implies an increase in the friction coefficient on the tool-sheet contact interface, which in turn, partially explains the increase in roughness. However, waviness continuously decreases from the base of the frustum down to the measurement spot 5 (~ 70%). This is mainly associated with the continuous increase in the wall angle from the base towards the apex. Constant pitch size in the toolpath results in a reduction in the scallop height of the tool's footprint as the wall angle increases. The unexpected increase of waviness in the vicinity of the apex must be related to the minor wrinkling effects in this region as reported before (Figure 2.17b). Figure 2.19 shows SEM images from the external surface of the benchmark specimens close to their apex. Also, an SEM image from the POM blank (as received) is provided in the figure for comparison. By scrutinizing these SEM images, it was noticed that the larger the strain that specimen underwent, the larger the voids being visible on the surface. However, the increase in temperature resulted in shrinking the voids. Under such competing conditions between the two affecting factors, the number of voids increases with an increase in temperature.

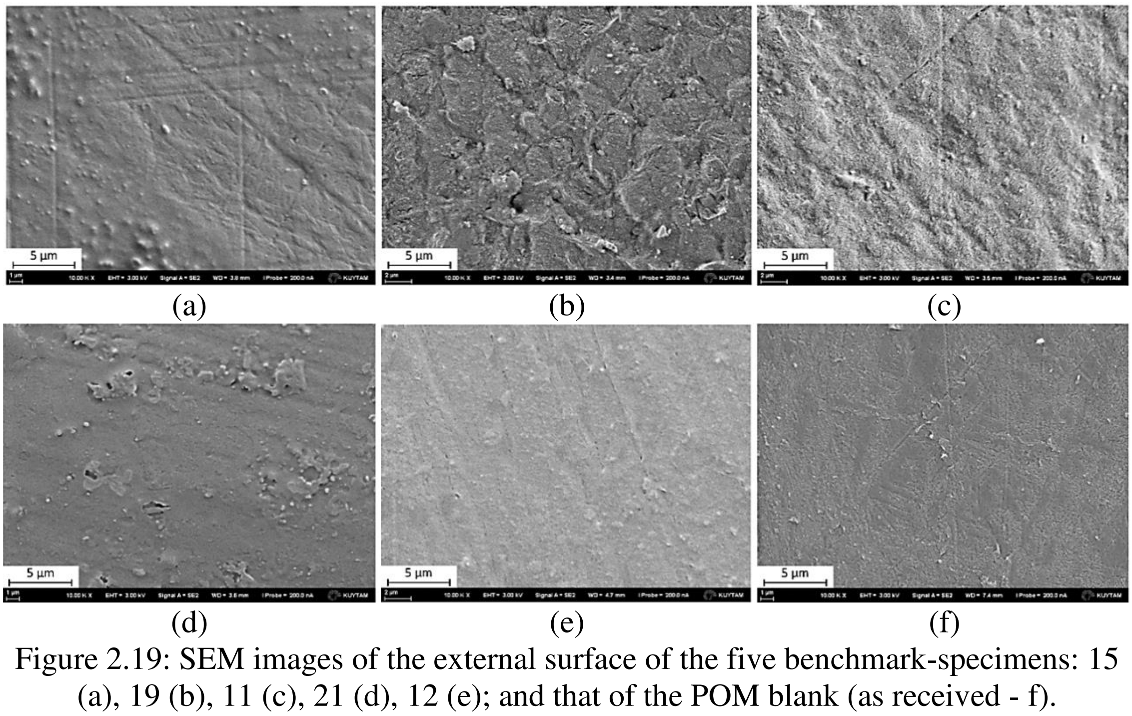

(a) (b) (c)

(d) (e) (f)

Figure 2.19: SEM images of the external surface of the five benchmark-specimens: 15 (a), 19 (b), 11 (c), 21 (d), 12 (e); and that of the POM blank (as received - f).

2.3.8 Properties of deformed material

Figure 2.20 presents a diffractogram acquired by employing X-Ray Diffraction (XRD) technology with a Bruker D8 Advance Diffractometer. Samples from benchmark POM specimens and blank (as-received) were prepared for XRD analysis. Figure 2.20b shows a zoomed view of the main peak (POM copolymer), clarifying differences in intensities and diffraction angles among the samples' peaks. While little differences in diffraction angles appear to be negligible in Figure 2.20b, a significant difference among intensities is evident. Such variation translates to a difference in the order of molecular chain orientation and percentage of crystallinity, which are affected by strain and heat.

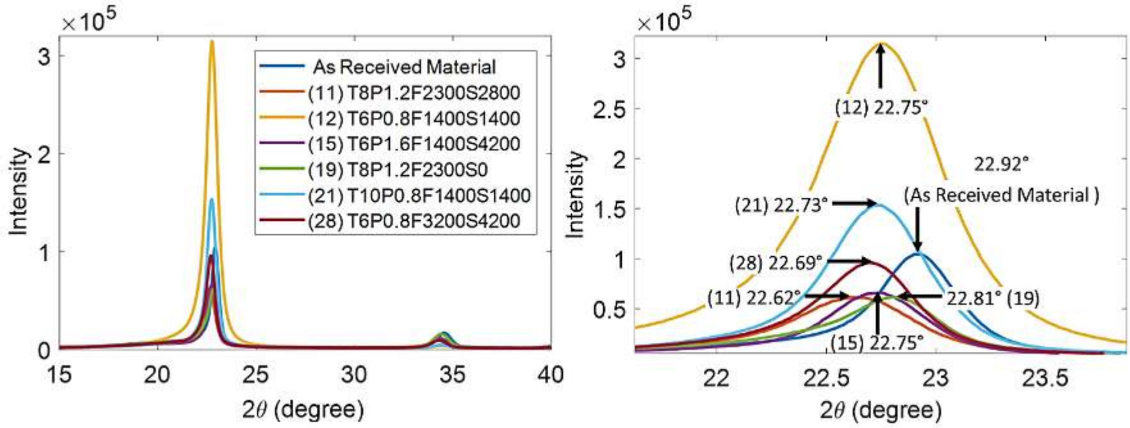

(a) (b)

Figure 2.20: Integrated intensity versus diffraction angle acquired from XRD analysis corresponding to benchmark specimens along with POM blank; general view (a), detailed view (b).

DIFFRAC.EVA software connected to the Bruker Diffractometer was used to quantitatively compare the crystallinity of the samples as reflected in Figure 2.21. It can be observed from this figure that crystallinity increased from 72% for POM blank (as received) to 89% for the best-case formability (specimen 12). The better the formability, the larger the strain the material undergoes. This is what is referred to as strain-induced crystallinity in the literature. Lozano-Sánchez et al. [130] observed the same phenomena when performing XRD analysis on polypropylene random copolymer (PPRC) samples being cut from the ISF specimens. One may notice from Figure 2.21 that the crystallinity of sample 19 is almost similar to that of as-received material and slightly less than that of sample15, while it underwent a larger strain. Comparing the two samples of the same formability (12 and 21), the latter shows a lower percentage of crystallinity. The reason is sample 19 represents the zero-spindle-speed case, therefore, the minimum failure temperature (34°C) was observed in this case. Heat-induced softening is believed to enhance the reorientation of the molecular chains and encourage further crystallization under the effect of the strain. However, excessive heat destroys the crystalline structure, which to some extent compensates for strain-induced crystallization. It seems to be the case for sample 21, where failure temperature reached 91°C. The results and justifications provided here also corroborate the findings of Wang et al. [131]. They used XRD for inspecting crystalline orientation of semicrystalline poly (lactic acid) under uniaxial drawing. They reported that by exceeding 100% strain at 80°C, partial destruction of the crystalline phase resulted in a significant reduction in the peak height in the diffractogram. This again highlights the fact that though the heat can improve the formability of POM and crystalline structure of the material, heating rate, and temperature must be carefully controlled to prevent damage.

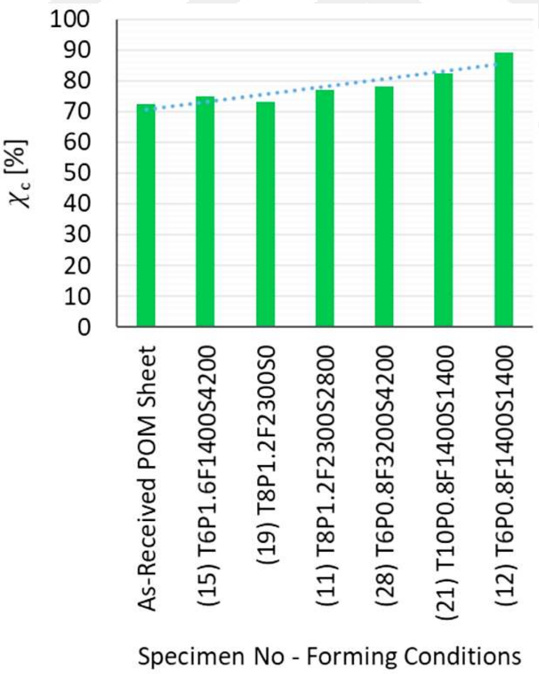

Figure 2.21: Evolution of crystallinity corresponding to benchmark forming conditions and POM blank (as received), acquired from XRD analysis.

It was noticed that those specimens of high formability were embrittled as compared to as-received POM blank. To further investigate the mechanical properties of deformed POM, a set of Nano-Indentation tests was conducted. A standard triangular pyramid

Berkovich indenter was adopted in the Agilent G200 machine by using the continuous stiffness measurement (CSM) technique. The maximum applied force, loading, and holding time were 7 mN, 100 s, and 20 s, respectively. Twelve spots were tested on each sample, which in the case of the incrementally formed samples, were located at the external surface of the specimens. Hardness and elastic modulus were calculated by using the acquired force-displacement data in the algorithm developed in MATLAB based on the approach adopted by Briscoe et al. [132]. Figure 2.22 represents the load as a function of displacement in the replicated tests on POM blank, samples 12 and 21 (after removing failed indentations). The average hardness of 190, 198, and 217 MPa, along with the average elastic modulus of 2.76, 2.82, and 3.08 MPa were derived for as-received POM sheets, samples 12 and 21, respectively.

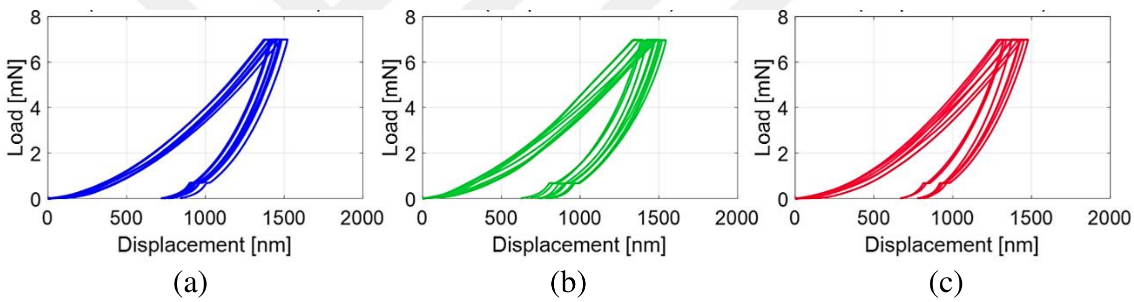

Figure 2.22: Load as a function of displacement in Instrumented Nano-Indentation tests performed on POM blank (as received - a) and samples corresponding to tests 12 (b), and 21 (c).

An increase in hardness [133] and modulus of elasticity [134] due to an increase in crystallinity of polymers have been reported in the literature. This explains why incrementally formed POM samples rendered higher hardness and elastic modulus as compared to the as-received material. Though sample 12 represented more crystallinity than sample 21, it exhibited less hardness and elastic medullas. This could be explained by the heat-induced degradation of POM in sample 21 and the higher volume density of voids in sample 12. In agreement with the findings reported here, Jiang et al. [135] reported that by increasing the mold temperature from 30°C to 80°C, the elastic modulus of the polypropylene samples (tested by nanoindentation) increased significantly. Instrumented nanoindentation test is partially sensitive to the surface quality and defects of the samples. Therefore, examination of the processed polymer samples must be performed with careful attention, and the results should be interpreted with caution.

2.4 Discussion on failure

In semicrystalline polymers, such as POM, amorphous segments are less stiff as compared to the crystalline structure, so they play a major role in the deformation mechanism. Deformation in such materials is due to crazing and cavitation under the effect of tensile stresses or plastic deformation derived by shear stress. Cavitation is more expected above the glass transition temperature in semicrystalline polymers undergoing tensile stresses. In contrast, crazing is more likely to happen around the glass transition temperatures and below that. Usually, crazing voids are significantly smaller than voids created by cavitation. The major difference is that there is no internal structure inside voids created by cavitation while they might be separated by fibrils from outside. In opposite, crazing voids can still transfer stresses via the fibrillary structure connecting their walls from inside [136]. Reviewing the literature, one can see these two terms have been interchangeably used for describing the same phenomenon. It has been thus far agreed upon that increase in volume [137] and stress whitening [138] are physical signs of significant void nucleation in semicrystalline polymers. It is also well established that by an increase in temperature [139], and a decrease in strain rate, cavitation becomes less pronounced. Under such conditions, the deformation mechanism shifts from cavitation towards slip and shear plastic flow in the material. Castagnet and Deburck [140] and Laiarinandrasana et al. [141] highlighted the effect of stress triaxiality on the level of cavitation in PVDF showing that large positive hydrostatic stress encourages further cavitation. It was also reported that whitening could be resulting from the growth of the initial voids, rather than the nucleation of new voids. Reviewing the literature, a brittle-ductile transition is also possible when polymers are stretched. Therefore, there should be some threshold conditions in terms of temperature, strain rate, and stress triaxiality at which both shear plasticity and cavitation coexist.

The translational forming speed, pitch size, and tool diameter are the parameters contributing to the strain rate of the sheet material in the ISF process. Strain rate is inversely related to the total forming time required for completely forming the FSISF specimens (regardless of fracture or failure) under each specific forming condition. Hence, the total forming time corresponding to each forming condition was calculated by using the relevant toolpath. The inverse values of the total forming times are reported in

Table 2.6 under the title Forming Rate Indicator (FRI [s^{-1}]). According to the theoretical framework provided by Silva et al. [113, 142] based on a membrane analysis, triaxiality is to a large extent controlled by the tool diameter in the ISF process. Therefore, the larger the tool diameter, the larger the triaxiality. Silva et al. [143] elaborating on the effect of tool size on the level of triaxiality and formability in incremental forming of aluminum AA1050-H111 derived a similar conclusion.

Table 2.6: Magnitudes of the Forming Rate Indicator (FRI) for FSISF tests.

Test No.	Tool Diameter [mm]	Pitch Size [mm]	Feed Rate [mm/min]	Spindle Speed [rpm]	FRI [10^{-3} s^{-1}]
1	6	1.6	1400	1400	6.05
2	6	0.8	1400	4200	3.02
3	10	1.6	1400	4200	6.74
4	8	2	2300	2800	13.10
5	6	1.6	3200	1400	13.82
6	10	1.6	3200	4200	15.40
7	10	1.6	3200	1400	15.40
8	8	0.4	2300	2800	2.62
9	8	0.4	2300	2800	7.86
10	10	1.6	1400	1400	6.74
11	8	1.2	2300	2800	7.86
12	6	0.8	1400	1400	3.02
13	10	0.8	3200	4200	7.70
14	10	0.8	3200	1400	7.70
15	6	1.6	1400	4200	6.05
16	12	1.2	2300	2800	8.79
17	6	1.6	3200	4200	13.82
18	10	0.8	1400	4200	3.37
19	8	1.2	2300	0	7.86
20	8	1.2	4100	2800	14.01
21	10	0.8	1400	1400	3.37
22	8	1.2	500	2800	1.71
23	8	0.4	2300	2800	7.86
24	4	1.2	2300	2800	7.08
25	8	0.4	2300	2800	7.86
26	6	0.8	3200	1400	6.91
27	8	1.2	2300	5600	7.86
28	6	0.8	3200	4200	6.91

Figure 2.23 provides SEM images from side views of the cracks corresponding to six different FSISF forming conditions showing different fracture mechanisms. Considering what has been said above and the morphology of the cracks, a brittle fracture is evident in Figure 2.23d corresponding to the forming conditions leading to the least formability. According to Table 2.5, the corresponding failure temperature to this test (44°C) was the closest to that of the zero-spindle-speed case (34°C). The forming rate indicator (FRI) also turned out to be 6.05e-3 s^{-1}. The average value of FRI was 7.86e-3 s^{-1}, corresponding to the tests 11 (average formability) and 19 (zero-spindle-speed). The tool size, as an indicator for the level of triaxiality, is relatively small (6 mm). Zooming on the image, a crazing-like effect is evident at the crack tip and edges. Since fracture occurred at the very beginning of the forming process, it could be under the effect of bending imposed by boundary conditions. Under such conditions, any material flaw can inspire significant stress concentration and initiate the crack, which could rapidly propagate at a relatively low temperature.

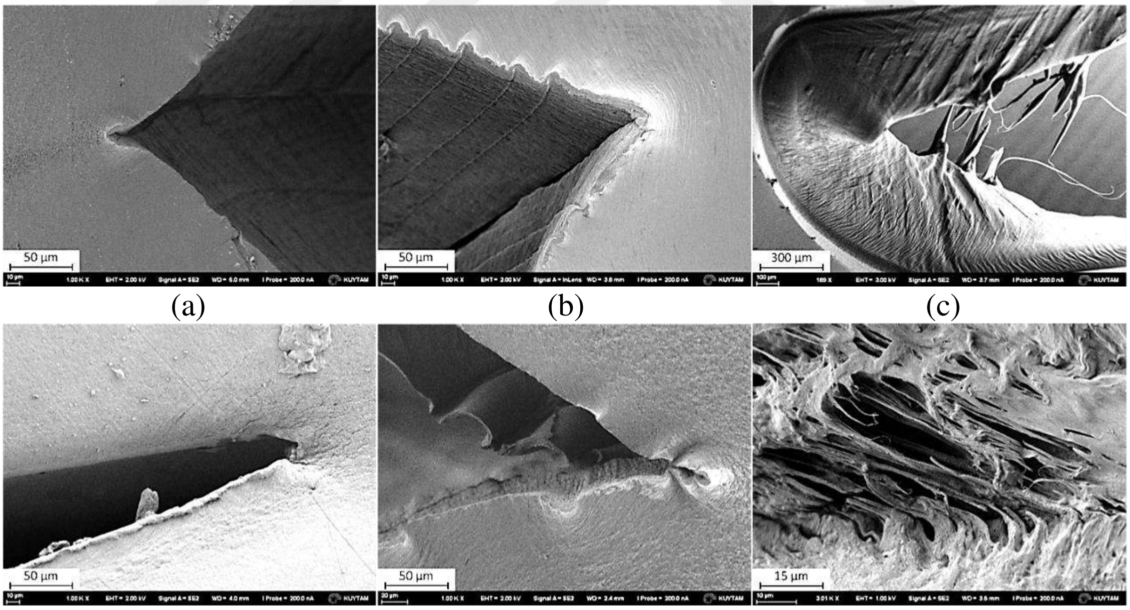

(a) (b) (c)

(d) (e) (f)

Figure 2.23: SEM images (side view) of crack tips in FSISF specimens 11 (a), 26 (b), 18 (c), 15 (d), 28 (e), and 22 (f).

Figures 2.23a, 2.23b, and 2.23e represent a semi-brittle fracture. The white area at crack tip and edges in Figures 2.23b is probably because of cavitation. In this case, the failure temperature was 45°C, which is under the average. The LHRI was also 0.21°Cs^{-1}, which is the second least in the list. The FRI was 6.91e-3 s^{-1}, which is also under average.

Tool diameter is small, which implies a relatively low level of triaxiality. However, the measure of formability is over average ($\phi_{max} = 73°$).

The key factors enhancing the formability of the POM sheet seem to be a low strain rate and a low heating rate. Figures 2.23a, and 2.23e corresponding to tests 11 and 28, both represent average formability (ϕ_{max}~67°). The relevant failure temperatures of 62°C and 59°C are also very close to the average value. Heating rates are 0.55°Cs^{-1} (the average value), and 0.43°Cs^{-1}, respectively. The strain rate indicators were also 7.86e-3 s^{-1} and 6.91e-3 s^{-1}, respectively. The tool diameter of the former case (8 mm) was also larger than that of the latter case (6 mm). Therefore, a delicate trade-off among the factors that affect the fracture mechanism results in a value of formability equal to that of the average value. This observation once again infers the high level of interactivity among the process parameters, when formability and failure of POM sheet in ISF process are concerned.

Failure topography in test 22 as shown by Figures 2.23f exemplifies severe cavitation. In this case, the failure temperature, LHRI, FRI, and tool diameter are 74°C, 0.22 °Cs^{-1}, 1.71e-3 s^{-1}, and 8 mm, respectively. Though the foregoing FRI represents the minimum value in the list, failure temperature is well above the average. The heating rate is also among the least in the list, while tool diameter represents a moderate size. As mentioned before, high temperatures and low strain rates are not in favor of cavitation. In addition, merely a moderate tool size cannot boost triaxiality to stimulate a significant amount of cavitation. Instead, such fracture topography might be because of localized melting of POM under adiabatic heating. Such heating accompanied by a significant stress concentration result in delamination and destruction of the crystalline structure. Gent and Madan [144] also pointed out that such a mechanism could explain the yielding in several semicrystalline polymers, namely PE, PP, PB, and PTEF under uniaxial stretching condition. In addition, Kennedy et al. [145] conducting tensile tests on linear PE sheet materials of two different molecular weights, explained the yielding of the material partially based on the aforesaid mechanism.

In Figures 2.23c, the crack morphology looks quite different from the previous cases. A clear ductile tearing is evident from the SEM image. In this case, the failure temperature, LHRI, FRI, and tool diameter were 90°C, 0.58 °Cs^{-1}, 3.37e-3 s^{-1}, and 10 mm, respectively. It is worth mentioning that the yield strength of POM can reduce by

50% at such a temperature [146]. The maximum failure temperature in the list, accompanied by average FRI, average LHRI, and upper average tool size in test 18 resulted in a formability measure well below the average. The topography of the fracture surface can provide further information on the relation between the processing conditions and the mechanism of failure in FSISF. Figure 2.24 allows comparison among four fracture surfaces corresponding to specimens 10, 19, 11, and 28.

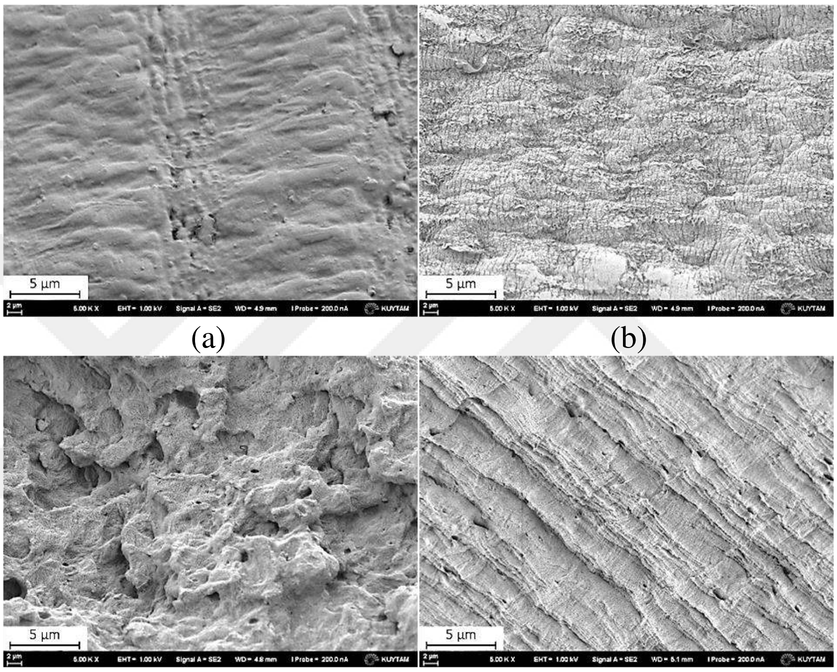

(a) (b)

(c) (d)

Figure 2.24: SEM images of the crack cross-sections in FSISF specimens 10 (a), 11 (b), 19 (c), and 28 (d).

Although the side views of the cracks in tests 11 and 28 look quite similar, the fractured sections look quite different. Under the effects of entirely different process parameters, the two specimens delivered similar formability. By scrutinizing Figure 2.24b, a semi-dimple structure similar to that of Figure 2.24c is visible, but in a smaller size and more delicate spherulitic structure. The SEM images from other spots in the same fracture plane show close similarities to Figure 2.24c. The delicate semi-dimple structure in Figure 2.24b is covered by macro craze fibers rising upward. There is also no evident indication of voids on the surface. Considering Figure 2.24d, those inclined lines on the surface resemble slip lines, which can imply the presence of shear. At the same time, several voids are distributed over the surface. This fracture surface indicates signs of stretching and shear together. The forming conditions corresponding to tests 11 and 28 introduce a brittle-ductile transition threshold in the process. At the beginning of this section, the feasibility of such coexistence was concluded from the literature. Figure 2.24c clearly shows a dimple structure accompanied by relatively large voids. Recalling the least failure temperature (34°C) and an average FIR magnitude of 7.86e-3 s^{-1} for test 19, a brittle fracture under the effect of tensile stresses is expected. A combination of shear bands in a highly crystallized structure and minor cavitation in the amorphous phase is visible in Figure 2.24a. In this case, the failure temperature, LHRI, and FRI of 74°C, 0.37 °Cs^{-1}, and 6.74e-3 s^{-1} resulted in high formability (third-place in the list). Figure 2.25 shows SEM images of the crazing fibers in microvoids near the crack tip in the FSISF specimen 28. This figure also presents the relevant forming force components as a function of time, which indicate the stress transitioning quality of the crazing fibers.

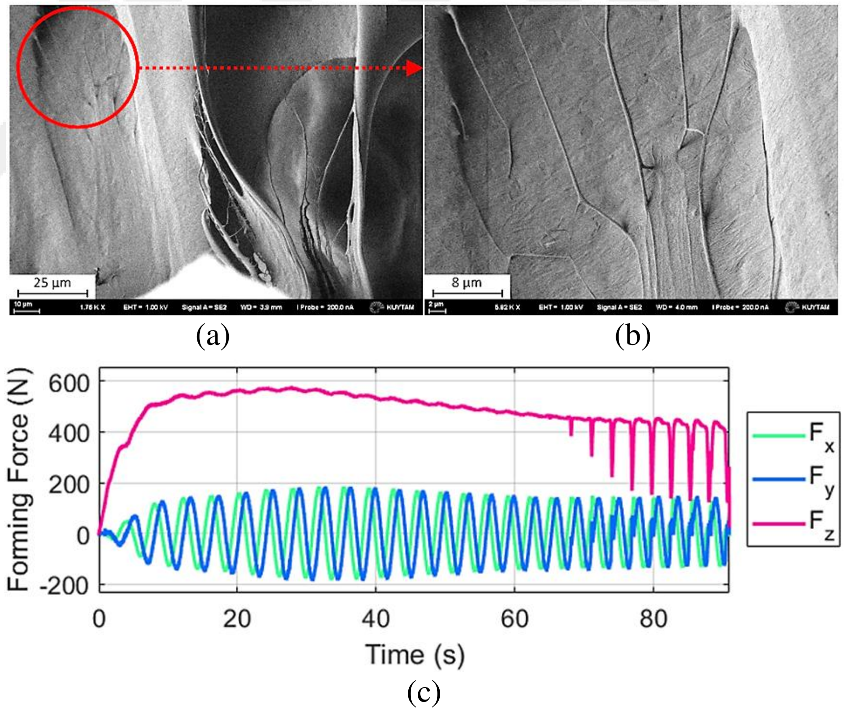

Figure 2.25: Macro voids (a), crazing-like fibers around the crack tip (b), and the corresponding effect on the forming force components (c) in FSISF test 28.

To conclude this section, the incremental sheet forming research community has been divided on the mechanism of failure in the process. One school of thought supports the necking mechanism and decisive influence of shear. From the other side, researchers suggest mechanisms by which necking is suppressed; therefore, stretching remains the driving mechanism behind the failure. Both groups provide solid experimental evidence and analytical frameworks supporting their point of view. However, the majority of the researchers from both sides have targeted the ISF of metallic alloys at room temperature. In this study, FSISF of POM as a semicrystalline polymer of semi-brittle behavior at room temperature was investigated. The research outcomes provide clear evidence and proper physical justifications for the possibility of brittle, brittle-ductile, and ductile fracture of POM under interactive effects of the ISF process parameters.

Chapter 3

ANALYTICAL AND NUMERICAL INVESTIGATION

3.1 Introduction and overview

As detailed in the previous chapters, in the very limited number of studies conducted by employing POM in the ISF process, this thermoplastic has shown very low formability at room temperature. However, POM is known as a semicrystalline engineering thermoplastic of very good mechanical and chemical characteristics along with high surface quality. This chapter aims to address the problem by proposing a combined numerical-analytical discipline to efficiently predict the force and temperature at the tool-sheet contact interface in friction stir incremental sheet forming (FSISF) of POM. As a result, the forming mechanism could be systematically exposed, and the forming conditions leading to a premature failure could be analyzed and prevented. A threshold boundary for the maximum allowable temperature at the tool-sheet contact interface was established in the previous chapter. Therefore, by adopting the proposed numerical-analytical framework in this chapter, FSISF process parameters could be adjusted to safeguard the high formability of the POM sheet whereas heat-induced defects are avoided. At the end of the chapter, analytical predictions for the major FSISF benchmarks are compared against the experimental measurements, and good compliance is presented.

3.2 Mechanism of deformation

As explained in the section of the introduction, deformation, and failure of polymers in the ISF process are mainly derived by meridional stretching. Therefore, Silva et al. [112] employed a pressure-modified version of the Tresca yield criterion as proposed by Whitney and Andrews [147] to develop an analytical framework based on membrane analysis. Figure 3.1 presents a cross-section view of the geometry of the problem, and the stresses acting along meridional (ϕ), circumferential (θ) and radial or thickness (t) directions.

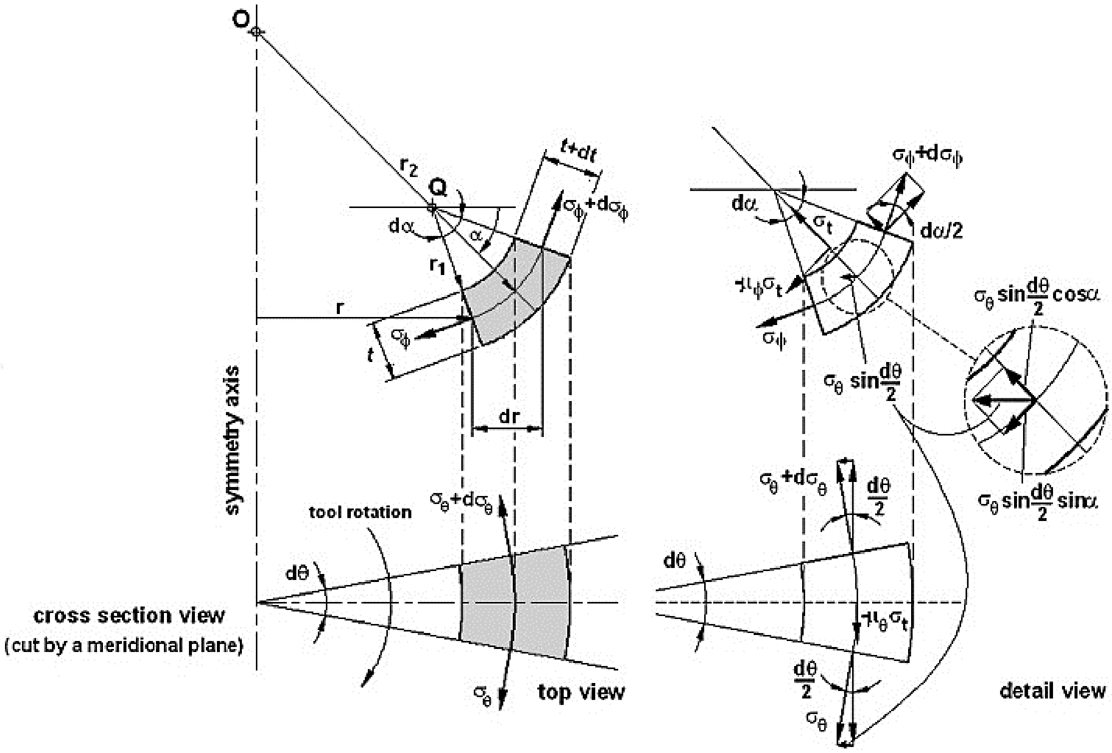

Figure 3.1: A cross-section view of the geometry of the ISF problem, and the acting stresses based on membrane analysis [112].

For the aforesaid membrane analysis, the material was assumed incompressible based on several research outcomes. By neglecting the effects of temperature and strain rate, the polymer was also assumed to behave perfectly plastic. Considering the force equilibrium, assuming that $\sigma_1 = \sigma_\phi$, $\sigma_2 = \sigma_\theta$ and $\sigma_3 = \sigma_t$ are the principal stresses ($\sigma_\phi > 0$; $\sigma_t < 0$), and by neglecting the higher-order and small terms based on the geometry of the process (Figure 3.1), they concluded that:

$$\sigma_t = -\frac{t}{r_t}\sigma_\phi \tag{3.1}$$

Considering the significance of temperature and strain rate in the plastic behavior of polymers, the aforesaid analytical framework is extended to investigate the FSISF of POM in this chapter. In this regard, the compressive and tensile yield strengths of POM experimentally measured by Pae [148], under the effect of several hydrostatic stresses ($0.1 \leq \sigma_m \leq 689.5$ MPa), provide valuable information. According to the available data, the average ratio of the compressive yield strengths (σ_{YC}) to the tensile yield strengths (σ_{YT}) is 1.05. It means the unsymmetrical quality in compressive-tensile yielding is not significant. In the current study, magnitudes of hydrostatic stresses (σ_m) in the FSISF of POM were predicted by using the membrane analysis framework. For this purpose, several sheet thicknesses (0.5 to 2 mm) and tool radiuses (2 to 6 mm) were employed according to the experimental design of the current study. As a result, the maximum hydrostatic stress was estimated as 40% of the yield strength. Considering the data provided by Pae [148], such a magnitude of hydrostatic stress results in an increase of 5.5% in the geometric mean yield strength, $\sigma_Y = \sqrt{\sigma_{YC}.\sigma_{YT}}$, which is not significant. Therefore, it was concluded that the general form of the von Mises yield criterion can be safely used for predicting the forming forces in FSISF of POM. The Johnson-Cook (JC) constitutive model was calibrated by performing tensile tests on POM dog-bone sheet samples at speeds of 5 and 250 mm/min and temperatures of 25 (ambient), 40, 80 and 120 °C. The calibration process and the model parameters are detailed in the next chapter. The JC model has the following form:

$$\bar{\sigma} = \left[A + B\bar{\varepsilon}_{pl}^{n}\right]\left[1 + C\ln\left(\frac{\dot{\bar{\varepsilon}}_{pl}}{\dot{\varepsilon}_0}\right)\right]\left[1 - \left(\frac{T - T_{ref}}{T_{melt} - T_{ref}}\right)^m\right] \tag{3.2}$$

Where, $\bar{\sigma}$, $\bar{\varepsilon}_p$, $\dot{\bar{\varepsilon}}_{pl}$ are the equivalent stress, equivalent plastic strain, and equivalent plastic strain rate, respectively. By considering the plain-strain condition in incremental forming of polymers:

$$\sigma_\theta = \frac{1}{2}(\sigma_\phi + \sigma_t) \tag{3.3}$$

Considering the von Mises yield criterion, the equivalent stress can be calculated as:

$$\bar{\sigma} = \sqrt{\frac{1}{2}\left[(\sigma_\phi - \sigma_\theta)^2 + (\sigma_\theta - \sigma_t)^2 + (\sigma_t - \sigma_\phi)^2\right]} = \frac{\sqrt{3}}{2}\left(\sigma_\phi - \sigma_t\right) \tag{3.4}$$

Combining the Equations 3.1 to 3.4:

$$\sigma_\phi = \frac{2}{\sqrt{3}}\frac{r_t}{t + r_t}\bar{\sigma} \tag{3.5}$$

Therefore:

$$\sigma_t = -\frac{2}{\sqrt{3}}\frac{t}{t + r_t}\bar{\sigma} \tag{3.6}$$

$$\sigma_\theta = \frac{1}{\sqrt{3}}\frac{r_t - t}{t + r_t}\bar{\sigma} \tag{3.7}$$

And the hydrostatic stress, σ_m, is:

$$\sigma_m = \frac{1}{\sqrt{3}}\frac{r_t - t}{t + r_t}\bar{\sigma} \tag{3.8}$$

Therefore, the stress triaxiality can be calculated as:

$$\eta = \frac{1}{\sqrt{3}}\frac{r_t - t}{t + r_t} \tag{3.9}$$

As stated before, the "Sine Law" or "Cosine Law" has been widely used in the literature to calculate the real-time thickness of the sheet in the ISF process. The same approach is taken here:

$$t_s = t_0 \cos\varphi \tag{3.10}$$

Where, t_0 is the initial sheet thickness, φ denotes the slope angle of the deformed sheet with respect to the initial undeformed state, and t_s is the real-time sheet thickness. Assuming that the variation of sheet thickness in the slab sheet under the tool is linear, the average real-time sheet thickness beneath the tool, t_{s_avg}, is:

$$t_{s\_avg} = \frac{t_0}{2}(1 + \cos\varphi) \tag{3.11}$$

Replacing the above equation in Equations 3.5 to 3.7:

$$\sigma_\phi = \frac{2}{\sqrt{3}}\frac{2r_t}{t_0(1 + \cos\varphi) + 2r_t}\bar{\sigma} \tag{3.12}$$

$$\sigma_t = -\frac{2}{\sqrt{3}}\frac{t_0(1 + \cos\varphi)}{t_0(1 + \cos\varphi) + 2r_t}\bar{\sigma} \tag{3.13}$$

$$\sigma_\theta = \frac{1}{\sqrt{3}}\frac{2r_t - t_0(1 + \cos\varphi)}{t_0(1 + \cos\varphi) + 2r_t}\bar{\sigma} \tag{3.14}$$

Neglecting the bending effect on the mid-plane of the sheet and considering the plan strain condition as stated before:

$$\varepsilon_{\phi} = -\varepsilon_t = \ln\left(\frac{t_0}{t}\right) = \ln\left(\frac{t_0}{t_{s\_avg}}\right) = \ln\left(\frac{2}{1+\cos\varphi}\right) \tag{3.15}$$

$$\bar{\varepsilon} = \sqrt{\frac{2}{9}\left[(\varepsilon_{\phi}-\varepsilon_{\theta})^2 + (\varepsilon_{\theta}-\varepsilon_t)^2 + (\varepsilon_t-\varepsilon_{\phi})^2\right]} = \frac{2}{\sqrt{3}}\ln\left(\frac{2}{1+\cos\varphi}\right) \tag{3.16}$$

3.2.1 A brief discussion on stretch-bending in sheet

As stated before, the bending effect was neglected on the mid-plane of the sheet to calculate the meridional strain as shown by Equation 3.15. To take into account the bending effect in the slab sheet under the tool, a similar approach to Morales et al. [149] was taken to calculate ε_{ϕ} and $\bar{\varepsilon}$. Figure 3.2 provides a 1D illustration of a sheet strip being under stretch-bending.

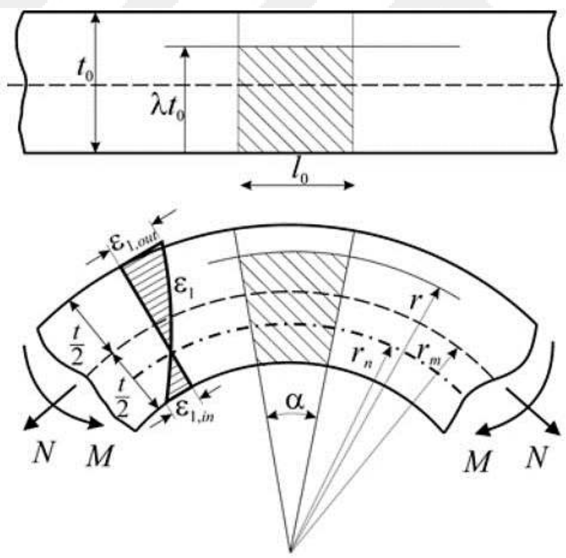

Figure 3.2: A 1D illustration of the stretch-bending in a sheet strip [149].

The sheet strip of thickness t in Figure 3.2 is stretch-bent around the ISF tooltip with the radius of $r_{in} = r_t$. ϕ (or α as shown in Figure 3.2) is taken as the bending angle of the strip. r_m and r_n represent the radius of the sheet curvature in mid-thickness and the radius of the neutral axis, respectively. Also, r represents the radial position of each arbitrary point along the sheet thickness:

$$r = r_t + \varsigma t \, ; \; 0 \leq \varsigma \leq 1 \tag{3.17}$$

The thickness of the slab sheet under the tool is assumed constant along the circumferential direction. The thickness also varies linearly with ϕ along the meridional direction. At the radial position r_m, no bending strain is expected. The only strain along the meridional direction is due to stretching. Therefore:

$$\varepsilon_{\phi\_m} = ln\frac{l_m}{l_0} \tag{3.18}$$

Where, l_0 and l_m represent the initial non-strained and strained fiber at the mid sheet thickness. Considering that at the mid sheet thickness no bending effect is present, and assuming the incompressibility of the strained material [150] and the overall plane-strain condition in the process:

$$ln\frac{l_m}{l_0} = ln\frac{t_0}{t} \rightarrow l_m = l_0\frac{t_0}{t} \tag{3.19}$$

Considering the strain along the meridional direction is zero on the neutral axis represented by r_n:

$$\varepsilon_{\phi\_n} = 0 \; \rightarrow \; l_n = l_0 \tag{3.20}$$

$$\phi = \frac{l_m}{r_m} = \frac{l_n}{r_n} \tag{3.21}$$

Therefore:

$$\frac{l_0 t_0}{r_m t} = \frac{l_0}{r_n} \; \rightarrow \; r_n = r_m\frac{t}{t_0} \tag{3.22}$$

$$r_m = r_t + \frac{t}{2} \tag{3.23}$$

$$r_n = \frac{(2r_t + t)t}{2t_0} \tag{3.24}$$

The overall meridional strain can be calculated as:

$$\varepsilon_\phi = ln\frac{r}{r_n} \tag{3.25}$$

In other words:

$$\varepsilon_\phi = ln\frac{\frac{r}{r_m}}{\frac{r_n}{r_m}} = ln\frac{r}{r_m} - ln\left(r_m\frac{t}{t_0}\frac{1}{r_m}\right) = ln\frac{r}{r_m} - ln\left(\frac{t}{t_0}\right) = ln\frac{r}{r_m} + ln\left(\frac{t_0}{t}\right) \tag{3.26}$$

Therefore:

$$\varepsilon_\phi = ln\frac{rt_0}{r_m t} \tag{3.27}$$

The above relation is also used by Fang et al. [151] in reference to Chakrabarty [152]. Accordingly the meridional strain, ε_ϕ, can be defined as follows:

$$\varepsilon_\phi = ln\frac{2(r_t + \varsigma t)t_0}{(2r_t + t)t} \tag{3.28}$$

As stated before, ε_ϕ varies with meridional contact angle, ϕ, along the tool-sheet contact interface. Also, sheet thickness, t, is a linear function of ϕ, and ς represents the radial position of the arbitrary point along the sheet thickness. To calculate the average value of the meridional strain in the sheet slab beneath the tool, the average values of the sheet thickness, t_{s_avg}, and $\varsigma_{avg} = 1/2$ can be replaced in Equation 3.28. Therefore, one can notice that the average meridional plastic strain by including the bending effect can be still derived by using Equation 3.15.

3.3 Tool-sheet contact interface: area and velocity

Two approaches are developed here to estimate the area of the tool-sheet contact interface and the relative velocities with respect to the contact patch in the FSISF process. The majority of the analytical outcomes presented in this chapter are produced by adopting the first approach. However, no substantial difference was observed in the results derived by adopting each of these methods. Except that the second approach provides a minimum error versus FEA results in the initial stage of deformation. The second approach is also more straightforward. Both methods are discussed here in detail.

3.3.1 Tool-sheet contact interface: the first approach

Figure 3.3 illustrates 2D and 3D views of the ISF tool-sheet contact interface projected by taking a geometrical approach. The tool-sheet interface is shown as discrete contact patches created by the tool when it imposes localized deformation on the sheet. Two major tool-sheet contact scenarios (I and II) are supposed as shown in Figure 3.3. Another short scenario is conceivable only at the beginning of the process (Figure 3.3[0. 3D]).

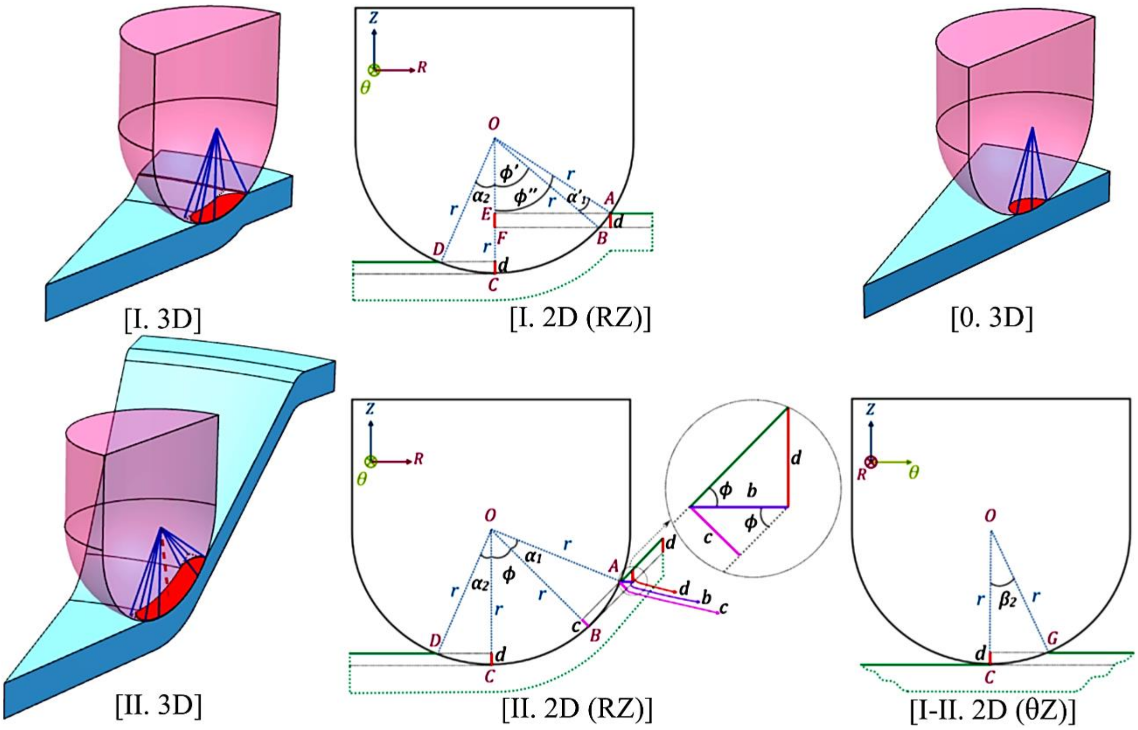

Figure 3.3: The tool-sheet contact geometry and contact scenarios in the ISF process (first approach).

Considering the geometry of the contact scenarios as presented in Figure 3.3, the following relationship is generally assumed regarding the indentation angles:

$$\begin{cases} \beta_2 = \alpha_2 \\ \beta_1 = \alpha_1 \end{cases} \tag{3.29}$$

Where α and β are the indentation angles along the meridional and the circumferential directions, respectively. Considering the dominant contact scenario (II), when $|\ Z_{tt}\ | \geq r_t[1 - \cos(\varphi + \alpha_1)]$:

$$b = dcot\varphi \tag{3.30}$$

$$c = bsin\varphi = dcos\varphi \tag{3.31}$$

$$\alpha_1 = \cos^{-1}\left(1 - \frac{c}{r_t}\right) = \cos^{-1}\left(1 - \frac{d}{r_t}cos\varphi\right) \tag{3.32}$$

$$\alpha_2 = \cos^{-1}\left(1 - \frac{d}{r_t}\right) \tag{3.33}$$

Where, Z_{tt} represents the lowest tooltip position along the Z direction in a fixed Cartesian coordinate system attached to the center of the undeformed sheet (Figure 3.4).

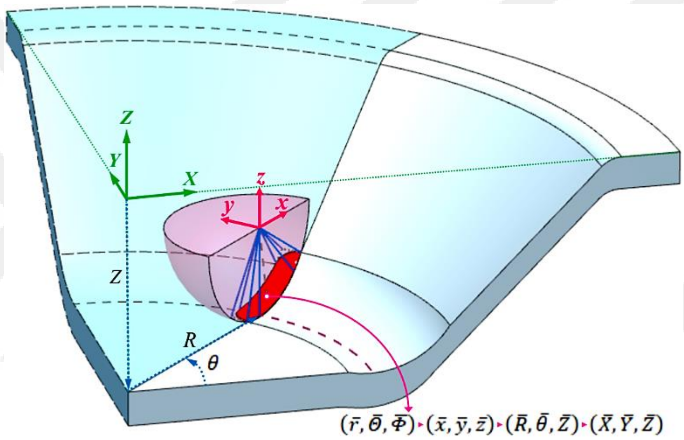

Figure 3.4: ISF specimen, tool, contact patch, and coordinate systems.

r_t represents the radius of the hemispherical tool-head. d denotes the penetration of the tool to the sheet. In the first contact scenario (I), the angle $\acute{\alpha}_1$ is assumed to linearly decrease from α_2 at the final instant of the initial contact scenario (0), to α_1 at the beginning of the main contact scenario (II). φ' is also assumed to linearly increase from 0 to φ in the same transition period. Considering the main contact scenario (II), the tool-sheet interface area can be calculated as follows:

$$\begin{aligned} A_c = \int_{\frac{\pi}{2}}^{\pi}\int_{\pi-\alpha_2}^{\pi} r^2 \sin\Phi d\Phi d\Theta + \int_{\frac{\pi}{2}}^{\pi}\int_{\pi-\alpha_1}^{\pi} r^2 \sin\Phi d\Phi d\Theta \\ + \int_{\alpha_2}^{\alpha_1}\int_{\pi-\varphi}^{\pi} r^2 \sin\Phi d\Phi d\Theta + \int_{\pi-\varphi}^{\pi} r^2\,\alpha_2\,d\Phi \end{aligned} \tag{3.34}$$

$$A_c = {r_t}^2 \left[\frac{\pi}{2}(2 - \cos\alpha_2 - \cos\alpha_1) + (\alpha_1 - \alpha_2)(1 - \cos\varphi) + \varphi\alpha_2\right] \tag{3.35}$$

Where Φ and Θ are the meridional and circumferential components of a spherical coordinate system attached to the hemispherical tool-head (Figure 3.4). The interface area for the contact scenario (I) can be calculated by replacing α_1 and φ with α_1' and φ', respectively. Also, considering the initial contact scenario (0):

$$A_c = \pi {r_t}^2 (1 - \cos\alpha_2) \tag{3.36}$$

To facilitate the calculation of the average velocity of the tooltip with respect to the contact patches, $\bar{v}_t$, the part of the tool-sheet interface that is affiliated to α_1 can be approximated by a rectangular strip of the same width and area. Then, the length of the strip along the meridional direction can be associated with λ_1, so that:

$$\lambda_1 = \frac{\pi(1 - cos\alpha_1)}{2\alpha_1} \tag{3.37}$$

In the case of the main contact scenario (II), $\bar{v}_t$ can be calculated as follows:

$$\bar{v}_t = \frac{\omega r}{4}\left[\frac{\frac{\pi}{2}(2\alpha_2 - \sin 2\alpha_2) + (\alpha_1 - \alpha_2)(2\varphi - \sin 2\varphi) + 4\alpha_2(1 - cos\varphi) + 4\alpha_1(cos\varphi - \cos(\varphi + \lambda_1))}{\frac{\pi}{2}(2 - \cos\alpha_2 - \cos\alpha_1) + (\alpha_1 - \alpha_2)(1 - \cos\varphi) + \varphi\alpha_2}\right] \tag{3.38}$$

Again, $\bar{v}_t$ for the contact scenario (I) can be calculated by replacing α_1 and φ with α_1' and φ', respectively. Also, considering the initial contact scenario (0):

$$\bar{v}_t = \frac{\omega r_t}{4}\left[\frac{2\alpha_2 - \sin 2\alpha_2}{1 - \cos\alpha_2}\right] \tag{3.39}$$

The relative velocity of the sheet with respect to the contact patches can be calculated as:

$$v_s = (1.67e - 5)\dot{f} \tag{3.40}$$

Which, $\dot{f}$ [mm/min] represents the feed rate or the forming speed. Therefore, the relative velocity of tool and sheet is:

$$\bar{v} = \bar{v}_t + v_s \tag{3.41}$$

Finally, the contact force along the normal of the contact patch, F_t, can be calculated as follows:

$$F_t = A_c \sigma_t \tag{3.42}$$

3.3.2 Tool-sheet contact interface: the second approach

By further investigating the geometry of the tool-sheet interface through the experimental observations and FEA, a more straightforward methodology for the prediction of contact area and estimation of the relative velocities was developed. Figure 3.5 shows the geometry of the tool-sheet interface based on the new approach. The contact patch as portrayed in Figure 3.5a can be divided into two segments. The BDC segment is a quadrant spherical cap, and the ABC segment can be considered as a quadrant spherical ellipse (as detailed in Figure 3.5.b). The definition of a spherical ellipse is the same as the planar ellipse, which is a "curve surrounding two focal points, such that for all points on the curve, the sum of the two distances to the focal points is a constant" [153]. Figure 3.5.c presents a planar ellipse that is created by the projection of the spherical ellipse to the x-y plane (parallel to the blank before forming). In this figure, F_1 and F_2 are the two focal points; and *a*, *b*, and *c* represent the half-length (semi-major axis), half-width (semi-minor axis), and foci of the illustrated ellipse, respectively.

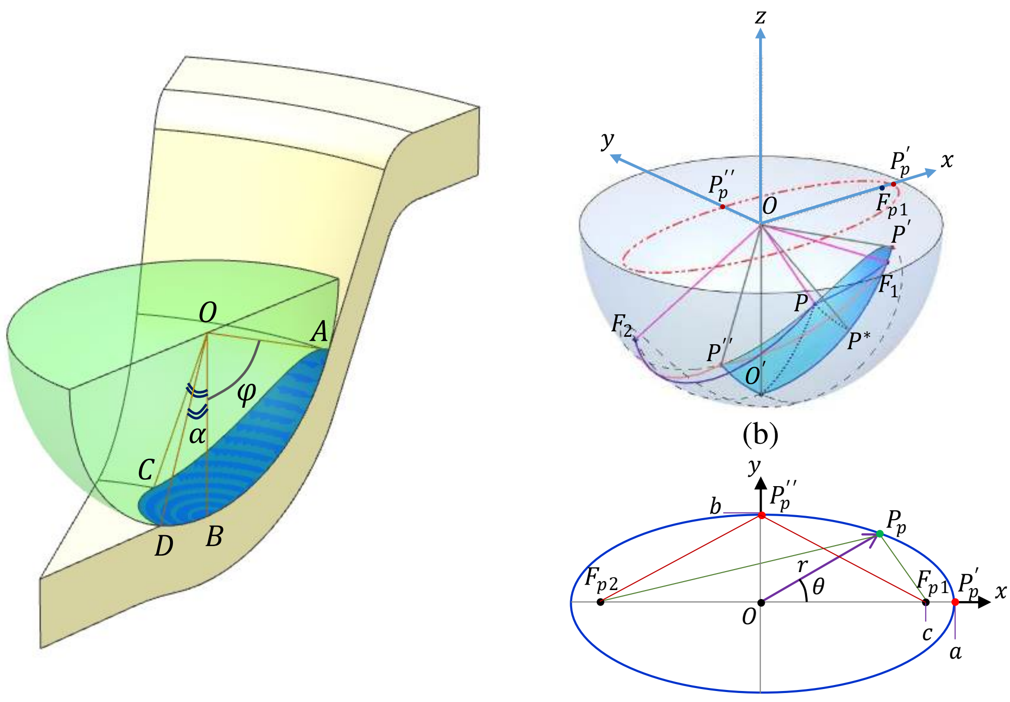

(a) (c)

Figure 3.5: Geometry of the tool-sheet interface in ISF (second approach); 3D view (a), part of the contact patch represented by a quadrant spherical ellipse (b), and projection of the quadrant spherical ellipse to the sheet plane (c).

Details on the calculation of the area and centroid of the spherical ellipse are omitted here. Briefly, the area of the spherical elliptical surface is calculated in a similar way as the area of the plain elliptical surface. Considering a quadrant spherical elliptical surface as shown by Figure 3.5, the area is:

$$A_{qse} = \frac{\pi}{4}ab = \frac{\pi}{4}r_t^2\alpha\varphi \tag{3.43}$$

The area of the quadrant spherical cap is:

$$A_{qsc} = \frac{\pi}{2}r_t^2(1 - cos\alpha) \tag{3.44}$$

Therefore, the total tool-sheet contact area can be estimated by:

$$A_c = \frac{\pi r_t^2}{2}\left[1 - cos\alpha + \frac{\alpha\varphi}{2}\right] \tag{3.45}$$

This method was used to estimate the area of the quadrant spherical ellipse in a CAD model of a hypothetical tool-sheet contact interface in ISF. Figure 3.6 shows the geometry of the interface and its dimension. The area was calculated by using the lengths of the semi-minor and semi-major axis of the quadrant spherical elliptical surface as presented in Figure 3.6 ($A_{cal} = 5.3378\ mm^2$). The area of the quadrant spherical elliptical contact surface is also measured in the CAD software (NX) as shown in the same figure ($A_{cad} = 5.5646\ mm^2$). Therefore, an error of 3.9% was derived, which is insignificant.

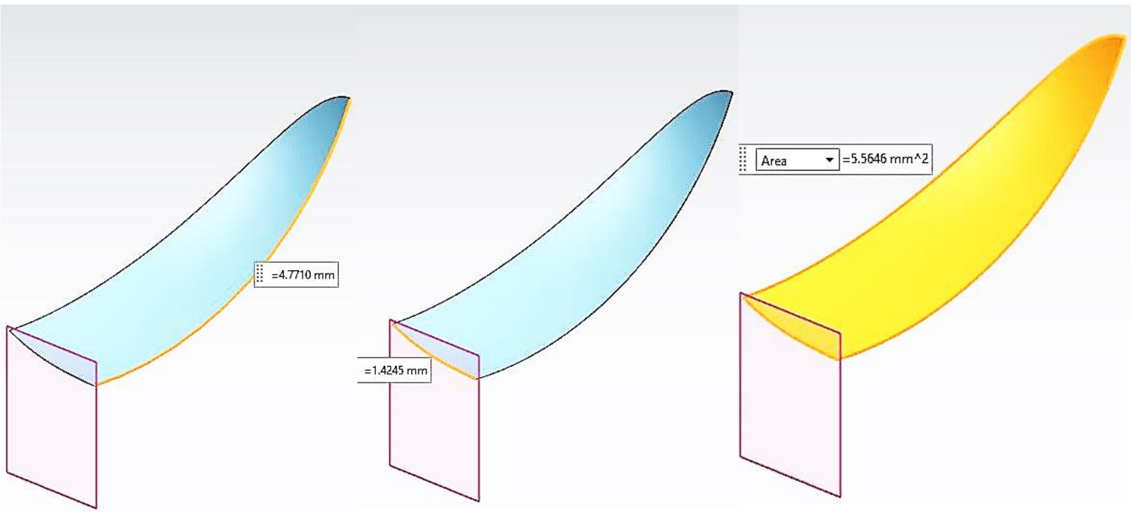

(a) (b) (c)

Figure 3.6: A CAD model of a hypothetical tool-sheet contact surface in ISF: half-length (semi-major axis: a), half-width (semi- minor axis: b), and the area of the quadrant spherical-elliptical contact surface (c).

The average relative velocity is attributed to the centroid of the tool-sheet contact patch. Considering Figure 3.5, the components of the centroid in the spherical coordinate system (attached to the center of the hemispherical tooltip) can be calculated as follows:

$$\bar{\varphi} = \frac{4\varphi}{3\pi} \tag{3.46}$$

$$\bar{\alpha} = \frac{4\alpha}{3\pi} \tag{3.47}$$

Therefore, the relative velocity corresponding to the quadrant spherical ellipse can be calculated as follows:

$$v_{qse} = 2\pi\omega r_t \sqrt{\sin^2\left(\frac{4\varphi}{3\pi}\right) + \sin^2\left(\frac{4\alpha}{3\pi}\right)} \tag{3.48}$$

Considering the spherical-cap segment of the contact patch, and the definition of the geometrical centroid:

$$A_{qsc}\bar{R}_z = \int_a^b R_z dA \tag{3.49}$$

Where the distance of the point on the sphere to the Z-axis is R_z. Considering the spherical coordinate system:

$$R_z = r_t \sin\Phi \tag{3.50}$$

$$r_t sin\overline{\Phi} = \frac{\int_{\pi/2}^{\pi}\int_{\pi-\alpha}^{\pi} r_t^3 \sin^2\Phi \, d\Phi d\Theta}{\frac{\pi}{2} r_t^2(1 - cos\alpha)} = \frac{2\alpha - \sin 2\alpha}{4(1 - cos\alpha)} r_t \tag{3.51}$$

Therefore, the relative velocity corresponding to the quadrant spherical cap can be calculated as follows:

$$\bar{v}_{qsc} = \frac{\pi(2\alpha - \sin 2\alpha)}{2(1 - cos\alpha)} r_t \omega \tag{3.52}$$

Finally, the overall relative velocity of the tool with respect to the contact patch can be calculated as follows:

$$\bar{v} = \left[\frac{\alpha\varphi}{8(1 - \cos\varphi)}\right] \bar{v}_{qse} + \frac{1}{4}\bar{v}_{qsc} + \bar{v}_s \tag{3.53}$$

Where, $\bar{v}_s$ is given by Equation 3.40. The characteristic length of the contact patch is also required in heat analysis, for instance, for the calculation of the Peclet number as discussed in the coming sections. The circumference of a plane ellipse can be approximated based on an empirical relation proposed by Indian mathematician Srinivasa Ramanujan [154].

$$p_c \approx \frac{\pi}{4}\left[3(a+b) - \sqrt{(3a+b)(a+3b)}\right] \tag{3.54}$$

Therefore:

$$p_c \approx \frac{\pi r_t}{4}\left[3(\alpha+\varphi) - \sqrt{(3\varphi+\alpha)(\varphi+3\alpha)}\right] \tag{3.55}$$

Accordingly, the characteristic length of the contact patch can be calculated as:

$$L_c = \frac{A_c}{p_c} \approx \frac{2r_t\left[1 - cos\alpha + \frac{\alpha\varphi}{2}\right]}{\left[3(\alpha+\varphi) - \sqrt{(3\varphi+\alpha)(\varphi+3\alpha)}\right]} \tag{3.56}$$

3.4 Pronounced bending effect in the initial stage of FSISF

Both experimental observations and numerical investigations (FEA) confirm the presence of a dominant elastic bending in the initial stage of FSISF. For example, Figure 3.7 presents the equivalent plastic deformation along the thickness of the sheet slab beneath the tool in FEA of FSISF test 20 at time instances 5s and 11.2s. As it is evident from Figure 3.7a, a very small plastic strain is present on the backside of the sheet at time instance 5s (displacement along tool direction is ~2mm). Considering Figure 3.7b, when tool displacement along its axis is ~4.4 mm, the top side of the sheet still shows no plastic deformation. Details of the aforesaid FAE are provided in the next chapter.

A closed-form solution first proposed by Michell [155] is adopted here to develop an analytical framework for the estimation of force during the initial stage of deformation under the dominant effect of elastic bending. Figure 3.8 shows the geometry of the problem of a circular plate under the bending effect of a lateral concentrated force in an analytical $r_1 - r_2$ coordinate system [156].

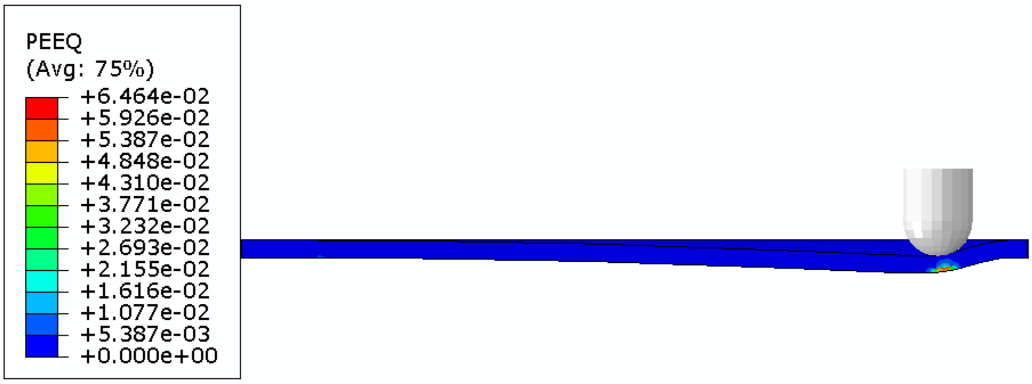

(a)

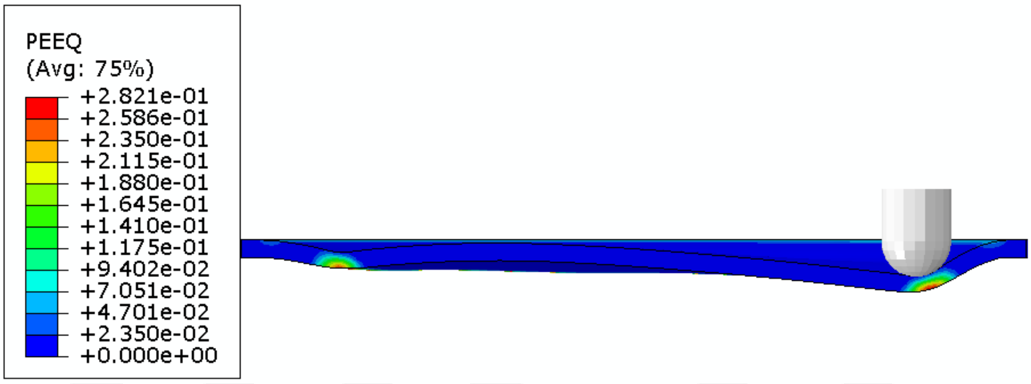

(b)

Figure 3.7: The equivalent plastic deformation along the thickness of the sheet slab beneath the tool in FSISF test 20 at time instances 5s (a) and 11.2s (b).

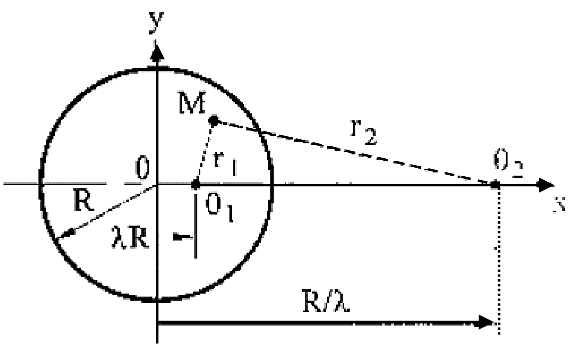

Figure 3.8: A schematic view of a circular plate under the bending effect due to a lateral concentrated force (in $r_1 - r_2$ coordinate system) [156].

In this Figure, R_s (*R* in Figure 3.8) is the radius of the base circle. *O* and *O₁* are the center of the circular plate and the point at which the concentrated load, *P*, is applied, respectively. O_2 is a fixed point, by which a circle with the center *O* and radius R_s in the x-y CSYS can be defined in $r_1 - r_2$ CSYS. M, with the coordinate (x, y) or (r_1, r_2), is an arbitrary point at which the deflection is measured. Therefore:

$$|O_1 O| = \lambda R_s \quad (3.57)$$

$$|O_1 O_2| = \frac{R_s}{\lambda} \quad (3.58)$$

Considering a set of fixed points O_1, and O_2, the transformation from x-y CSYS to the $r_1 - r_2$ CSYS can be performed by using the following equations:

$$\begin{cases} r_1^2 = (x - \lambda R_s)^2 + y^2 \\ r_2^2 = \left(x - \frac{R_s}{\lambda}\right)^2 + y^2 \end{cases} \quad (3.59)$$

Where λ is a constant value that can be used to transfer a circle of radius R_s and center of O in the x-y CSYS, to the $r_1 - r_2$ CSYS by using a set of fixed points, namely $O_1$and O_2. Therefore, by relocating point O_1 in the x-y CSYS, at which the load is applied, the second fixed point, O_2, the $r_1 - r_2$ CSYS, and λ change. The general solution for the deflection, w, of a circular plate under the effect of bending due to a lateral concentrated force is:

$$w = \frac{P}{8\pi D}\left[r_1^2 ln\frac{r_1}{\lambda r_2} + \frac{1}{2}(\lambda^2 r_2^2 - r_1^2)\right] \quad (3.60)$$

Where, Flexural Rigidity of the plate, *D* (has the same role as *EI* in beam bending), is defined as:

$$D = \frac{E_s t_s^3}{12(1 - \nu^2)} \quad (3.61)$$

E_s is the elastic (secant) modulus of the sheet material, t_s is the sheet thickness, and ν is the Poison's ratio. At the load-locus, where $r_1 = 0$ and $r_2 = R_s(1 - \lambda^2)/\lambda$, deflection, w_p, can be calculated as:

$$w_p = \frac{P{R_s}^2}{16\pi D}(1 - \lambda^2)^2 \quad (3.62)$$

As during the initial stage of the process where the elastic bending is the dominant mechanism of deformation, $w_p = |Z_{tooltip}|$, the force that is inducing the elastic bending can be calculated as:

$$P = \frac{4\pi E_s}{3(1-\nu^2)} \frac{|Z_{tooltip}| t_s^3}{[R_s(1-\lambda^2)]^2} \tag{3.63}$$

In the above relation, E_s is calculated based on the strain, strain rate, and temperature at a depth equal to the quadrant of the sheet thickness. This is because the distribution of the in-plane strain-stress is linear along the sheet thickness, and zero at the mid-plane. Therefore, at the first time step, E_s equals to the maximum value of the secant modulus of the sheet (for POM copolymer: ~2640 MPa). Subsequently, E_s for each time step is calculated from the nonlinear relation provided in the next section (Equation 4.25), as a function of the strain, strain rate, and temperature at the previous time step. Considering the same relation for the deflection at the load-locus:

$$w = \frac{2w_p}{(1-\lambda^2)^2 {R_s}^2} \left[r_1^2 ln \frac{r_1}{\lambda r_2} + \frac{1}{2}(\lambda^2 r_2^2 - r_1^2) \right] \tag{3.64}$$

Force P is exerted at point O_1, and w_p is the deflection at this point. Therefore, deflection at the load-locus is equal to the tooltip position along the z-axis ($Z_{tooltip}$) at the beginning of the process, where bending is the dominant mechanism of deformation. Thus, by substituting the known deflection at the load-locus in the general form of the relation:

$$w = \frac{2|Z_{tooltip}|}{(1-\lambda^2)^2 {R_s}^2} \left[r_1^2 ln \frac{r_1}{\lambda r_2} + \frac{1}{2}(\lambda^2 r_2^2 - r_1^2) \right] \tag{3.65}$$

The above relation can be used to estimate the deflection in the vicinity of the load-locus (tool-sheet contact interface), where the material stiffness is not significantly affected by the variation of strain, strain rate, and temperature. For this purpose, a transformation to a Cartesian CSYS is desired. As the sheet is assumed circular in FSISF specimens, the deflection on the diameter of the circular sheet that passes through the load-locus is required. Considering the axisymmetric condition, the load-locus can be always assumed as located along the horizontal axis of a fixed Cartesian CSYS $(x_b. y_b. z_b)$ in the space. The center of this Cartesian CSYS is assumed at the center of the circular sheet. Therefore, the motion of the tool can be assumed restricted along the horizontal axis and towards the center of the CSYS, while the circular sheet is assumed to rotate around its center so that the linear speed at the load-locus equals the forming speed in the process. In such a case, the horizontal axis is assumed to be along the polar coordinate R:

$$\begin{cases} x_b \geq x_{bp}: r_{1b} = \sqrt{x_b^2 + y_b^2} - \lambda R_s \\ x_b < x_{bp}: r_{1b} = \lambda R_s - \sqrt{x_b^2 + y_b^2} \end{cases} \tag{3.66}$$

$$\begin{cases} x_b \geq x_{bp}: r_{2b} = \dfrac{R_s}{\lambda} - \sqrt{x_b^2 + y_b^2} \\ x_b < x_{bp}: r_{2b} = \dfrac{R_s}{\lambda} - \sqrt{x_b^2 + y_b^2} \end{cases} \tag{3.67}$$

Also, according to the geometry of the problem:

$$\lambda = \frac{x_{bp}}{R_s} \tag{3.68}$$

Where, x_{bp} is the horizontal coordinate of the load-locus in the $x_b - y_b - z_b$ CSYS. Considering the definition of load-locus as stated above and the general *x-y-z* CSYS in which the toolpath is generated:

$$x_{bp} = R = \sqrt{X_{tooltip}^2 + Y_{tooltip}^2} \tag{3.69}$$

Therefore:

$$\lambda = \frac{\sqrt{X_{tooltip}^2 + Y_{tooltip}^2}}{R_s} \tag{3.70}$$

Where, $X_{tooltip}$ and $Y_{tooltip}$ represent the coordinate of the load-locus or the tooltip (according to the toolpath). To calculate the tool indentation, considering the hemispherical shape of the tooltip, deflection along a line passing through the center of the CSYS and the load-locus is desired. Such a line is equated as:

$$y = \frac{Y_{tooltip}}{X_{tooltip}} x \tag{3.71}$$

Therefore, the deflection function can be only defined as a function of x. Due to the geometry of the sheet and toolpath, the deflection should be only calculated for the first half-quadrant of the Cartesian CSYS. Therefore, the absolute magnitude of the coordinates' components must be substituted into the equations of deflection. The following figure depicts a schematic view of the ideal sheet bending under the effect of a lateral concentrated force (bending is artistically exaggerated for illustration purposes).

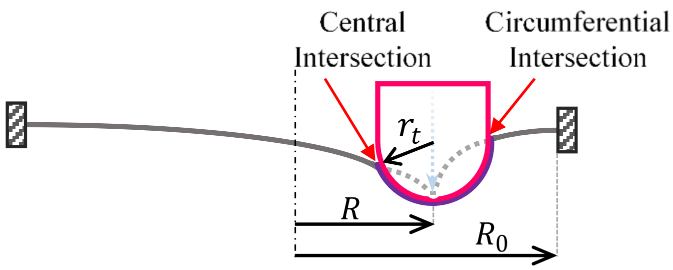

Figure 3.9: An artistic exaggerated schematic view of the sheet deflection under the effect of the ISF tool.

To calculate the tool indentation, the intersection points between the deflection profile and the hemispherical tool-head profile at the circumferential and central segments of the sheet must be calculated. The tool-head profile can be calculated as (z is positive downward):

$$z = \left[r_t^2 - \left[(x^2 + y^2)^{\frac{1}{2}} - \left(X_{tooltip}^2 + Y_{tooltip}^2\right)^{\frac{1}{2}}\right]^2\right]^{\frac{1}{2}} + Z_{tooltip} - r_t \tag{3.72}$$

As stated before, the deflection is calculated on the line passing through the sheet center and the load-locus. Therefore, y in the above equation can be expressed in terms of x (Equation 3.71). To calculate the indentation angles at each step time in the incremental solution, the system of equation consisting of the tool-head profile and the deflection function can be numerically solved in the following range of x:

$$\begin{cases} X_{tooltip} \le x \le X_{tooltip}\left[1 + \dfrac{r_t}{\sqrt{X_{tooltip}^2 + Y_{tooltip}^2}}\right]; Circumferential\ \ Indentation \\ X_{tooltip}\left[1 - \dfrac{r_t}{\sqrt{X_{tooltip}^2 + Y_{tooltip}^2}}\right] \le x \le X_{tooltip}; Central\ Indentation \end{cases} \tag{3.73}$$

To calculate the corresponding strain and stress ($0 \le \varsigma \le 1$):

$$\varepsilon_x^{\varsigma} = -\varsigma \frac{t_s}{2} \frac{\partial^2 w}{\partial x^2} \tag{3.74}$$

$$\varepsilon_y^{\varsigma} = -\varsigma \frac{t_s}{2} \frac{\partial^2 w}{\partial y^2} \tag{3.75}$$

$$\gamma_{xy}^{\varsigma} = -\varsigma t_s \frac{\partial^2 w}{\partial x \partial y} \tag{3.76}$$

$$\varepsilon_z^{\varsigma} = \gamma_{xz}^{\varsigma} = \gamma_{yz}^{\varsigma} = 0 \tag{3.77}$$

For example, $\varepsilon_x^{\varsigma}$ represents the logarithmic strain at distance $\varsigma \frac{t_s}{2}$ $(0 \leq \varsigma \leq 1)$ from the middle plane of the sheet under bending. The von Mises equivalent strain is:

$$\varepsilon_{eqv}^{\varsigma} = \sqrt{\frac{2}{9}\left[\left(\varepsilon_x - \varepsilon_y\right)^2 + \left(\varepsilon_y - \varepsilon_z\right)^2 + (\varepsilon_z - \varepsilon_x)^2\right] + \frac{1}{3}\left[\gamma_{xy}^2 + \gamma_{yz}^2 + \gamma_{zx}^2\right]} \tag{3.78}$$

By calculating the average equivalent strain under tool during the bending process (as explained above), the proper elastic modulus (secant modulus) can be estimated for calculation of the equivalent stress, force and indentation angles as follows:

$$\sigma_x = \frac{E}{1 - \upsilon^2}\left(\varepsilon_x^{\varsigma} + \upsilon \varepsilon_y^{\varsigma}\right) \tag{3.79}$$

$$\sigma_y = \frac{E}{1 - \upsilon^2}\left(\varepsilon_y^{\varsigma} + \upsilon \varepsilon_x^{\varsigma}\right) \tag{3.80}$$

$$\tau_{xy} = G \gamma_{xy}^{\varsigma} \tag{3.81}$$

$$G = \frac{E}{2(1 + \upsilon)} \tag{3.82}$$

$$\tau_{xz} = \frac{E}{2(1 - \upsilon^2)}\left(\left(\varsigma \frac{t_s}{2}\right)^2 - \frac{t_s^2}{4}\right) \frac{\partial}{\partial x} \nabla^2 w \tag{3.83}$$

$$\tau_{yz} = \frac{E}{2(1 - \upsilon^2)}\left(\left(\varsigma \frac{t_s}{2}\right)^2 - \frac{t_s^2}{4}\right) \frac{\partial}{\partial y} \nabla^2 w \tag{3.84}$$

$$\sigma_z = -\frac{E}{2(1 - \upsilon^2)}\left(\frac{t_s^3}{12} - \frac{t_s^2\left(\varsigma \frac{t_s}{2}\right)}{4} + \frac{\left(\varsigma \frac{t_s}{2}\right)^3}{3}\right) \nabla^2 \nabla^2 w \tag{3.85}$$

However, the magnitude of the out-of-plane stress components is negligible as compared to the in-plane normal and shear stresses, thus, out-of-plane stresses can be omitted in the calculation of the equivalent stress [156]. The equivalent von Mises stress can be calculated as:

$$\sigma_{eqv} = \sqrt{\frac{1}{2}[(\sigma_{11}-\sigma_{22})^2+(\sigma_{22}-\sigma_{33})^2+(\sigma_{33}-\sigma_{11})^2+6(\sigma_{23}^2+\sigma_{31}^2+\sigma_{12}^2)]} \tag{3.86}$$

By calculating the equivalent von Mises stress in the sheet under the tool and comparing this value with the initial yield stress calculated from the JC model (as a function of temperature), the onset of full plasticity or the elastic to full-plastic transition can be estimated as follows:

$$\bar{\sigma}_{initial\ yiled} = A\left[1-\left(\frac{T-T_{ref}}{T_{melt}-T_{ref}}\right)^m\right] \tag{3.87}$$

$$\begin{cases} Elastic\ Region: \bar{\sigma}_{eqv.bend} < \bar{\sigma}_{initial\ yiled} \\ Plastic\ Region: \bar{\sigma}_{eqv.bend} \geq \bar{\sigma}_{initial\ yiled} \end{cases} \tag{3.88}$$

3.5 Friction-induced heat

The heat partitioning between tool and sheet is thoroughly discussed in the next chapter. In this section, calculation of the heat-partitioning factor is briefly pointed out. The velocity-dependent heat partitioning factor, $\beta_{hp.v}$, can be estimated by using the relative velocities of the tool and the sheet with respect to the contact patch as follows [157]:

$$\beta_{hp.v} = \frac{\sqrt{k_{wc}\rho_{wc}c_{wc}\bar{v}_t}}{\sqrt{k_{wc}\rho_{wc}c_{wc}\bar{v}_t}+\sqrt{k_{pom}\rho_{pom}c_{pom}v_s}} \tag{3.89}$$

The area-dependent heat partitioning factor, $\beta_{hp.a}$, can be also estimated by adopting the area of the contact interface and the area of the tooltip swept by the contact patch as follows [158]:

$$\beta_{hp.a} = \frac{S_{tool}\sqrt{k_{wc}c_{wc}\rho_{wc}}}{S_{tool}\sqrt{k_{wc}c_{wc}\rho_{wc}} + S_{sheet}\sqrt{k_{pom}c_{pom}\rho_{pom}}} \tag{3.90}$$

Where, k, ρ, and c represent thermal conductivity, density, and special heat capacity of the tool (WC) and the sheet (POM) as reflected in Table 3.1. $S_{sheet} = A_c$, and S_{tool} can be calculated as follows (for the main contact scenario):

$$S_{tool} = 2\pi r^2[2 - \cos\alpha_2 - \cos(\varphi + \alpha_1)] \tag{3.91}$$

To calculate S_{tool} at the beginning of the process (contact scenario 0), $\varphi = 0$ and $\alpha_1 = \alpha_2$. In the transition period to the main contact scenario (i.e. during the contact scenario I), S_{tool} can be calculated by replacing α_1 and φ with α_1' and φ', respectively. In this study, the average of the two above heat partitioning factors, $\beta_{hp} = (\beta_{hp.v} + \beta_{hp.a})/2$, is employed. It means $\beta_{hp}\dot{\bar{Q}}$ part of the friction-induced heat goes to the forming tool. The average friction-induced heat transfer rate can be calculated as:

$$\dot{\bar{Q}}_{fr} = \xi\bar{\mu}F_t\bar{v} \tag{3.92}$$

Where ξ is a constant determining the amount of frictional work converting to heat (as frequently noted in the literature, $\xi \cong 0.9$).

Table 3.1: Physical properties of POM and WC.

Properties	WC	POM
k [W/mK]	80	0.31
ρ [kg/m^3]	14600	1410
C [J/kgK]	230	1470

3.6 Finite difference analysis

The temperature at the tooltip contact interface is equal to the temperature at the sheet contact interface [157]. Different FSISF process outputs including formability and surface integrity can be investigated under the effect of temperature at the contact interface. In this section, an explicit solution is provided for the Finite Difference Analysis (FDA) of temperature distribution in the FSISF tool-sheet system due to the friction-induced heat at the contact interface.

Initially, an experimental simulation of the problem was performed by heating the tooltip and measuring the temperature at the tooltip and several points on the tool shank by using the PID-thermocouple setup as described in the previous chapter. Finite element simulations of the experimental procedures using COMSOL Multiphysics resulted in a temperature distribution consistent with the experimental measurements. The simulation also revealed that the distribution of temperature in the tool could be safely regarded as a 1D distribution along the tool's length. Specifically, temperature distribution was demonstrated by parallel flat isothermal surfaces in the tool (FEA results). In addition, the Peclet Number was evaluated using Equations 3.56 and 4.30, and by considering the minimum of the average contact area for the range of velocities in the current FSISF campaign. The large resultant values endorse the assumption of 1D heat transfer in this study.

3.6.1 FDA of tool

Figure 3.10 demonstrates the discretization of the FSISF tool. The length of different FDA elements. Δz_S, Δz_N and Δz_D represent the length of the tool elements in the shank section, the narrow section, and the geometrical discontinuity which connects the two aforesaid sections, respectively.

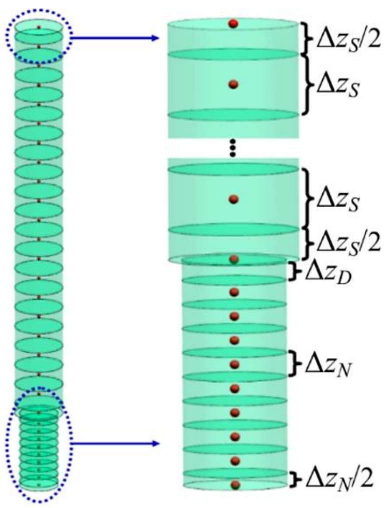

Figure 3.10: The discretization of the FSISF tool for finite difference analysis.

The tool elements and the time steps are indexed by i and j, respectively. In addition, n_D represents the index number of the tool element that connects the shank and the narrow section. If $1 < i < n$:

$$T_{(i,j+1)} = \frac{\Delta t}{\rho_{wc} C_{wc}} \left[\frac{2h_{s(i,j)}}{r_{(i)}} \left[T_\infty - T_{(i,j)} \right] + \frac{K_{wc}}{\Delta z_S{}^2} \left[T_{(i-1,j)} - 2T_{(i,j)} + T_{(i+1,j)} \right] \right] + T_{(i,j)} \quad (3.93)$$

Where, $\Delta t = 0.02\ s$, is the time increment in FDM. Considering the element at the tooltip ($i = 1$):

$$T_{(i,j+1)} = \frac{2\Delta t}{\rho_{wc} C_{wc}} \left[\frac{h_{s(i,j)}}{r_{(i)}} \left[T_\infty - T_{(i,j)} \right] + \frac{K_{wc}}{\Delta z_N{}^2} \left[T_{(i+1,j)} - T_{(i,j)} \right] + \frac{\beta_{hp}}{\pi r_{(i)}^2 \Delta z_N} \dot{\bar{Q}}_{fr.j} \right] + T_{(i,j)} \quad (3.94)$$

As detailed in the previous chapter, tooltip temperature was measured by using a thermocouple after raising the tool from the sheet surface (see Table 2.5). In the Finite Difference algorithm, after raising the tool and during the cooling course, the friction-induced heart rate ($\dot{\bar{Q}}_{fr}$ from Equation 3.92) equals zero. Considering the element at the flat side of the tool ($i = n$):

$$T_{(i,j+1)} = \frac{2\Delta t}{\rho_{wc} C_{wc}} \left[\frac{h_{s(i,j)}}{r_{(i)}} \left[T_\infty - T_{(i,j)} \right] + \frac{h_{e(i,j)}}{\Delta z_S} \left[T_\infty - T_{(i,j)} \right] + \frac{K_{wc}}{\Delta z_S{}^2} \left[T_{(i-1,j)} - T_{(i,j)} \right] \right] + T_{(i,j)} \quad (3.95)$$

Specifically, at the node corresponding to the geometrical discontinuity ($i = n_D = 10$):

$$T_{(i,j+1)} = \frac{\Delta t}{\rho_{wc} C_{wc} (r_N^2 \Delta z_D + r_S^2\, \Delta z_S/2)} \left[(2r_N \Delta z_D + r_S \Delta z_S) h_{s(i,j)} \left[T_\infty - T_{(i,j)} \right] + \frac{r_N^2 K_{wc}}{(\Delta z_D + \frac{\Delta z_N}{2})} \left[T_{(i-1,j)} - T_{(i,j)} \right] + \frac{r_S^2 K_{wc}}{\Delta z_S} \left[T_{(i+1,j)} - T_{(i,j)} \right] \right] + T_{(i,j)} \quad (3.96)$$

Heat transfer coefficients, h_s and h_e, corresponding to the cylindrical shank and the flat end of the tool were evaluated at T_{evl} [159]:

$$T_{evl} = \frac{T + T_\infty}{2} \tag{3.97}$$

Where, T_∞ represents the ambient temperature (25°C). As evident from Equations 3.93 to 3.95, convection is allowed at the cylindrical sides of all volume elements and the top flat end of the tool. The term $\beta_{hp}\dot{Q}_{fr}$ in Equation 3.94 defines the heat source associated with the element located at the tooltip. The initial condition is defined by assuming all the nodes being at the ambient temperature at the beginning of the process.

3.6.2 FDA of sheet

Figure 3.11 demonstrates a 2D discretization of the slab sheet located beneath the forming tool in the FSISF process. The required boundary conditions for finite difference analysis (FDA) are also presented (Figure 3.11a). Figure 3.11b shows the tool-sheet interaction at sequential time increments, j. In this figure and the following equations, X, Y, and Z respectively translate to meridional (φ), thickness (t), and circumferential (θ) directions in a spherical coordinate system describing the sheet slab being deformed under the hemispherical tooltip. Accordingly, the required areas and volume for FDA are calculated as follows:

$$\begin{cases} A_x = \Delta y \times \Delta z \\ A_y = \Delta x \times \Delta z \\ V_{element} = \Delta x \times \Delta y \times \Delta z \end{cases} \tag{3.98}$$

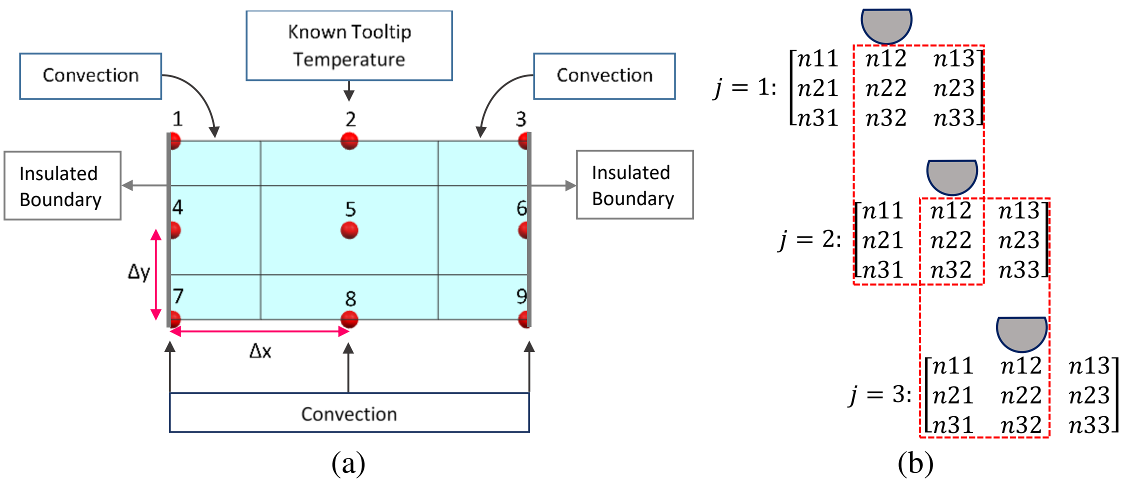

Figure 3.11: A 2D discretization of the slab sheet located beneath the forming tool in the FSISF process (a), and tool-sheet interaction at sequential time increments (b).

Equating FDA elements with the slab-sheets located under contact patches, the distance among the nodes along the meridional direction is quite larger than the distances in circumferential and thickness directions. Considering, very low heat conductivity (0.36 W/mK) and relatively high specific heat capacity (1420 J/kgK) of POM, the heat flux and the resultant temperature alternation in meridional direction can be overlooked as compared to the other two directions. This assumption is in agreement with the experimental measurements by using the thermocouples at the center and periphery of the conical specimens as discussed in the previous chapter. In addition, FEA results, as presented in the next chapter, justify such an assumption. Therefore, a 2D FDA with three elements along each direction is used as presented by Figure 3.11 to estimate the average temperature in the sheet slab formed under the ISF tool. Based on the spherical coordinate system considered for the specimen, and the slab sheet under the tool:

$$\begin{cases} \Delta z = R_t(\varphi_j + \alpha_j) \\ \Delta y = \dfrac{t_{s_{avg}.j}}{2} \\ \Delta x = \dfrac{A_{c.j}}{R_t(\varphi_j + \alpha_j)} \end{cases} \tag{3.99}$$

Therefore, for the elements with node number, *i*, equal to 1, 3:

$$T_i^{j+1} = \frac{\Delta t}{\rho C}\left[\frac{4h_{sh}}{t_{s_{avg}.j}}\left(T_\infty - T_i^j\right) + \frac{2kR_t^2(\varphi_j + \alpha_j)^2}{A_{c.j}^2}\left(T_{i+1}^j - T_i^j\right) + \frac{8k}{t_{s_{avg}.j}^2}\left(T_{i+3}^j - T_i^j\right)\right] + T_i^j \tag{3.100}$$

For the elements with node number, *i*, equal to 7, and 9:

$$T_i^{j+1} = \frac{\Delta t}{\rho C}\left[\frac{4h_{sh}}{t_{s_{avg}.j}}\left(T_\infty - T_i^j\right) + \frac{2kR_t^2(\varphi_j + \alpha_j)^2}{A_{c.j}^2}\left(T_{i+1}^j - T_i^j\right) + \frac{8k}{t_{s_{avg}.j}^2}\left(T_{i-3}^j - T_i^j\right)\right] + T_i^j \tag{3.101}$$

For the elements with node number *i*=4:

$$T_i^{j+1} = \frac{\Delta t}{\rho C}\left[\frac{4k}{t_{s_{avg}\cdot j}^2}\left(T_{i-3}^j - 2T_i^j + T_{i+3}^j\right) + \frac{2kR_t^2(\varphi_j + \alpha_j)^2}{A_{c.j}^2}\left(T_{i+1}^j - T_i^j\right)\right] + T_i^j \tag{3.102}$$

For the elements with node number i=6:

$$T_i^{j+1} = \frac{\Delta t}{\rho C}\left[\frac{4k}{t_{s_{avg}\cdot j}^2}\left(T_{i-3}^j - 2T_i^j + T_{i+3}^j\right) + \frac{2kR_t^2(\varphi_j + \alpha_j)^2}{A_{c.j}^2}\left(T_{i-1}^j - T_i^j\right)\right] + T_i^j \tag{3.103}$$

For the elements with node number i=5:

$$T_i^{j+1} = \frac{\Delta t}{\rho C}\left[\frac{4k}{t_{s_{avg}\cdot j}^2}\left(T_{i-3}^j - 2T_i^j + T_{i+3}^j\right) + \frac{kR_t^2(\varphi_j + \alpha_j)^2}{A_{c.j}^2}\left(T_{i-1}^j - 2T_i^j + T_{i+1}^j\right)\right] + T_i^j \tag{3.104}$$

For the elements with node number i=8:

$$T_i^{j+1} = \frac{\Delta t}{\rho C}\left[\frac{4h_{sh}}{t_{s_{avg}\cdot j}}\left(T_\infty - T_i^j\right) + \frac{kR_t^2(\varphi_j + \alpha_j)^2}{A_{c.j}^2}\left(T_{i-1}^j - 2T_i^j + T_{i+1}^j\right) + \frac{8k}{t_{s_{avg}\cdot j}^2}\left(T_{i-3}^j - T_i^j\right)\right] + T_i^j \tag{3.105}$$

For the elements with node number i=2:

$$T_i^{j+1} = \frac{\Delta t}{\rho C}\left[\frac{kR_t^2(\varphi_j + \alpha_j)^2}{A_{c.j}^2}\left(T_{i-1}^j - 2T_i^j + T_{i+1}^j\right) + \frac{8k}{t_{s_{avg}\cdot j}^2}\left(T_{i+3}^j - T_i^j\right) + \frac{4}{A_{c.j}t_{s_{avg}\cdot j}}(1-\beta)\dot{Q}_{fr.j}\right] + T_i^j \tag{3.106}$$

Also:

$$T_{2.\ sheet}^{j+1} = T_{1.\ tool}^{j+1} \tag{3.107}$$

The heat convection coefficient, h_{sh}, can be estimated by considering the slab sheet as an inclined plate of angle δ with the vertical direction. Therefore:

$$\delta \approx \frac{\pi}{2} - \frac{\varphi}{2} \tag{3.108}$$

By using the inclination angle, and estimating the relevant Rayleigh number, Nusselt number, and the characteristics length of the sheet elements in FDA, the free convection from the lower surface of a hot inclined plate can be evaluated as explained by Cengel [159], and from the top surface of a hot inclined plate as investigated by Fujii and Imura [160].

Considering the discussion provided at the beginning of this section, the FEA results in terms of the temperature in sheet (presented in the next chapter) were scrutinized for several FSISF tests. In addition, Peclet numbers (88.52 to 725.84) were evaluated for the sheet by considering the average contact area and the range of forming speed (500-4100 mm/min) for the FSISF process in this study. Therefore, the assumption of 1D heat flow in the sheet was found to be fairly valid and very efficient in terms of the simulation cost (time). Figure 3.12 shows a 1D discretization of the slab sheet located beneath the forming tool in the FSISF process.

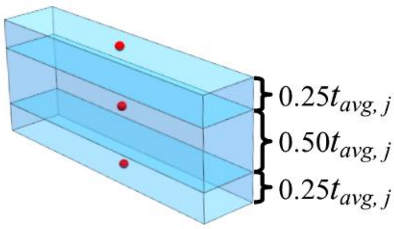

Figure 3.12: A 1D discretization of the slab sheet located beneath the forming tool in the FSISF process.

$t_{avg.j}$ or $t_{s_{avg}\cdot j}$ as presented in Figure 3.12, and Equations 109 to 111, represent the average sheet thickness at the time increment j. The FDA node temperatures are calculated as follows. For the elements with node number i=1:

$$\acute{T}_{(1,j+1)} = \frac{4\Delta t}{\rho_{pom} C_{pom}} \left[\frac{2k_{pom}}{t^2{}_{s_{avg}\cdot j}} \left[\acute{T}_{(2,j)} - \acute{T}_{(1,j)} \right] + \frac{1-\beta}{A_{c.j} t_{s_{avg}\cdot j}} \dot{Q}_{fr.j} + \dot{\bar{q}}_{pl.j} \right] + \acute{T}_{(1,j)} \tag{3.109}$$

For the elements with node number i=2:

$$\acute{T}_{(2,j+1)} = \frac{2\Delta t}{\rho_{pom}C_{pom}}\left[\frac{2k_{pom}}{t^2{}_{s_{avg}\cdot j}}\left[\acute{T}_{(1,j)} - \acute{T}_{(2,j)}\right] + \frac{2k_{pom}}{t^2{}_{s_{avg}\cdot j}}\left[\acute{T}_{(3,j)} - \acute{T}_{(2,j)}\right] + \dot{\bar{q}}_{pl.j}\right] + \acute{T}_{(2,j)} \tag{3.110}$$

For the elements with node number *i*=3:

$$\acute{T}_{(3,j+1)} = \frac{4\Delta t}{\rho_{pom}C_{pom}}\left[\frac{2k_{pom}}{t^2{}_{s_{avg}\cdot j}}\left[\acute{T}_{(2,j)} - \acute{T}_{(3,j)}\right] + \frac{h_{s(i.j)}}{t_{s_{avg}\cdot j}}\left[T_\infty - \acute{T}_{(3,j)}\right] + \dot{\bar{q}}_{pl.j}\right] + \acute{T}_{(3,j)} \tag{3.111}$$

In Equations 3.109 to 3.111, $\acute{T}_{(i,j+1)}$ represent the temperature at node i, and the time increment $j+1$. $\dot{Q}_{fr.j}$ and $\dot{\bar{q}}_{pl.j}$ represent the average friction-induced heat rate, and the average heat (per unit volume) produced due to plastic deformation for the time increment j, respectively. $\dot{\bar{q}}_{pl}$ can be calculated as:

$$\dot{\bar{q}}_{pl} = \zeta\bar{\sigma}\dot{\bar{\varepsilon}} \tag{3.112}$$

Where, ζ is a constant determining the amount of plastic work converting to heat. Further investigations showed that the heat generated due to plastic deformation is negligible as compared to friction-induced heat. It is noteworthy that the heat partitioning coefficient, β, can be also calculated numerically. For this purpose, the FDA equations for nodal temperatures in tool and sheet must be solved simultaneously in a system of equations, which is relatively more expensive in terms of simulation time. In such a system of equations, the nodal temperatures at the tooltip and the top surface of the sheet are assumed equal as stated before.

3.7 Results and discussion

Interdependency between forming force and friction-induced heat and their contribution towards output quality of the FSISF process highlights the need for a model that predicts force and temperature as presented in the previous sections. Such an analytical-numerical framework is established on four pillars, namely a geometrical model for tool-sheet contact interface, the stress-strain state in the slab sheet under the tool, an FDA algorithm to predict the temperature in the contact area, and a proper material model.

Figure 3.13 provides a comparison between the area of the tool-sheet contact interfaces acquired by adopting the analytical framework provided in this chapter and by conducting FEA as presented in the next chapter. For this purpose, the second approach for estimation of the tool-sheet contact interface is adopted without considering the nonlinear strain-dependent elastic behavior of the material at the initial stage of deformation. Taking into account the aforesaid nonlinearity by using Equation 4.25, predictions at the initial stages improves significantly.

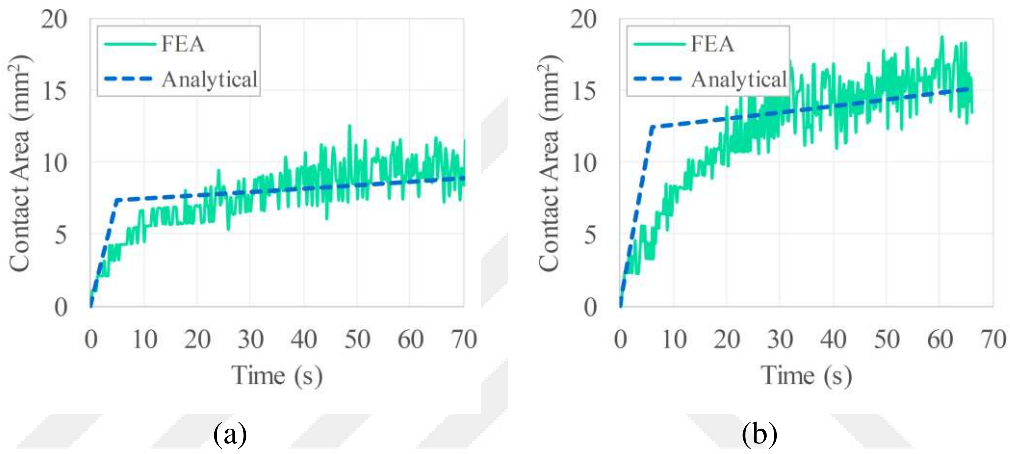

Figure 3.13: Area of the tool-sheet contact interfaces acquired from the analytical framework and FEA corresponding to FSISF tests 26 (a), and 27(b).

Figure 3.14 presents the predicted total force magnitudes and forming force components experimentally acquired for the five major FSFIS forming conditions as pointed out before. As shown by this figure, predicted forces are acceptably validated by the experimental results (the maximum deviation is roughly 20%). The results presented by this figure are acquired by employing the first approach for estimation of the tool-sheet contact interface. The temperature at the tool-sheet interface can increase as the tool further slides over the sheet. As the tool keeps forming the sheet, a balance among decreasing sheet thickness, temperature alternation, and increasing forming angle affect the magnitude of the forming force.

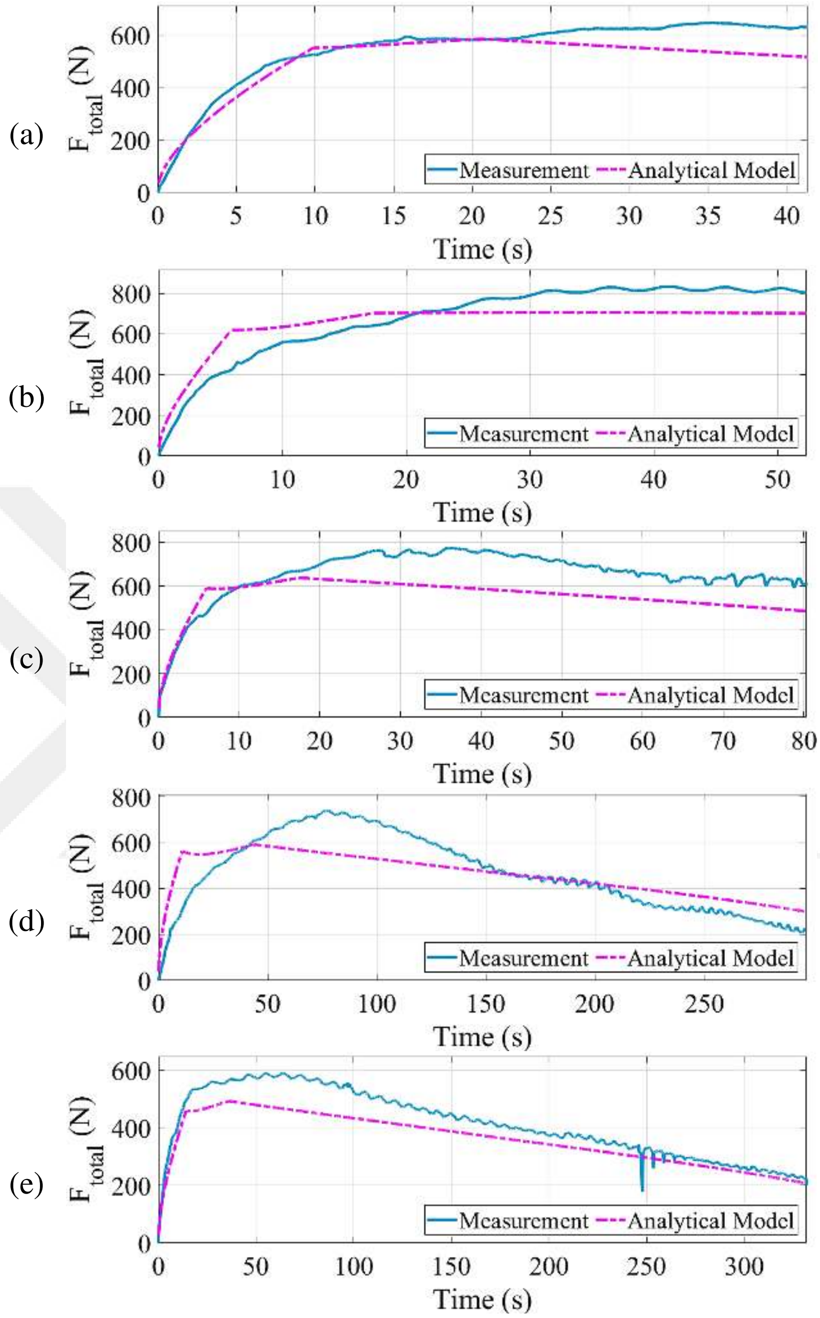

Figure 3.14: Predicted versus experimental total forming force acquired for the five major FSFIS benchmarks 15 (a), 19 (b), 11 (c), 21, (d), 12 (e).

Figure 3.15 shows the FDA simulation results along with the pointwise temperature of the contact interface in tests 12 and 21 measured by using the pyrometer (during the forming process) and the thermocouple (5 s after disconnecting the tool and sheet). To evaluate the accuracy of the FDA algorithm independent of the predicted force magnitudes, experimental force data was employed for this simulation. The graph also shows the effect of a minor crack in FSISF specimen 12 that is probably opened from a surface scratch or a material defect. The crack could quickly propagate in the case of cold ISF, but it is contained in this case because of the proper friction-induced heating. FDA also reveals that the interface temperature in test 12, almost for half of the forming time, is slightly above the upper working limit of POM (~85°C). It can explain the minor surface degrading of the POM specimen as pointed out before. Surface thermal defects (Figure 2.15a) and the wavy form of specimen 21 around its waist can be also explained by the maximum temperature of ~125°C around the mid-forming time as presented by Figure 3.15. Such heat-induced geometrical waviness is also evident from the force plot as presented before.

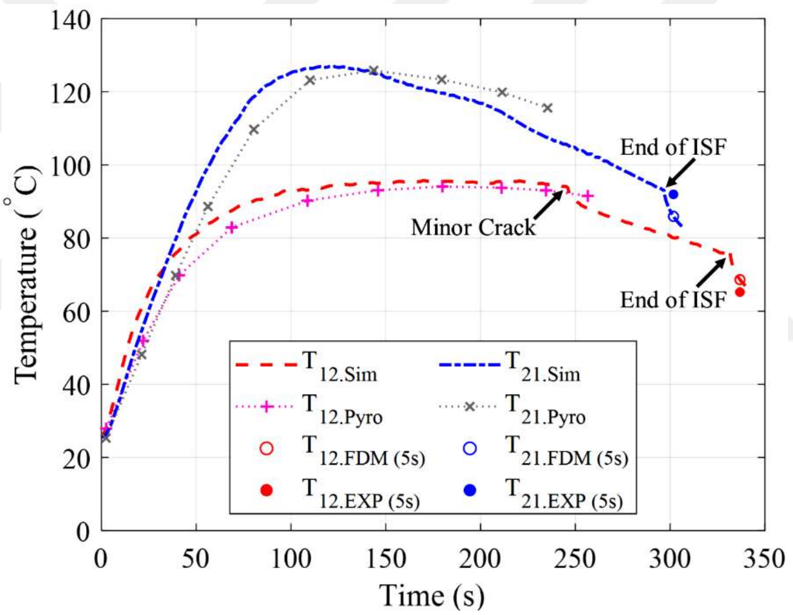

Figure 3.15: Tooltip temperatures in tests 12 and 21 derived from simulation (FDA) and measured by pyrometer and thermocouple.

Figure 3.16 represents the friction-induced heat rate as a function of the equivalent plastic strain in the five benchmark FSISF tests. Except for test 19 in which spindle speed is set to zero, the worst (test 15) and the best (test 12) process conditions in terms of formability reflect the maximum and minimum friction-induced heat rates, respectively.

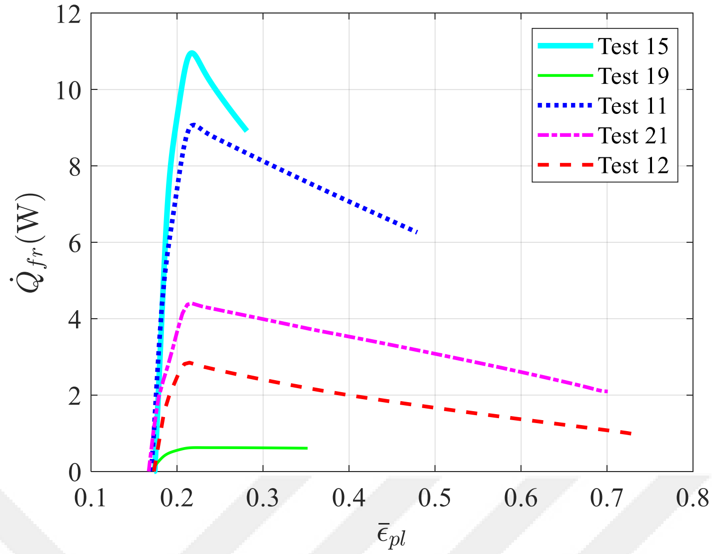

Figure 3.16: Friction-induced heat rate as a function of the equivalent plastic strain in the five benchmark FSISF tests.

Figure 3.17 shows σ_ϕ , the most contributing component of stress to the forming and failure of the sheet in the ISF process, as a function of the equivalent plastic strain. Exceptionally, in test 19 (with zero spindle speed), due to the minor effect of friction-induced heat, the strain hardening effect results in ascending meridional stress by an increase in plastic strain. In opposite, a large friction heating rate in test 15 results in a sharply descending meridional stress. The good and moderate cases in terms of formality show similar decreasing rates.

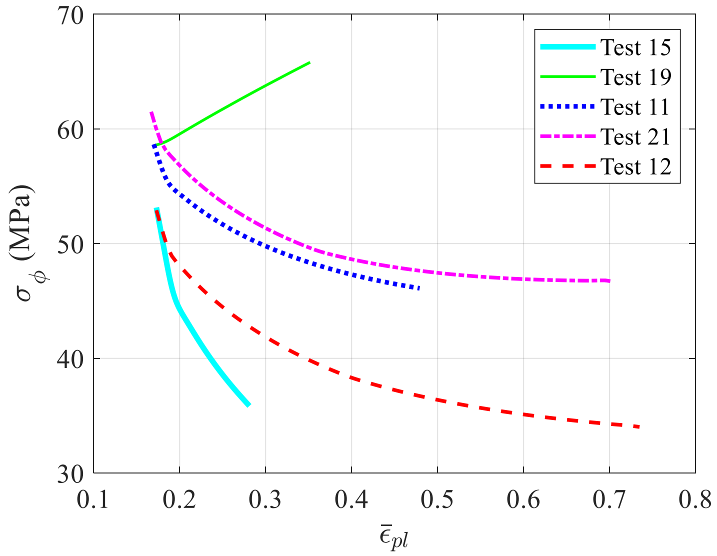

Figure 3.17: The major meridional stress component as a function of the equivalent plastic strain in the five benchmark FSISF tests.

Figure 3.18 depicts the ratio of the plastic strain energy density to the triaxiality as a function of the equivalent plastic strain at the final point of the process (either the failure or the completion of the specimen). This is evident from the figure that the ratio of the plastic strain energy density to the triaxiality can be associated with the equivalent plastic energy with a linear trend. This figure also shows that as the ratio of the plastic strain energy to the triaxiality increases, formality increases as well.

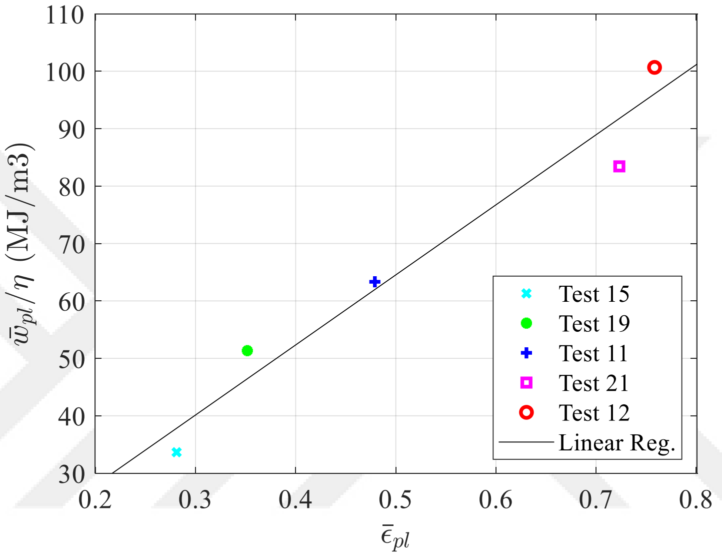

Figure 3.18: The ratio of the plastic strain energy density to the triaxiality as a function of the final equivalent plastic strain for five benchmark FSISF tests

Chapter 4

FINITE ELEMENT ANALYSIS

4.1 Introduction and overview

Considering the literature on heat-assisted ISF, a very limited number of studies are conducted on heat-assisted ISF of polymers (4% of the reviewed literature). As detailed in the first chapter, the mechanism of ISF at room temperature is complicated due to localized plastic deformation and the contribution of several mechanisms namely, contact stress, bending under tension, shear, cyclic straining, and hydrostatic stress [44]. The presence of heat further complicates the prediction of the material behavior, sheet thickness distribution, failure, final geometry, and forming forces in the process. The majority of investigations in hot ISF, as reviewed before, are merely experimental. A very limited number of analytical studies in the field are available, including the extensive analytical investigation published by the author [161] as detailed in the previous chapter. However, analytical solutions are based on simplifying assumptions. Though analytical simulations are less expensive in terms of calculation time and hardware, Finite Element Analysis (FEA) provides a unique opportunity to gain an insight into the mechanism of hot ISF. Moreover, the material behavior and process outputs can be predicted much more accurately. The FEA of laser-assisted [63, 65], friction-assisted [95, 96], and electric [72, 77] hot ISF, as reviewed before, are merely focused on metallic alloys. These studies also lack details on thermal boundary conditions and heat partitioning between tool and sheet, which may undermine the reliability of the predictions. As shown in the first chapter, there has been a research gap in terms of FEA of the ISF of thermoplastics, specifically by considering the effects of elevated temperatures, and strain rate. An obstacle to achieving this goal, apart from the complexity of the process, has been high simulation costs. Therefore, a framework for a fairly accurate and timely efficient FEA of FSISF of thermoplastics is proposed in this section.

This chapter continues with a brief discussion on Implicit and Explicit solutions. Afterward, a detailed discussion is provided on the selection of a proper material model for the FSISF of POM. The material constitutive models namely Two-Layer Viscoplastic (TLV), Parallel Rheological Framework (PRF), Three Network (TN), and Johnson-Cook (JC) are discussed and calibrated. In addition, a phenomenological nonlinear elastic model with acceptable accuracy is proposed and calibrated. Detailed and comparative discussions are provided on meshing strategies, FSISF tool definition, element type, element size, and mass scaling to achieve the objective of fairly accurate and timely efficient FEA of the process. Following these sections, heat partitioning between tool and sheet is discussed in detail. For this purpose, a precise review is provided on heat partitioning in problems involving friction-induced heat such as pin-on-disk, disk-brake, and rail-wheel contact problems. The friction coefficient is briefly discussed along with an FEA that is validated by experimental results. Benchmark FSISF tests are considered for simulation. To demonstrate the capability of the proposed FEA methodology, the simulation case studies reflect a broad range of sheet formability, temperature, and stress triaxiality (as a measure of ductile fracture). The simulation results are validated against experimental results (mainly in terms of forming force), and a good compliance is presented. In addition, a brief discussion and a numerical investigation are provided on damage evolution and failure in FSISF of POM.

4.2 Implicit or explicit solution

FEA, as a numerical solution, is applied to a variety of problems in the science and engineering fields, including structural analysis and heat transfer. The problems are mathematically defined as partial differential equations (PDEs). PDEs in FEA can be reframed as either linear or nonlinear matrix equations. The sources of nonlinearity are material (e.g. large plastic deformation), geometry (thin sheets), and boundary conditions (e.g. contact). Localized plastic deformation triggers a high degree of nonlinearity in the ISF process. This is due to the geometry of the process, application of second-order meshing elements, the elastoplastic and viscoplastic behavior of material (in metals and polymers respectively), dynamic and cyclic loading, contact pressure, and friction. The significance of the forming temperature and strain rate in the deformation of thermoplastics further complicates the FEA of the FSISF of POM. Therefore, the selection of a proper material model for the FEA of such a process plays a major role in maintaining a justifiable equilibrium between accuracy and efficiency in simulations. Generally, two types of solutions are available for PDEs in FEA namely, implicit and explicit. For static or quasi-static problems (such as the majority of the forming problems):

$$[k_{(x)}]\{x\} = \{f\} \tag{4.1}$$

Where, $[k_{(x)}]$ is the nonlinear stiffness matrix, $\{x\}$ is the displacement matrix, and $\{f\}$ is the force matrix. For the linear dynamic problems:

$$[M]\{\ddot{x}\} + [C]\{\dot{x}\} + [K]\{x\} = \{f\} \tag{4.2}$$

Where, $\{\ddot{x}\}$ is the acceleration matrix, $\{\dot{x}\}$ is the velocity matrix, $[M]$ is the mass matrix, $[C]$ is the damping matrix. The implicit solution is based on matrix inversion. In nonlinear problems, the solution is obtained through a stepwise routine, where the solution at each step is dependent on the solution in the previous strep. Therefore, for large-size nonlinear problems, the solution involves advanced iterative (or direct) methods, which imposes high simulation costs in terms of time and hardware. Despite the aforesaid disadvantage, implicit solutions are unconditionally stable (larger time steps can be adopted). Taking the explicit approach, the problem is solved for acceleration, where in most of the cases mass matrix is diagonal, thus, the inversion process is less expensive. However, the time step should be smaller than the required time for the sound wave to be transferred through the element. In other words, conversion in explicit solution is not a matter of concern, but the results could be very inaccurate if too large time steps are adopted. An implicit solution was adopted for the FEA of ISF of an aluminum alloy at room temperature (conducted by the author) using COMSOL Multiphysics. As stated before, the time cost of a relatively short implicit simulation was very high (67 hours on a workstation of 2 CPUs @ 2.30 GHz {24 Cores} and 64 GB RAM). In this chapter, a significantly more complex simulation of FSISF of POM is aimed by using ABAQUS on an ordinary laptop (single Intel(R) Core i5 CPU @ 2.70GHz and 8 GB RAM). Therefore, this chapter presents an explicit FEA framework to reduce the simulation costs in terms of time and hardware, while the accuracy of the results is reasonably preserved. Accordingly, the selection and calibration of proper martial models for such simulations are discussed in the next section.

4.3 Material models

Yonan et al. [117] developed a finite extension of a viscoplastic material model proposed by the same authors before [116]. They also conducted an FEA of ISF of PVC at room temperature by implementing the material model via UMAT subroutine in Abaqus. To calibrate the model, the authors performed three strain-controlled monotonic tensile tests until necking occurred (at low strains). In addition, tensile tests with several holding stages during the loading-unloading periods (including strain-dependent recovery stages) were performed. They used solid C3D8R elements to model the sheet (three elements along thickness), whereas the tool was assumed rigid. The initial calibration turned out to provide FEA results with significant deviation from experimental data. However, recalibrating the material model by using inverse method and optimization, the material model and the FEA outcomes were improved. Therefore, the planar force components were overestimated by about 40% and 50% for initial sheet thickness of 1 mm and 2 mm, respectively. Error in the prediction of normal force components is lower as compared to that of planar force components. Beyond this in-depth research work on FEA of cold ISF of thermoplastics, genuine studies on the subject are very rare. Recently, Kulkarni et al. [162] attempted FEA of ISF of PC (single conical specimen of constant wall angle) under the convective effect of hot air by implementing three network material model in ANSYS. Durante et al. [163] also attempted FEA of ISF of PC at room temperature, to investigate the formability of the material under the effect of tool size and sheet thickness. They employed shell elements in Abaqus to simulate the ISF of cone and pyramid specimens, but the material model was not specified.

Considering the two extensive literature reviews published on ISF of polymers [26] and thermoplastics [121] very recently, almost no genuine study on FEA of ISF of thermoplastics, specifically at elevated temperatures, is conducted so far (except for the cases cited here). Therefore, a research record on proper material models for numerical simulation of a complicated forming process such as FSISF is very limited. A proper constitutive material model, in this case, should reliably predict the flow stress under the effect of strain, strain rate, and temperature. Sophisticated nonlinear viscoelastic and viscoplastic constitutive models with the aforesaid capabilities have been developed so far to provide a fairly accurate prediction of the forces and deformed geometries in complex forming processes.

A Constitutive model was developed and investigated through simulation of dynamic impact test on high-density polyethylene (HDPE) [164]. A nonlinear small-strain viscoplastic model was developed and validated in FEA of the unidirectional and multidirectional tensile tests of polypropylene (with interim holding and loading-unloading stages) at room temperature [165]. A non-linear optimization method was used to calibrate the nonlinear viscoelastic Schapery model by performing several tensile and compressive tests on POM (homo-polymer) employing the optical measurements techniques at room temperature [166]. By adding rate-dependent and temperature-dependent functions to the quasi-linear viscoelastic (QLV) model, a new model was introduced to predict the nonlinear viscoelastic behavior of POM (homo-polymer) at various temperatures (23-80°C) [167]. By implementing a single integral constitutive representation into a multi-network model, a new constitutive model was developed to predict the nonlinear viscoelastic behavior of polymers due to deformation-induced microstructure changes [168]. Uniaxial ramped tensile tests with creep-recovery stages were performed on POM (homo-polymer) at room temperature to evaluate the accuracy of this model. A similar framework (multiple natural configurations) was used to incorporate the effect of microstructure changes on viscoelastic response (at room temperature) of thermoplastics (Tenac 3010 POM homo-polymer) by assuming two networks representing the initial and the deforming configuration of the material [169]. A viscoelastic-viscoplastic model including an isotropic damage material degradation section was developed [170] for semicrystalline thermoplastics at room temperature, and validated by FEA of creep test using POM (homo-polymer).

Such models as cited here, require several parameters (e.g. 16 parameters [164]) to be calibrated through several mechanical tests at different rates and temperatures, which in turn, requires advanced apparatuses and significant resources. In addition, implementation of such material models in the FEA framework (Abaqus in this case) is expected to be expensive in terms of the required simulation time and hardware. For the purpose of the FEA of FSISF of POM, several material models were investigated. Among them, the material constitutive models namely Two-Layer Viscoplastic (TLV), Parallel Rheological Framework (PRF), Three Network (TN), and Johnson-Cook (JC) are discussed and calibrated in this section. At the end of this section, the most efficient and fairly accurate model is picked up for the simulations presented in this chapter.

4.3.1 Two-layer viscoplastic model

According to the Abaqus user's manual [171], Two-Layer Viscoplastic (TLV) model is suitable for the prediction of the material behavior, where time-dependent and plastic deformation is significant. More specifically, this is a proper model where fluctuating thermomechanical loading within a broad range of temperatures is expected. The model can be represented by a network of two parallel branches namely, elastic-plastic and elastic-viscous (Figure 4.1). This is in contrast to other common network models, where the viscous and plastic elements are defined in serial order within a single branch.

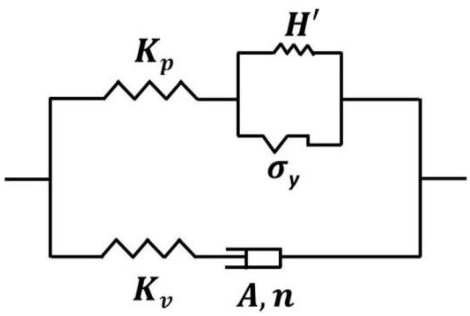

Figure 4.1: 1D ideal representation of TLV model [172].

Regarding the yield criteria, both Mises (used in this study) or Hill models can be implemented along with the TLV constitutive model in Abaqus standard for an implicit FEA of the ISF process. The elastic response of the material in both branches is linear, and Poison's ratios are similar in both branches. The parameter f, as the ratio of the elastic stiffness of the elastic-viscous branch to the total elastic stiffness of the material is defined as follows:

$$f = \frac{K_v}{K_v + K_p} \tag{4.3}$$

Where, K_v and K_p are the modulus of elastic-viscous and elastic-plastic branches in the network, respectively. Also, H', σ_y, A, and n represent the hardening parameter, initial yield stress, and rate parameters in the Norton-Hoff power law equation, respectively. Therefore, the plastic portion can be defined by static hardening data without considering any rate-dependent effect. Time-dependent viscous behavior of the material can be defined by using the Norton-Hoff power law ($m = 0$), as follows:

$$\dot{\varepsilon}_V = A\sigma_V^n \tag{4.4}$$

The subscript V in the above equation emphasizes that the parameters are related to the elastic-viscous branch. Therefore, six parameters, namely K_v, K_p (or f, instead), H', σ_y, A, and n are to be calibrated to define the TLV model at a specific temperature. K_p, H', σ_y can be determined from a static tensile test at which, the effect of strain rate is assumed to be negligible. f, A, and n can be either determined by using the following equations, or by adopting the inverse method i.e. performing several FEA of the tensile tests at high rates and calibrating the parameters by optimization.

$$\sigma = A^{\frac{-1}{n}}\dot{\varepsilon}_0^{\frac{-1}{n}} + \sigma_y + H'\varepsilon \tag{4.5}$$

Where, the hardening modulus is assumed to be negligible as compared to elastic modulus ($K_p \gg H'$). The elastic strain can be defined as:

$$\varepsilon^{el} = f\varepsilon_V^{el} + (1 - f)\varepsilon_P^{el} \tag{4.6}$$

Where, ε_V^{el} and ε_P^{el} represent the viscous strain in the elastic-viscous branch and plastic strain in the elastic-plastic branch. In this thesis, the second method as mentioned before i.e. inverse method by conducting repetitive FEA and optimization is used. For the calibration purpose, ABAQUS-Isight was used in a parallel configuration as shown in Figure 4.2. In this configuration, time-displacement and time-force are the input and the output of the simulations, respectively. First, an extensive FEA campaign was conducted by using the experimental flow stress data in a static tensile test to investigate the effects of the simulation parameters on the results.

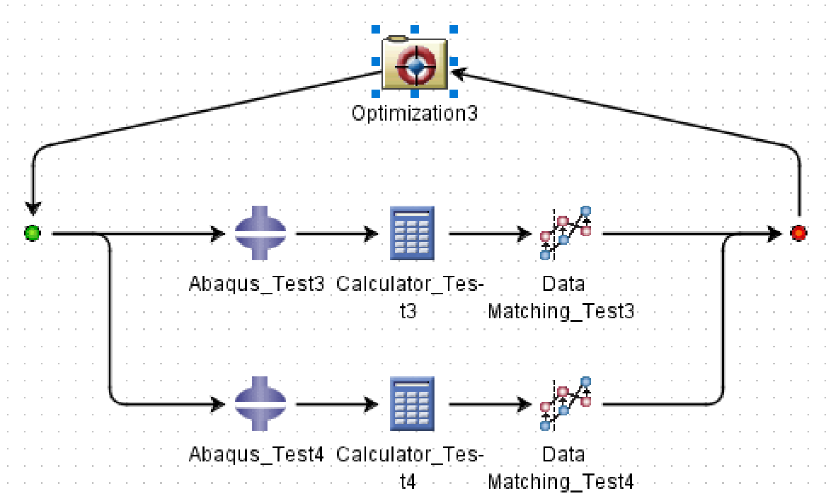

Figure 4.2: Calibration of the TLV model using a parallel configuration in ABAQUS-Isight by adopting the inverse method and performing repetitive FEA of tensile tests and optimization.

Figure 4.3 shows the stress-strain curve in the static tensile test. The two-yield or the idealized tri-linear flow stress model is adopted here as frequently used in the literature [173]. The first yield point is determined through a stepwise procedure with the objective to minimize the Root Mean Square Error (RMSE) between the idealized and experimental data (Figure 4.4). Investigating the tested POM tensile specimen, no significant localized plastic deformation or necking is evident. By assuming the volumetric strain negligible in the tensile static test, the post-yield true stress-strain section is defined based on the available engineering stress-strain data.

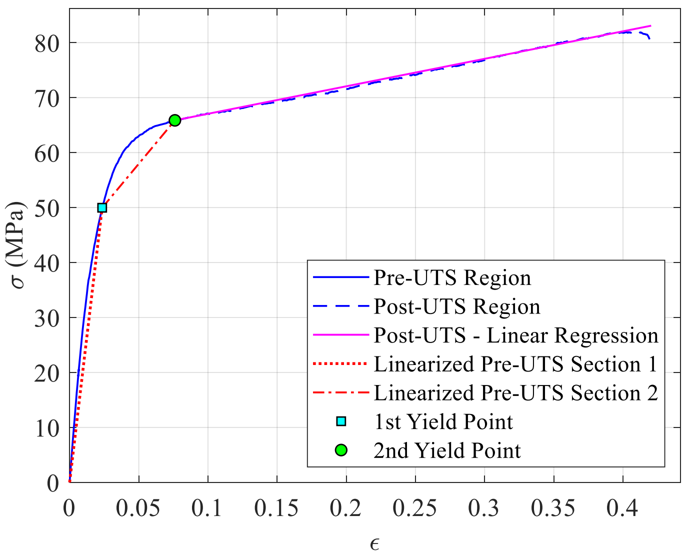

Figure 4.3: An idealized tri-linear representation of flow stress data in the static tensile test of POM.

Both solid (C3D8R with enhanced hourglass) and shell elements (CPS8R and S4R with enhanced hourglass) were adopted to perform simulations by using quarter, half, and full-size specimens. After several trial simulations, a full-size specimen uniformly discretized with S4R shell elements was found to provide fairly accurate results at a reasonable simulation time. To shorten the iterative FEA-Optimization process, the first 40 seconds of the static tensile test (including plastic deformation) was initially used for simulation. Then, full-time simulations were conducted to evaluate the overall results.

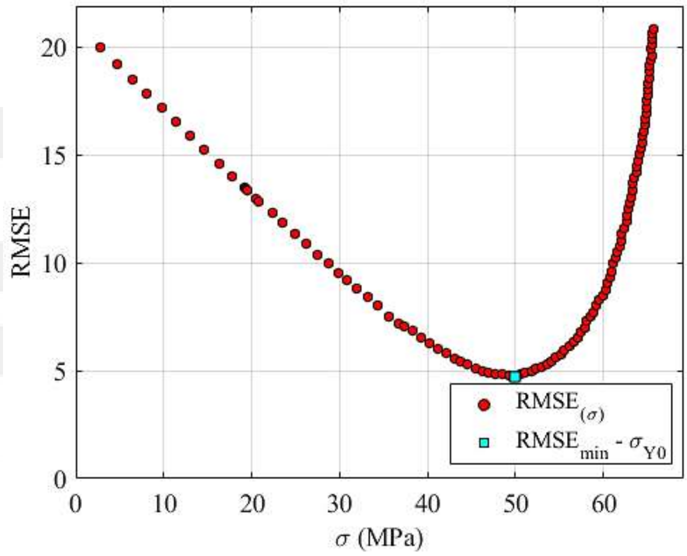

Figure 4.4: Determination of the first yield point in the idealized tri-linear representation of the flow stress by minimizing the RMSE.

Figure 4.5 shows the initial results at time instance 90 s.

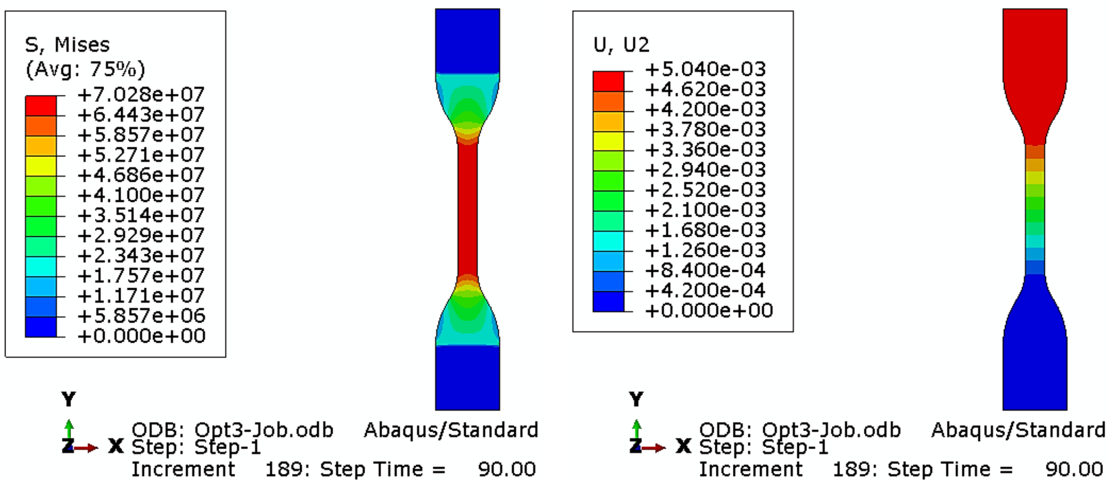

Figure 4.5: Initial FEA results (left: von Mises stress – right: displacement) for static tensile test on POM.

The initial results showed deficiencies in terms of force prediction. Moreover, a mesh-dependency was noticed in the results. More specifically, very fine mesh creates a kind of excessive stiffness in the model, which leads to an overestimation of the force, especially during the post-UTS period. In opposite, a very rough mesh leads to excessive and unphysical reduction of the force due to an unrealistic necking and possibly mesh distortion. Therefore, the overall seed size was also included in the optimization (by using Hooke-Jeeves method [174]), and seed size of 2.85 mm was found to provide the best results (Figure 4.6).

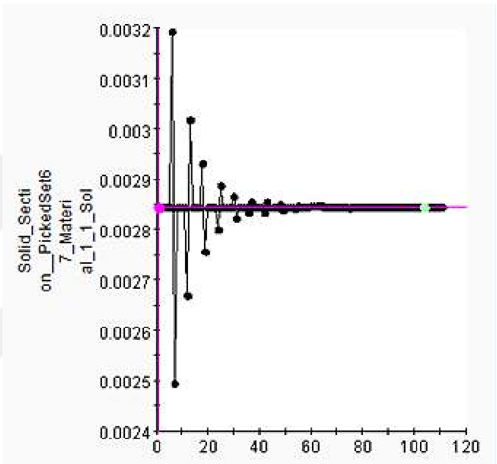

Figure 4.6: Optimization of the mesh size in FEA of static tensile test of POM.

The upper-lower bands of the TLV model parameters f, A, and n was set according to Table 4.1. The results of the optimization by using the Hooke-Jeeves method [174] and performing 100 simulations by using static tensile test data, are shown in Figure 4.7. It is worth mentioning that the application of other optimization methods such as different variations of the NSGA method [174] turned out to produce no significant difference in the results.

Table 4.1: The upper-lower limits, initial value, and optimization results in calibrating TLV model parameters by repetitive FEA-optimization of a tensile test at a nominal speed of 50 mm/min.

Isigth Code	Parameter	Lower Boundary	Initial Value	Upper Boundary	Optimized Value
[0,3]	f	0.01	0.09	0.17	0.09437
[0,1]	n	2.628034	5.256068	7.884101	5.23554
[0,0]	A	0.169443	0.338886	0.508329	0.35212

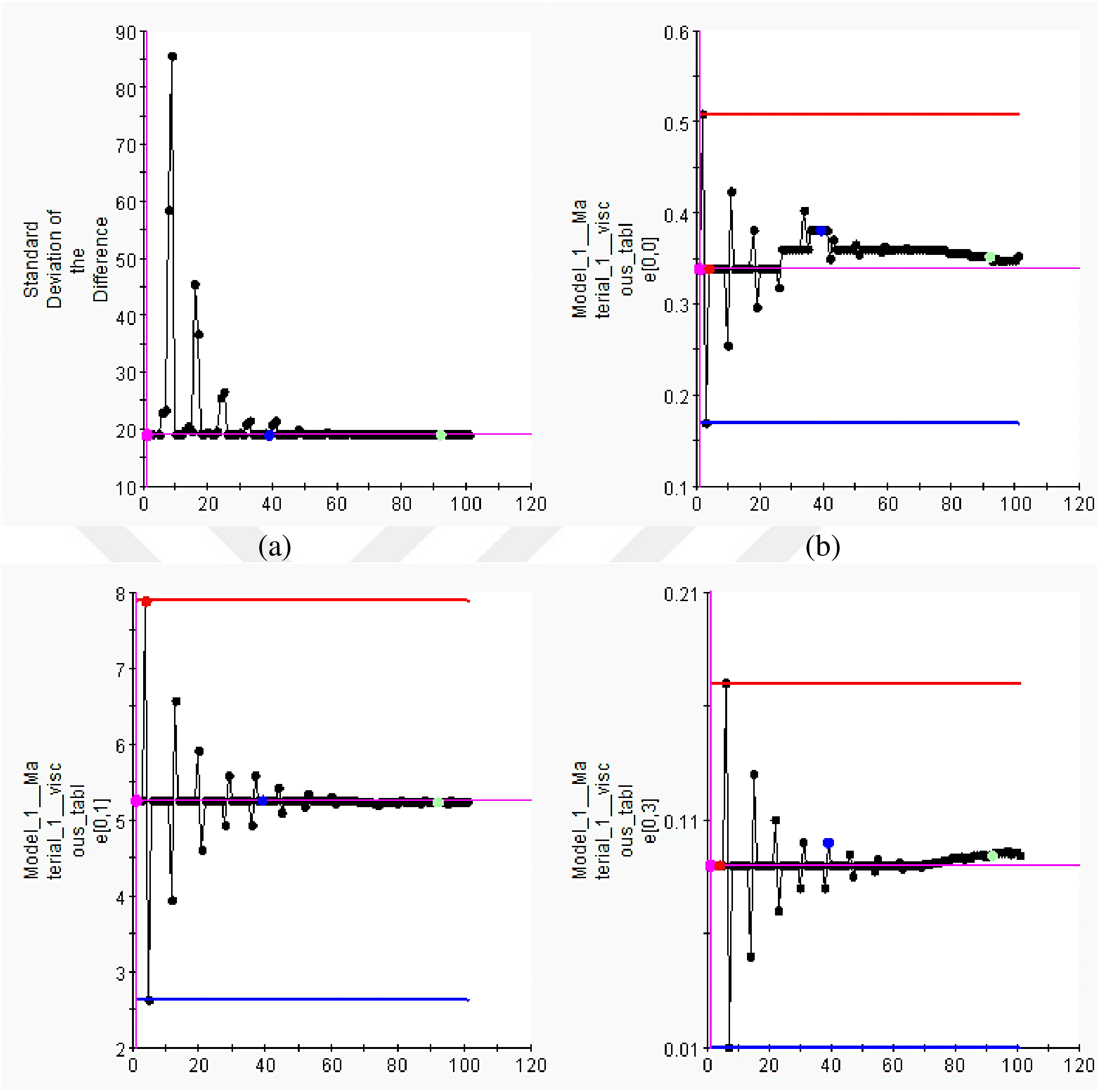

Figure 4.7: The results of the optimization by using Hooke-Jeeves method and 100 FEA simulations using Abaqus-Isight; Standard deviation of difference in terms of force-time (a); and calibration of the TLV model parameters A (b), n (c), and f (d).

As no significant rate-effect (viscous effect) is evident by comparing the tensile test results at nominal speeds of 5 mm/min and 50 mm/min, further investigations showed that the calibration of the TLV model parameters must be performed at significantly higher speeds. A similar FEA-optimization approach was taken for the calibration of the TLV model parameters based on the tensile test at 250 mm/min. Therefore, the effects of the parameters on the predicted force are shown in Figure 4.8 (parameter's values are close to the optimized values).

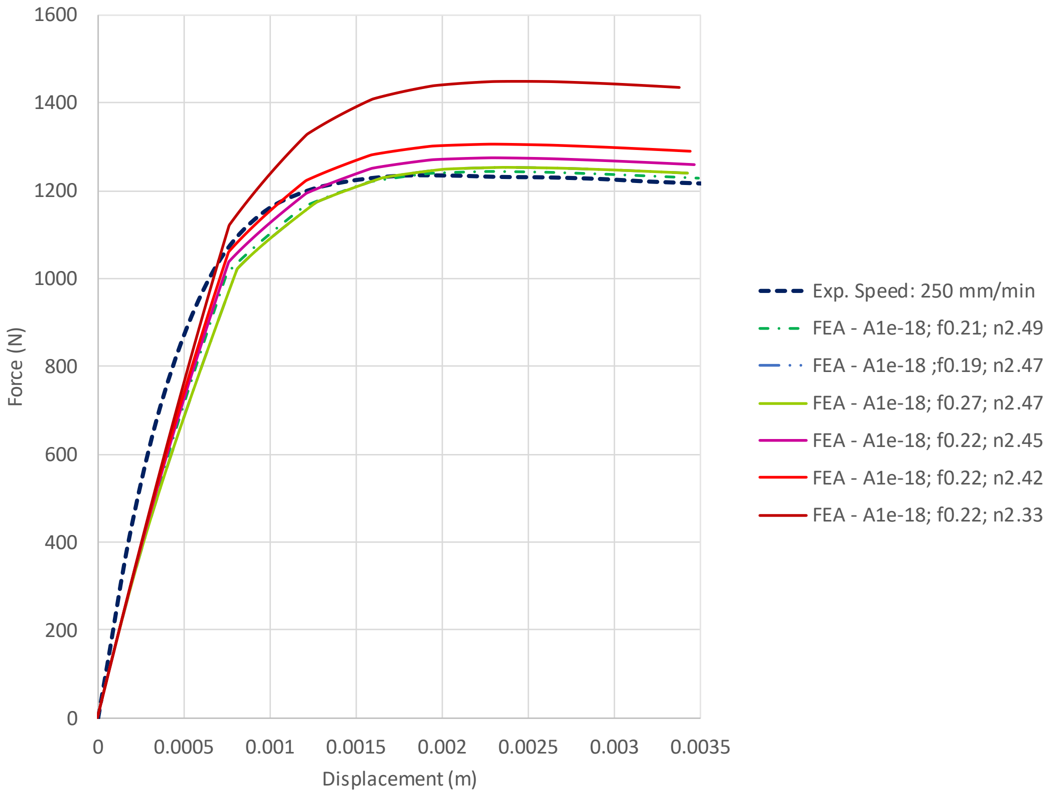

Figure 4.8: The effects of the TLV model parameters' values on the predicted force in the tensile test at 250 mm/min.

Further investigations on the viscous parameters in the TLV model are in agreement with the presented results here:

- As f decreases, the force-time curve moves leftwards. However, the relation between the tensile force and the parameter is not linear.
- As A decreases, force increases. However, the resultant force is far less sensitive to the value of this parameter as compared to that of the two other parameters (n and f).
- As n decreases, the resultant force increases.

4.3.2 Parallel rheological framework (PRF)

The Parallel Rheological Framework (PRF) [175] can be used for modeling polymers that exhibit permanent nonlinear viscous behavior and undergo large deformations. This model consists of multiple viscoelastic networks and, optionally, an elastoplastic network in parallel. To predict the elastic behavior, PRF uses a hyperelastic material model. Figure

4.9 shows a schematic view of the PRF model. It is noteworthy that the equilibrium network response (network 0 in the figure) might be purely elastic or elastoplastic.

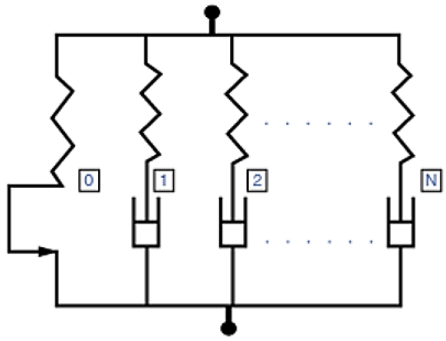

Figure 4.9: A schematic view of the PRF material model.

Figures 4.10 to 4.12 show the initial attempts to calibrate the PRF model based on tensile, cyclic compressive, and short-time creep test results at ambient temperature by using MCalibration software [176]. Calibrated PRF material parameters are presented in Table 4.2.

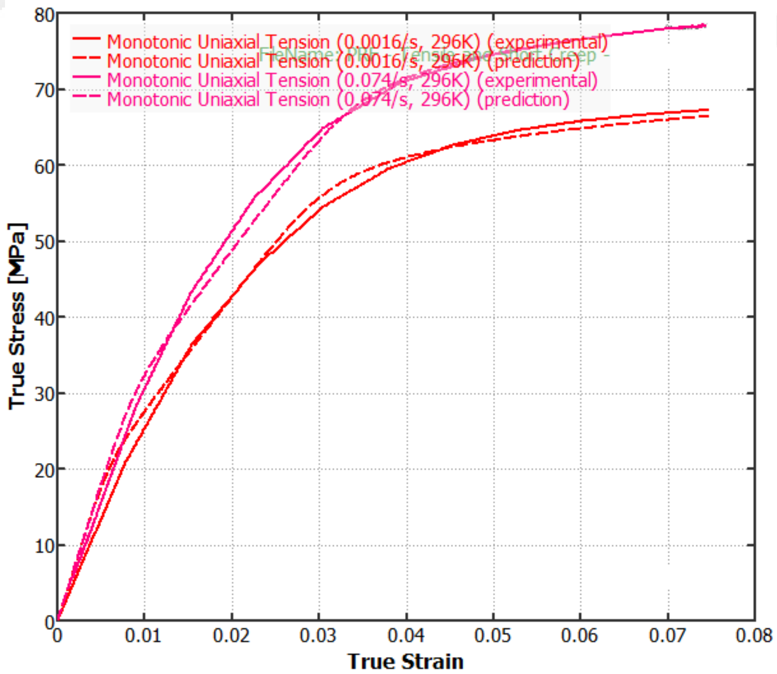

Figure 4.10: The results of the initial attempt to calibrate the PRF model based on tensile test data at two different rates.

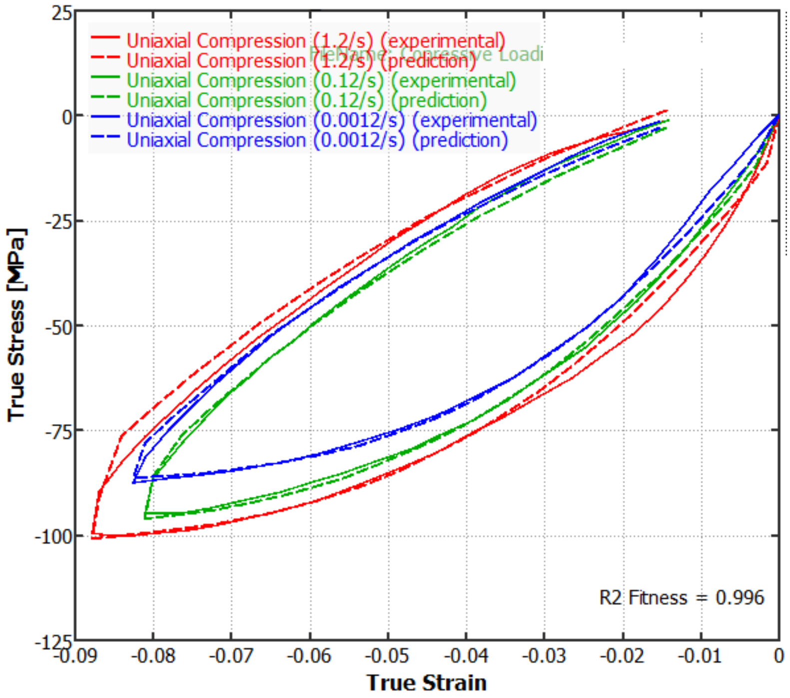

Figure 4.11: The results of the initial attempt to calibrate the PRF model based on cyclic compression test data at three different rates.

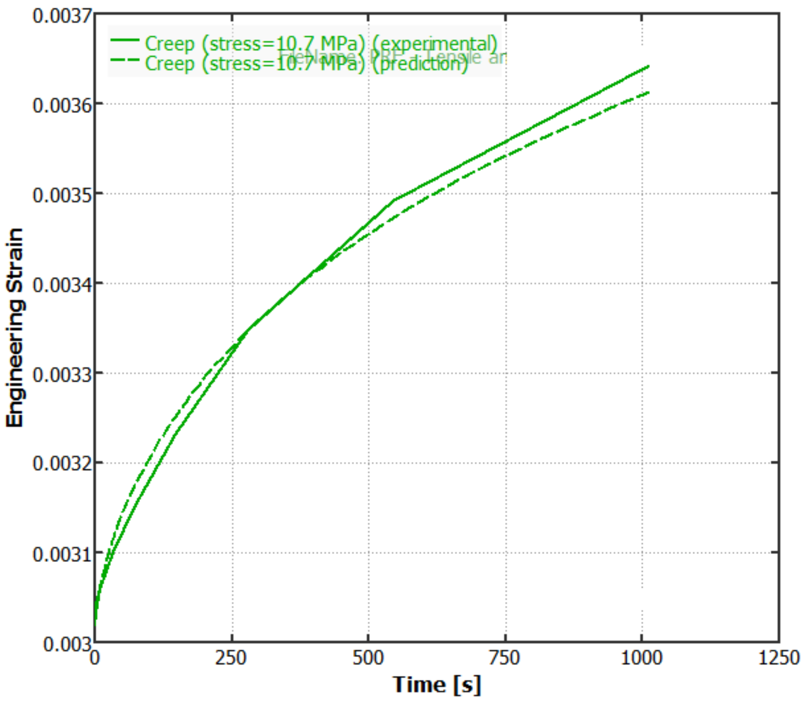

Figure 4.12: The results of the initial attempt to calibrate the PRF model based on short-time creep test data.

Table 4.2: Calibrated PRF material parameters.

Parameter	Value	Parameter	Value
C10	4.9026	a1	0
C20	-0.0413	$\dot{e}_1$	1
C30	0.0004	s2	47.976
κ	5934.7	q2	49.625
S1	80.701	n2	13.0757
q1	34.373	m2	-0.64266
n1	6.9837	a2	0
m1	-0.3199	$\dot{e}_2$	1.6468e-6

4.3.3 Three network (TN)

The Three Network (TN) model is a specialized version of the more general PRF model, which is developed by J. S. Bergstrom to be more numerically efficient for modeling the viscoplastic behavior of thermoplastics [177]. As evident by the name of the model, the kinematics of TN model contains three parallel branches. A schematic rheological view of the model is presented below.

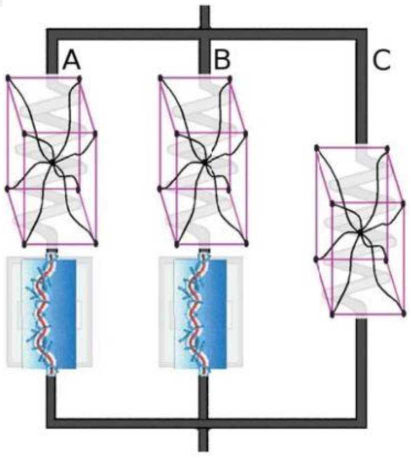

Figure 4.13: A rheological view of the TN model [177].

The deformation gradient in branch A is decomposed (multiplicatively) into elastic and viscoplastic sections. Therefore:

$$F = F_A^e F_A^v \tag{4.7}$$

The stress in branch A is calculated as:

$$\sigma_A = \frac{\mu_A}{J_A^e \overline{\lambda_A^{e*}}}\left[1 + \frac{\theta - \theta_0}{\hat{\theta}}\right]\frac{L^{-1}\left(\overline{\lambda_A^{e*}}/\lambda_L\right)}{L^{-1}(1/\lambda_L)} dev[b_A^{e*}] + \kappa(J_A^e - 1)I \tag{4.8}$$

Where, $J_A^e = det[F_A^e]$, μ_A is the initial shear modulus, λ_L is the chain locking stretch. κ denotes the bulk modulus. θ, θ_0 and $\hat{\theta}$ represent the current temperature, the reference temperature, and the parameter identifying the temperature-dependent response of the stiffness, respectively. The Cauchy-Green deformation tensor is defined as:

$$b_A^{e*} = (J_A^e)^{-2/3} F_A^e (F_A^e)^T \tag{4.9}$$

The effective chain stretch is:

$$\overline{\lambda_A^{e*}} = (tr[b_A^{e*}]/3)^{1/2} \tag{4.10}$$

In Equation 4.8, $L_{(x)}^{-1}$ is the inverse Langevin function:

$$L_{(x)} = \coth(x) - 1/x \tag{4.11}$$

The deformation in branch B is also decomposed into viscoplastic and elastic components ($F = F_B^e F_B^v$). The Cauchy stress in branch B is defined in a similar way to branch A (Equation 4.8). The effective shear modulus evolves with the plastic strain from its initial measure (μ_{Bi}):

$$\dot{\mu}_{Bi} = -\beta\left[\mu_B - \mu_{Bf}\right] \cdot \dot{\gamma}_A \tag{4.12}$$

Where, $\dot{\gamma}_A$ is the viscoplastic flow rate. The Cauchy stress in branch B is defined as:

$$\sigma_C = \frac{1}{1+q}\left\{\begin{aligned} &\frac{\mu_C}{J\overline{\lambda}^*}\left[1 + \frac{\theta - \theta_0}{\hat{\theta}}\right]\frac{L^{-1}\left(\overline{\lambda}^*/\lambda_L\right)}{L^{-1}(1/\lambda_L)} dev[b^*] \\ &+\kappa(J-1)I + q\frac{\mu_C}{J}\left[I_1^* b^* - \frac{I_2^*}{3} I - (b^*)^2\right] \end{aligned}\right\} \tag{4.13}$$

Where, μ_C is the initial shear modulus; $J = det[F]$; $\overline{\lambda}^* = (tr[b^*]/3)^{1/2}$ denotes the effective chain strain [178]; $b^* = J^{-2/3} F(F)^T$ denotes the Cauchy-Green deformation tensor. Therefore, by using the TN model framework, the total Cauchy stress is defined as:

$$\sigma = \sigma_A + \sigma_B + \sigma_C \tag{4.14}$$

For further details and discussion on the calibration of the TN model, one may refer to J. S. Bergstrom and J. E. Bischoff [177]. In this thesis, the model was calibrated by using MCalibration, and PolyUMod was used to define the material model in Abaqus by using the VUMAT subroutine. Figures 4.14 and 4.15 represent the calibration results based on the tensile and compressive tests at various rates and temperatures. The calibrated material parameters are provided in Table 4.3. Apart from the numerical efficiency of the TN model, another advantage of the model is that fewer parameters should be calibrated as compared to similar models, for example, the base PRF model. Moreover, the tests data at various temperatures can be simultaneously used for calibration, which, in turn, results in an efficient and fairly accurate calibration by using the minimum available test data.

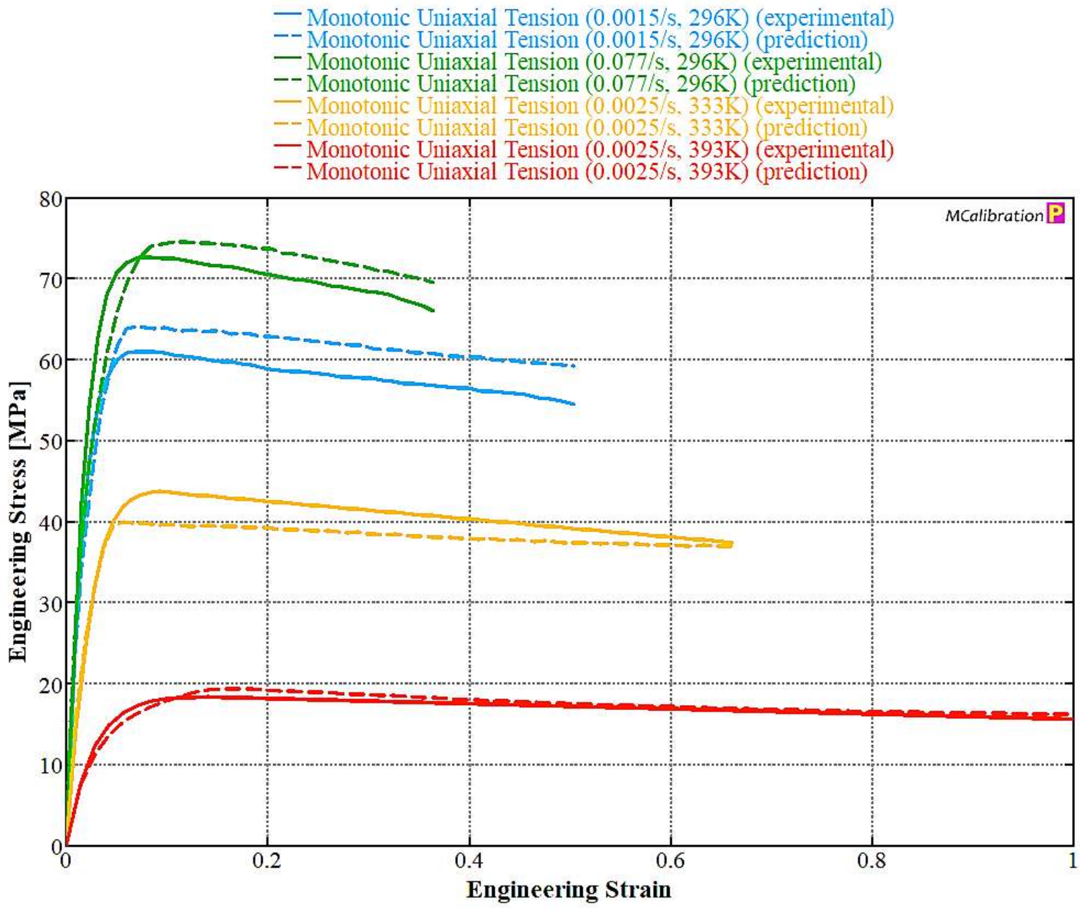

Figure 4.14: The TN model calibration results based on the tensile tests at various rates and temperatures.

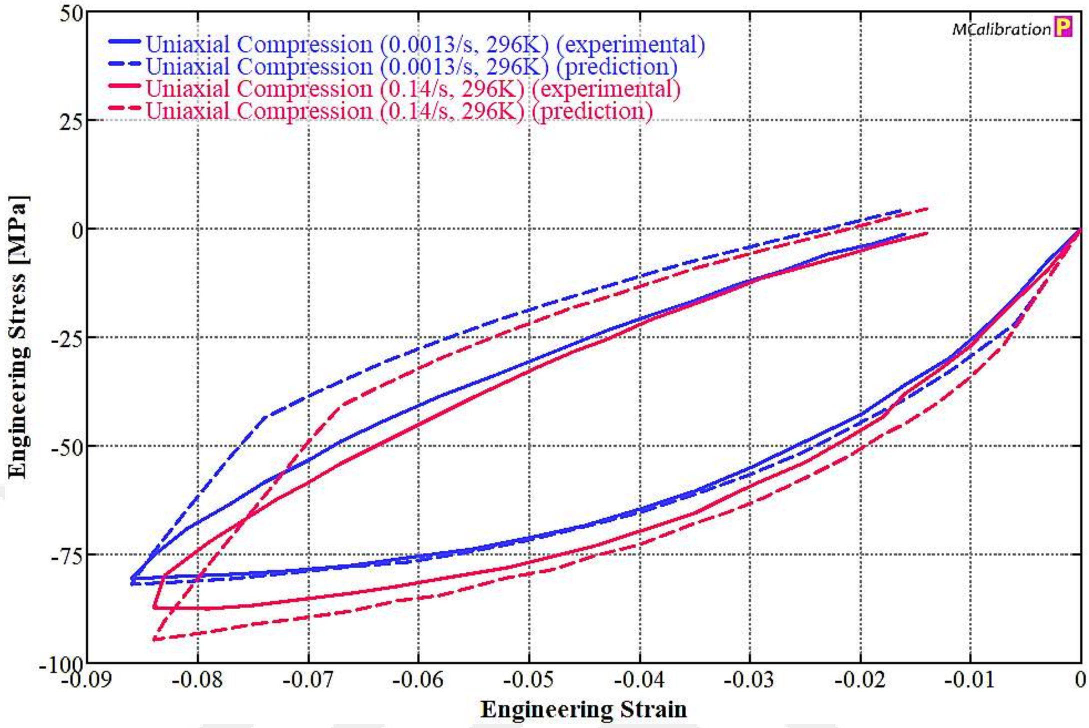

Figure 4.15: The TN model calibration results based on the compressive tests at various rates.

Table 4.3: Calibrated TN material parameters.

Parameter	Value	Parameter	Value
μ_A	460.964	μ_{Bi}	478.955
$\hat{\theta}$	-92.4896	μ_{Bf}	106.952
λ_L	6.09764	β	16.6013
κ	4517.69	$\hat{\tau}_B$	38.5916
$\hat{\tau}_A$	5.31373	m_B	24.2077
a	0.09786	μ_C	9.41161
n	94.3391	θ_0	332.704
m_A	14.4555	$q = \alpha$	0

4.3.4 Johnson-Cook (JC)

Johnson-Cook (JC) model falls in the category of Mises plasticity. The model consists of an analytical hardening law, and the elastic behavior is assumed linear. This model can be used in conjugation with different failure models in Abaqus namely, JC dynamic failure model, tensile failure model, and progressive ductile damage and failure model. The JC model has been extensively used for modeling metallic alloys. Thermoplastics are also modeled by using this phenomenological model in the literature [179–184]. The JC constitutive model has the following form:

$$\bar{\sigma} = \left[A + B\bar{\varepsilon}_{pl}^{n}\right]\left[1 + C\ln\left(\frac{\dot{\bar{\varepsilon}}_{pl}}{\dot{\varepsilon}_0}\right)\right]\left[1 - \left(\frac{T - T_{ref}}{T_{melt} - T_{ref}}\right)^{m}\right] \tag{4.15}$$

Where, $\bar{\varepsilon}_{pl}$, $\dot{\bar{\varepsilon}}_{pl}$, $\dot{\varepsilon}_0$ denote the equivalent plastic strain, the equivalent plastic strain rate, and the reference plastic strain rate, respectively. Deformation at rates below $\dot{\varepsilon}_0$ is assumed rate-independent. *A*, *B*, *n*, *m*, and *C* are the material parameters to be calibrated. T, T_{melt}, T_{ref} represent the current temperature, melting temperature, and reference temperature. Deformation at temperatures below T_{ref} is assumed temperature-independent. If the forming process is entirely performed at or above room temperature, T_{ref} could be assumed equal to the room temperature. The JC constitutive model was first calibrated by using MCalibration, and the data of tensile tests performed on POM (Copolymer - CELCONE M90) at ambient temperature and two different rates (5 and 250 mm/min or 0.0017 and 0.08 $1/s$) along with the stress-strain data available in the elastic region and elevated temperatures (25 {ambient}, 40, 80, and 120 °C). Figures 4.16 to 4.19 show the results based on a stepwise calibration approach (R^2 varies from 89% to 92%). Table 4.4 shows the calibrated material model parameters.

Table 4.4: Calibrated JC constitutive material model parameters (first calibration).

A	B	C	n	m	$\dot{\varepsilon}_0$	T_{ref} (°C)	T_{melt} (°C)
44.2509	45.6502	0.0463438	0.284806	0.845325	0.0017	25	165

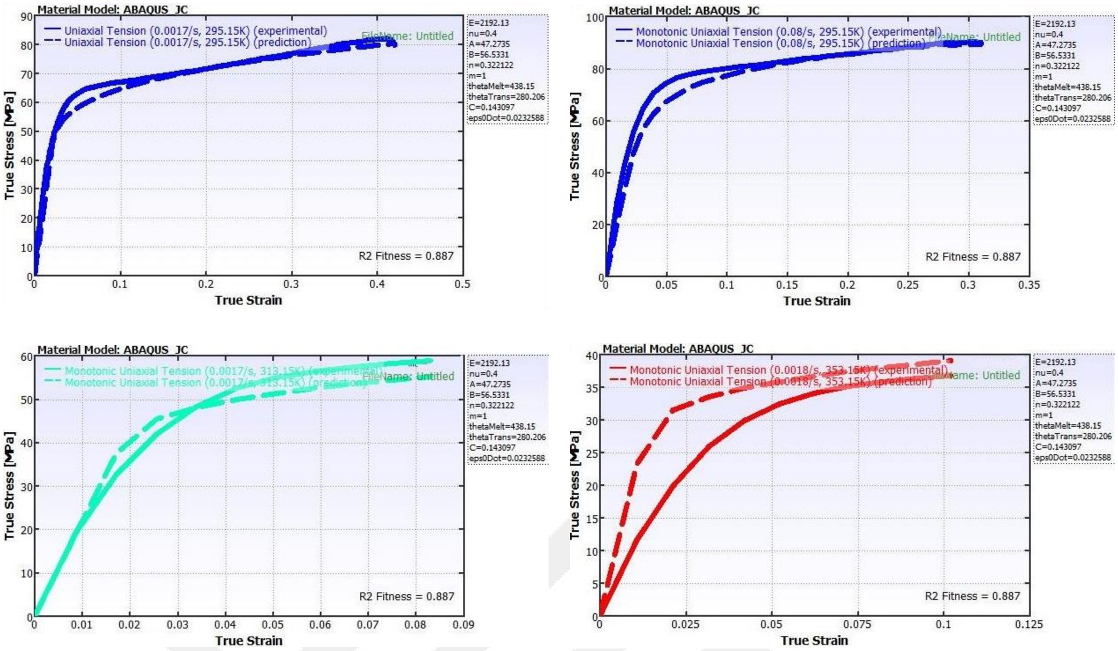

Figure 4.16: JC model calibration at strain rates, namely 5 and 250 s^{-1} and temperatures 295, 313, and 353 K; first calibration.

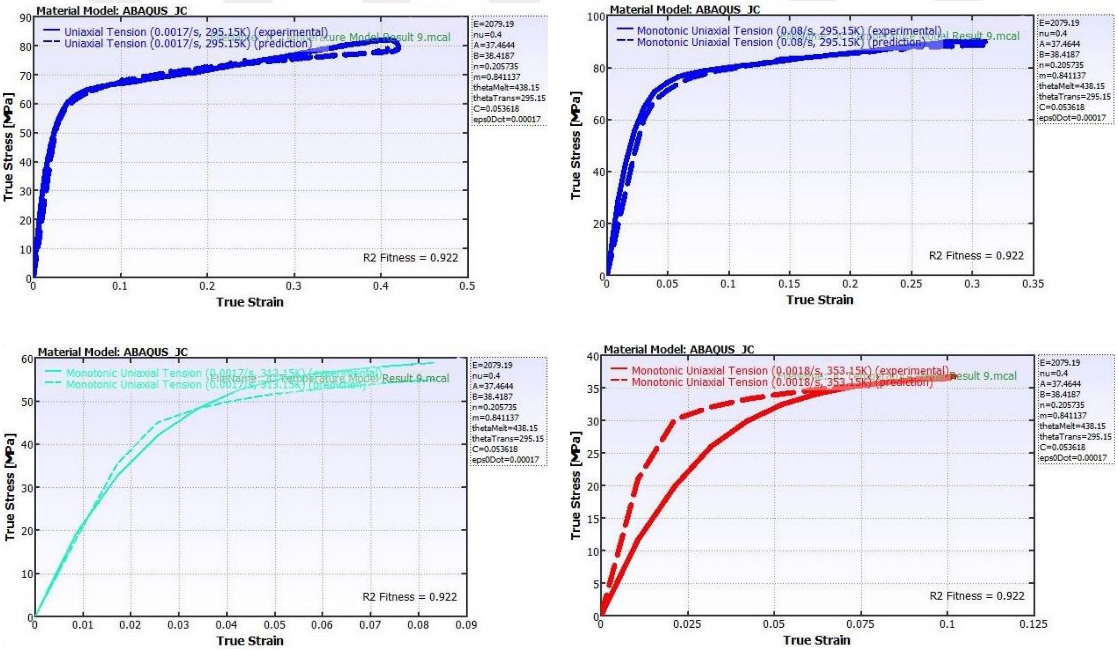

Figure 4.17: JC model calibration at strain rates, namely 5 and 250 s^{-1} and temperatures 295, 313, and 353 K; second calibration.

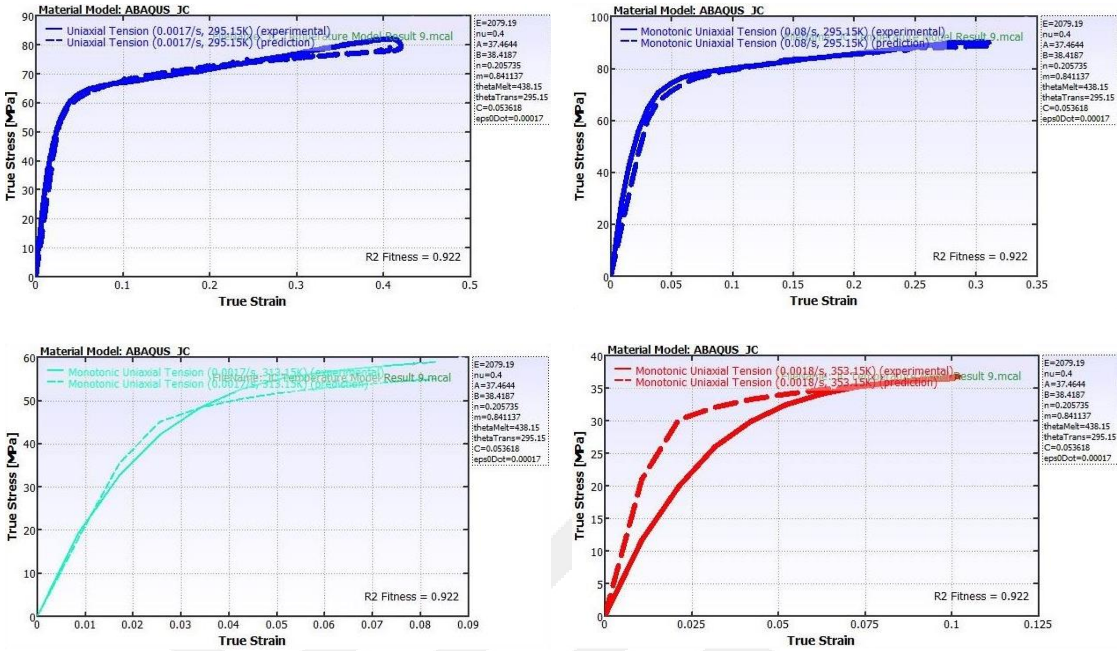

Figure 4.18: JC model calibration at strain rates, namely 5 and 250 s^{-1} and temperatures 295, 313, and 353 K; third calibration.

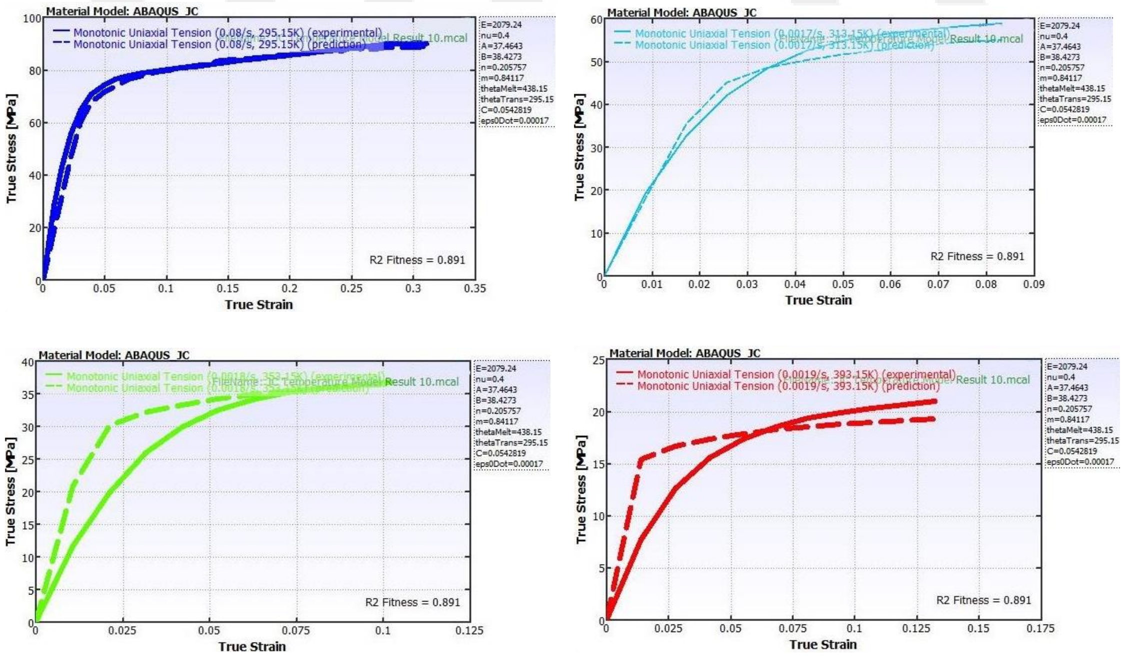

Figure 4.19: JC model calibration at strain rates, namely 5 and 250 s^{-1} and temperatures 295, 313, 353, and 393 K. Stepwise calibration based on temperature-independent elasticity.

In the above-presented calibration, the elastic modulus of POM was assumed to be constant within the elastic range. Therefore, the elastic modulus was averaged as a function of temperature as tabulated below (Table 4.5):

Table 4.5: Average elastic modulus corresponding to the first calibration of the JC model.

T [°C]	25	40	80	120
E [MPa]	2804.57	1894.81	932.669	546.287
ν	0.37	0.372	0.377	0.382

However, the viscoelastic behavior of POM (Copolymer) is a nonlinear function of strain. Moreover, by taking the aforesaid calibration approach (using MCalibration), the transition point from reversible elastic deformation to permanent plastic deformation (i.e. yield point) is not defined based on physical evidence. Instead, the transition point from reversible to permanent deformation is defined merely based on the best fit to the initial so-called linear section and the following nonlinear section of the stress-strain curve. To address this issue, the second calibration of the JC model was performed in MATLAB. The true stress-strain data was derived based on the assumption of negligible volume strain and insignificant necking effect as observed through the tensile tests performed by the author (Figure 4.20). As the tensile test data at the reference strain rate of 0.0020 s^{-1} (crosshead speed of 5 mm/min) does not invoke the strain rate segment of the JC model, in the first step, this data was used to calibrate the true stress as the dependent variable of two independent variables, namely plastic strain and temperature:

$$\bar{\sigma} = \left[A + B\bar{\varepsilon}_{pl}^{n}\right]\left[1 - \left(\frac{T - T_{ref}}{T_{melt} - T_{ref}}\right)^{m}\right] \tag{4.16}$$

Figure 4.21 shows the result of the calibration by using the nonlinear least square method in MATLAB.

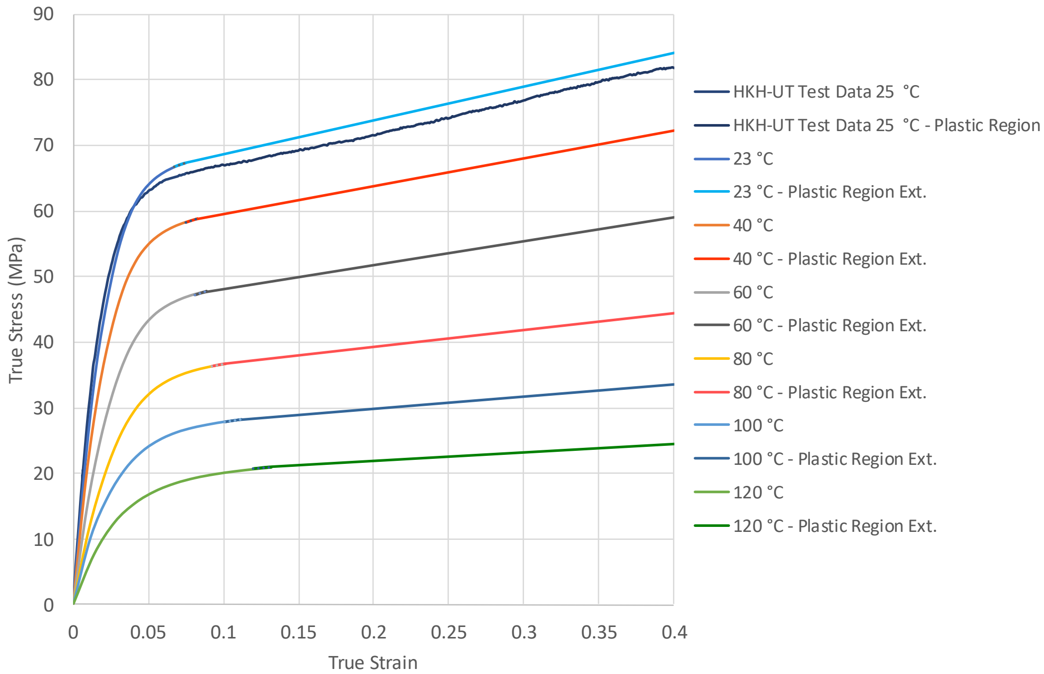

Figure 4.20: True stress-strain data from static tensile tests of POM at several temperatures.

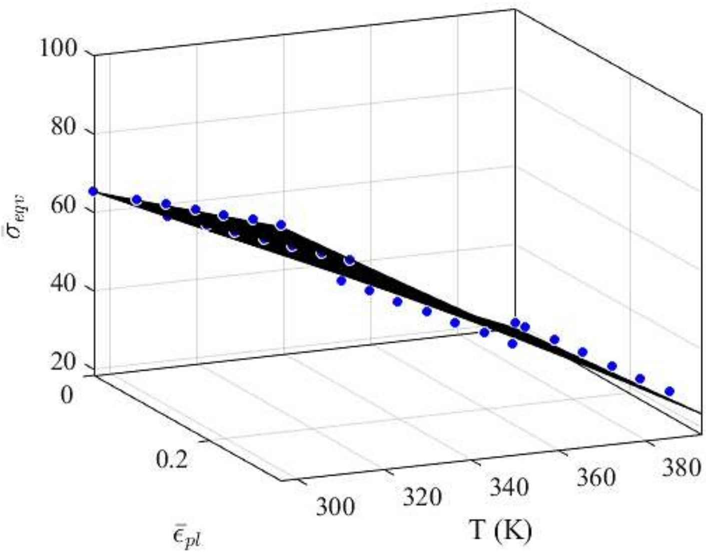

Figure 4.21: Comparison between the experimental data and the calibrated response surface (Equation 4.16) by using the nonlinear least square method in MATLAB.

As a result, four model coefficients (A, B, n, and m) were determined, and the good of fitness measures $R^2$and R^2_{adj} of 0.9962 and 0.9957 were achieved, respectively. In the second step, by using the model coefficients derived from the previous stage, the second linear (or nonlinear) least square regression was performed to fit the data for tensile tests at several temperatures and strain rate of 0.0995 s^{-1} (crosshead speed of 250 mm/min). To do so, two independent variables were defined as follows:

$$v_1 = \left[A + B\bar{\varepsilon}_{pl}^{n}\right]\left[1 - \left(\frac{T - T_{ref}}{T_{melt} - T_{ref}}\right)^{m}\right] \tag{4.17}$$

$$v_2 = \left[A + B\bar{\varepsilon}_{pl}^{n}\right]\left[1 - \left(\frac{T - T_{ref}}{T_{melt} - T_{ref}}\right)^{m}\right]\ln\left(\frac{\dot{\bar{\varepsilon}}_{pl}}{\dot{\varepsilon}_0}\right) \tag{4.18}$$

Therefore, true flow stress was linearly fit to the above two new variables, to derive the JC model coefficient *C* as follows:

$$\bar{\sigma} = v_1 + Cv_2 \tag{4.19}$$

Accordingly, the good of fitness measures R^2 and R_{adj}^2 of 0.9790 were achieved. Figure 4.22 provides a comparison between the experimental data and the calibrated response surface (Equation 4.19) by using the linear least square method in MATLAB. Therefore, the coefficient of the JC model according to the second calibration is provided in Table 4.6:

Table 4.6: JC plastic model parameters according to the second calibration.

A	B	C	n	m	$\dot{\varepsilon}_0$	T_{ref} (°C)	T_{melt} (°C)
65.3000	56.6961	0.0331	1.0150	1.0989	0.0020	23	165

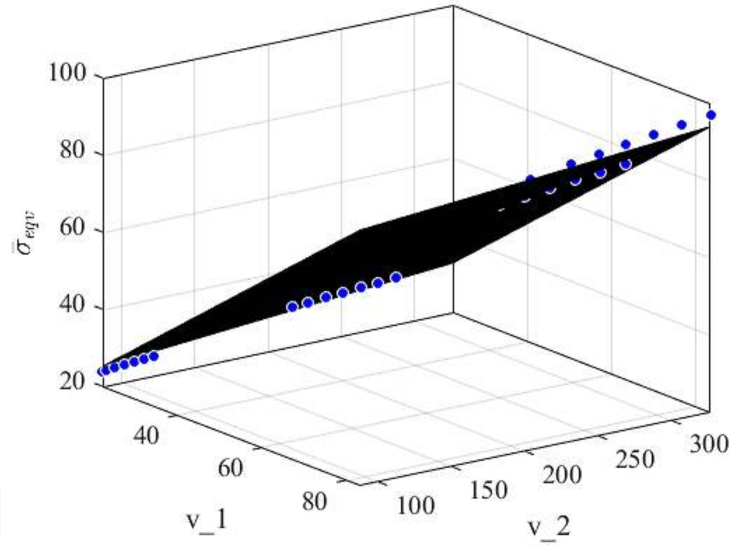

Figure 4.22: Comparison between the experimental data and the calibrated response surface (Equation 4.19) by using linear least square method in MATLAB.

As stated before, the recent calibration of the JC model was performed by considering the true plastic strain and the corresponding true stress at several temperatures (25 {ambient}, 40, 80 and 120 °C) and two strain rates (0.0020 s^{-1} {crosshead speed of 5 mm/min} and 0.0995 s^{-1} {crosshead speed of 250 mm/min}). To model the nonlinear elastic behavior of POM copolymer as a function of strain, rate, and temperature, a similar equation to the JC plastic model can be employed. Calibrating such a model, the secant modulus can be derived by dividing the true stress over the elastic true strain. However, such an equation does not fit well with the available experimental data. Instead, the following phenomenological model of the same number of constants provides very good fitness in the elastic (viscoelastic) region.

$$\bar{\sigma}_e = [A_e \sin(\bar{\varepsilon}_{el} - \pi) + B_e(\bar{\varepsilon}_{el} - 10)^2 + N_e] \times \left[1 + C_e \ln\left(\frac{\dot{\bar{\varepsilon}}_{el}}{\dot{\varepsilon}_{0e}}\right)\right] \times \left[1 - \left(\frac{T - T_{ref}}{T_{melt} - T_{ref}}\right)^{m_e}\right] \tag{4.20}$$

The initial step of calibration is performed by considering the true elastic strain and the corresponding true stress at several temperatures (25 {ambient}, 40, 80, and 120 °C), and the reference strain rate (0.0016 s^{-1} {crosshead speed of 5 mm/min}). Therefore, $\bar{\sigma}_e$ is considered as the dependent variable and $\bar{\varepsilon}_{el}$ and T are the independent variables in a nonlinear least square regression as follows:

$$\bar{\sigma}_e = [A_e \sin(\bar{\varepsilon}_{el} - \pi) + B_e(\bar{\varepsilon}_{el} - 10)^2 + N_e]\left[1 - \left(\frac{T - T_{ref}}{T_{melt} - T_{ref}}\right)^{M_e}\right] \quad (4.21)$$

As a result, four model coefficients (A_e, B_e, N_e and M_e) were determined, and the good of fitness measures R^2 and R^2_{adj} of 0.9883 and 0.9877 were achieved, respectively (Figure 4.23).

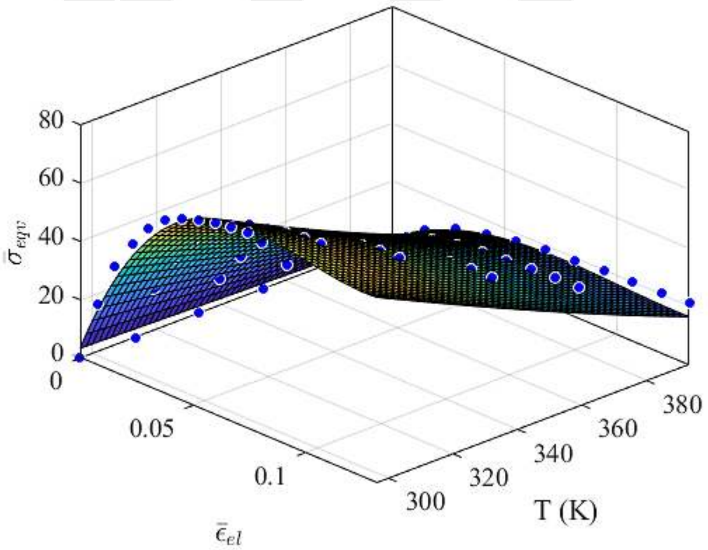

Figure 4.23: Comparison between the elastic experimental data and the calibrated response surface (Equation 4.21) by using the nonlinear least square method in MATLAB.

In the second stage, to calibrate the model for higher strain rates, the tensile test data corresponding to the crosshead speed of 250 mm/min was used to perform a linear (or nonlinear) least square regression by defining two new variables:

$$v_{e1} = [A_e \sin(\bar{\varepsilon}_{el} - \pi) + B_e(\bar{\varepsilon}_{el} - 10)^2 + N_e]\left[1 - \left(\frac{T - T_{ref}}{T_{melt} - T_{ref}}\right)^{M_e}\right] \quad (4.22)$$

$$v_{e2} = [A_e \sin(\bar{\varepsilon}_{el} - \pi) + B_e(\bar{\varepsilon}_{el} - 10)^2 + N_e]\left[1 - \left(\frac{T - T_{ref}}{T_{melt} - T_{ref}}\right)^{M_e}\right] \ln\left(\frac{\dot{\bar{\varepsilon}}_{pl}}{\dot{\varepsilon}_0}\right) \quad (4.23)$$

Therefore, true stress (in the elastic region) was linearly fit to the above two variables, to derive the JC model coefficient C_e as follows:

$$\bar{\sigma} = v_{e1} + C_e v_{e2} \quad (4.24)$$

Accordingly, the good of fitness measure R^2 of 0.9796 was achieved. The coefficient of the nonlinear elastic model according to the recent calibration is provided in Table 4.7:

Table 4.7: Nonlinear elastic model parameters according to the second calibration.

A_e	B_e	C_e	N_e	M_e	$\dot{\varepsilon}_0$	T_{ref} (°C)	T_{melt} (°C)
4.6123e5	-2.3171e4	0.0307	2.3171e6	1.1824	0.0016	23	165

Therefore, the secant modulus, E_s, can be achieved as follows:

$$E_s = \frac{\bar{\sigma}_e}{\bar{\varepsilon}_{el}} = \left[\frac{A_e \sin(\bar{\varepsilon}_{el} - \pi) + B_e(\bar{\varepsilon}_{el} - 10)^2 + N_e}{\bar{\varepsilon}_{el}}\right] \times \left[1 + C_e \ln\left(\frac{\dot{\bar{\varepsilon}}_{el}}{\dot{\varepsilon}_{0e}}\right)\right] \times \left[1 - \left(\frac{T - T_{ref}}{T_{melt} - T_{ref}}\right)^{M_e}\right] \quad (4.25)$$

Figure 4.24 shows the engineering stress-strain curves in tensile tests at nominal rates namely, 5 (in rolling and transverse directions), 50, and 250 mm/min.

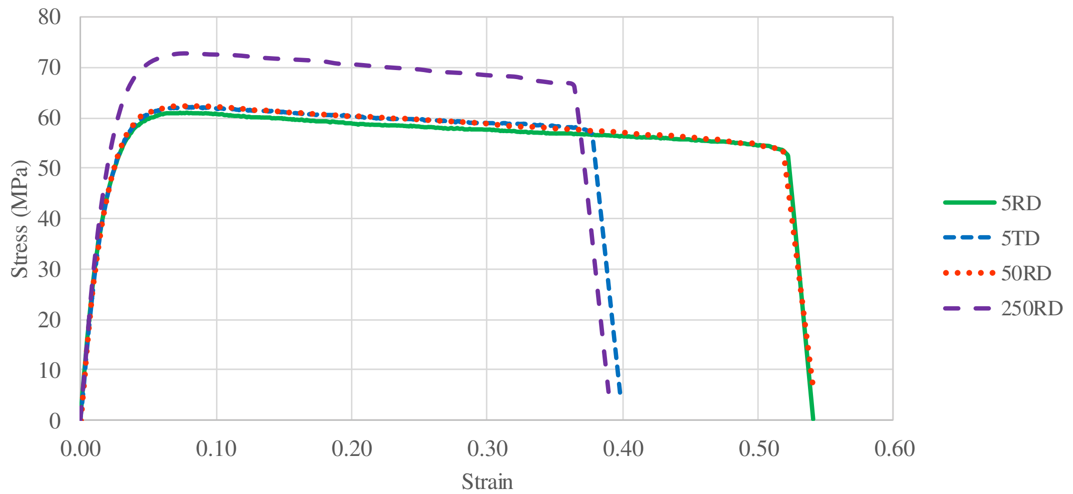

Figure 4.24: Engineering stress-strain curves in tensile tests on POM (copolymer) at nominal rates namely, 5 (in rolling and transverse directions), 50, and 250 mm/min.

Considering this figure, no significant anisotropic effect is evident as static tensile tests at rolling (RD) and transverse (TD) directions result in the same level of flow stress. As expected, no significant rate effect is evident by increasing the nominal speed from 5 to 50 mm/min. By further investigation of the fractured tensile test specimen, it was noticed that the post-UTS deformation could be also considered as perfectly plastic (with a tolerable error). Based on these observations, the JC constitutive model was calibrated for the third time. Considering the perfectly plastic assumption, $B = n = 0$. A also equals the initial yield point in the static tensile test at reference (room) temperature. The reference strain rate, $\dot{\varepsilon}_0$, is also specifically measured in the plastic region. To calibrate C, based on the tensile test data at the nominal speed of 250 mm/min:

$$C = \left[\frac{\sigma_0}{A} - 1\right] \Big/ \ln\left(\frac{\dot{\bar{\varepsilon}}_{pl}}{\dot{\varepsilon}_0}\right) \tag{4.26}$$

After defining the JC rate parameter, C, the initial static yield data at elevated temperatures were used to define the JC temperature parameter, m, as follows:

$$\ln\left(1 - \frac{\sigma_0}{A}\right) = m \ln\left(\frac{T - T_{ref}}{T_{melt} - T_{ref}}\right) \tag{4.27}$$

Equation 4.27 represent a linear relation in which the dependent variable is $Y^* = \ln\left(1 - \frac{\sigma_0}{A}\right)$, and the independent variable is $X^* = \ln\left(\frac{T - T_{ref}}{T_{melt} - T_{ref}}\right)$. Figure 4.25 shows the linear relation based on the available initial static yield data at elevated temperatures. The JC temperature parameter, m, equals the slope of the line in this figure.

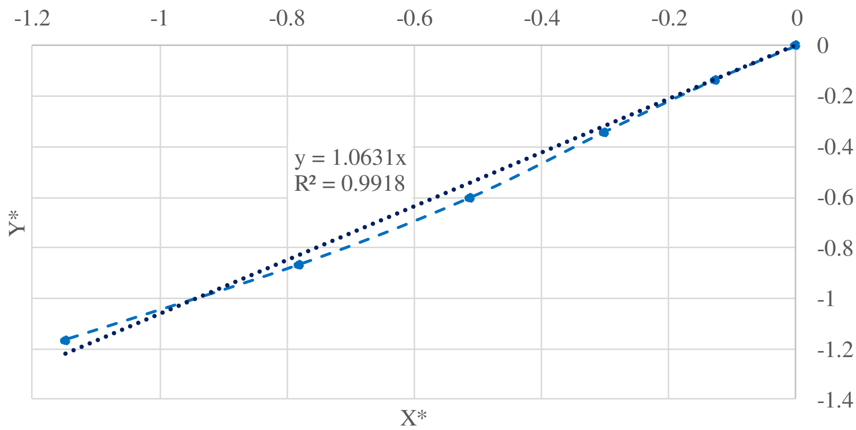

Figure 4.25: The calibrated JC temperature parameter, m (third calibration).

The JC constitutive model parameters acquired from the third calibration are tabulated below (Table 4.8). Table 4.9 provides the experimental initial yield values, the initial yield values predicted by the JC model (the third calibration), and the corresponding error. As evident from this table, the average error is 3.54%; therefore, the constitutive model predicts the fellow stress with good accuracy.

Table 4.8: The JC constitutive model parameters acquired from the third calibration.

A	B	C	n	m	$\dot{\varepsilon}_0$	T_{ref} (°C)	T_{melt} (°C)
67.225	0	0.071	1	1.063	0.006	23	165

Table 4.9: The experimental initial yield, the predicted initial yield by the JC model (third calibration), and the corresponding error.

Temperature (°C)	Nominal Deformation Speed (mm/min)	$\sigma_{0_{Exp}}$	$\sigma_{0_{JC}}$	Error (%)
23	5	67.23	67.23	0
23	250	78.76	78.76	0
40	5	58.79	59.18	0.67
60	5	47.75	49.71	4.10
80	5	36.80	40.24	9.36
100	5	28.23	30.77	8.99
120	5	20.95	21.30	1.68

The elastic modulus at each temperature can be estimated by averaging the secant modulus at that temperature. Figure 4.26 provides the secant modulus of the POM (copolymer) as a function of strain and temperature. Figure 4.27 provides the estimated average E (secant modulus) as a function of temperature.

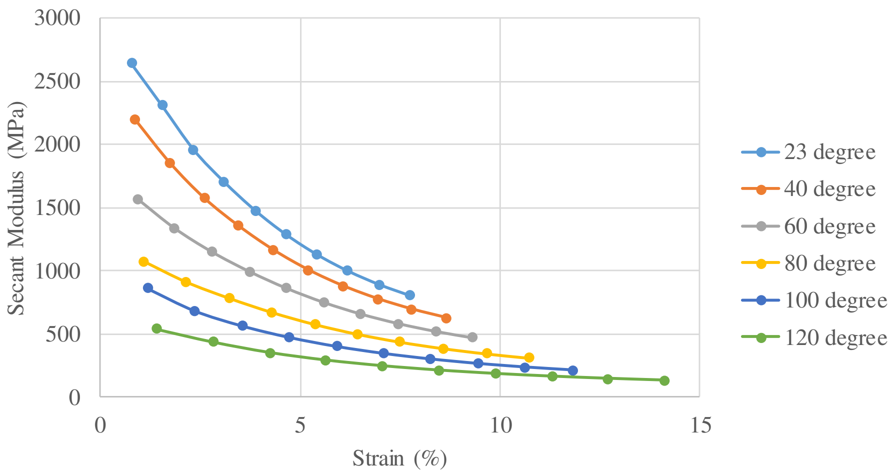

Figure 4.26: The secant modulus of the POM (copolymer) as a function of strain and temperature (°C) [185].

The reasons for each of the calibrations presented in this section were discussed before. In the next section, the best calibration in terms of the accuracy of the force prediction in the FEA of FSISF will be introduced.

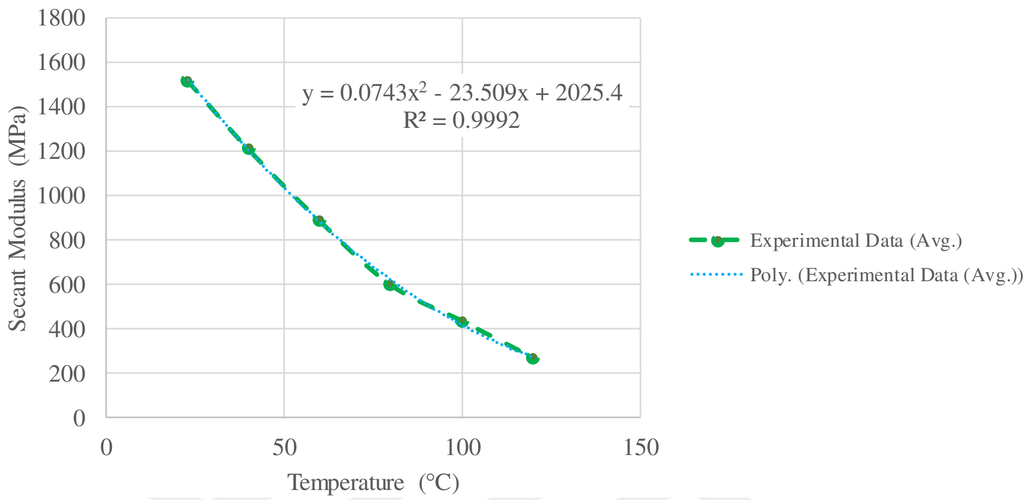

Figure 4.27: The average E (secant modulus) as a function of temperature

4.3.5 Selection of the constitutive material model

The Two-Layer Viscoplastic (TLV) model is available with Abaqus standard (implicit). Initial investigations show that a very fine mesh (0.2 to 0.7 mm) is required for implicit simulation of the ISF of the POM sheet. In addition, a very small time-increment (with the order of -4 to -5) is required. Therefore, a single simulation of a full FSISF process by using Abaqus-Implicit on the available computer would take a minimum of 22 days (not only based on calculations but according to the experience), which is not reasonable. Moreover, calibration of the model for elevated temperatures requires several tests. The calibration at elevated temperatures is also numerically troublesome. Therefore, the application of the TLV model within an implicit FEA is dismissed. The advanced Parallel Rheological Framework (PRF) model, which is calibrated here for room temperature, requires repeating all the tests at several higher temperatures and rates to calibrate the model for FEA of FSISF. Moreover, according to the author’s experience and as suggested by the literature, the application of the PRF model is numerically far more expensive as compared to the TN model [177]. More specifically, performing the same FSISF process by adopting PRF and TN models showed that the latter is at least three times faster than the former. In addition, the calibration of the TN model for elevated temperatures can be managed with far fewer test data as presented here. As stated before, the main focus of this chapter is to establish an FEA framework that provides fairly accurate results in a highly efficient way in terms of the simulation cost (time and hardware). Therefore, the application of the TN model within an explicit simulation was further investigated. Figure 4.28 shows the results for simulation of test 19[1] (von Mises stress and displacement along z-direction).

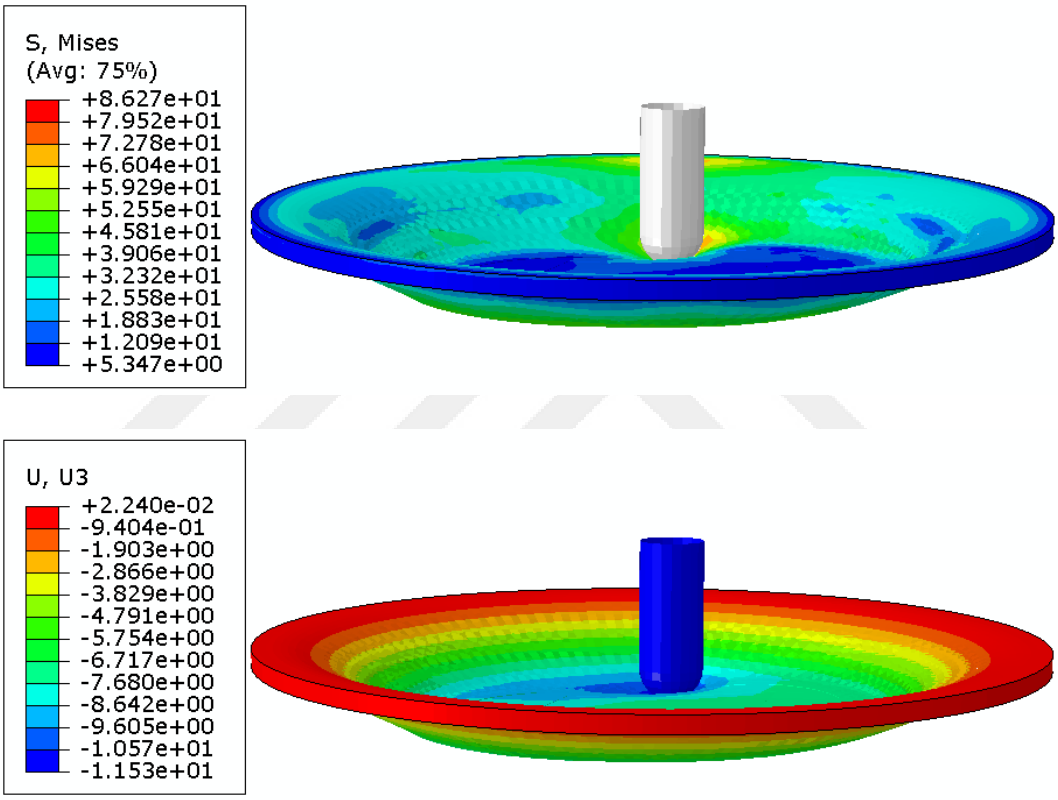

Figure 4.28: von Mises stress (top) and displacement along z-direction (bottom) in FEA of ISF test 19 by implementing TN material model.

For this simulation, the circular sheet of 90 mm in dimeter and 2 mm in thickness was discretized by using 29590 C3D8RT solid elements with hourglass enhancement (four elements along thickness). Figure 4.29 shows the meshing, back plate, and the forming tool (considered analytically solid). The meshing strategies will be further discussed in the coming sections. The simulation of 49.4 s of the ISF process took 523 min (8.72 hours) on an ordinary laptop (single Intel(R) Core i5 CPU @ 2.70GHz and 8 GB RAM)[2].

[1] Tool Diameter: 8 mm; Step Size: 1.2 mm; Feed Rate: 2300 mm/min; Spindle Speed: 0 rpm.
[2] All the simulations presented in this chapter are performed on the same computer.

This shows that the FEA strategy including defining the geometry, discretizing approach, boundary conditions, mass scaling (100,000 to 500,000), and selection of the material model has been relatively successful in providing an efficient FEA in terms of the simulation costs (time and hardware). However, by scrutinizing the results, some defects were observed as shown in Figure 4.30. A mesh distortion is evident on the top surface of the sheet as a result of contact with tool. Though such mesh distortion could be avoided by implementing smaller mesh and mass scale factor, these remedies directly result in significantly longer simulation. As the main objective of this chapter is to provide a framework for an accurate FEA with affordable simulation costs, the application of the advance (and relatively efficient) TN model is omitted through the coming sections, and the JC model will be implemented instead.

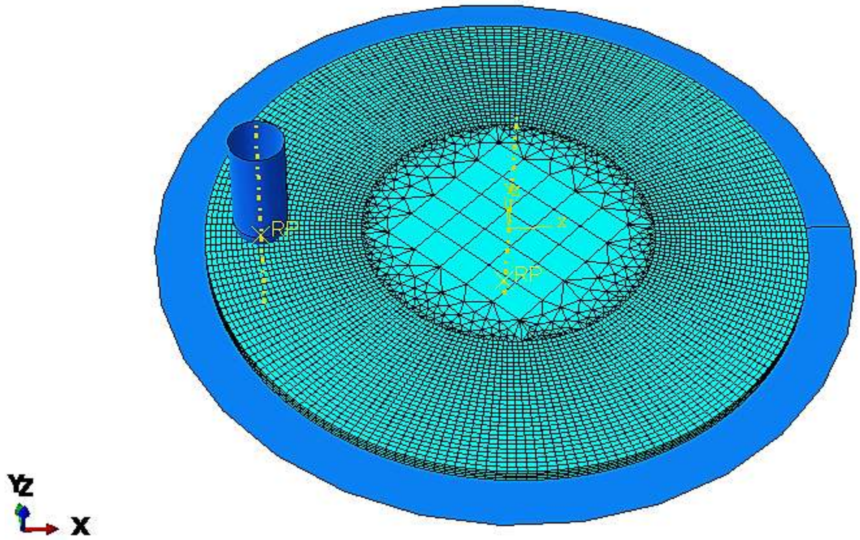

Figure 4.29: The meshing, back-plate, and the forming tool in FEA of ISF test 19.

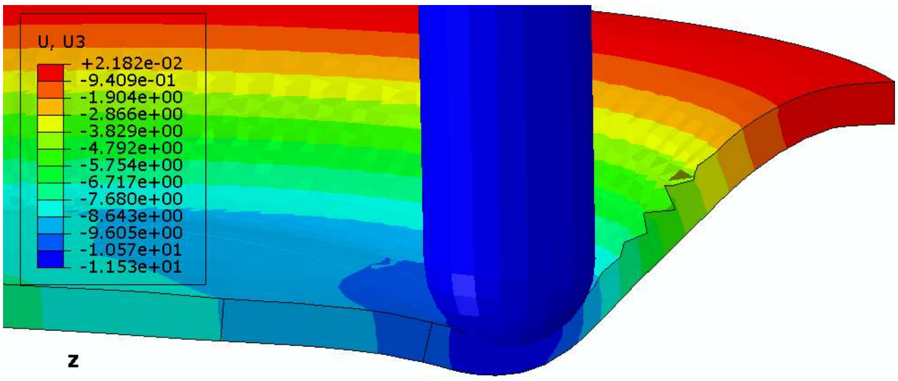

Figure 4.30: A cross-section view of the deformed specimen (displacement along tool direction) in FEA of ISF test 19.

4.4 Meshing strategies

Meshing strategy has a significant effect on both the accuracy and efficiency of the simulation. More specifically, elements could be highly distorted under significant plastic deformation as was observed in the case of the TN model of relatively large element size and large mass scaling factor. Even if the majority of the elements in the sheet have acceptable size, but a very limited number of elements (even a single element) have a significantly smaller size, it would dramatically increase the simulation time cost. This is because the stable time increment is calculated based on the smallest element in the simulation. For example, meshing techniques presented in Figures 4.35 and 4.36 are examples of meshing with high size variance with elements of significantly smaller size in the central area, but with 0% elements with a warning. Apart from the number of elements, which directly affects the simulation cost, the quality of the meshes can be partially evaluated by using the "Verify Mesh" tool in Abaqus (to see the percentage of the potentially problematic elements). In each of the following figures, the number of the elements is provided along with the percentage of the potentially problematic elements. In this section, different meshing techniques are presented and investigated as follows.

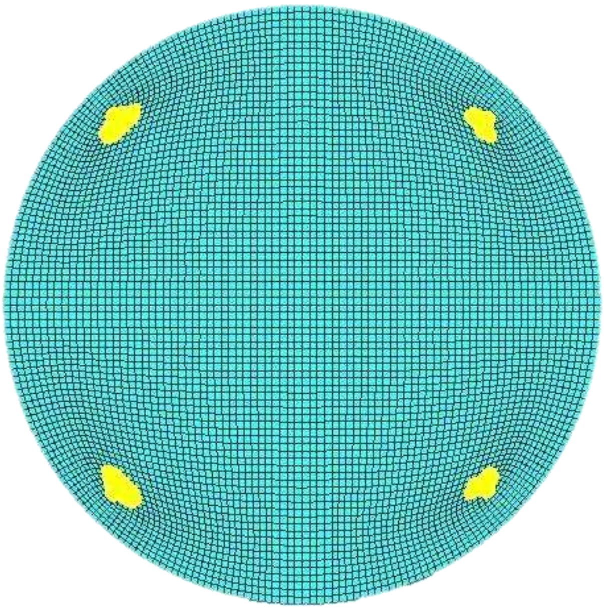

Figure 4.31: Meshing technique No. 1.1 by using a circular shape sheet (four layers along thickness; elements #:25736; elements with a warning: 0.79%).

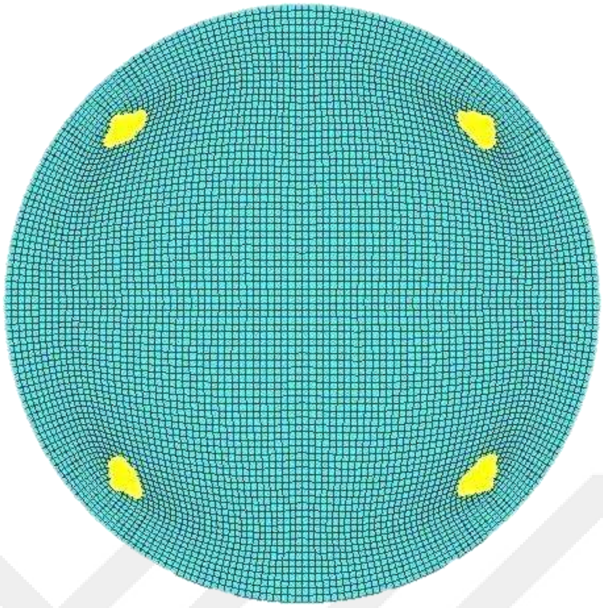

Figure 4.32: Meshing technique No. 1.2 by using a circular shape sheet (four layers along thickness; elements #:27296; elements with a warning: 0.87%).

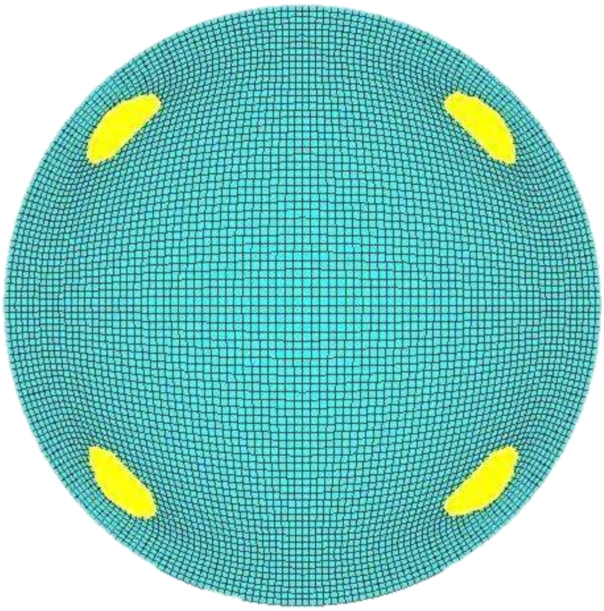

Figure 4.33: Meshing technique No. 1.3 by using a circular shape sheet (four layers along thickness; elements #:25216; elements with a warning: 3.66%).

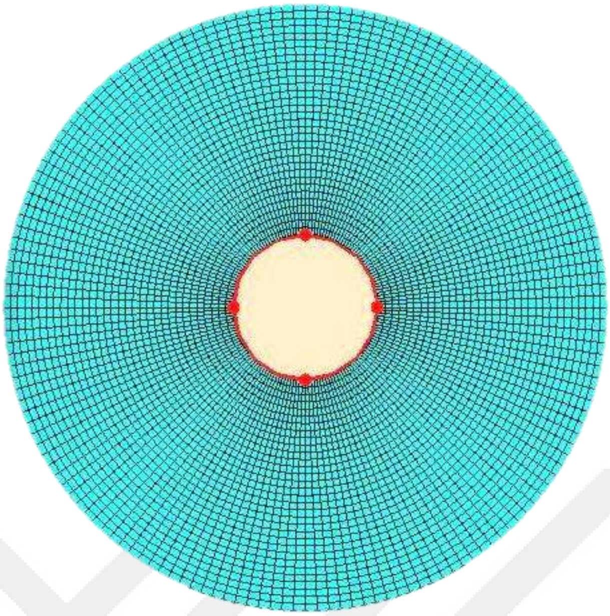

Figure 4.34: Meshing technique No. 2 by using a circular shape sheet (structured mesh is not feasible at the center).

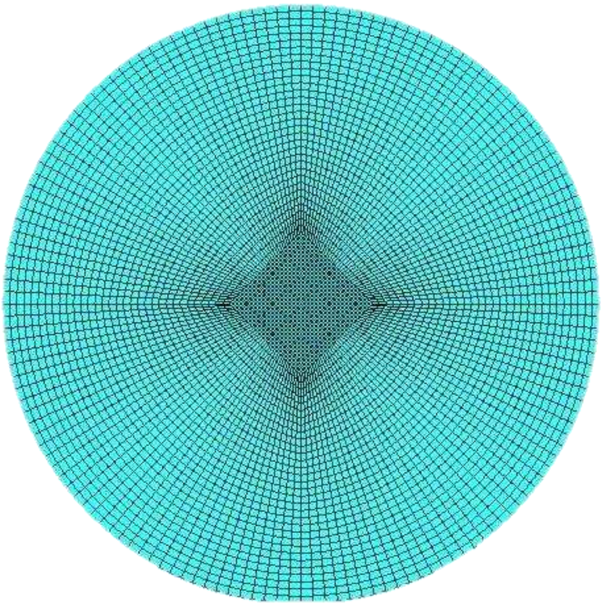

Figure 4.35: Meshing technique No. 3 by using a circular shape sheet (four layers along thickness; elements #:25232; elements with a warning: 0%).

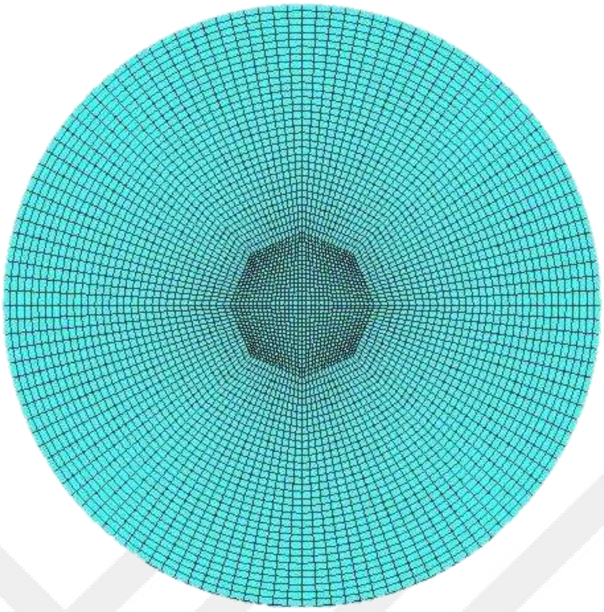

Figure 4.36: Meshing technique No. 4 by using a circular shape sheet (two layers along thickness; elements #:10240; elements with a warning: 0%).

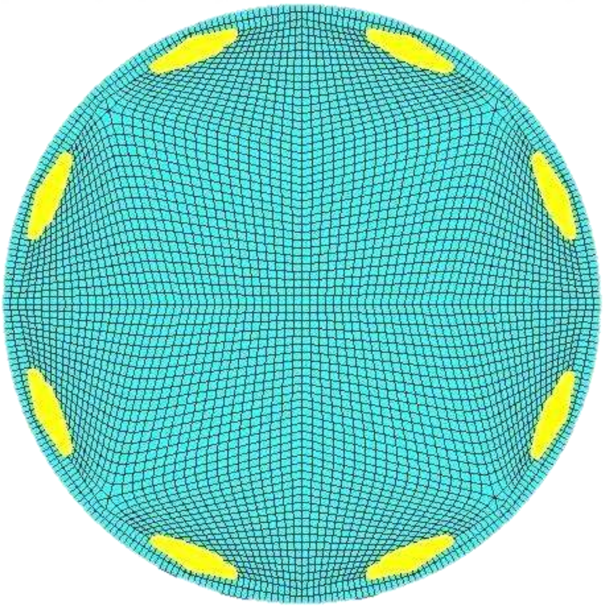

Figure 4.37: Meshing technique No. 5 by using a circular shape sheet (two layers along thickness; elements #:9288; elements with a warning: 5.78%).

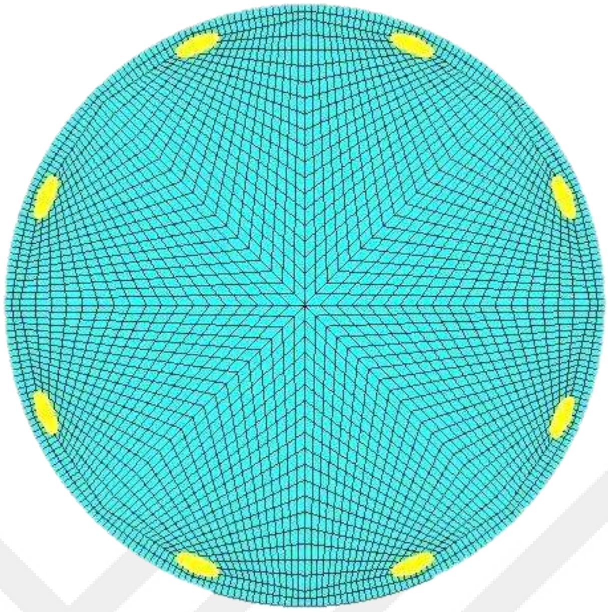

Figure 4.38: Meshing technique No. 6 by using a circular shape sheet (two layers along thickness; elements #:6416; elements with a warning: 1.50%).

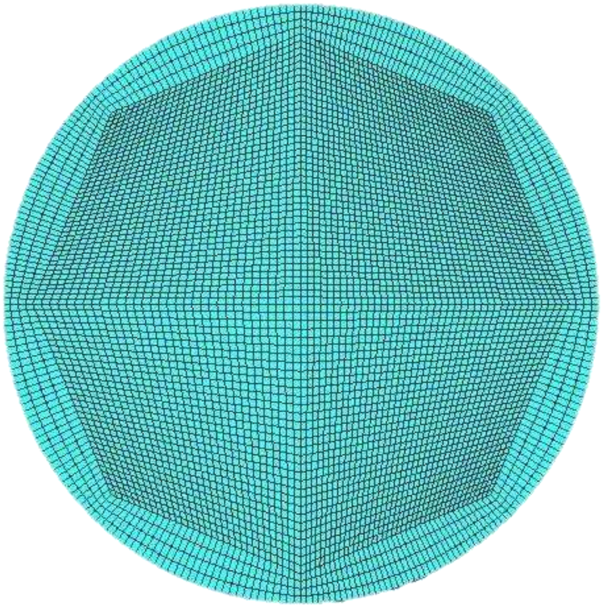

Figure 4.39: Meshing technique No. 7 by using a circular shape sheet (four layers along thickness; elements #:25344; elements with a warning: 0%).

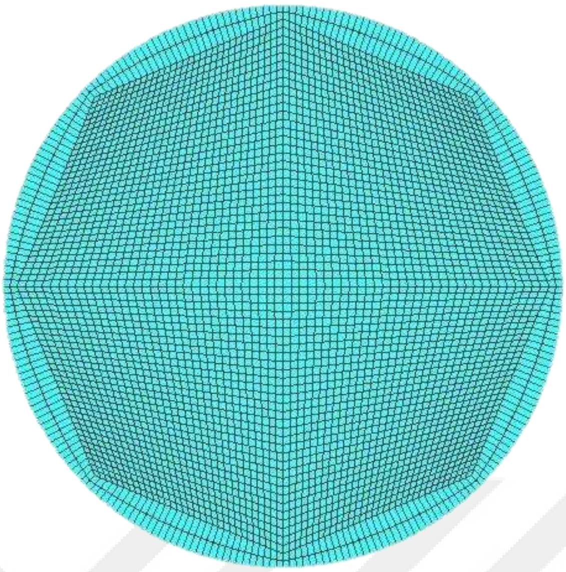

Figure 4.40: Meshing technique No. 8 by using a circular shape sheet (four layers along thickness; elements #:18432; elements with a warning: 0%).

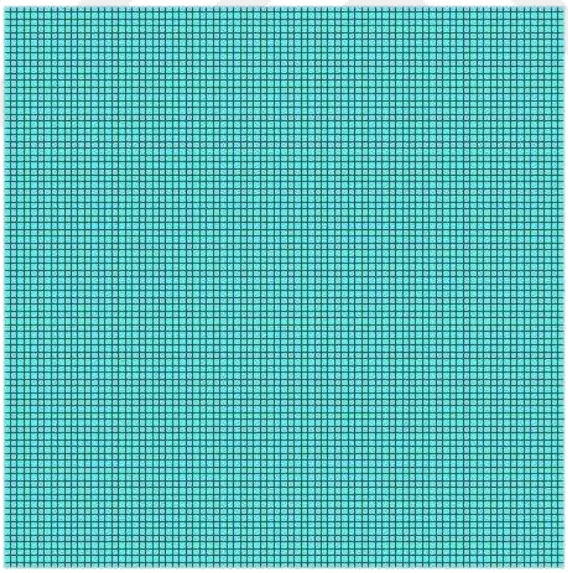

Figure 4.41: Meshing technique No. 9 by using a rectangular standard shape sheet (four layers along thickness; elements #:27556; elements with a warning: 0%).

Figure 4.40 shows ideal meshing with zero potentially problematic elements and elements of very small variation in size. The elements of significantly larger size are located in the clamping area, which is far from the forming region; therefore, this region is not mesh-sensitive. By taking this approach, the number of elements is significantly reduced. This reduction is about 33% as compared to a uniform standard structured meshing of full sheet size (as represented by Figure 4.41). However, this meshing strategy has minor deficiencies as well. One is that the mesh size gets slightly larger towards the center of the circle, the region where partially embodies the forming area. The other disadvantage is that if a finer mesh is required in the forming area, some elements at the corners will be prone to significant distortions. Therefore, other meshing strategies were developed as follows. The meshing strategy represented in Figure 4.42 (half of the sheet is presented for the sake of better visibility) is specifically applicable for sell elements, not solid elements (due to some technical limitations in Abaqus). The number of shell elements across the sheet is 7840 and the average size of the elements in the forming region is 0.5×1.32 mm. The advantage of this meshing strategy is that the size of elements reduces by moving from the periphery towards the center of the sheet within the forming area. This characteristic reduces the chance of elements distortion under severe plastic deformation. However, at the central region that undergoes no plastic deformation (excreted by the forming tool), the size of elements is significantly larger.

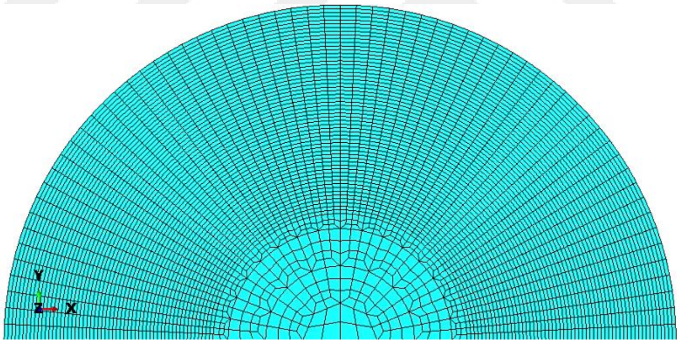

Figure 4.42: The optimum meshing strategy when implementing shell elements.

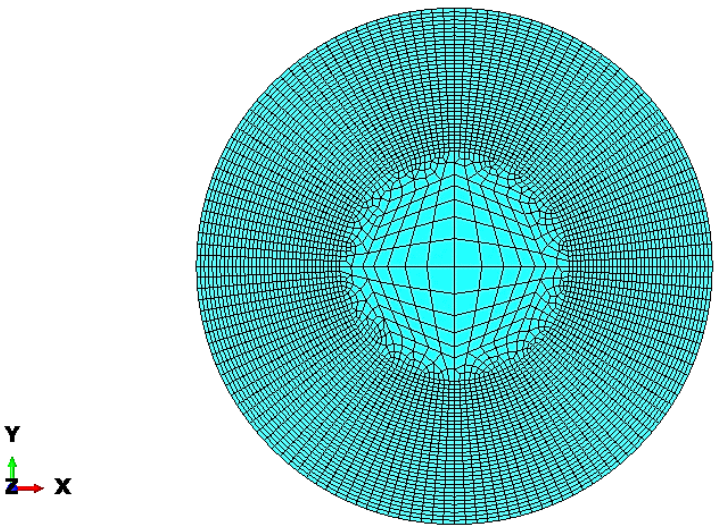

Figure 4.43: The optimum meshing strategy when implementing solid elements.

Figure 4.43 presents the optimum meshing strategy when implementing solid elements. A similar approach to the optimum meshing with shell element is taken, except that due to some technical limitations in Abaqus, a similarly structured meshing at the center is not possible with solid elements. The sheet was discretized with 22604 solid elements (four elements along the sheet thickness).

4.5 FSISF tool definition

Generally, two options are available for the definition of the tool, namely analytically rigid tool and solid tool with rigid constraint. The third option is to define the tool as a deformable part. However, considering the relative stiffness of the POM sheet to that of the WC tool, this option is dismissed as it significantly increases the simulation time with no benefit. Considering solid tools with rigid constraint, the full size of the tool or scaled tool size (along its length) could be employed. Each option is investigated in this section in terms of its effects on the accuracy of the results (specifically, the sheet temperature), and the simulation cost (time). For the sake of comparison, FSISF test 26[3] was simulated by using each of the forgoing tool definitions, while the rest of the simulation parameters were kept unchanged. Before presenting the results, the application of the scaled rigid-solid tool is briefly discussed here.

The objective of scaling the tool is to reduce the number of elements, increase the time-efficiency while preserving the accuracy of the simulation. In this section, a similar approach to Wang et al. [186] is taken, except that a different scale factor was applied to the shank of the tool. Moreover, no virtual speed was applied to avoid an undesirable effect on rate-sensitive sheet material behavior. As a result, there is no need to scale the convection coefficient. In addition, numerically more efficient discretization method and element type was employed for the tool (C3D8T versus C3D10MT). Therefore, the shank of the tool was scaled down along its length by the factor of 1/20, while the lower narrow section of the tool was kept unchanged. Therefore, the original material properties of the WC were assigned to the lower narrow section of the tool, while scale factors of 1/20 and 20 were applied to the conductivity and density of the scaled tool shank, respectively. Figure 4.44 provides a comparison between the full-size and scaled tools. Figure 4.45

[3] Tool Dimeter: 6 mm; Step Size: 0.8 mm; Feed Rate: 3200 mm/min; Spindle Speed: 1400 rpm.

shows further details of the discretization of the tools. Full-size and scaled tools were meshed by 3688, and 2624 elements, respectively. In both cases, the sheet was discretized by using 5852 S4RT shell elements. In both cases, a similar calibration of the JC constitutive model was adopted. Figures 4.46 to 4.49 provide a comparison between FEA results by employing full-size and scaled tools.

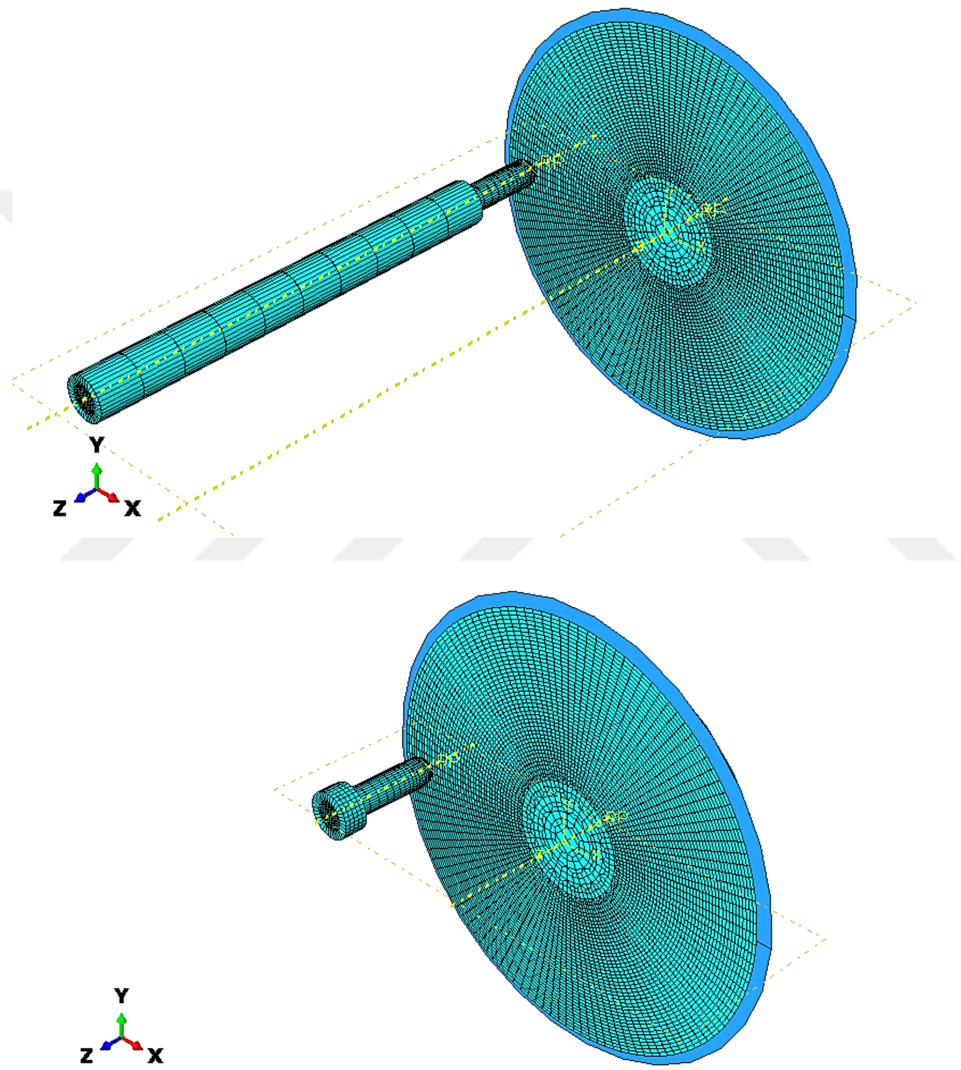

Figure 4.44: The geometries of the simulation with a full-size tool (top), and a scaled tool (bottom).

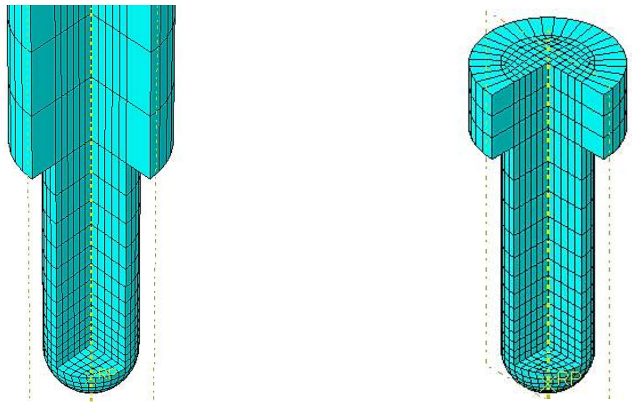

Figure 4.45: The discretization of the full-size tool (left) and the scaled tool (right).

As evident from Figures 4.46 to 4.49, no significant difference in FEA outcomes is present because of employing either a full-size tool or a scaled tool. Interestingly, simulations of the 40 s of the process by using full-size and scaled tools show no significant difference in terms of the time cost. Both simulations last for about 14 hours by implementing a mass scale factor of 1000.

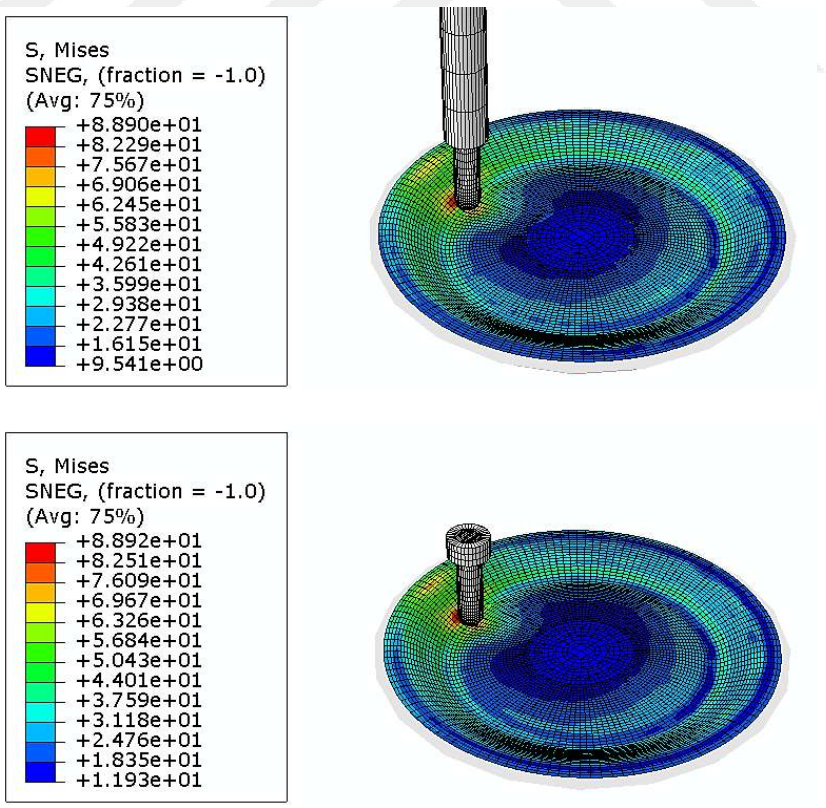

Figure 4.46: von Mises stress in FEA of FSISF test 26 by using full-size (top) and scaled (bottom) tools.

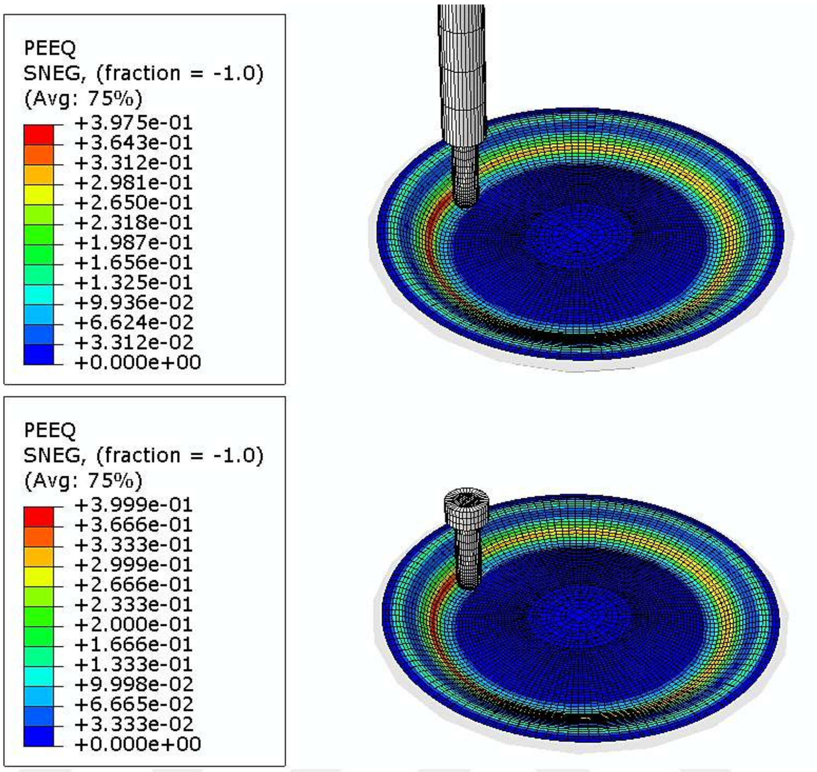

Figure 4.47: Equivalent plastic strain in FEA of FSISF test 26 by using full-size (top) and scaled (bottom) tools.

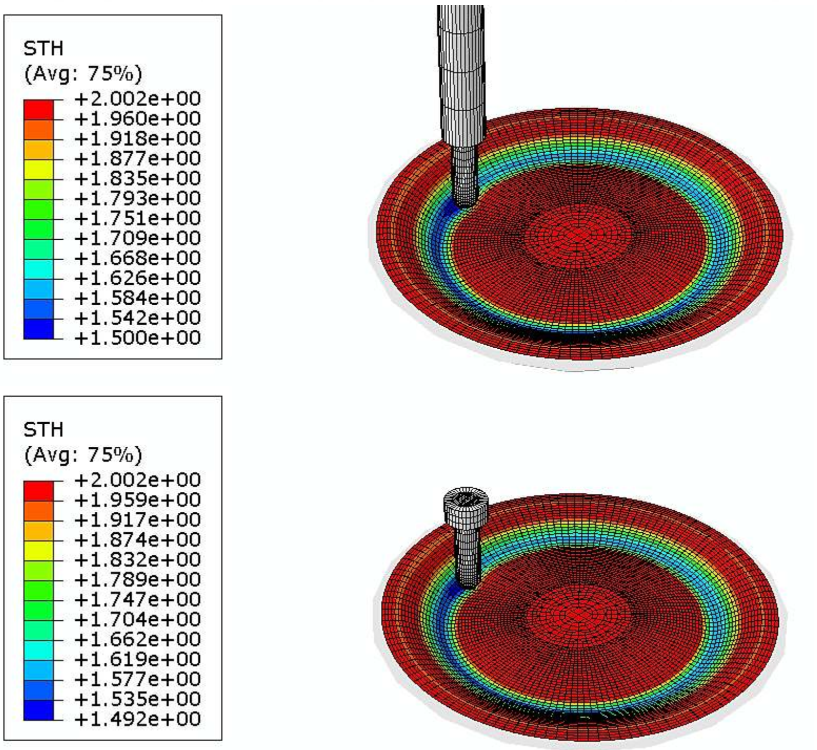

Figure 4.48: Sheet thickness in FEA of FSISF test 26 by using full-size (top) and scaled (bottom) tools.

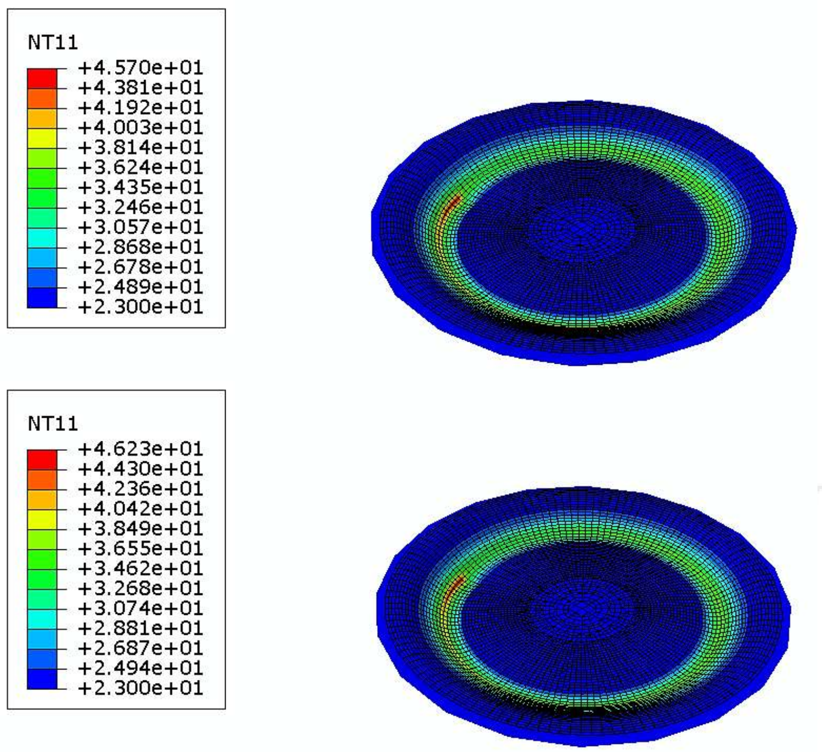

Figure 4.49: Surface temperature in FEA of FSISF test 26 by using full-size (top) and scaled (bottom) tools.

It is also worth mentioning that the maximum kinetic energy in the previous simulations was about 16860 mJ, while the maximum total energy of the system was about 1.27e6 mJ. It means that the kinetic energy of the system (due to the mass scaling) was about 1.33% of the total energy of the system. Therefore, a larger mass-scaling factor could be used in favor of reducing the simulation cost (time). The next simulation was performed by using an analytically rigid tool. It is noteworthy that in this case, a thermal capacitance must be properly defined for the tool. The results are shown in Figure 4.50. As evident from this figure, no significant difference is present in the FEA results by employing the full-size tool and the analytically rigid tool. However, the simulation time was reduced from 14 to approximately 11 hours, which translates to an approximately 20% reduction in simulation cost (time). For all simulations by using shell elements, 5 to 7 integration points were assigned along the sheet thickness. In comparative simulations, the same number of integration points was assigned.

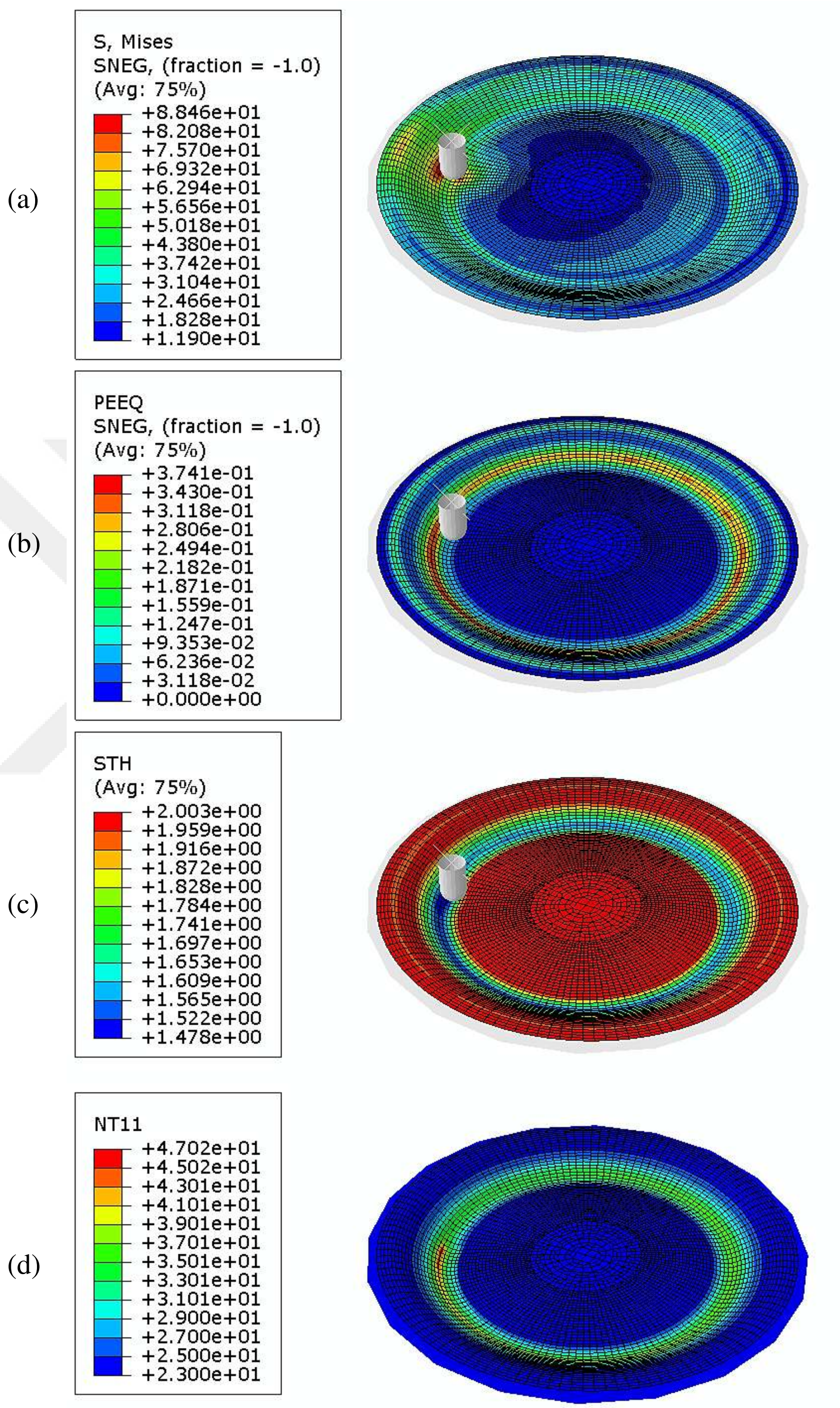

Figure 4.50: The results of FEA of FSISF test 26 by using an analytically rigid tool (MSF: 1000): von Mises Stress (a), equivalent plastic strain (b), sheet thickness (c), and surface temperature (d).

It is noteworthy that the maximum kinetic energy of the system, in this case, was approximately 51mJ, while the maximum total energy of the system was 606483 mJ. It means that the kinetic energy of the system (due to the mass scaling) was about 0.008% of the total energy of the system, which is negligible. Therefore, a significantly larger mass-scaling factor (MSF) could be used in favor of reducing the simulation cost (time). This assumption was investigated by performing a similar simulation with a significantly larger mass-scaling factor (MSF) of 50,000 (50 times larger than before). The results are presented in Figure 4.52. As evident from this figure, no significant difference is present in the FEA results by employing a scale factor of 50,000 (as compared to the previous value of 1000). Interestingly, the simulation time was significantly reduced to approximately 2 hours, which translates to reductions in simulation time by 450% and 600% with respect to the previous simulation by adopting an analytically rigid tool, and the solid tools (with MSF of 1000), respectively. Figure 4.51 shows the ratio of the kinematic to the total energy of the system as a function of time in the last simulations. As it is evident from this figure, the kinetic energy of the system (due to the mass scaling) is still negligible. To summarize this section, an analytically rigid tool (along with a relatively large mass-scaling factor) can be employed for the FEA of the FSISF process to significantly reduce the simulation cost (time), whereas the accuracy of the simulation is preserved.

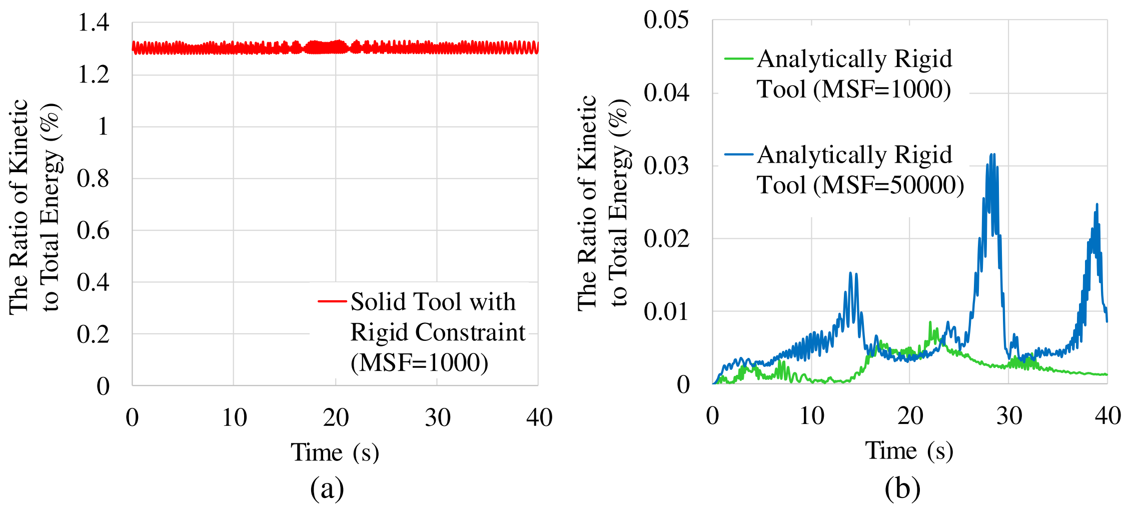

Figure 4.51: The ratio of the kinematic to the total energy of the system in FEA by employing a solid tool with rigid constraint (a), and an analytically rigid tool (b).

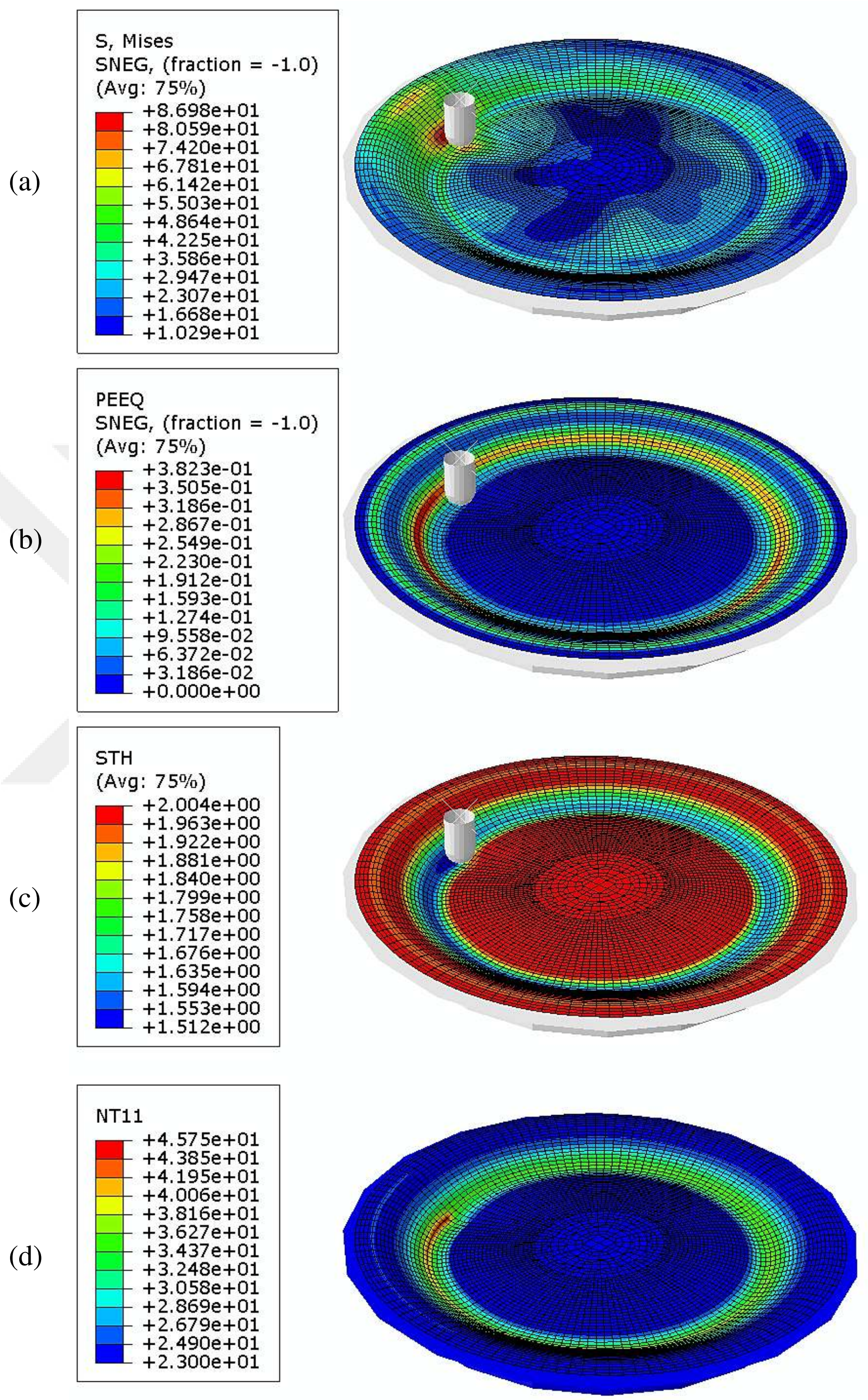

Figure 4.52: The results of FEA of FSISF test 26 by using an analytically rigid tool (MSF: 50000): von Mises Stress (a), equivalent plastic strain (b), sheet thickness (c), and surface temperature (d).

4.6 Discussion on element type, element size, and mass scaling

In the previous section, the effect of the mass scaling on simulation cost (time) and results was investigated by using shell elements. Here, the FEA of FSISF test 19 is simulated to investigate the effects of element types, namely solid element (C3D8RT) and shell element (S4RT). In both simulations, the average seed size (mesh size) of 1.4 mm and mass scale factor of 1000 is adopted along with the same calibration of the JC material model (other simulation parameters are the same). The results in terms of forming force are compared in Figure 4.53.

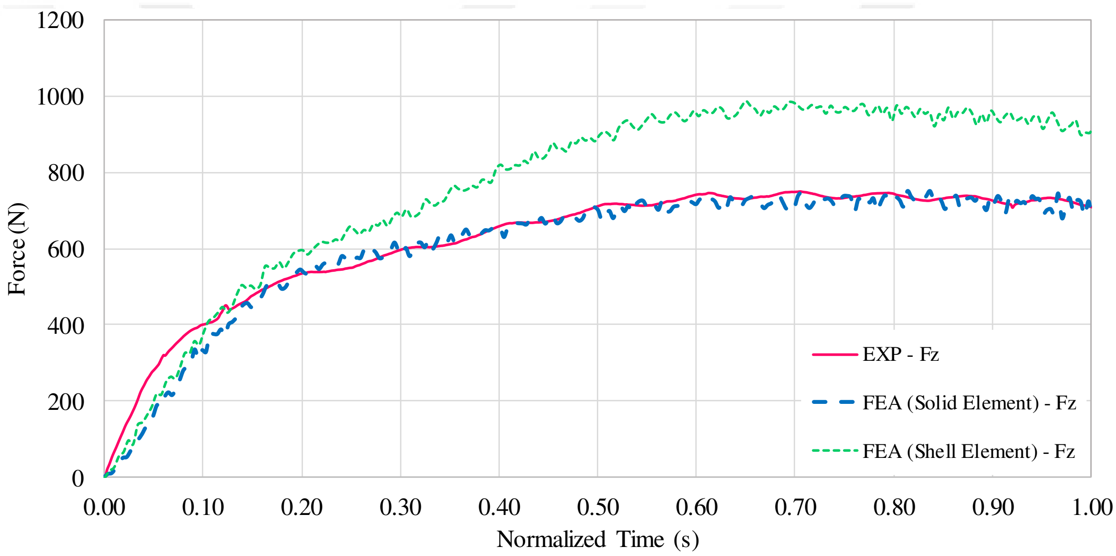

Figure 4.53: Force in FEA of ISF Test 19 using solid and shell elements.

As it is evident from the above figure, the force predicted by using shell elements is significantly overestimated as compared to the experimental measurement. However, the predicted force by using solid elements is in perfect agreement with the experimentally measured force. It is also noteworthy that the simulation took 10.5 and 20 hours by using the shell and solid elements, respectively. Therefore, the application of solid elements imposes an increase of approximately 100% in simulation cost (time).

The effect of the mass scaling and mesh size on the time cost of an explicit FEA of ISF was also investigated. Adopting solid elements (C3D8RT), the mass scaling was increased from 10^3 to 10^4 and 10^5. As a result, the kinetic energy of the system remained negligible as compared to the total energy of the system. However, the time cost of the simulation was reduced from about 20 hours to about 6.5 hours (MSF: 10^4) and 1.7 hours

(MSF: 10^5), which translates to approximately 208%, and a 1076% reduction in simulation cost (time). Figure 4.54 provides a comparison of the effect of the mass-scaling factor (MSF) on the predicted force. As it is evident from this figure, increasing the MSF merely increases noise in the predicted normal force component, and has no significant effect on the magnitude of the force. Figure 4.54 also shows a good agreement between planar force components measured experimentally and those of predicted components acquired by adopting an MSF of 10^3.

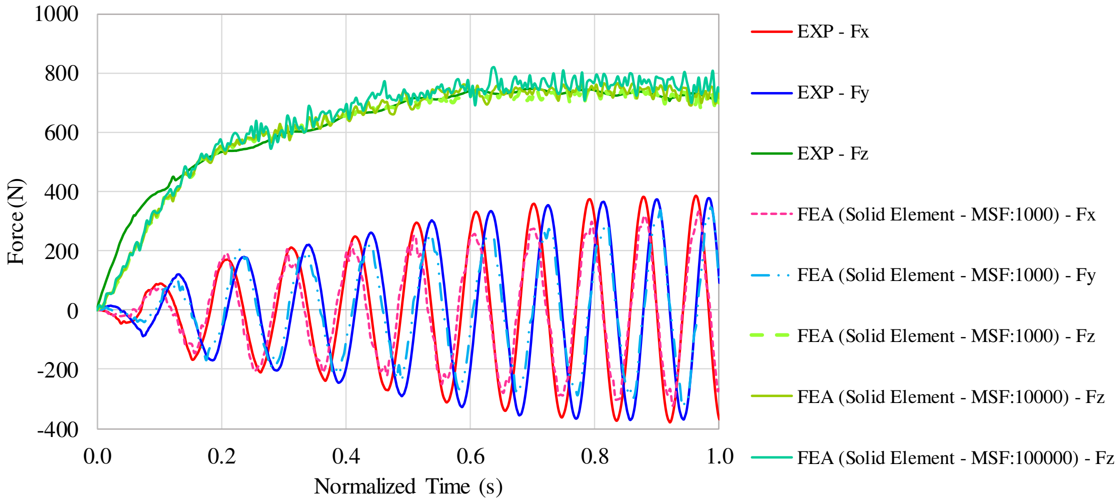

Figure 4.54: The effect of mass scaling on forming force in explicit FEA of ISF test 19.

It is worth mentioning that the above-discussed simulation was performed by discretizing the full-size square sheet with 15123 elements (3 elements along thickness) of 1.4 mm size. Figures 4.55 and 4.56 provide a comparison between von Mises stress and equivalent plastic strain in simulations (~52 s of the ISF test 19) by using MSFs of 10^3, $10^{4,}$ and 10^5. As represented by these figures, no significant difference is present. It means a mass scaling of 10^4 to 10^5 can be safely used to significantly lower the simulation cost (time), while the accuracy of predictions is preserved. Such a relatively large MSF works perfectly fine in the case of test 19 with zero spindle speed and a moderate feed rate. However, such large MSFs should be adopted with more cautions in the cases of relatively high speeds.

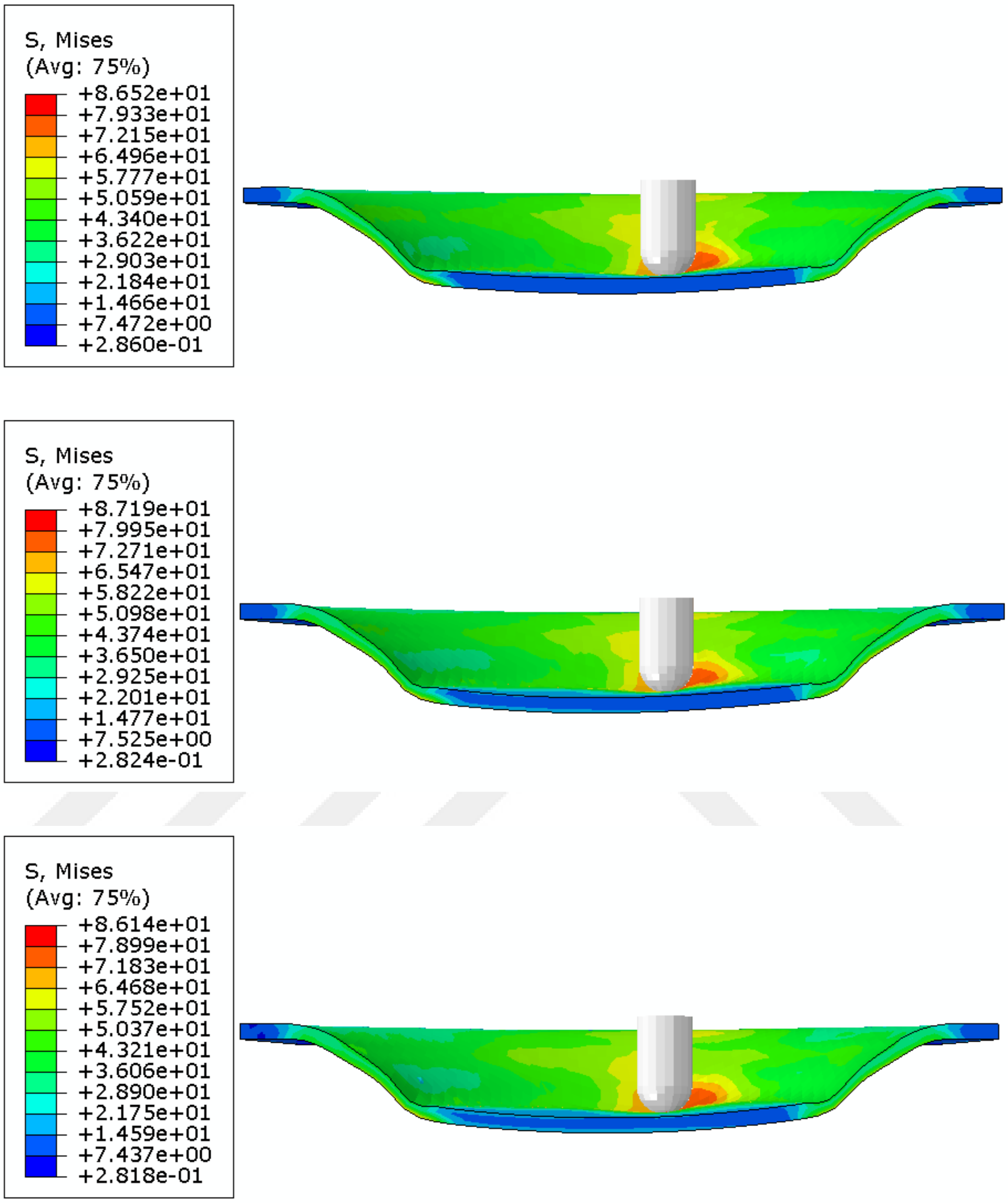

Figure 4.55: von Mises stress in simulations by using MSFs of 10^3 (top), 10^4 (middle), and 10^5 (bottom).

To investigate the effect of element size and the number of elements along the sheet thickness, the number of elements was increased from 15,120 (three elements along thickness) in the previous simulation to 40,000 (four elements along thickness). Therefore, the size of the elements was reduced by 50%, whereas the mass scaling and other parameters were kept unchanged. Therefore, the time-cost of the simulations was increased from about 2.15 hours to 8.15 hours. Shear components of the principal stresses-strains corresponding to each simulation are provided in Figures 4.57 to 4.62.

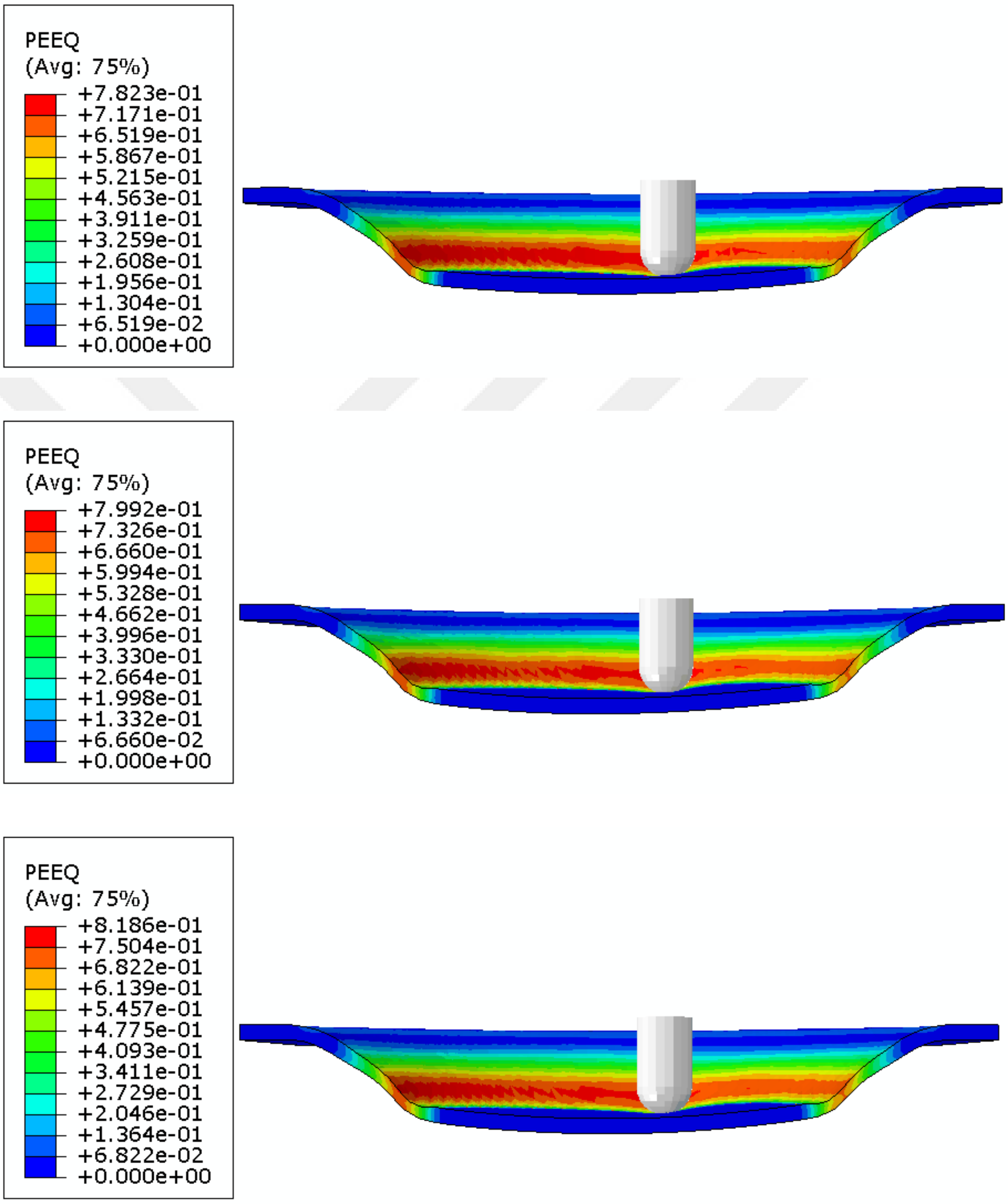

Figure 4.56: Equivalent plastic strain in simulations by using MSFs of 10^3 (top), 10^4 (middle), and 10^5 (bottom).

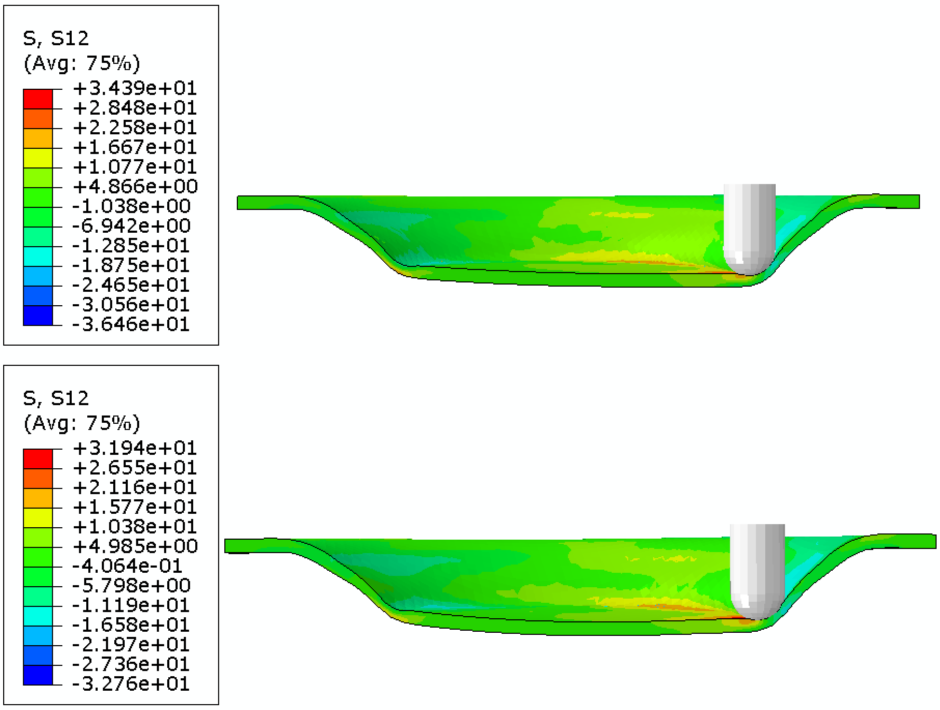

Figure 4.57: Principal stress (S12) corresponding to the FEA of ISF test 19 by employing elements of 1×1×0.5 mm^3 (top), and elements of 1.4×1.4×0.67 mm^3 (bottom).

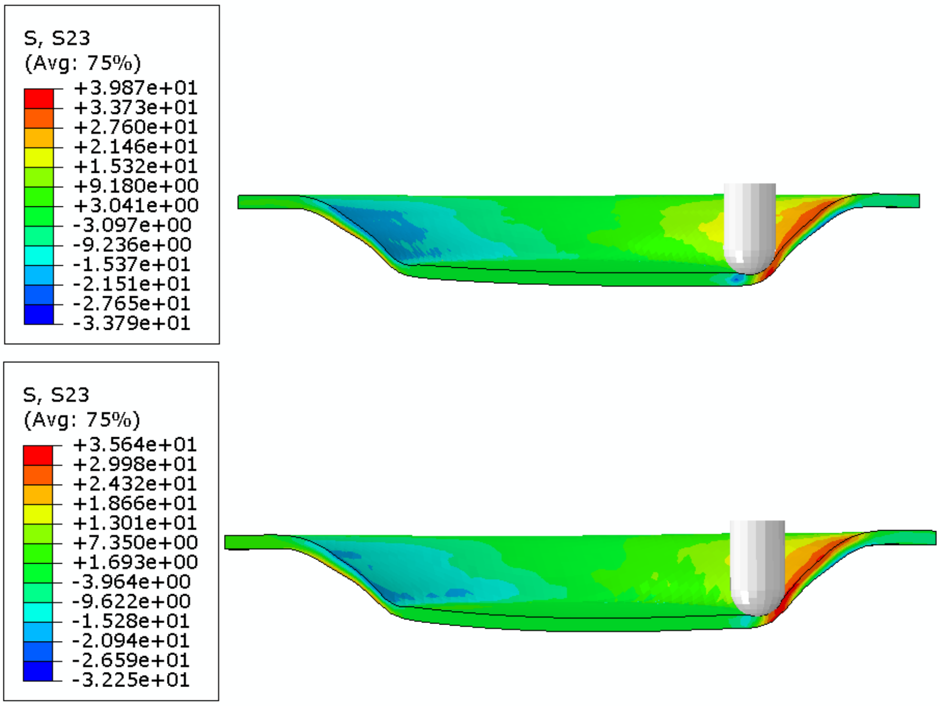

Figure 4.58: Principal stress (S23) corresponding to the FEA of ISF test 19 by employing elements of 1×1×0.5 mm^3 (top), and elements of 1.4×1.4×0.67 mm^3 (bottom).

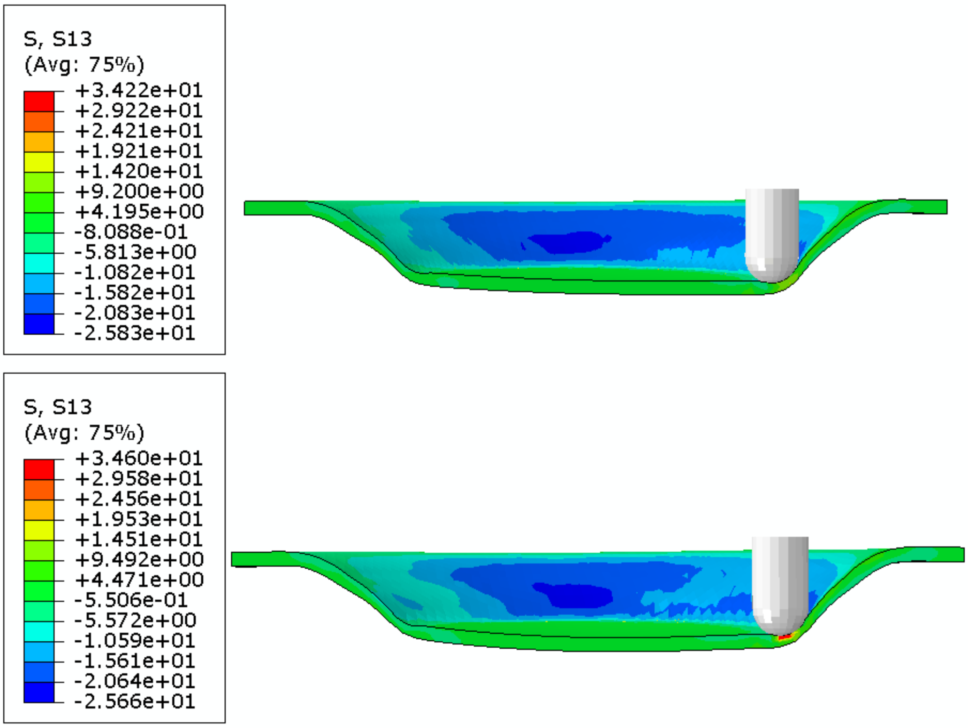

Figure 4.59: Principal stress (S13) corresponding to the FEA of ISF test 19 by employing elements of 1×1×0.5 mm^3 (top), and elements of 1.4×1.4×0.67 mm^3 (bottom).

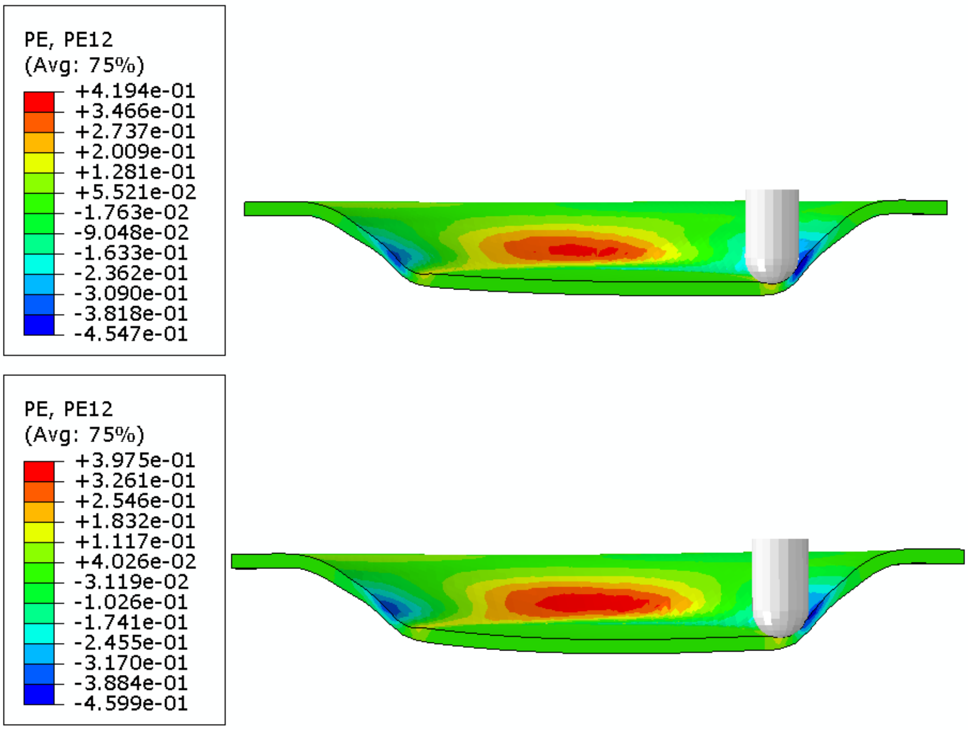

Figure 4.60: Principal plastic strain (PE12) corresponding to the FEA of ISF test 19 by employing elements of 1×1×0.5 mm^3 (top), and elements of 1.4×1.4×0.67 mm^3 (bottom).

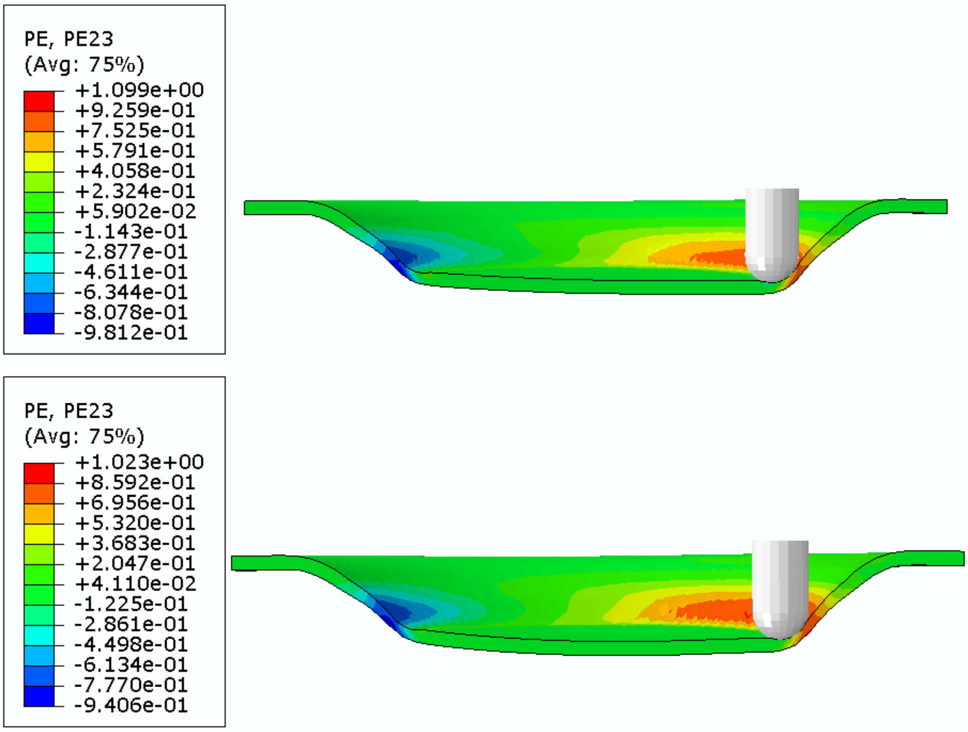

Figure 4.61: Principal plastic strain (PE23) corresponding to the FEA of ISF test 19 by employing elements of 1×1×0.5 mm^3 (top), and elements of 1.4×1.4×0.67 mm^3 (bottom).

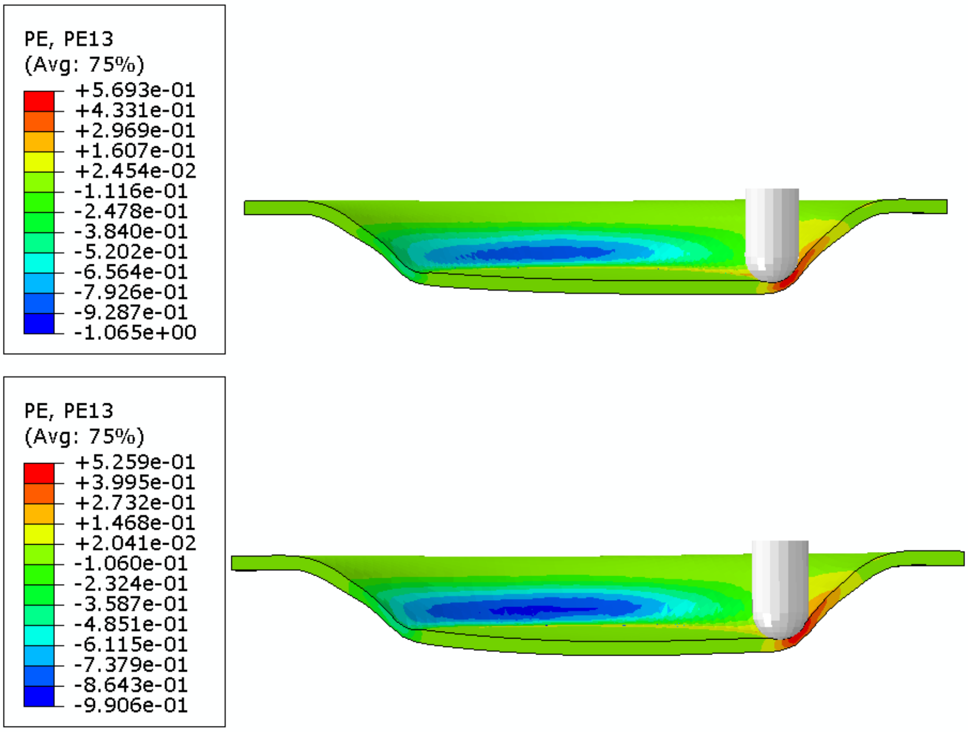

Figure 4.62: Principal plastic strain (PE13) corresponding to the FEA of ISF test 19 by employing elements of 1×1×0.5 mm^3 (top), and elements of 1.4×1.4×0.67 mm^3 (bottom).

Considering the above-presented shear stresses-strains, differences of approximately 11% and 9% in the upper limit of S12 and the lower limit of S23 are evident. Other differences are relatively insignificant. Such a difference is supposed to be more due to the number of the elements along the sheet thickness than the planar size of the elements. As frequently reported in the literature, a minimum number of 3 to 5 elements is required along the sheet thickness to properly capture the bending-unbending effects [187, 188]. Therefore, for the following simulations, the sheet is discretized by four elements along the sheet thickness (initially 2 mm). The size of elements, specifically along the direction that sheet undergoes significant plastic deformation, is assigned to be less than 1 mm (in the majority of the cases, 0.5 mm). To reduce the overall number of the elements and the simulation cost (time), only the circular part of the sheet that is fully supported (form the periphery by the sheet-clamping device) is used for discretization as shown before. By adopting this strategy, the sheet was meshed by a total number of 18432 solid elements (with four elements along the sheet thickness). This number of elements translates to less than 50% of the element numbers as compared to the previous simulation with elements of $1 \times 1 \times 0.5$ mm^3 in size, four elements along thickness, and full-size square sheet. A large MSF of 500000 was also adopted. Contrary to all the previous FEA runs, only two cores out of four cores of CPU were initially employed for parallelization (the simulation lasted for less than 6 hours). Therefore, it is concluded that parallelization with four CPU cores better serves for a low-time-cost simulation than parallelization with two CPU cores. A good agreement was found between the experimental and the predicted force. Compared to the previous FEA runs, a relatively noisier force signal was observed because of using a relatively high mass-scaling factor. However, the maximum total kinetic energy of the system remained negligible as compared to the total energy of the system. As stated before, such large MSFs should be adopted with more caution in high-speed FSISF cases.

4.7 Heat partitioning between tool and sheet

As stated before, the limited number of the available numerical studies on ISF (using metallic alloys) at elevated temperatures [72, 77, 86, 95] have not discussed the heat partitioning between tool and sheet. In a more recent investigation [186], the heat partitioning factor is simply set to the default value of the FEA package (0.5). Such deficiency may significantly undermine the reliability of the predictions. In this section, a brief review is provided on heat partitioning in problems involving friction-induced heat such as pin-on-disk, disk-brake, and rail-wheel contact problems. The objective is to find a reliable and straightforward methodology to define the heat-partitioning coefficient for a fairly accurate and low-cost simulation of the FSISF process.

In their magnificent research works on heat analysis in sliding contact, Blok [189] and Jaeger [190] proposed approximate heat partitioning relations based on the assumption of equal maximum (or average) temperature on in-contact surfaces. Heat convections from the contact interface and residual heats (e.g. on disk) are generally neglected in approximate solutions for heat partitioning. However, these approximate relations have been frequently reported to deliver accurate results versus exact solutions and experimental evidence [191–193]. Talati and Jalalifar [194], in their frequently cited research work, developed the governing transient heat equations for disk and brake pad. Considering a uniform constant contact pressure, they proposed the following equation for heat partition factor:

$$\sigma = \frac{S_d\sqrt{k_d c_d \rho_d}}{S_d\sqrt{k_d c_d \rho_d} + S_p\sqrt{k_p c_p \rho_p}} \tag{4.28}$$

Where, subscript d and p stand for disk and pad, respectively ($q_d = \sigma q$). k, c, and ρ denote heat conductivity, specific heat, and density of the materials, respectively. S_d stands for the total area of the disk or the total area of the disk swept by the pad. S_p simply represents the total area of the brake pad. Federici et al. [195], in their FEA (by using ANSYS) and experimental investigation of pin-on-disk friction test, adopted a similar heat partitioning relation to Talati and Jalalifar [194]. Therefore, they reported very good temperature predictions in pin-on-disc testing by using a low-metallic friction material sliding over cast Iron. Kennedy et al. [196] attempted to propose a straightforward and fairly accurate methodology to predict the interface temperature in a pin-on-disk sliding contact problem. To adopt proper heat partitioning factors for their FEA by using COMSOL Multiphysics, they referred to the major studies conducted based on the assumption of the equality of temperature on in-contact surfaces [192, 193, 195, 197–199]. Therefore, they proposed a heat-partitioning factor, $\alpha = \frac{q_p}{q_d}$, of the following form [196]:

$$\alpha = \frac{\frac{1}{\bar{h}_c}\left(\frac{a}{{r_0}^2}\right) + \frac{2}{k_d\sqrt{\pi(1.273 + Pe)}}}{\frac{1}{k_p}\left[\frac{4al_p}{d^2} + 1\right]} \tag{4.29}$$

Where, subscripts *p* and *d* stand for pin and disk, respectively. $\bar{h}_c$ denotes the average heat convection coefficient from the surface of the disk. r_0 represents the external diameter of the disk and *a* is the contact radius. The mean contact pressure was given by $\bar{p} = \frac{F_N}{\pi a^2}$ (F_N is the normal load). l_p and d_p represent the length and the diameter of the pin, respectively. Pe stands for Peclet Number:

$$Pe = \frac{Lv\rho c}{k} \tag{4.30}$$

Where L is the characteristic length and v is the local flow velocity. L is usually assumed equal to the half-width of the contact area (e.g. radius in circular contact) or $L = \sqrt{A/\pi}$ (A is the contact area). *k*, *c*, and *ρ* denote heat conductivity, specific heat, and density, respectively. Rowe et al. [200] experimentally investigated the frictional heating and temperature rise due to sliding contact between a hemispherical rubber pin and a calcium fluoride disk. An infra-red camera was used to measure the temperature, while the normal force, speed, and temperature rise varied in the ranges of 100-1000 mN, 250-1000 mm/s, and 3-26 °C. They concluded that in comparison to their experimental measurements, the heat partitioning models proposed by Jaeger [190] and Archard [201] provide fairly accurate predictions. The heat partitioning factor based on Jaeger [190] model is:

$$\alpha = \frac{0.849K_d\sqrt{Pe}}{0.849K_d\sqrt{Pe} + 1.064K_p} \tag{4.31}$$

The heat partitioning factor based on Archard [201] model is:

$$\alpha = \frac{0.785K_d\sqrt{Pe}}{0.785K_d\sqrt{Pe} + 0.974K_p} \tag{4.32}$$

Ertz and Knothe in their frequently cited research work [157], presented analytical and numerical solutions for the frictional heating in rail-wheel contact problem. Based on the assumption of equal temperatures on in-contact surfaces and a constant heat fellow, they proposed the following analytical relation for heat partitioning:

$$\beta = \frac{\sqrt{k_w \rho_w c_w v_w}}{\sqrt{k_w \rho_w c_w v_w} + \sqrt{k_r \rho_r c_r v_0}} \tag{4.33}$$

Where subscript *w* and *r* denote wheel and rail. $v_0 = v_r$ denotes the relative speed of the rail with respect to the contact patch that is equal to the translational speed of the wheel. $v_w = v_s + v_0$ denotes the relative speed of the wheel with respect to the contact patch that is equal to the sliding velocity of the wheel with respect to the rail, v_s, summed up with the translational speed of the wheel (v_0). They showed that for normal operating conditions in rail-wheel contact (very large Peclet numbers), the error resulted from the assumption of one-dimensional heat fellow is negligible. Therefore, predicted temperatures by using Equation 4.33 and exact numerical solutions were in good agreement. Laraqi et al. [202] proposed a 3D exact analytical solution for the prediction of the friction-induced heat flux partitioning and the rise of temperature due to sliding contact in a pin-on-disc tribometer. They showed that for Peclet numbers larger than 30, an increase in the relative velocity has no effect on the heat partition between pin and disk. Therefore, beyond the aforesaid threshold, the heat partitioning factor remains approximately constant.

In this research work, the heat-partitioning factor (HPF) is initially calculated based on Equations 4.28, 4.31, 4.32, and 4.33 for the sake of comparison. For this purpose, the analytical relations developed for the estimation of the contact area and the average relative velocities of tool and sheet (in the previous chapter) are employed. Eventually, the HPF corresponding to each FSISF test was calculated by using Equations 4.28 and 4.33, and the averaging value over the course of forming period was adopted for FEA. Figures 4.63 to 4.65 show the results for FSISF tests 3[4], 19, and 26.

[4] Tool Dimeter: 6 mm; Step Size: 0.8 mm; Feed Rate: 1400 mm/min; Spindle Speed: 4200 rpm.

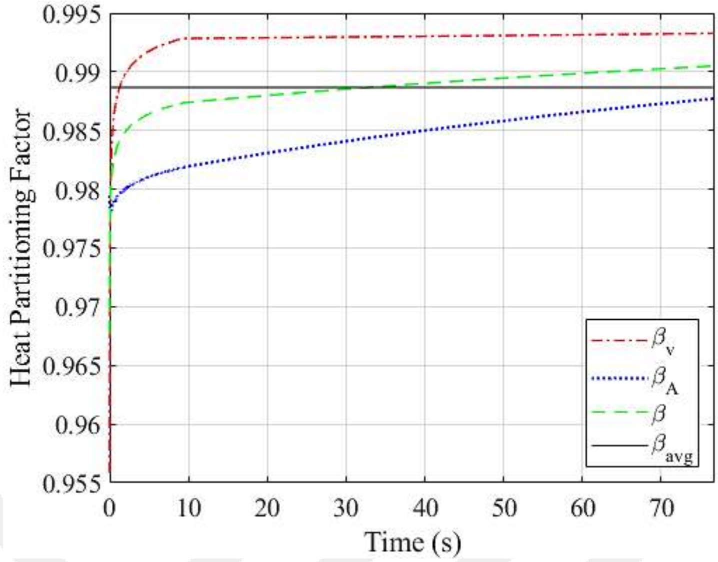

Figure 4.63: Heat partitioning factors based on different criteria in FSISF test 3.

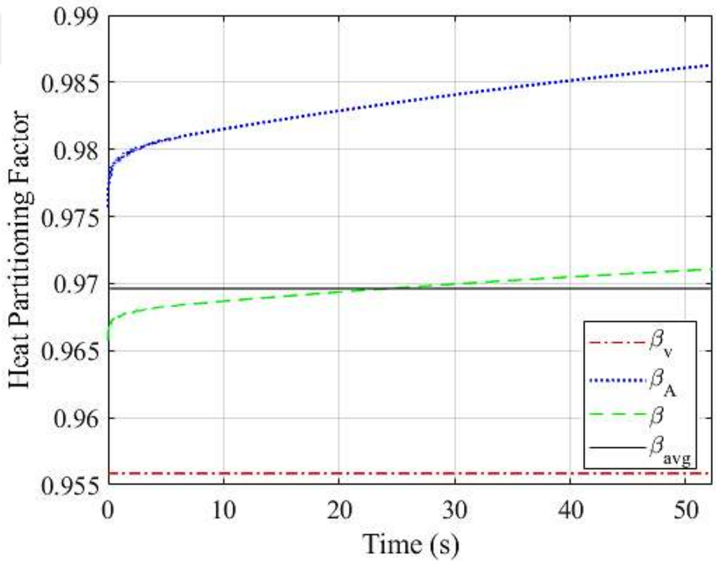

Figure 4.64: Heat partitioning factors based on different criteria in FSISF test 19.

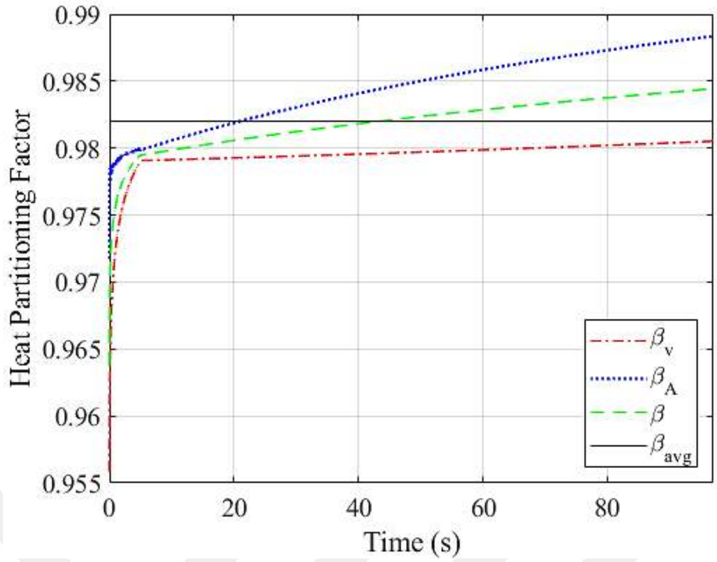

Figure 4.65: Heat partitioning factors based on different criteria in FSISF test 26.

In Figures 4.63 to 4.65, β_v and β_A correspond to the HPFs calculated based on Equations 4.33 and 4.28, respectively. β represents the average of the β_v and β_A as a function of time through the course of forming. β_{avg} is the average of β_v and β_A over the course of forming, which is adopted for FEA. It is also worth mentioning that by considering the minimum of the average contact area, Peclet numbers of 88.52 to 725.84 were calculated corresponding to the range of forming speed (500-4100 mm/min) for the FSISF process in this study. Therefore, the assumption of 1D heat flow and single-value HPF for each FSISF test is valid.

4.8 Friction coefficient: A brief discussion on the numerical investigations

The friction measurement setup is presented and discussed in chapter 2. In summary, for evaluation of the friction coefficient under the effects of elevated temperatures and normal load, tools of different diameters were employed with several pitch sizes, translational speeds, and rotational speeds. To measure the temperature and force, a pyrometer and a dynamometer were imbedded in the CNC machine. Here, an explicit FEA of a sample friction test is presented and discussed briefly. The test parameters are presented in Table 4.10.

Table 4.10: Friction test process parameters used for Explicit-Dynamic FEA simulation.

Tool Diameter (mm)	Step Size (mm)	Feed Rate (mm/min)	Spindle Speed (rpm)
9	0.4	2300	0

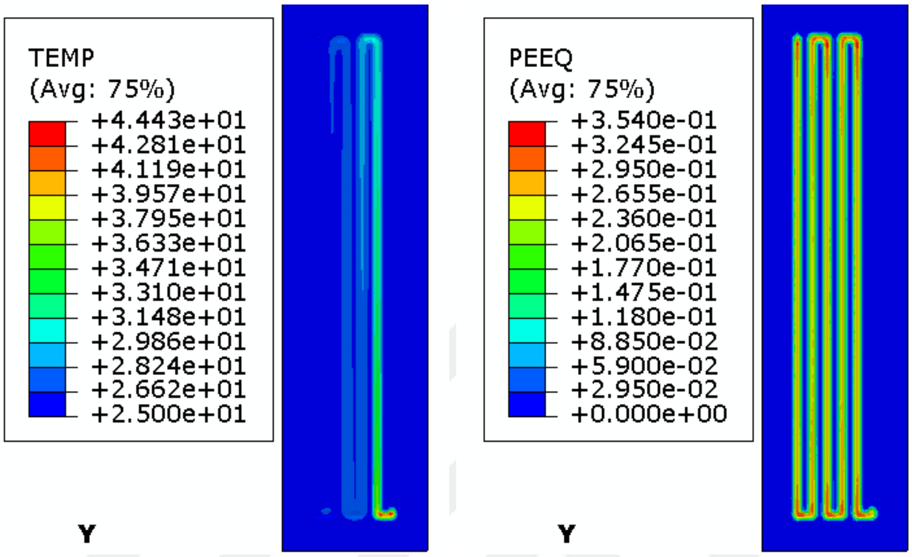

(a) (b)

Figure 4.66: Surface temperature (a) and equivalent plastic strain (b) in FEA of friction test on POM copolymer.

Figures 4.66 and 4.67 show the results of FEA (for the first 40 s of the test) and experimental surface temperature measurements by using a pyrometer as detailed in the second chapter. As evident from these figures, predicted surface temperature is in good agreement with the experimental results.

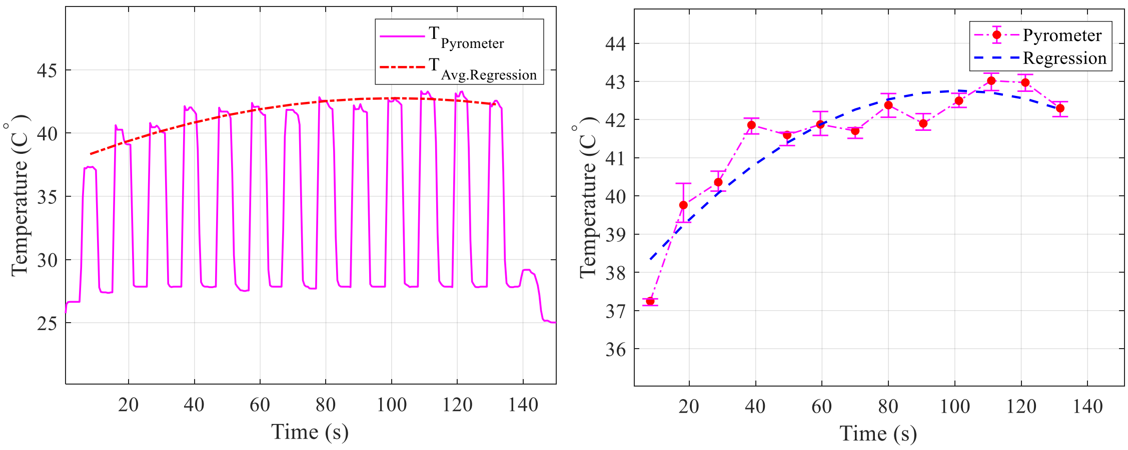

(a) (b)

Figure 4.67: Surface temperature (left: raw data – right: average tool-sheet interface temperature) recorded by pyrometer in a friction test on POM copolymer.

Figures 4.68 provides a comparison between the experimental force signal filtered by using a low-pass filter and the predicted force component by FEA in the friction test. As evident from this figure, force components are accurately predicted.

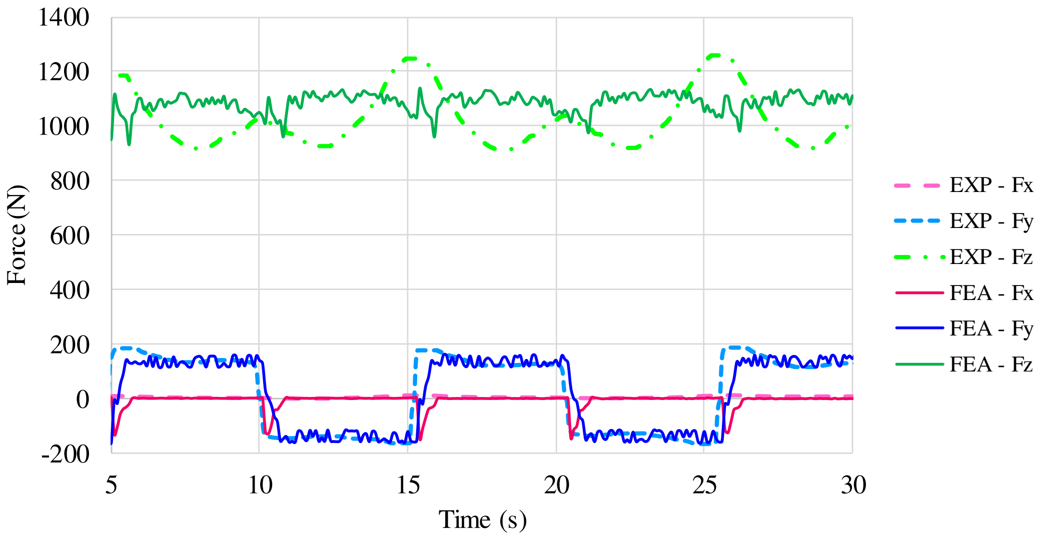

Figure 4.68: Experimental and the predicted force component by FEA in a friction test on POM copolymer.

The fluctuation of experimental force along the normal direction, as shown in Figure 4.68, is due to the sheet clamping conditions. FEA results are used to provide an estimation of Coulomb's friction coefficient under the test conditions. Therefore, the average Coulomb's friction coefficient of ~0.12 is presented in Figure 4.69.

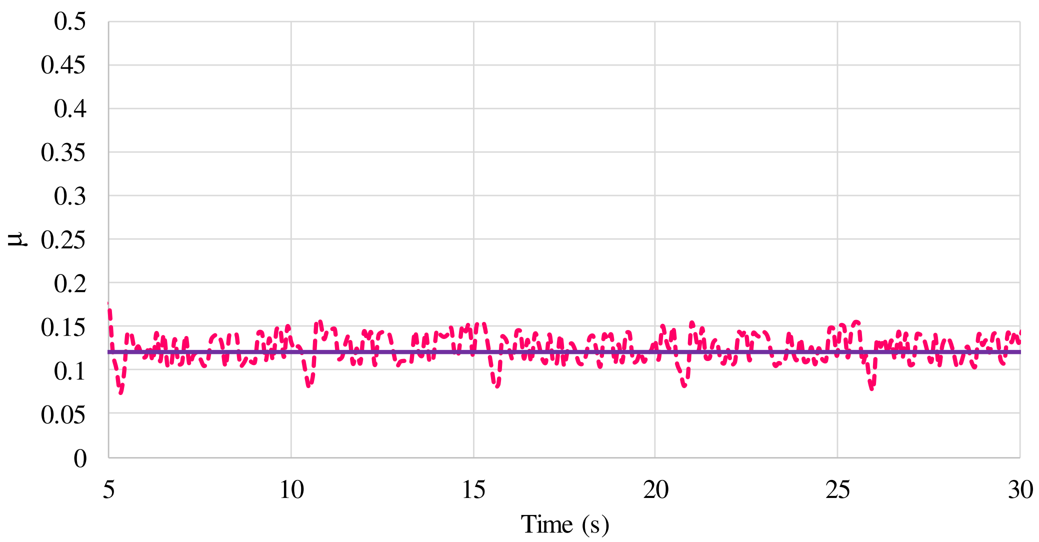

Figure 4.69: Coulomb's friction coefficient estimated for the test conditions stated in Table 4.10.

4.9 Case studies and a brief discussion on damage evolution in FEA of FSISF

Traditionally the phenomenological fracture models are calibrated by conducting FEAs validated based on experimental results of uniaxial tensile tests, notched tensile tests, plane strain tensile tests, and in-plane shear tests. Taking a similar approach, Mirnia and Shamsari [203] adopted the phenomenological modified Mohr-Coulomb (MMC3) model to investigate the ductile fracture in cold ISF of aluminum AA6061-T6 by assuming a plane stress condition. The values of triaxiality, η, and normalized load angle, $\bar{\theta}$, vary with the plastic strain during the aforesaid tests. Therefore, authors used the average values of the triaxiality and the normalized load angle in each test to calibrate the model by employing the surface fitting tool in MATLAB. This is a conventional method frequently adopted by researchers in the field of fracture [204, 205]. For example, Johnson and Cook [206] maintained that the values of the JC fracture model variables (η, $\dot{\varepsilon}^*$, θ^*) are assumed to be constant in each test, so the average values must be used when they are not constant. In such cases, a linear damage accumulation relation is used as follows:

$$D = \int_0^{\bar{\varepsilon}^p} \frac{d\bar{\varepsilon}^p}{\bar{\varepsilon}^p_{fr}(\eta.\bar{\theta})} \tag{4.34}$$

Where, $\bar{\varepsilon}^p_{fr}$ represent fracture equivalent plastic strain. By drawing η and $\bar{\theta}$ as a function of the equivalent plastic strain, $\bar{\varepsilon}^p$, Mirnia and Shamsari [203] concluded that the loading path is not proportional. They concluded that the average values of η and $\bar{\theta}$ cannot exactly describe the stress state in the calibrating tests and ISF. Therefore, using the history of η and $\bar{\theta}$ as a function of $\bar{\varepsilon}^p$, they calibrated the three constants of the MMC model by minimizing the following objective function:

$$\psi(C_1, C_2, C_3) = \sqrt{\frac{1}{n_t}\sum_{i=1}^{n_t}\left(1 - \int_0^{\bar{\varepsilon}^i_{fr}} \frac{d\bar{\varepsilon}^p}{\bar{\varepsilon}^p_{fr}(\eta,\bar{\theta})}\right)^2} \tag{4.35}$$

By drawing the fracture envelope ($\bar{\varepsilon}^p_{fr}$ as a function of η) and comparing the model constants calibrated by using the two aforesaid methods, they concluded that both methods result in similar fracture envelopes (the model constants were almost equal). The average error of ~5% was derived by using the calibrated model and a linear damage accumulation relation for simulation of uniaxial, notched, and plane-strain tensile tests and in-plane shear test. However, the application of this model for the prediction of fracture in a simple groove test resulted in an error of 44%. Therefore, the authors concluded that the traditional calibration approach is counterproductive for the prediction of fracture in ISF. Instead, they used several groove tests to calibrate the model based on an inverse approach. Therefore, fracture in ISF could be predicted with ~10% error.

As discussed in the first and second chapters, fracture of semicrystalline thermoplastics is more complicated as compared to metallic alloys. This is due to the influence of different mechanisms, namely slip, cavitation, and crazing. The fracture could be ductile or brittle. Moreover, temperature, strain rate, and the level of triaxiality significantly affect these mechanisms. In addition, the evolution of microstructure and damage evolution during the plastic deformation affects the load-bearing properties of thermoplastics. Investigation of such complicated deformation and fracture mechanisms has been a subject of ongoing research, so it is out of the scope of the current thesis. However, a straightforward method is proposed here to include the effect of damage evolution in the material model used for the FEA of the process. This method could be extended later to calibrate a phenomenological fracture model such as the JC model.

To conventionally calibrate a ductile damage model, for example by using the tensile test data, damage is assumed to initiate at ultimate tensile stress (UTS). The post-UTS stress-strain curve is extrapolated to estimate the zero-stress or the fracture point. Damage evolution energy is calculated by using the corresponding area under the curve. Here, the maximum total forming force is assumed to correspond to the damage initiation point. By using the analytical framework provided in the previous chapter, the equivalent plastic strain, strain rate, and triaxiality corresponding to the damage initiation point are calculated (Equations 3.9 to 3.16). Forming force curve is extrapolated to derive the zero-force point corresponding to the complete fracture. Then, the effective plastic displacement is calculated based on the area under the equivalent plastic strain rate between the damage initiation and fracture points. This data is adopted in ductile damage (damage evolution) fields in the material model defined for FEA.

To demonstrate the capability of the FEA framework established in this chapter, several FSISF benchmark tests are simulated by adopting the last calibration of the JC model as described in section 4.3.4. The FEA results are presented in the following sections.

4.9.1 FEA of benchmark test 7

This simulation approximately took 4.7 hours. Figure 4.70 presents the heat-partitioning factor estimated for benchmark test 7 by adopting the method explained in section 4.7.

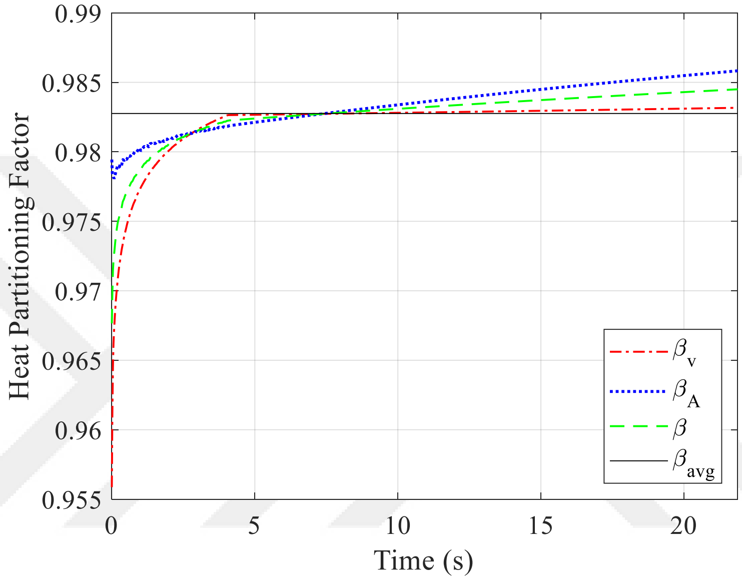

Figure 4.70: Heat partitioning factor estimated for benchmark test 7.

Figure 4.71 provides a comparison between the force component acquired from FEA and the experiment corresponding to benchmark test 7.

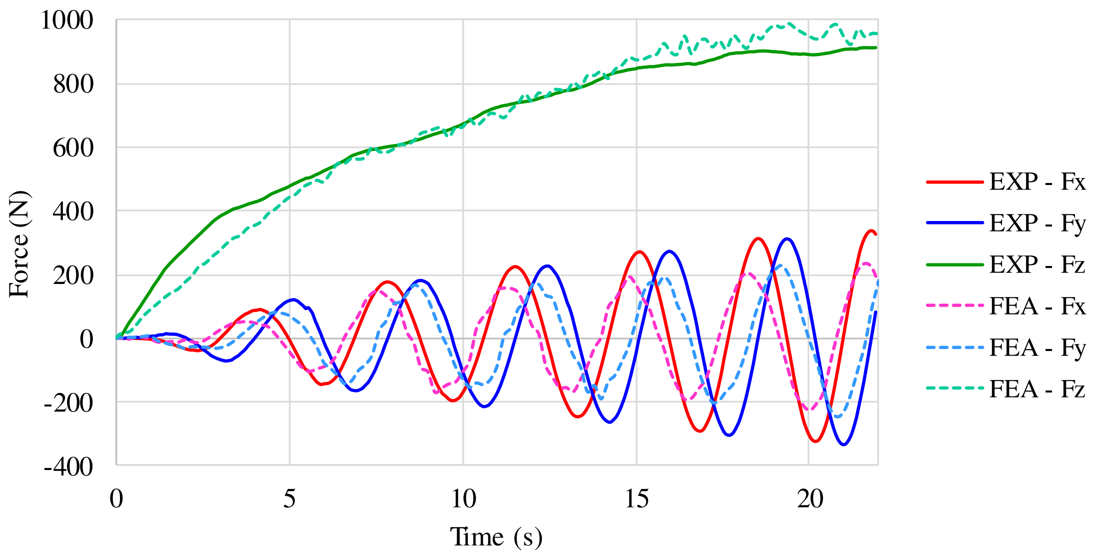

Figure 4.71: Force component acquired from FEA and experiment corresponding to benchmark test 7.

Figure 4.72 presents von Mises stress (a), equivalent plastic strain (b), and surface temperature in Kelvin (c) in FEA of FSISF benchmark 7.

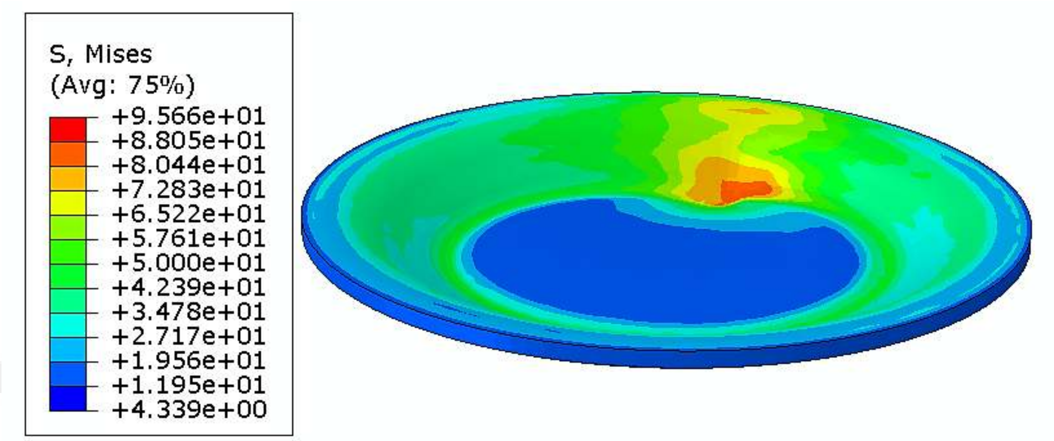

(a)

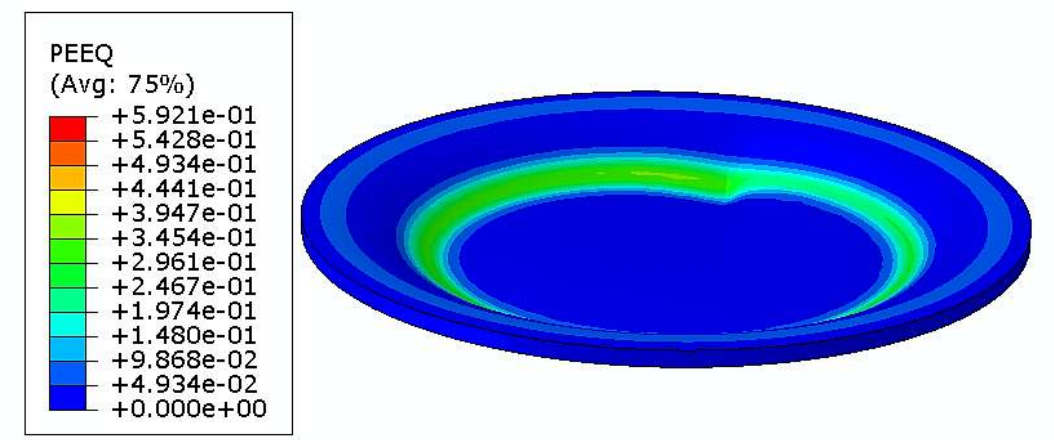

(b)

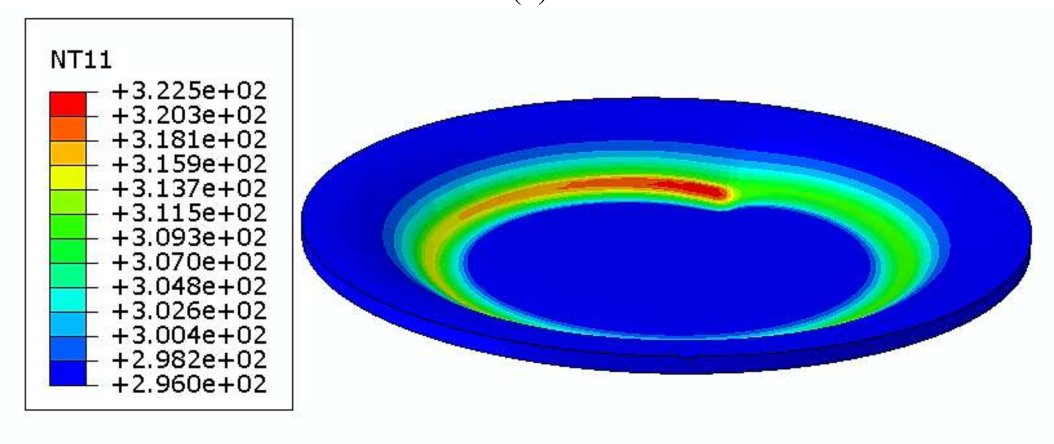

(c)

Figure 4.72: von Mises stress (a), equivalent plastic strain (b), and surface temperature (c) in FEA of FSISF benchmark 7.

4.9.2 FEA of benchmark test 19

This simulation approximately took 4 hours. Figure 4.73 presents the heat-partitioning factor estimated for benchmark test 19 by adopting the method explained in section 4.7.

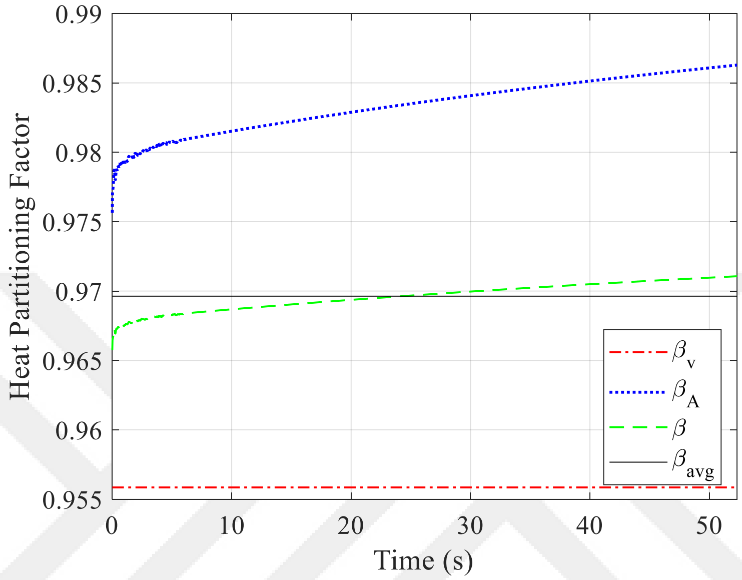

Figure 4.73: Heat partitioning factor estimated for benchmark test 19.

Figure 4.74 provides a comparison between the force component acquired from FEA and the experiment corresponding to benchmark test 19.

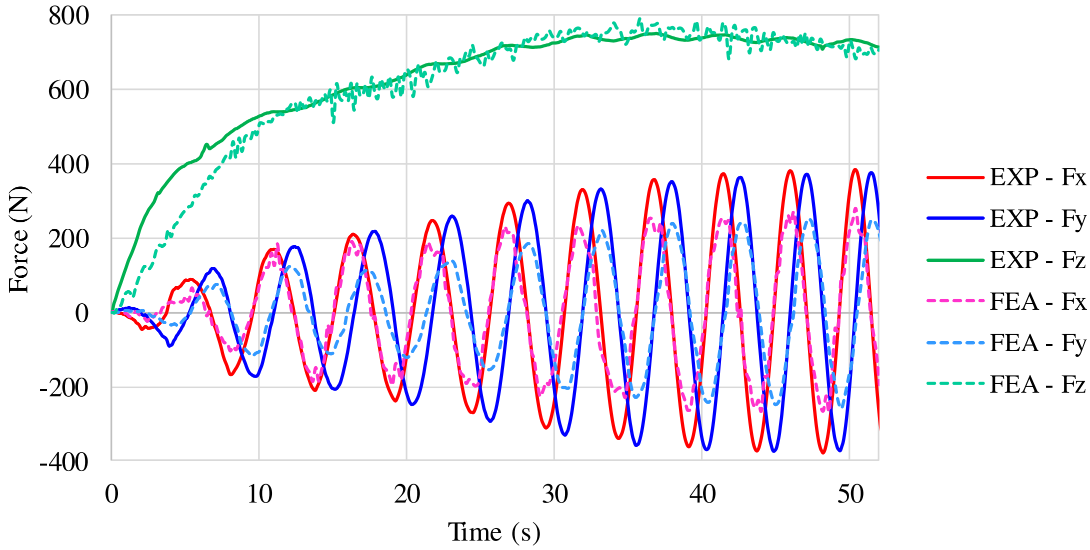

Figure 4.74: Force component acquired from FEA and experiment corresponding to benchmark test 19.

Figure 4.75 presents von Mises stress (a), equivalent plastic strain (b), and surface temperature in Kelvin (c) in FEA of FSISF benchmark 19.

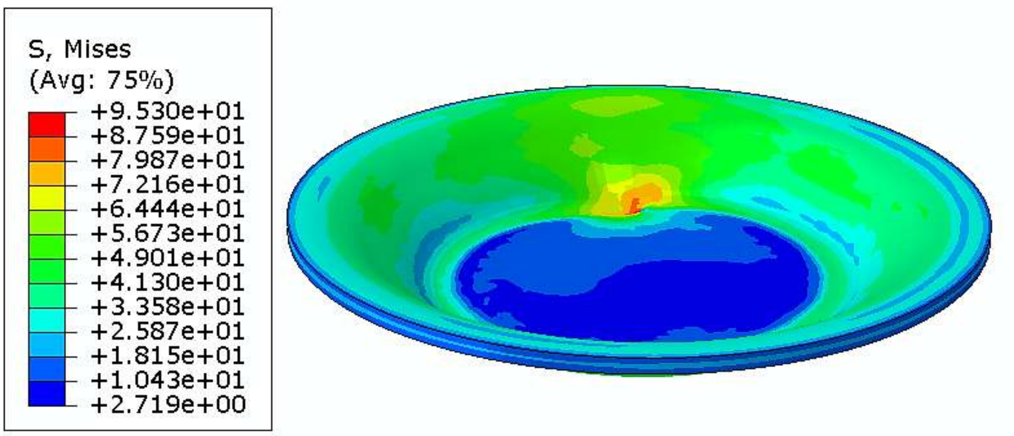

(a)

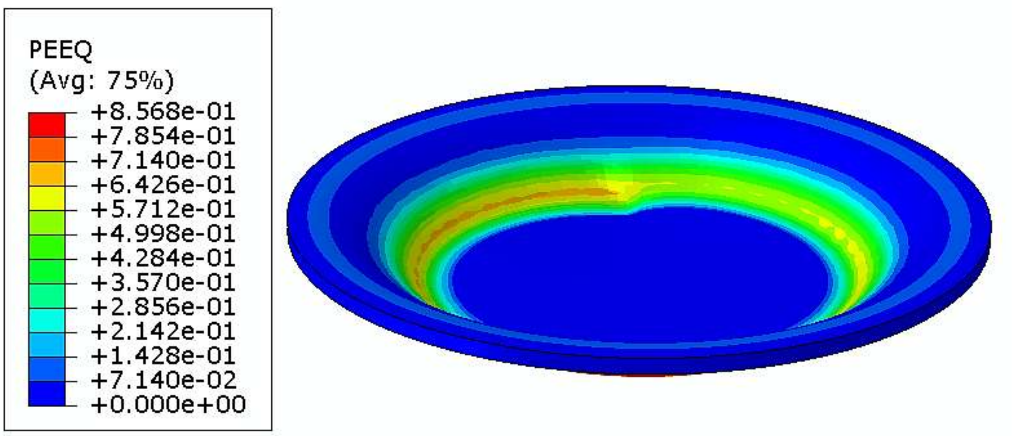

(b)

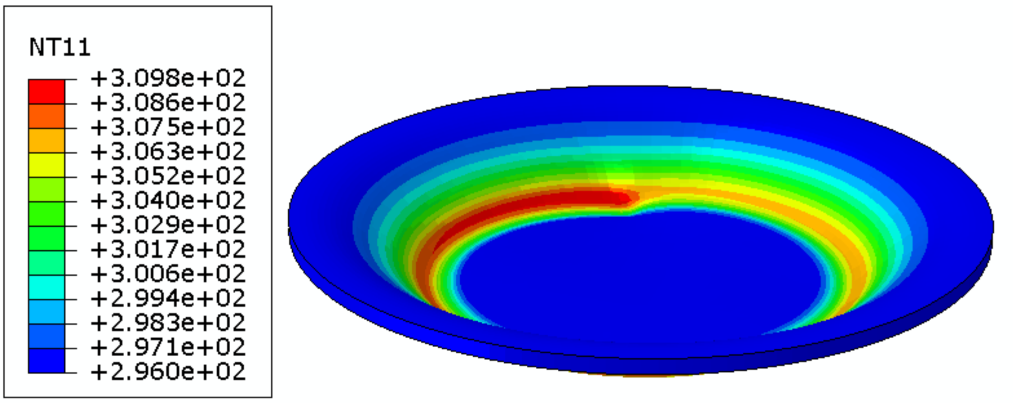

(c)

Figure 4.75: von Mises stress (a), equivalent plastic strain (b), and surface temperature (c) in FEA of FSISF benchmark 19.

4.9.3 FEA of benchmark test 20

This simulation approximately took 3.1 hours. Figure 4.76 presents the heat-partitioning factor estimated for benchmark test 20 by adopting the method explained in section 4.7.

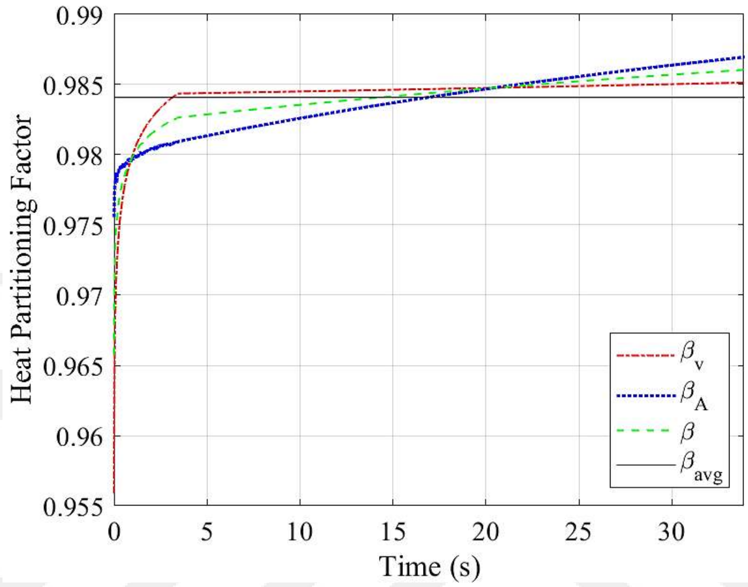

Figure 4.76: Heat partitioning factor estimated for benchmark test 20.

Figure 4.77 provides a comparison between the force component acquired from FEA and the experiment corresponding to benchmark test 20.

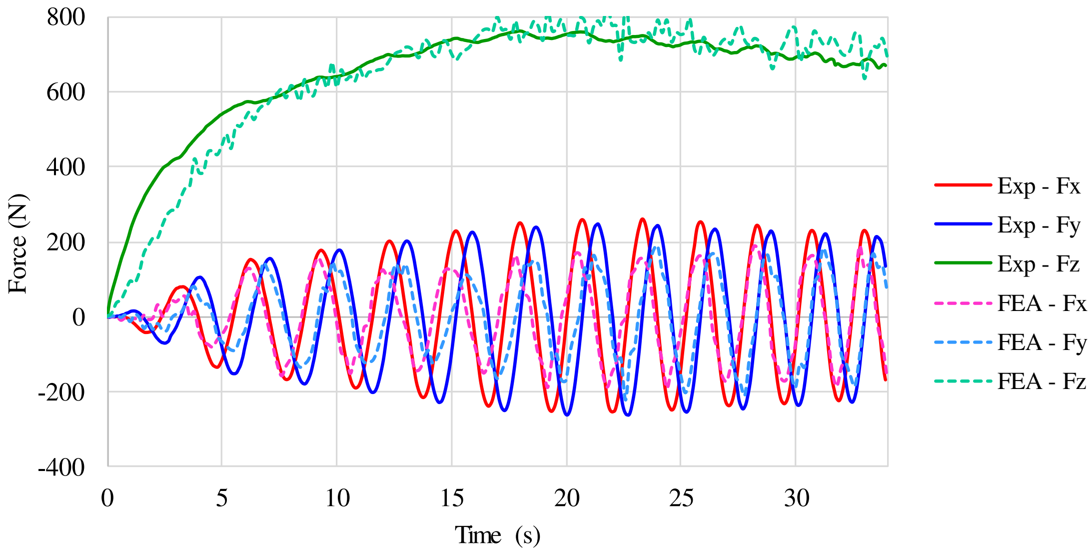

Figure 4.77: Force component acquired from FEA and experiment corresponding to benchmark test 20.

Figure 4.78 presents von Mises stress (a), equivalent plastic strain (b), and surface temperature in Kelvin (c) in FEA of FSISF benchmark 20.

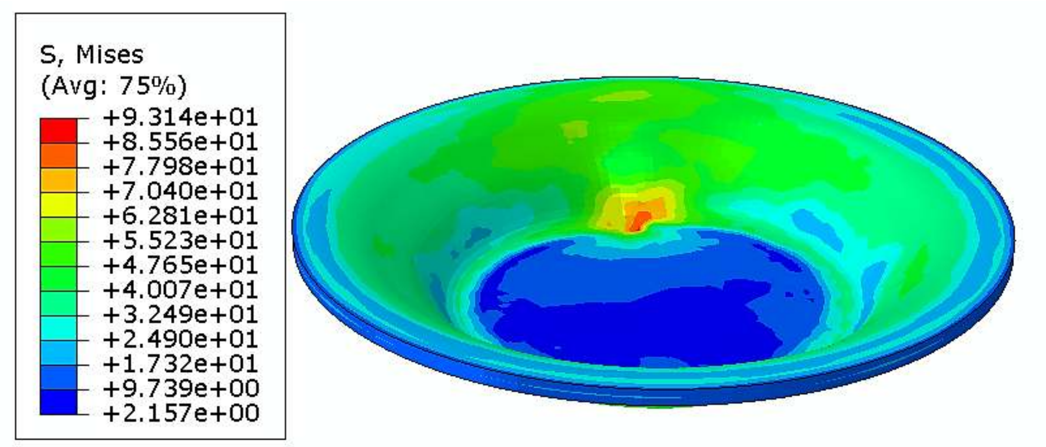

(a)

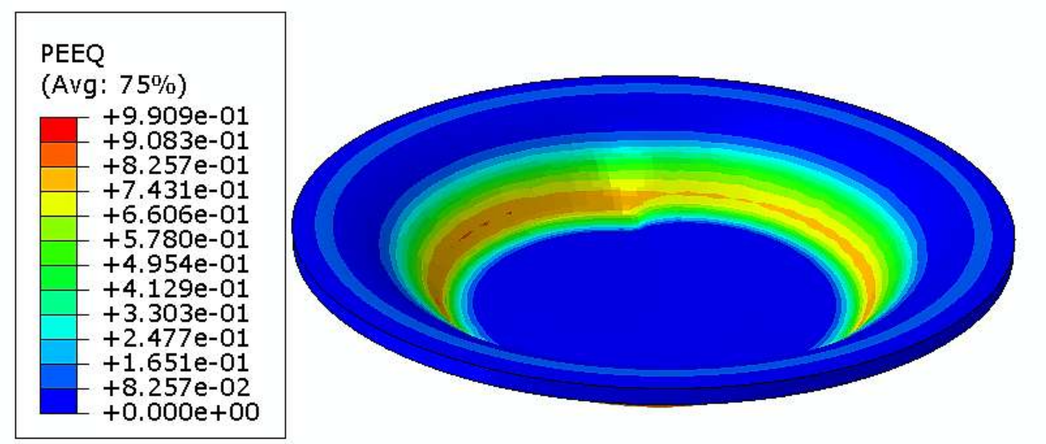

(b)

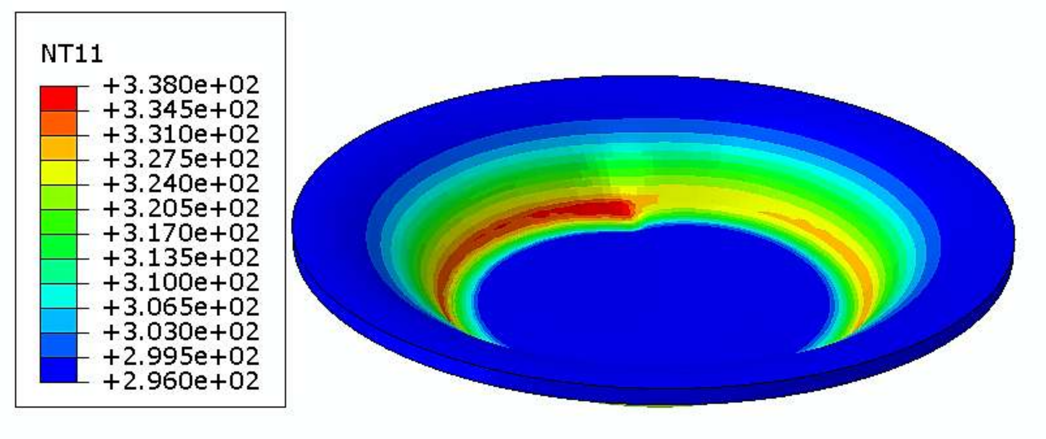

(c)

Figure 4.78: von Mises stress (a), equivalent plastic strain (b), and surface temperature (c) in FEA of FSISF benchmark 20.

4.9.4 FEA of benchmark test 27

This simulation approximately took 5.7 hours. Figure 4.79 presents the heat-partitioning factor estimated for benchmark test 27 by adopting the method explained in section 4.7.

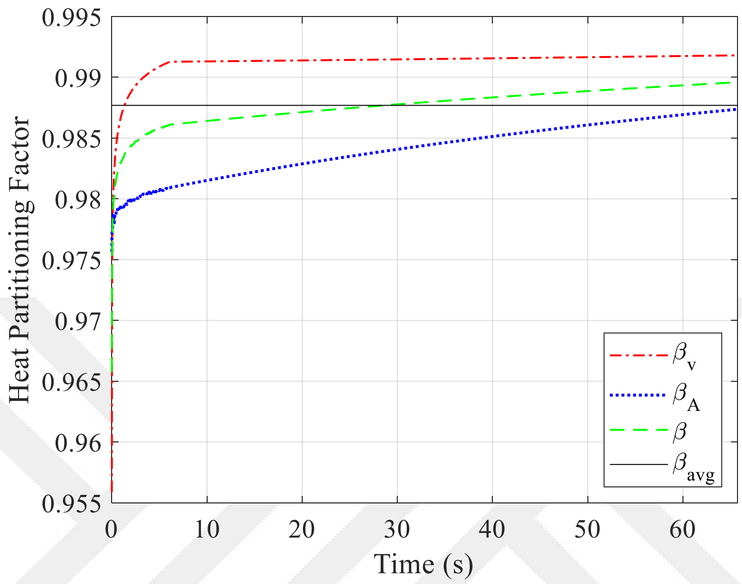

Figure 4.79: Heat partitioning factor estimated for benchmark test 27.

Figure 4.80 presents the effective plastic displacement, as a measure of damage evolution, calculated for benchmark test 27.

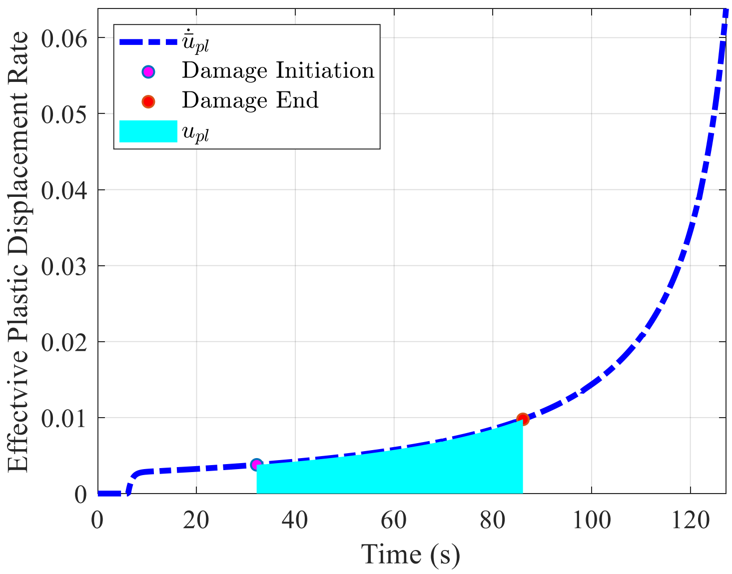

Figure 4.80: Effective plastic displacement (as a measure of damage evolution) calculated for benchmark test 27.

Figure 4.81 provides a comparison between the force component acquired from FEA and the experiment corresponding to benchmark test 27.

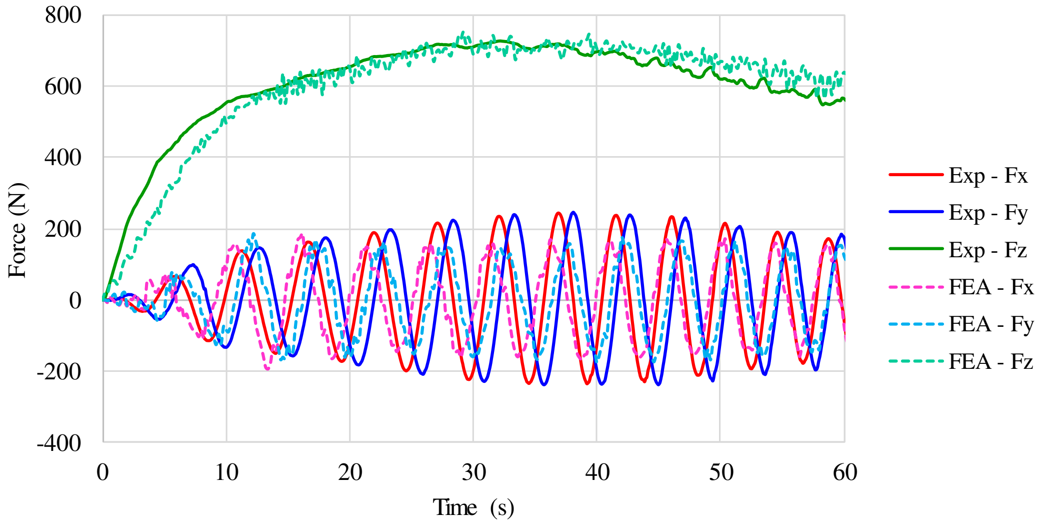

Figure 4.81: Force component acquired from FEA and experiment corresponding to benchmark test 27.

Figure 4.82 presents von Mises stress (a), equivalent plastic strain (b), and surface temperature in Kelvin (c) in FEA of FSISF benchmark 27.

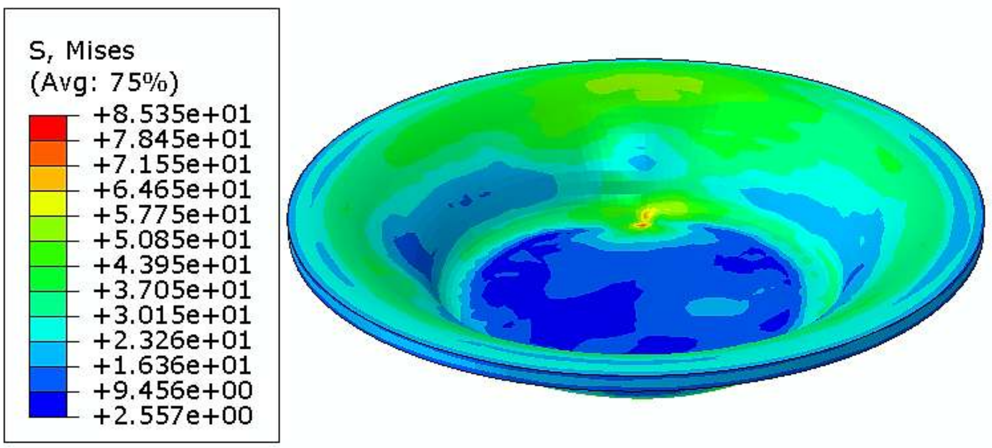

(a)

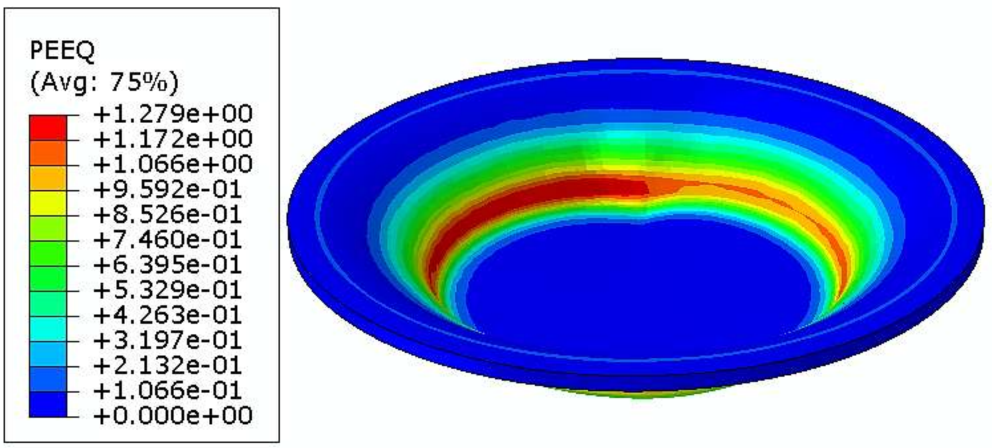

(b)

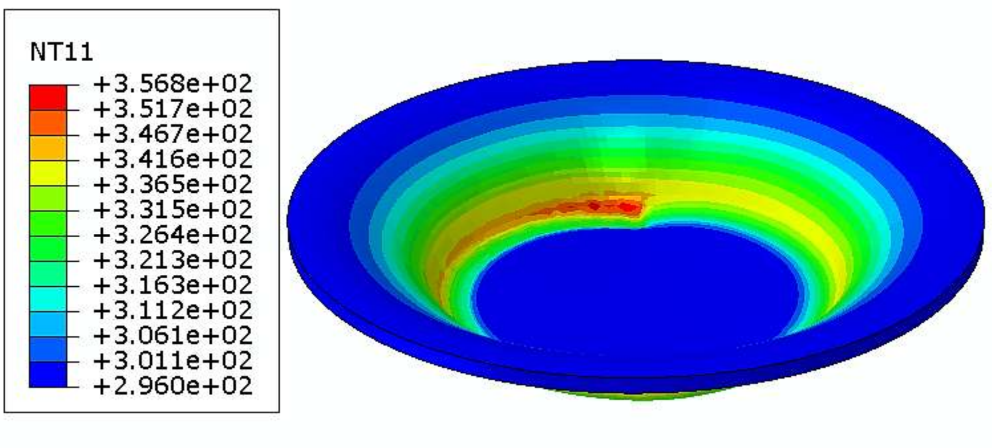

(c)

Figure 4.82: von Mises stress (a), equivalent plastic strain (b), and surface temperature (c) in FEA of FSISF benchmark 27.

4.9.5 A brief discussion on the latest FEA results

The comparison provided among the experimental and FEA force results for benchmark FSISF tests presented in the previous sections reflect very good compliance between predicted and measured normal force components. The decline of the normal force, when damage evolution and degradation of the material is significant, has been captured by FEA as specifically demonstrated for the FSISF tests 27 (Figure 4.81). Planar force components are also predicted with acceptable accuracies. The maximum deviation of the predicted force with respect to the measured magnitudes is most evident around the pick normal force. Such an underestimation of the planar force components is also reported by a few research works conducted on the FEA of polymers at ambient temperature (as reflected in the first chapter, Figure 1.15). The planar force deviation around the pick normal force could be attributed to the nonlinear interactive effects of temperature and contact pressure on the friction coefficient. Though in this study, the friction coefficient was investigated both experimentally and numerically, further investigation is required in the future.

As shown by the contour plots of the equivalent plastic strain throughout the previous sections, the maximum sheet thinning occurs around the utmost upper contact line between tool and sheet. This is where the stress triaxiality is maximum and cracks start to grow from the outer surface of the sheet. The initial attempts to include the ductile damage evolution effect as described in this section (reflected by Figures 4.80 and 4.81) resulted in an overestimation of the fracture by approximately 18%. Figure 4.83 presents the von Mises stress (a), equivalent plastic strain (b), and stress triaxiality (c) at the backside of the FSISF benchmark 3 just before fracture. Figure 4.84 presents the same parameters on the inside surface of the same specimen when fracture occurred.

As discussed in the first and second chapters, fracture of semicrystalline thermoplastics is very complicated due to the participation of different mechanisms namely, slip, cavitation, and crazing. Temperature, strain rate, and the level of triaxiality significantly affect ductile, semi-ductile, and brittle fractures in thermoplastics. In addition, the evolution of microstructure and nonlinear damage evolution during the plastic deformation affects the load-bearing properties of thermoplastics. The complex mechanism of deformation in ISF further complicates an accurate prediction of fracture.

Therefore, extensive investigation on the fracture of thermoplastics in the ISF process at elevated temperatures is required in the future.

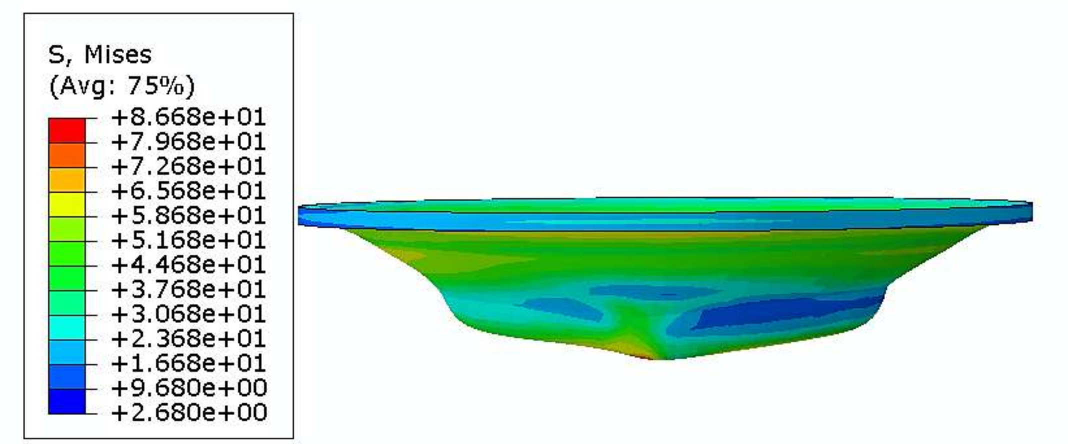

(a)

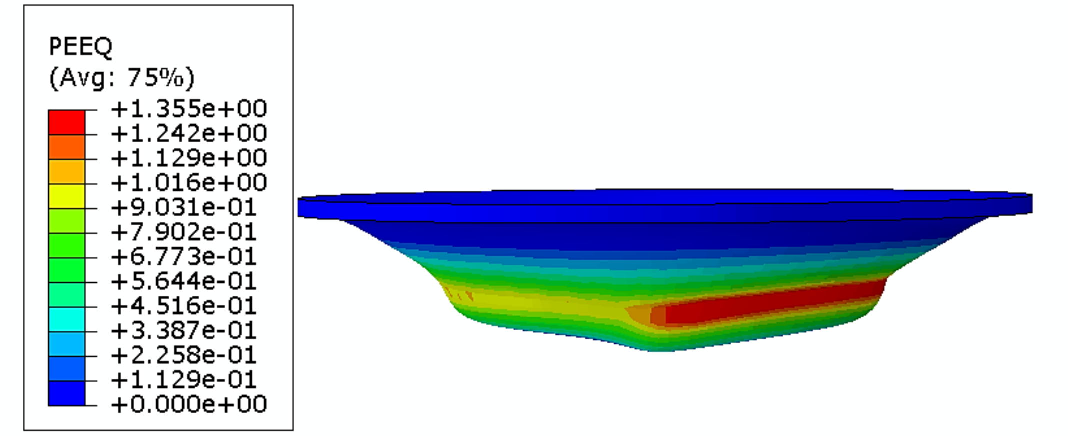

(b)

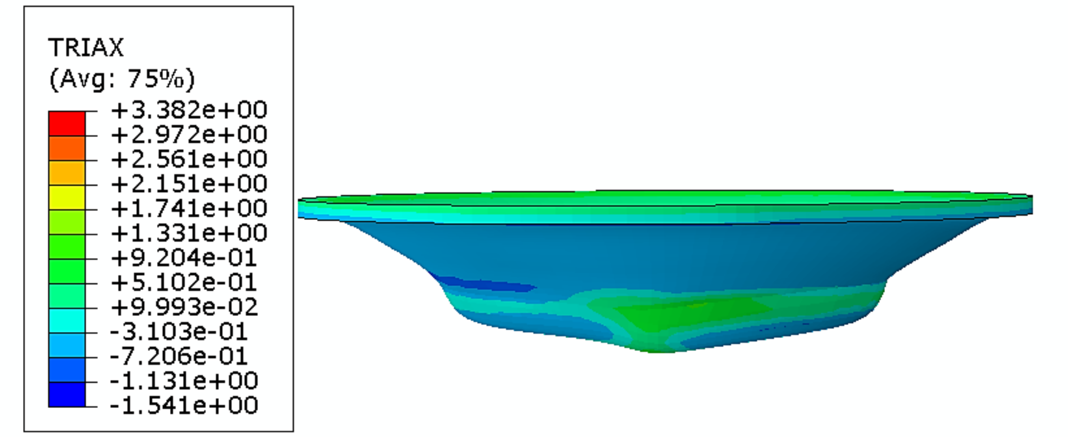

(c)

Figure 4.83: von Mises stress (a), equivalent plastic strain (b), and stress triaxiality (c) in FEA of FSISF benchmark 3 just before fracture occurs.

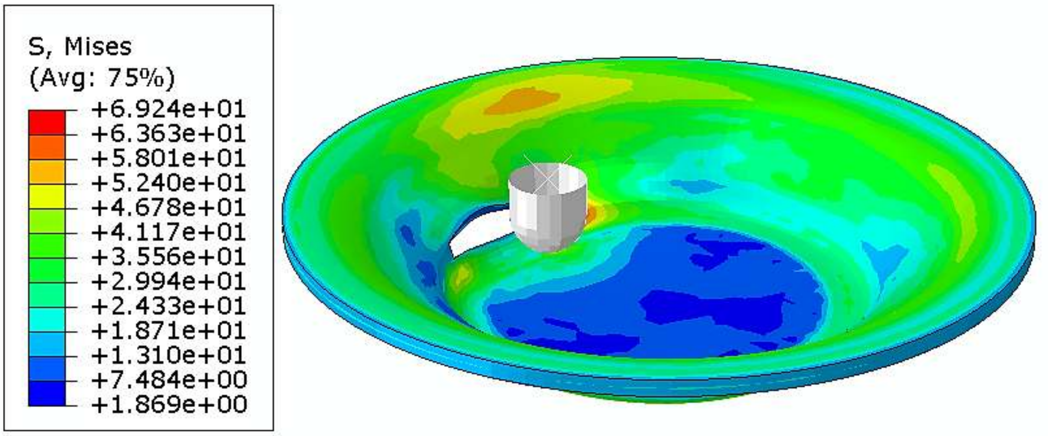

(a)

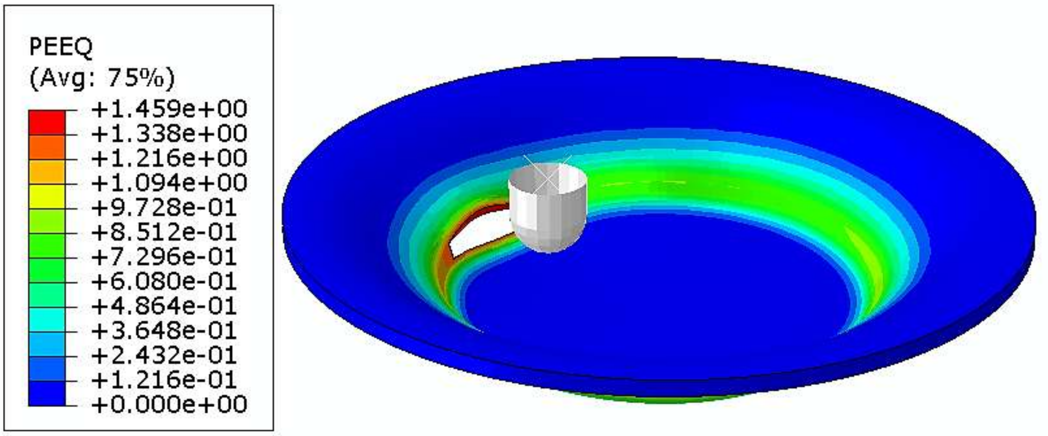

(b)

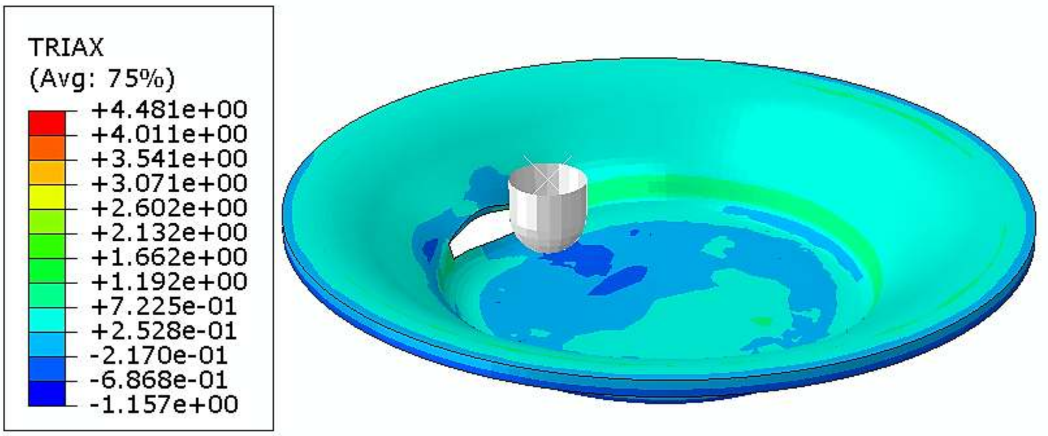

(c)

Figure 4.84: von Mises stress (a), equivalent plastic strain (b), and stress triaxiality (c) in FEA of FSISF benchmark 3 at the fracture instant.

Chapter 5

CONCLUSION

As detailed in the first chapter, there has been a growing demand for lightweight and customized products in the manufacturing sector. Such a tendency has led to a continuous growth in the consumption of thermoplastics, for example, in the automotive sector. The new trend also reinforces the need for a novel sheet forming technology to cope with the requirements of customized manufacturing. Such a forming process is deemed to provide a flexible and highly capable tooling system. By employing the computer numerical control (CNC) technology and simple tooling, Incremental Sheet Forming (ISF) offers a die-less forming possibility. Therefore, ISF promises more flexibility in the process, lower production cost, and shorter lead-time, in addition to improved formability of material as compared to the conventional sheet forming processes.

During the last decade, scholars to understand the mechanism and the governing rules of the ISF process have devoted a great deal of effort. Several attempts have been also made to investigate the effect of process parameters on process outputs. These studies have mostly targeted sheet metals namely aluminum, steel, titanium, and magnesium. As pointed out by the literature review provided in the first chapter, heat-assisted ISF appears very promising in terms of improving the sheet formability, enhancing the dimensional accuracy, and reducing the ISF processing time. However, as stated in the section on heat-assisted ISF, only 4% of the research work in the field has been related to heat-assisted ISF of polymers. Polyoxymethylene (POM) is the least investigated thermoplastic among the engineering polymers used for ISF. In a very few research works conducted by using POM, it has been dismissed for ISF, mainly due to its low formability at room temperature. However, POM is known as a semicrystalline thermoplastic of good creep and fatigue durability, high resistance against chemicals, oil, and fuel corrosion, accompanied by a good surface finish and friction resistance quality.

Therefore, this thesis aimed at a comprehensive experimental, analytical and numerical (FEA) investigation of Friction Stir Incremental Sheet Forming of Polyoxymethylene. The objective was to establish analytical and FEA frameworks that provide fairly accurate predictions with an affordable simulation cost in terms of the computation time and the required hardware.

In the first chapter, a brief discussion was provided on the current and future trends in sheet forming technology. This introduction was followed by a literature review on incremental sheet forming (ISF) in general. Afterward, a detailed review of ISF at elevated temperatures was conducted. Then, a brief but detailed discussion was provided on the application of thermoplastics in the automotive industry. At the end of the section, a critical review was provided on the ISF of polymers to highlight the research gaps and the research objective of the current thesis.

In the second chapter, a comprehensive FSISF experimental campaign was presented with the objective to achieve maximum formability while heat-induced defects are avoided. Experiments were conducted by adopting the Design of Experiment (DOE) and response surface methods. Individual and interactive effects of the process parameters, namely tool size, step size, feed rate, and spindle speed on the process outputs were discussed in terms of forming force, contact temperature, heating rate, deformation rate, and stress triaxiality. An empirical model was provided to predict the total forming force as a function of the process parameters and time. A similar model was also provided for the maximum force. The effect of specimens' geometry on sheet formability was discussed and a new formability criterion was proposed for ISF. Friction in FSISF of POM was experimentally evaluated and briefly discussed. The temperature at the tool-sheet contact interface, at the center, and the base of the specimens was measured throughout the experimental campaign. A response surface was provided to demonstrate the interface temperature as a function of the process parameters. The interdependent effects of force, forming angle, and temperature were discussed by providing physical explanations. Dimensional integrity, thickness distribution, surface quality as well as the evolution of crystallinity, surface hardness, and elastic modulus of POM under specific forming conditions were discussed. This approach was adopted to better understand and explain the material behavior under different ISF forming conditions. Taking into account the outputs of the study in terms of the sheet formability, surface quality, and geometrical integrity of the specimens, a threshold band was set for the maximum allowable tool-tip temperature. The temperature range of 70°C to 75°C can be regarded as a threshold band not to be exceeded to avoid significant damage. At the end of the chapter, a discussion was provided on fracture in FSISF of POM based on the morphology of the cracks acquired by Scanning Electron Microscopy (SEM).

As shown by the literature review provided in the first chapter, there has been a dispute among the researchers on the effect of process parameters on process outputs in ISF of polymers. This is due to the complex interactive effects of the process parameters, and material-dependent effects of physical factors, namely heat and temperature, strain rate, and stress triaxiality. As highlighted by the literature reviews, there has been a research gap in terms of an analytical framework for the simulation of heat-assisted ISF of polymers by considering the aforesaid influential physical factors. Therefore, a combined numerical-analytical discipline was proposed in the third chapter to efficiently predict the force and temperature at the tool-sheet contact interface in the FSISF of thermoplastics. First, the mechanism of deformation and stress-strain state was defined based on a membrane analytical framework, and by considering the stretch-bending in the sheet. The area of the tool-sheet contact interface was estimated by proposing two geometrical approaches. Then, the pronounced bending effect in the initial stage of the forming process was investigated by extending an available analytical framework for deflection of a circular sheet under lateral concentrated load. Calculation of the friction-induced heat and heat partitioning was briefly discussed. Temperature distribution in tool and sheet was calculated by adopting the Finite Difference Method (FDM). At the end of the chapter, analytical results were validated by the experimental measurements. More specifically, analytically predicted contact areas for some benchmark cases were compared with validated FEA results, and overall acceptable compliance was presented. The predicted total force for five major FSISF benchmarks was compared against the experimental results, and overall good compliance was presented. Tooltip temperature estimated by using the analytical framework was also compared against the temperature experimentally recorded by using a pyrometer and overall acceptable compliance was presented. Friction-induced heat rate and meridional stress component were presented as functions of the equivalent plastic strain in the five major FSISF benchmarks. The ratio of the plastic strain energy density to the triaxiality was also presented as a function of the final equivalent plastic strain for the FSISF benchmarks. Accordingly, a brief discussion was provided on the sheet failure in the FSISF process.

As shown by the literature review provided in the first chapter, there has been a research gap in terms of FEA of the ISF of thermoplastics, specifically by considering the effects of elevated temperatures, and strain rate. An obstacle to achieving this goal, apart from the complexity of the process, has been high simulation costs. Therefore, a framework for a fairly accurate and timely-efficient FEA of FSISF of thermoplastics was established in the fourth chapter. A brief discussion was provided on Implicit and Explicit solutions. Afterward, a detailed discussion was provided on the selection of a proper material model for the FSISF of POM. The material constitutive models namely Two-Layer Viscoplastic (TLV), Parallel Rheological Framework (PRF), Three Network (TN), and Johnson-Cook (JC) were discussed and calibrated. In addition, a phenomenological nonlinear elastic model with acceptable accuracy was proposed and calibrated. A series of comparative FEAs along with detailed discussions were provided on meshing strategies, FSISF tool definition, element type, element size, and mass scaling for an optimum FEA framework. Following these sections, heat partitioning between tool and sheet was discussed in detail. For this purpose, a precise review was provided on heat partitioning in problems involving friction-induced heat such as pin-on-disk, disk-brake, and rail-wheel contact problems. The friction coefficient was briefly discussed along with an FEA that was validated by experimental results. Benchmark FSISF tests were considered for simulation. To demonstrate the capability of the proposed FEA methodology, the simulation case studies reflect a broad range of sheet formability, temperature, and stress triaxiality (as a measure of ductile fracture). The simulation results were validated against experimental results (mainly in terms of forming force), and good compliance was presented. A brief discussion and numerical investigation were provided on damage evolution and failure in FSISF of POM.

It is worth mentioning that the experimental, analytical, and FEA research approaches proposed here are readily applicable to other thermoplastics. These disciplines with some modifications are also applicable to FSISF of metallic alloys. In future investigations, it is possible to aim for a multi-objective process and toolpath optimization by employing the analytical-numerical framework proposed here. Therefore, better formability, higher dimensional accuracy, better surface finish, and shorter processing time could be achieved based on the preferred balance. In addition, further investigation on fracture prediction is required by extending the FEA framework exposed here.

BIBLIOGRAPHY

[1] Tisza, M. Recent Development Trends in Sheet Metal Forming. *Int. J. Microstruct. Mater. Prop.*, **2013**, *8* (1–2), 125–140.

[2] Wang, C.; Kinzel, G.; Altan, T. Mathematical Modeling of Plane-Strain Bending of Sheet and Plate. *J. Mater. Process. Technol.*, **1993**, *39* (3–4), 279–304.

[3] Oh, S. I.; Kobayashi, S. Finite Element Analysis of Plane-Strain Sheet Bending. *Int. J. Mech. Sci.*, **1980**, *22* (9), 583–594.

[4] Takalkar, A. S.; Mailan Chinnapandi, L. B. Deep Drawing Process at the Elevated Temperature: A Critical Review and Future Research Directions. *CIRP J. Manuf. Sci. Technol.*, **2019**, *27*, 56–67.

[5] S, T. A.; Babu, M. C. L. A Review on Effect of Thinning, Wrinkling and Spring-Back on Deep Drawing Process: *https://doi.org/10.1177/0954405417752509*, **2018**, *233* (4), 1011–1036.

[6] Music, O.; Allwood, J. M.; Kawai, K. A Review of the Mechanics of Metal Spinning. *J. Mater. Process. Technol.*, **2010**, *210* (1), 3–23.

[7] Xia, Q.; Xiao, G.; Long, H.; Cheng, X.; Sheng, X. A Review of Process Advancement of Novel Metal Spinning. *Int. J. Mach. Tools Manuf.*, **2014**, *85*, 100–121.

[8] Wong, C. C.; Dean, T. A.; Lin, J. A Review of Spinning, Shear Forming and Flow Forming Processes. *Int. J. Mach. Tools Manuf.*, **2003**, *43* (14), 1419–1435.

[9] Karbasian, H.; Tekkaya, A. E. A Review on Hot Stamping. *J. Mater. Process. Technol.*, **2010**, *210* (15), 2103–2118.

[10] Merklein, M.; Wieland, M.; Lechner, M.; Bruschi, S.; Ghiotti, A. Hot Stamping of Boron Steel Sheets with Tailored Properties: A Review. *J. Mater. Process. Technol.*, **2016**, *228*, 11–24.

[11] Tong, C.; Rong, Q.; Yardley, V. A.; Li, X.; Luo, J.; Zhu, G.; Shi, Z. New Developments and Future Trends in Low-Temperature Hot Stamping Technologies: A Review. *Met. 2020, Vol. 10, Page 1652*, **2020**, *10* (12), 1652.

[12] Araghi, B. T.; Manco, G. L.; Bambach, M.; Hirt, G. Investigation into a New Hybrid Forming Process: Incremental Sheet Forming Combined with Stretch Forming. *CIRP Ann.*, **2009**, *58* (1), 225–228.

[13] Ohring, M. MATERIALS PROCESSING AND FORMING OPERATIONS. *Eng. Mater. Sci.*, **1995**, 371–IX.

[14] Li, L.; Liu, F.; Li, C. Customer Satisfaction Evaluation Method for Customized Product Development Using Entropy Weight and Analytic Hierarchy Process. *Comput. Ind. Eng.*, **2014**, *77*, 80–87.

[15] Tao, F.; Cheng, Y.; Zhang, L.; Nee, A. Y. C. Advanced Manufacturing Systems: Socialization Characteristics and Trends. *J. Intell. Manuf. 2015 285*, **2015**, *28* (5), 1079–1094.

[16] Yang, C.; Lan, S.; Shen, W.; Huang, G. Q.; Wang, X.; Lin, T. Towards Product Customization and Personalization in IoT-Enabled Cloud Manufacturing. *Clust. Comput. 2017 202*, **2017**, *20* (2), 1717–1730.

[17] Dilberoglu, U. M.; Gharehpapagh, B.; Yaman, U.; Dolen, M. The Role of Additive Manufacturing in the Era of Industry 4.0. *Procedia Manuf.*, **2017**, *11*, 545–554.

[18] Khalatbari, H.; Iqbal, A.; Shi, X.; Gao, L.; Hussain, G.; Hashemipour, M. High-Speed Incremental Forming Process: A Trade-Off between Formability and Time Efficiency. *Mater. Manuf. Process.*, **2015**, *30* (11), 1354–1363.

[19] Leacock, A. G. The Future of Sheet Metal Forming Research. *http://dx.doi.org/10.1080/10426914.2011.551960*, **2012**, *27* (4), 366–369.

[20] Echrif, S. B. M.; Hrairi, M. Research and Progress in Incremental Sheet Forming Processes. *https://doi.org/10.1080/10426914.2010.544817*, **2011**, *26* (11), 1404–1414.

[21] Altan, T.; Tekkaya, A. E. *Sheet Metal Forming: Processes and Applications*; ASM international, 2012.

[22] Mittal, R. K.; others. *Incremental Sheet Forming Technologies: Principles, Merits, Limitations, and Applications*; CRC Press, 2020.

[23] Mallick, P. K. *Materials, Design and Manufacturing for Lightweight Vehicles*; Woodhead publishing, 2020.

[24] Weill, D.; Klink, G.; Roullioux, G. Plastics: The Future for Automakers and Chemical Companies. *ATKearney: Ideas and Insights*, **2014**.

[25] Shaw, M. T. Cold Forming of Polymeric Materials. *Annu. Rev. Mater. Sci.*, **1980**, *10* (1), 19–42.

[26] Hassan, M.; Hussain, G.; Wei, H.; Qadeer, A.; AlKahtani, M. Progress on Single-Point Incremental Forming of Polymers. *International Journal of Advanced Manufacturing Technology*. Springer Science and Business Media Deutschland GmbH May 1, 2021, pp 1–26.

[27] Patel, S. H.; Xanthos, M. Environmental Issues in Polymer Processing: A Review

on Volatile Emissions and Material/Energy Recovery Options. *Adv. Polym. Technol. J. Polym. Process. Inst.*, **2001**, *20* (1), 22–41.

[28] Mason, B. Sheet Metal Forming for Small Batches. *Bachelor thesis, Univ. Nottingham*, **1978**.

[29] Iseki, H.; Kato, K.; Sakamoto, S. Flexible and Incremental Sheet Metal Forming Using a Spherical Roller. *Proc. 40th JJCTP*, **1989**, *41*, 44.

[30] Kitazawa, K.; Nakane, M. Hemi-Ellipsoidal Stretch-Expanding of Aluminum Sheet by CNC Incremental Forming Process with Two Path Method. *Keikinzoku*, **1997**, *47* (8), 440–445.

[31] Kitazawa, K.; Hayashi, S.; Yamazaki, S. Hemispherical Stretch-Expanding of Aluminum Sheet by Computerized Numerically Controlled Incremental Forming Process with Two Path Method. *Keikinzoku*, **1996**, *46* (5), 219–224.

[32] Kitazawa, K. Limit Strains for CNC Incremental Stretch-Expanding of Aluminum Sheets. *Keikinzoku*, **1997**, *47* (3), 145–150.

[33] Kitazawa, K.; Wakabayashi, A.; Murata, K.; Yaejima, K. Metal-Flow Phenomena in Computerized Numerically Controlled Incremental Stretch-Expanding of Aluminum Sheets. *Keikinzoku*, **1996**, *46* (2), 65–70.

[34] Matsubara, S. Incremental Backward Bulge Forming of a Sheet Metal with a Hemispherical Head Tool-a Study of a Numerical Control Forming System II. *J. Japan Soc. Technol. Plast.*, **1994**, *35* (406), 1311–1316.

[35] Kim, T. J.; Yang, D. Y. Improvement of Formability for the Incremental Sheet Metal Forming Process. *Int. J. Mech. Sci.*, **2000**, *42* (7), 1271–1286.

[36] Hagan, E.; Jeswiet, J. A Review of Conventional and Modern Single-Point Sheet Metal Forming Methods. *Proc. Inst. Mech. Eng. Part B J. Eng. Manuf.*, **2003**, *217* (2), 213–225.

[37] Franzen, V.; Kwiatkowski, L.; Martins, P. a F.; Tekkaya, a. E. Single Point Incremental Forming of PVC. *J. Mater. Process. Technol.*, **2009**, *209* (1), 462–469.

[38] Bambach, M.; Hirt, G.; Junk, S. Modelling and Experimental Evaluation of the Incremental CNC Sheet Metal Forming Process. In *7th International Conference on Computational Plasticity, Barcelona, Spain*; 2003.

[39] Jeswiet, J.; Micari, F.; Hirt, G.; Bramley, A.; Duflou, J.; Allwood, J. Asymmetric Single Point Incremental Forming of Sheet Metal. *CIRP Ann. Technol.*, **2005**, *54* (2), 88–114.

[40] Sousa, R. Incremental Sheet Forming Technologies. *Ref. Modul. Mater. Sci. Mater. Eng.*, **2016**.

[41] Henrard, C. Numerical Simulations of the Single Point Incremental Forming Process. **2009**.

[42] Castañeda, E.; Lauret, B.; Lirola, J. M.; Ovando, G. Free-Form Architectural Envelopes: Digital Processes Opportunities of Industrial Production at a Reasonable Price. *J. Facade Des. Eng.*, **2015**, *3* (1), 1–13.

[43] States Department of Energy, U. Rapid Freeform Sheet Metal Forming. **2016**.

[44] Emmens, W. C.; van den Boogaard, A. H. An Overview of Stabilizing Deformation Mechanisms in Incremental Sheet Forming. *Journal of Materials Processing Technology*. Elsevier April 21, 2009, pp 3688–3695.

[45] Emmens, W. C.; Sebastiani, G.; van den Boogaard, A. H. The Technology of Incremental Sheet Forming—A Brief Review of the History. *J. Mater. Process. Technol.*, **2010**, *210* (8), 981–997.

[46] Taleb Araghi, B.; Göttmann, A.; Bambach, M.; Hirt, G.; Bergweiler, G.; Diettrich, J.; Steiners, M.; Saeed-Akbari, A. Review on the Development of a Hybrid Incremental Sheet Forming System for Small Batch Sizes and Individualized Production. *Prod. Eng. 2011 54*, **2011**, *5* (4), 393–404.

[47] Reddy, V.; Lingam, R.; Cao, J. Incremental Metal Forming Processes in Manufacturing. *Handb. Manuf. Eng. Technol.*, **2015**, 411–452.

[48] Gatea, S.; Ou, H.; McCartney, G. Review on the Influence of Process Parameters in Incremental Sheet Forming. *Int. J. Adv. Manuf. Technol. 2016 871*, **2016**, *87* (1), 479–499.

[49] McAnulty, T.; Jeswiet, J.; Doolan, M. Formability in Single Point Incremental Forming: A Comparative Analysis of the State of the Art. *CIRP J. Manuf. Sci. Technol.*, **2017**, *16*, 43–54.

[50] Li, Y.; Chen, X.; Liu, Z.; Sun, J.; Li, F.; Li, J.; Zhao, G. A Review on the Recent Development of Incremental Sheet-Forming Process. *Int. J. Adv. Manuf. Technol. 2017 925*, **2017**, *92* (5), 2439–2462.

[51] Behera, A. K.; de Sousa, R. A.; Ingarao, G.; Oleksik, V. Single Point Incremental Forming: An Assessment of the Progress and Technology Trends from 2005 to 2015. *J. Manuf. Process.*, **2017**, *27*, 37–62.

[52] Afonso, D.; Alves de Sousa, R.; Torcato, R. Integration of Design Rules and Process Modelling within SPIF Technology-a Review on the Industrial Dissemination of Single Point Incremental Forming. *Int. J. Adv. Manuf. Technol. 2017 949*, **2017**, *94* (9), 4387–4399.

[53] Duflou, J. R.; Habraken, A.-M.; Cao, J.; Malhotra, R.; Bambach, M.; Adams, D.; Vanhove, H.; Mohammadi, A.; Jeswiet, J. Single Point Incremental Forming: State-of-the-Art and Prospects. *Int. J. Mater. Form. 2017 116*, **2017**, *11* (6), 743–

773.

[54] Peng, W.; Ou, H.; Becker, A. Double-Sided Incremental Forming: A Review. *J. Manuf. Sci. Eng.*, **2019**, *141* (5).

[55] Ai, S.; Long, H. A Review on Material Fracture Mechanism in Incremental Sheet Forming. *Int. J. Adv. Manuf. Technol. 2019 1041*, **2019**, *104* (1), 33–61.

[56] Dewang, Y.; Tenguria, N.; Sharma, V.; Dubey, M. K. Formation of Hole Flanges Through Incremental Forming: A Review. *Lect. Notes Mech. Eng.*, **2019**, 547–561.

[57] Vignesh, G.; Pandivelan, C.; Sathiya Narayanan, C. Review on Multi-Stage Incremental Forming Process to Form Vertical Walled Cup. *Mater. Today Proc.*, **2020**, *27*, 2297–2302.

[58] Lu, H.; Liu, H.; Wang, C. Review on Strategies for Geometric Accuracy Improvement in Incremental Sheet Forming. *Int. J. Adv. Manuf. Technol. 2019 1029*, **2019**, *102* (9), 3381–3417.

[59] Cheng, Z.; Li, Y.; Xu, C.; Liu, Y.; Ghafoor, S.; Li, F. Incremental Sheet Forming towards Biomedical Implants: A Review. *J. Mater. Res. Technol.*, **2020**, *9* (4), 7225–7251.

[60] Duflou, J. R.; Callebaut, B.; Verbert, J.; De Baerdemaeker, H. Laser Assisted Incremental Forming: Formability and Accuracy Improvement. *CIRP Ann. - Manuf. Technol.*, **2007**, *56* (1), 273–276.

[61] Duflou, J. R.; Callebaut, B.; Verbert, J.; De Baerdemaeker, H. Improved SPIF Performance through Dynamic Local Heating. *Int. J. Mach. Tools Manuf.*, **2008**, *48* (5), 543–549.

[62] Göttmann, A.; Diettrich, J.; Bergweiler, G.; Bambach, M.; Hirt, G.; Loosen, P.; Poprawe, R. Laser-Assisted Asymmetric Incremental Sheet Forming of Titanium Sheet Metal Parts. *Prod. Eng. 2011 53*, **2011**, *5* (3), 263–271.

[63] Mohammadi, A.; Vanhove, H.; Van Bael, A.; Duflou, J. R. Towards Accuracy Improvement in Single Point Incremental Forming of Shallow Parts Formed under Laser Assisted Conditions. *Int. J. Mater. Form.*, **2016**, *9* (3), 339–351.

[64] Mohammadi, A.; Qin, L.; Vanhove, H.; Seefeldt, M.; Van Bael, A.; Duflou, J. R. Single Point Incremental Forming of an Aged AL-Cu-Mg Alloy: Influence of Pre-Heat Treatment and Warm Forming. *J. Mater. Eng. Perform.*, **2055**, *25*.

[65] Mohammadi, A.; Vanhove, H.; Bael, A. Van; Seefeldt, M.; Duflou, J. R. Effect of Laser Transformation Hardening on the Accuracy of SPIF Formed Parts. *J. Manuf. Sci. Eng. Trans. ASME*, **2017**, *139* (1).

[66] Göttmann, A.; Bailly, D.; Bergweiler, G.; Bambach, M.; Stollenwerk, J.; Hirt, G.; Loosen, P. A Novel Approach for Temperature Control in ISF Supported by Laser

and Resistance Heating. *Int. J. Adv. Manuf. Technol. 2012 679*, **2012**, *67* (9), 2195–2205.

[67] Ambrogio, G.; Filice, L.; Manco, G. L. Warm Incremental Forming of Magnesium Alloy AZ31. *CIRP Ann. - Manuf. Technol.*, **2008**, *57* (1), 257–260.

[68] Ambrogio, G.; Filice, L.; Gagliardi, F. Formability of Lightweight Alloys by Hot Incremental Sheet Forming. *Mater. Des.*, **2012**, *34*, 501–508.

[69] Fan, G.; Gao, L.; Hussain, G.; Wu, Z. Electric Hot Incremental Forming: A Novel Technique. *Int. J. Mach. Tools Manuf.*, **2008**, *48* (15), 1688–1692.

[70] Fan, G.; Sun, F.; Meng, X.; Gao, L.; Tong, G. Electric Hot Incremental Forming of Ti-6Al-4V Titanium Sheet. *Int. J. Adv. Manuf. Technol. 2009 499*, **2009**, *49* (9), 941–947.

[71] Fan, G.; Gao, L. Mechanical Property of Ti-6Al-4V Sheet in One-Sided Electric Hot Incremental Forming. *Int. J. Adv. Manuf. Technol.*, **2014**, *72* (5–8), 989–994.

[72] Fan, G.; Gao, L. Numerical Simulation and Experimental Investigation to Improve the Dimensional Accuracy in Electric Hot Incremental Forming of Ti-6Al-4V Titanium Sheet. *Int. J. Adv. Manuf. Technol.*, **2014**, *72* (5–8), 1133–1141.

[73] Van Sy, L.; Nam, N. T. Hot Incremental Forming of Magnesium and Aluminum Alloy Sheets by Using Direct Heating System. *Proc. Inst. Mech. Eng. Part B J. Eng. Manuf.*, **2013**, *227* (8), 1099–1110.

[74] Shi, X.; Gao, L.; Khalatbari, H.; Xu, Y.; Wang, H.; Jin, L. Electric Hot Incremental Forming of Low Carbon Steel Sheet: Accuracy Improvement. *Int. J. Adv. Manuf. Technol. 2013 681*, **2013**, *68* (1), 241–247.

[75] Adams, D.; Jeswiet, J. Single-Point Incremental Forming of 6061-T6 Using Electrically Assisted Forming Methods. *Proc. Inst. Mech. Eng. Part B J. Eng. Manuf.*, **2014**, *228* (7), 757–764.

[76] Bao, W.; Chu, X.; Lin, S.; Gao, J. Experimental Investigation on Formability and Microstructure of AZ31B Alloy in Electropulse-Assisted Incremental Forming. *Mater. Des.*, **2015**, *87*, 632–639.

[77] Honarpisheh, M.; Abdolhoseini, M. J.; Amini, S. Experimental and Numerical Investigation of the Hot Incremental Forming of Ti-6Al-4V Sheet Using Electrical Current. *Int. J. Adv. Manuf. Technol.*, **2016**, *83* (9–12), 2027–2037.

[78] Khazaali, H.; Fereshteh-Saniee, F. A Comprehensive Experimental Investigation on the Influences of the Process Variables on Warm Incremental Forming of Ti-6Al-4V Titanium Alloy Using a Simple Technique. *Int. J. Adv. Manuf. Technol.*, **2016**, *87* (9–12), 2911–2923.

[79] Liu, R.; Lu, B.; Xu, D.; Chen, J.; Chen, F.; Ou, H.; Long, H. Development of Novel

Tools for Electricity-Assisted Incremental Sheet Forming of Titanium Alloy. *Int. J. Adv. Manuf. Technol.*, **2016**, *85* (5–8), 1137–1144.

[80] Najafabady, S. A.; Ghaei, A. An Experimental Study on Dimensional Accuracy, Surface Quality, and Hardness of Ti-6Al-4 V Titanium Alloy Sheet in Hot Incremental Forming. *Int. J. Adv. Manuf. Technol.*, **2016**, *87* (9–12), 3579–3588.

[81] Xu, D. K.; Lu, B.; Cao, T. T.; Zhang, H.; Chen, J.; Long, H.; Cao, J. Enhancement of Process Capabilities in Electrically-Assisted Double Sided Incremental Forming. *Mater. Des.*, **2016**, *92*, 268–280.

[82] Li, Z.; Lu, S.; Zhang, T.; Zhang, C.; Mao, Z. 1060 Al Electric Hot Incremental Sheet Forming Process: Analysis of Dimensional Accuracy and Temperature. *Trans. Indian Inst. Met.*, **2018**, *71* (4), 961–970.

[83] Magnus, C. S. Joule Heating of the Forming Zone in Incremental Sheet Metal Forming: Part 2: Creating an Experimental Setup and Forming of Ti6Al4V. *Int. J. Adv. Manuf. Technol.*, **2017**, *89* (1–4), 295–309.

[84] Magnus, C. S. Joule Heating of the Forming Zone in Incremental Sheet Metal Forming: Part 1: State of the Art and Thermal Process Modelling. *Int. J. Adv. Manuf. Technol.*, **2017**, *91* (1–4), 1309–1319.

[85] Min, J.; Seim, P.; Störkle, D.; Thyssen, L.; Kuhlenkötter, B. Thermal Modeling in Electricity Assisted Incremental Sheet Forming. *Int. J. Mater. Form.*, **2017**, *10* (5), 729–739.

[86] Pacheco, P. A. P.; Silveira, M. E. Numerical Simulation of Electric Hot Incremental Sheet Forming of 1050 Aluminum with and without Preheating. *Int. J. Adv. Manuf. Technol.*, **2018**, *94* (9–12), 3097–3108.

[87] Al-Obaidi, A.; Kräusel, V.; Landgrebe, D. Hot Single-Point Incremental Forming Assisted by Induction Heating. *Int. J. Adv. Manuf. Technol.*, **2016**, *82* (5–8), 1163–1171.

[88] Al-Obaidi, A.; Kräusel, V.; Landgrebe, D. Induction Heating Validation of Dieless Single-Point Incremental Forming of AHSS. *J. Manuf. Mater. Process.*, **2017**, *1* (2), 5.

[89] Ambrogio, G.; Gagliardi, F.; Chamanfar, A.; Misiolek, W. Z.; Filice, L. Induction Heating and Cryogenic Cooling in Single Point Incremental Forming of Ti-6Al-4V: Process Setup and Evolution of Microstructure and Mechanical Properties. *Int. J. Adv. Manuf. Technol.*, **2017**, *91* (1–4), 803–812.

[90] Kim, S. W.; Lee, Y. S.; Kang, S. H.; Lee, J. H. Incremental Forming of Mg Alloy Sheet at Elevated Temperatures. In *Journal of Mechanical Science and Technology*; Korean Society of Mechanical Engineers, 2007; Vol. 21, pp 1518–1522.

[91] Ji, Y. H.; Park, J. J. Formability of Magnesium AZ31 Sheet in the Incremental Forming at Warm Temperature. *J. Mater. Process. Technol.*, **2008**, *201* (1–3), 354–358.

[92] Ji, Y. H.; Park, J. J. Incremental Forming of Free Surface with Magnesium Alloy AZ31 Sheet at Warm Temperatures. *Trans. Nonferrous Met. Soc. China (English Ed.*, **2008**, *18* (SPEC. ISSUE 1), s165–s169.

[93] Galdos, L.; De Argandoña, E. S.; Ulacia, I.; Arruebarrena, G. Warm Incremental Forming of Magnesium Alloys Using Hot Fluid as Heating Media. In *Key Engineering Materials*; Trans Tech Publications Ltd, 2012; Vol. 504–506, pp 815–820.

[94] Durante, M.; Formisano, A.; Langella, A.; Capece Minutolo, F. M. The Influence of Tool Rotation on an Incremental Forming Process. *J. Mater. Process. Technol.*, **2009**, *209* (9), 4621–4626.

[95] Duc-Toan, N.; Jin-Gee, P.; Young-Suk, K. Combined Kinematic/Isotropic Hardening Behavior Study for Magnesium Alloy Sheets to Predict Ductile Fracture of Rotational Incremental Forming. *Int. J. Mater. Form.*, **2010**, *3* (SUPPL. 1), 939–942.

[96] Nguyen, D. T.; Park, J. G.; Kim, Y. S. Ductile Fracture Prediction in Rotational Incremental Forming for Magnesium Alloy Sheets Using Combined Kinematic/Isotropic Hardening Model. *Metall. Mater. Trans. A Phys. Metall. Mater. Sci.*, **2010**, *41* (8), 1983–1994.

[97] Park, J.; Kim, J.; Park, N.; Kim, Y. Study of Forming Limit for Rotational Incremental Sheet Forming of Magnesium Alloy Sheet. *Metall. Mater. Trans. A Phys. Metall. Mater. Sci.*, **2010**, *41* (1), 97–105.

[98] Xu, D.; Wu, W.; Malhotra, R.; Chen, J.; Lu, B.; Cao, J. Mechanism Investigation for the Influence of Tool Rotation and Laser Surface Texturing (LST) on Formability in Single Point Incremental Forming. *Int. J. Mach. Tools Manuf.*, **2013**, *73*, 37–46.

[99] Buffa, G.; Campanella, D.; Fratini, L. On the Improvement of Material Formability in SPIF Operation through Tool Stirring Action. *Int. J. Adv. Manuf. Technol.*, **2013**, *66* (9–12), 1343–1351.

[100] Khalatbari, H.; Iqbal, A.; Shi, X.; Gao, L.; Hussain, G.; Hashemipour, M. High-Speed Incremental Forming Process: A Trade-Off between Formability and Time Efficiency. *Mater. Manuf. Process.*, **2015**, *30* (11).

[101] Davarpanah, M. A.; Mirkouei, A.; Yu, X.; Malhotra, R.; Pilla, S. Effects of Incremental Depth and Tool Rotation on Failure Modes and Microstructural Properties in Single Point Incremental Forming of Polymers. *J. Mater. Process. Technol.*, **2015**, *222*, 287–300.

[102] Wang, J.; Li, L.; Jiang, H. Effects of Forming Parameters on Temperature in Frictional Stir Incremental Sheet Forming. *J. Mech. Sci. Technol.*, **2016**, *30* (5), 2163–2169.

[103] Baharudin, B. T. H. T.; Azpen, Q. M.; Sulaima, S.; Mustapha, F. Experimental Investigation of Forming Forces in Frictional Stir Incremental Forming of Aluminum Alloy AA6061-T6. *Metals (Basel).*, **2017**, *7* (11), 484.

[104] Liu, Z. Friction Stir Incremental Forming of AA7075-O Sheets: Investigation on Process Feasibility. In *Procedia Engineering*; Elsevier Ltd, 2017; Vol. 207, pp 783–788.

[105] Uheida, E. H.; Oosthuizen, G. A.; Dimitrov, D. M.; Bezuidenhout, M. B.; Hugo, P. A. Effects of the Relative Tool Rotation Direction on Formability during the Incremental Forming of Titanium Sheets. *Int. J. Adv. Manuf. Technol.*, **2018**, *96* (9–12), 3311–3319.

[106] Lotus-Engineering-Inc. *An Assessment of Mass Reduction Opportunities for a 2017 – 2020 Model Year Vehicle Program*; The International Council on Clean Transportation : http://www.theicct.org/lotus-lightweighting-study, 2010.

[107] Szeteiová, K. Automotive Materials Plastics in Automotive Markets Today. *Inst. Prod. Technol. Mach. Technol. Mater. Fac. Mater. Sci. Technol. Trnava, Slovak Univ. Technol. Bratislava*, **2010**.

[108] Usman, K. Mechanical Behaviour of POM in Dependence on Molar Mass, Temperature and Loading Regime, Master's Thesis, Technische Universität Chemnitz, Chemnitz, Germany, 2019.

[109] Liu, Z. Heat-Assisted Incremental Sheet Forming: A State-of-the-Art Review. *Int. J. Adv. Manuf. Technol.*, **2018**, *98* (9–12), 2987–3003.

[110] Franzen, V.; Kwiatkowski, L.; Neves, J.; Martins, P. A. F.; Tekkaya, A. E. On the Capability of Single Point Incremental Forming for Manufacturing Polymer Sheet Parts. In *Proceedings of the 9th ICTP-international conference on technology of plasticity, Gyeongju, Korea*; 2008.

[111] Martins, P. A. F.; Kwiatkowski, L.; Franzen, V.; Tekkaya, A. E.; Kleiner, M. Single Point Incremental Forming of Polymers. *CIRP Ann. - Manuf. Technol.*, **2009**, *58* (1), 229–232.

[112] Silva, M. B.; Alves, L. M.; Martins, P. A. F. Single Point Incremental Forming of PVC: Experimental Findings and Theoretical Interpretation. *Eur. J. Mech. A/Solids*, **2010**, *29* (4), 557–566.

[113] Silva, M. B.; Skjoedt, M.; Martins, P. A. F.; Bay, N. Revisiting the Fundamentals of Single Point Incremental Forming by Means of Membrane Analysis. *Int. J. Mach. Tools Manuf.*, **2008**, *48* (1), 73–83.

[114] Marques, T. A.; Silva, M. B.; Martins, P. A. F. On the Potential of Single Point Incremental Forming of Sheet Polymer Parts. *Int. J. Adv. Manuf. Technol.*, **2012**, *60* (1–4), 75–86.

[115] Silva, M. B.; Martinho, T. M.; Martins, P. a. F. Incremental Forming of Hole-Flanges in Polymer Sheets. *Mater. Manuf. Process.*, **2013**, *28* (3), 330–335.

[116] Yonan, S. A.; Haupt, P.; Kwiatkowski, L.; Franzen, V.; Brosius, A.; Tekkaya, A. E. A Viscoplastic Material Model Based on Overstress for the Simulation of Incremental Sheet Forming of Thermoplastics. In *AIP Conference Proceedings*; American Institute of PhysicsAIP, 2011; Vol. 1353, pp 803–808.

[117] Alkas Yonan, S.; Soyarslan, C.; Haupt, P.; Kwiatkowski, L.; Tekkaya, A. E. A Simple Finite Strain Non-Linear Visco-Plastic Model for Thermoplastics and Its Application to the Simulation of Incremental Cold Forming of Polyvinylchloride (PVC). *Int. J. Mech. Sci.*, **2013**, *66*, 192–201.

[118] Alkas Yonan, S.; Haupt, P.; Kwiatkowski, L.; Franzen, V.; Brosius, A.; Tekkaya, E. Three-Dimensional Formulation and Validation of a New Viscoplastic Material Model for the Simulation of Incremental Forming of Thermoplastics. In *10th International Conference on Technology of Plasticity Aachen*; 2011; pp 973–977.

[119] Bagudanch, I.; Garcia-Romeu, M. L.; Centeno, G.; Elías-Zúñiga, a.; Ciurana, J. Forming Force and Temperature Effects on Single Point Incremental Forming of Polyvinylchloride. *J. Mater. Process. Technol.*, **2015**, *219*, 221–229.

[120] Durante, M.; Formisano, A.; Lambiase, F. Incremental Forming of Polycarbonate Sheets. *J. Mater. Process. Technol.*, **2018**, *253*, 57–63.

[121] Zhu, H.; Ou, H.; Popov, A. Incremental Sheet Forming of Thermoplastics: A Review. *Int. J. Adv. Manuf. Technol. 2020 1111*, **2020**, *111* (1), 565–587.

[122] *Polyoxymethylene Handbook*; Lüftl, S., P.M., V., Chandran, S., Eds.; John Wiley & Sons, Inc.: Hoboken, NJ, USA, 2014.

[123] Atkins, A. G.; Mai, Y.-W. *Elastic and Plastic Fracture: Metals, Polymers, Ceramics, Composites, Biological Materials*; Ellis Horwood; Halsted Press, 1985.

[124] Yonan, S. A.; Silva, M. B.; Martins, P. A. F.; Tekkaya, A. E. Plastic Flow and Failure in Single Point Incremental Forming of PVC Sheets. *Express Polym. Lett.*, **2014**, *8* (5), 301–311.

[125] Hussain, G.; Gao, L.; Dar, N. U. An Experimental Study on Some Formability Evaluation Methods in Negative Incremental Forming. *J. Mater. Process. Technol.*, **2007**, *186* (1–3), 45–53.

[126] Davarpanah, M. A.; Mirkouei, A.; Yu, X.; Malhotra, R.; Pilla, S. Effects of Incremental Depth and Tool Rotation on Failure Modes and Microstructural Properties in Single Point Incremental Forming of Polymers. *J. Mater. Process.*

Technol., **2015**, *222*, 287–300.

[127] Zsidai, L.; Samyn, P.; Vercammen, K.; Van Acker, K.; Kozma, M.; Kalácska, G.; De Baets, P. Friction and Thermal Effects of Engineering Plastics Sliding Against Steel and DLN-Coated Counterfaces. *Tribol. Lett.*, **2004**, *17* (2), 269–288.

[128] Aerens, R.; Eyckens, P.; Van Bael, A.; Duflou, J. R. Force Prediction for Single Point Incremental Forming Deduced from Experimental and FEM Observations. *Int. J. Adv. Manuf. Technol.*, **2010**, *46* (9–12), 969–982.

[129] Lüftl, S.; Visakh, P. M.; Chandran, S. *Polyoxymethylene Handbook: Structure, Properties, Applications and Their Nanocomposites*; John Wiley & Sons, 2014.

[130] Lozano-Sánchez, L. M.; Sustaita, A. O.; Soto, M.; Biradar, S.; Ge, L.; Segura-Cárdenas, E.; Diabb, J.; Elizalde, L. E.; Barrera, E. V.; Elías-Zúñiga, A. Mechanical and Structural Studies on Single Point Incremental Forming of Polypropylene-MWCNTs Composite Sheets. *J. Mater. Process. Technol.*, **2017**, *242*, 218–227.

[131] Wang, Y.; Zhang, H.; Li, M.; Cao, W.; Liu, C.; Shen, C. Orientation and Structural Development of Semicrystalline Poly(Lactic Acid) under Uniaxial Drawing Assessed by Infrared Spectroscopy and X-Ray Diffraction. *Polym. Test.*, **2015**, *41*, 163–171.

[132] Briscoe, B. J.; Fiori, L.; Pelillo, E. Nano-Indentation of Polymeric Surfaces. *J. Phys. D. Appl. Phys.*, **1998**, *31* (19), 2395.

[133] Calleja, F. J. B.; Flores, A.; Calleja, F. J. B.; Flores, A. Hardness. In *Encyclopedia of Polymer Science and Technology*; John Wiley & Sons, Inc.: Hoboken, NJ, USA, 2011.

[134] Friedrich, K. Crazes and Shear Bands in Semi-Crystalline Thermoplastics. In *Crazing in Polymers*; Springer-Verlag: Berlin/Heidelberg, 1983; pp 225–274.

[135] Jiang, J.; Wang, S.; Sun, B.; Ma, S.; Zhang, J.; Li, Q.; Hu, G.-H. Effect of Mold Temperature on the Structures and Mechanical Properties of Micro-Injection Molded Polypropylene. *Mater. Des.*, **2015**, *88*, 245–251.

[136] Pawlak, A.; Galeski, A.; Rozanski, A. Cavitation during Deformation of Semicrystalline Polymers. *Prog. Polym. Sci.*, **2014**, *39* (5), 921–958.

[137] Wendorff, J. H. Submicroscopic Defects in Strained Polyoxymethylene. In *Anwendungsbezogene physikalische Charakterisierung von Polymeren, insbesondere im festen Zustand*; Steinkopff: Darmstadt, 1979; pp 135–142.

[138] Jang, B. Z.; Uhlmann, D. R.; Vander Sande, J. B. Crazing in Polypropylene. *Polym. Eng. Sci.*, **1985**, *25* (2), 98–104.

[139] Liu, Y.; Kennard, C. H. L.; Truss, R. W.; Calos, N. J. Characterization of Stress-

Whitening of Tensile Yielded Isotactic Polypropylene. *Polymer (Guildf).*, **1997**, *38* (11), 2797–2805.

[140] Castagnet, S.; Deburck, Y. Relative Influence of Microstructure and Macroscopic Triaxiality on Cavitation Damage in a Semi-Crystalline Polymer. *Mater. Sci. Eng. A*, **2007**, *448* (1–2), 56–66.

[141] Laiarinandrasana, L.; Besson, J.; Lafarge, M.; Hochstetter, G. Temperature Dependent Mechanical Behaviour of PVDF: Experiments and Numerical Modelling. *Int. J. Plast.*, **2009**, *25* (7), 1301–1324.

[142] Silva, M. B.; Skjoedt, M.; Atkins, A. G.; Bay, N.; Martins, P. A. F. Single-point Incremental Forming and Formability—Failure Diagrams. *J. Strain Anal. Eng. Des.*, **2008**, *43* (1), 15–35.

[143] Silva, M. B.; Nielsen, P. S.; Bay, N.; Martins, P. A. F. Failure Mechanisms in Single-Point Incremental Forming of Metals. *Int. J. Adv. Manuf. Technol.*, **2011**, *56* (9–12), 893–903.

[144] Gent, A. N.; Madan, S. Plastic Yielding of Partially Crystalline Polymers. *J. Polym. Sci. Part B Polym. Phys.*, **1989**, *27* (7), 1529–1542.

[145] Kennedy, M. A.; Peacock, A. J.; Mandelkern, L. Tensile Properties of Crystalline Polymers: Linear Polyethylene. *Macromolecules*, **1994**, *27* (19), 5297–5310.

[146] Plummer, C. J. G.; Béguelin, P.; Kausch, H.-H. The Temperature and Strain-Rate Dependence of Mechanical Properties in Polyoxymethylene. *Polym. Eng. Sci.*, **1995**, *35* (16), 1300–1312.

[147] Whitney, W.; Andrews, R. D. Yielding of Glassy Polymers: Volume Effects. *J. Polym. Sci. Part C Polym. Symp.*, **1967**, *16* (5), 2981–2990.

[148] Pae, K. D. The Macroscopic Yielding Behaviour of Polymers in Multiaxial Stress Fields. *J. Mater. Sci.*, **1977**, *12* (6), 1209–1214.

[149] Morales, D.; Martinez, A.; Vallellano, C.; Garcia-Lomas, F. J. Bending Effect in the Failure of Stretch-Bend Metal Sheets. *Int. J. Mater. Form.*, **2009**, *2* (SUPPL. 1), 813–816.

[150] Silva, M. B.; Marques, T.; Martins, P. A. F. Single-Point Incremental Forming of Polymers. In *Mechatronics and Manufacturing Engineering*; Elsevier, 2012; pp 293–331.

[151] Fang, Y.; Lu, B.; Chen, J.; Xu, D. K.; Ou, H. Analytical and Experimental Investigations on Deformation Mechanism and Fracture Behavior in Single Point Incremental Forming. *J. Mater. Process. Technol.*, **2014**, *214* (8), 1503–1515.

[152] Chakrabarty, J. *Theory of Plasticity: Third Edition*; Elsevier Ltd., 2006.

[153] Xu, J.; Ma, X.; Zhou, A.; Duan, Q.; Wang, S. Path Selection for Seamless Service

Migration in Vehicular Edge Computing. *IEEE Internet Things J.*, **2020**, *7* (9), 9040–9049.

[154] Ramanujan, S. Ramanujan's Collected Works. *Chelsea, New York*, **1962**, *52*.

[155] Michell, J. H. The Flexure of a Circular Plate. *Proc. London Math. Soc.*, **1901**, *s1-34* (1), 223–234.

[156] Ventsel, E.; Krauthammer, T. *Thin Plates and Shells*, 1st Edition.; CRC Press, 2001.

[157] Ertz, M.; Knothe, K. A Comparison of Analytical and Numerical Methods for the Calculation of Temperatures in Wheel/Rail Contact. *Wear*, **2002**, *253* (3–4), 498–508.

[158] Talati, F.; Jalalifar, S. Analysis of Heat Conduction in a Disk Brake System. *Heat Mass Transf. und Stoffuebertragung*, **2009**, *45* (8), 1047–1059.

[159] Çengel, Y. A. *Heat Transfer: A Practical Approach*, 2nd Editio.; McGraw-Hill: New York, NY, USA, 2003.

[160] Fujii, T.; Imura, H. Natural-Convection Heat Transfer from a Plate with Arbitrary Inclination. *Int. J. Heat Mass Transf.*, **1972**, *15* (4), 755–767.

[161] Khalatbari, H.; Lazoglu, I. Friction Stir Incremental Forming of Polyoxymethylene: Process Outputs, Force and Temperature. *Mater. Manuf. Process.*, **2021**, *36* (1), 94–105.

[162] Kulkarni, S. S.; Mocko, G. M. A Finite Element Simulation Model of Convective Heat-Assisted Single-Point Incremental Forming of Thermoplastics. *Int. J. Adv. Manuf. Technol.*, **2020**, *111* (11–12), 3305–3317.

[163] Durante, M.; Formisano, A.; Lambiase, F. Formability of Polycarbonate Sheets in Single-Point Incremental Forming. *Int. J. Adv. Manuf. Technol.*, **2019**, *102* (5–8), 2049–2062.

[164] Torres, J. P.; Frontini, P. M.; Machado, M.; Major, Z. Deformation and Failure of Semicrystalline Polymers under Dynamic Tensile and Biaxial Impact Loading. *Int. J. Impact Eng.*, **2016**, *98*, 52–61.

[165] Kästner, M.; Obst, M.; Brummund, J.; Thielsch, K.; Ulbricht, V. Inelastic Material Behavior of Polymers - Experimental Characterization, Formulation and Implementation of a Material Model. *Mech. Mater.*, **2012**, *52*, 40–57.

[166] Tscharnuter, D.; Gastl, S.; Pinter, G. Modeling of the Nonlinear Viscoelasticity of Polyoxymethylene in Tension and Compression. *Int. J. Eng. Sci.*, **2012**, *60*, 37–52.

[167] Tscharnuter, D.; Muliana, A. Nonlinear Response of Viscoelastic Polyoxymethylene (POM) at Elevated Temperatures. *Polymer (Guildf).*, **2013**, *54* (3), 1208–1217.

[168] Muliana, A.; Rajagopal, K. R.; Tscharnuter, D.; Pinter, G. A Nonlinear Viscoelastic Constitutive Model for Polymeric Solids Based on Multiple Natural Configuration Theory. *Int. J. Solids Struct.*, **2016**, *100–101*, 95–110.

[169] Song, R.; Muliana, A.; Rajagopal, K. A Thermodynamically Consistent Model for Viscoelastic Polymers Undergoing Microstructural Changes. *Int. J. Eng. Sci.*, **2019**, *142*, 106–124.

[170] Zerbe, P.; Schneider, B.; Moosbrugger, E.; Kaliske, M. A Viscoelastic-Viscoplastic-Damage Model for Creep and Recovery of a Semicrystalline Thermoplastic. *Int. J. Solids Struct.*, **2017**, *110–111*, 340–350.

[171] Two-layer viscoplasticity https://abaqus-docs.mit.edu/2017/English/SIMACAEMATRefMap/simamat-c-viscous.htm (accessed Jul 2, 2021).

[172] Abdel-Wahab, A. A.; Ataya, S.; Silberschmidt, V. V. Temperature-Dependent Mechanical Behaviour of PMMA: Experimental Analysis and Modelling. *Polym. Test.*, **2017**, *58*, 86–95.

[173] Shirazi, H. A.; Mirmohammadi, S. A.; Shaali, M.; Asnafi, A.; Ayatollahi, M. R. A Constitutive Material Model for a Commercial PMMA Bone Cement Using a Combination of Nano-Indentation Test and Finite Element Analysis. *Polym. Test.*, **2017**, *59*, 328–335.

[174] der Velden, A.; Koch, P. Isight Design Optimization Methodologies. *ASM Handb.*, **2010**, *22*, 79.

[175] Ropers, S.; Kardos, M.; Osswald, T. A. A Thermo-Viscoelastic Approach for the Characterization and Modeling of the Bending Behavior of Thermoplastic Composites. *Compos. Part A Appl. Sci. Manuf.*, **2016**, *90*, 22–32.

[176] Bergström, J. Mechanics of Solid Polymers: Theory and Computational Modeling. *Mech. Solid Polym. Theory Comput. Model.*, **2015**, 1–509.

[177] Bergstrom, J. S.; Bischoff, J. E. An Advanced Thermomechanical Constitutive Model for UHMWPE. *Int. J. Struct. Chang. Solids*, **2010**, *2* (1), 31–39.

[178] Arruda, E. M.; Boyce, M. C. A Three-Dimensional Constitutive Model for the Large Stretch Behavior of Rubber Elastic Materials. *J. Mech. Phys. Solids*, **1993**, *41* (2), 389–412.

[179] Louche, H.; Piette-Coudol, F.; Arrieux, R.; Issartel, J. An Experimental and Modeling Study of the Thermomechanical Behavior of an ABS Polymer Structural Component during an Impact Test. *Int. J. Impact Eng.*, **2009**, *36* (6), 847–861.

[180] Manigandan, S. Computational Investigation of High Velocity Ballistic Impact Test on Kevlar 149. *Appl. Mech. Mater.*, **2015**, *766–767*, 1133–1138.

[181] Duan, Y.; Saigal, A.; Greif, R.; Zimmerman, M. A. Impact Behavior and Modeling of Engineering Polymers. *Polym. Eng. Sci.*, **2003**, *43* (1), 112–124.

[182] Dwivedi, A.; Bradley, J.; Casem, D. Mechanical Response of Polycarbonate with Strength Model Fits. *Army Reaserch Lab.*, **2012**, No. February, 1–22.

[183] Pulungan, D.; Yudhanto, A.; Goutham, S.; Lubineau, G.; Yaldiz, R.; Schijve, W. Characterizing and Modeling the Pressure- and Rate-Dependent Elastic-Plastic-Damage Behavior of Polypropylene-Based Polymers. *Polym. Test.*, **2018**, *68*, 433–445.

[184] Zhu, H.; Ou, H.; Popov, A. A New Phenomenological Constitutive Model for Thermoplastics. *Mech. Mater.*, **2021**, *157*, 103817.

[185] CAMPUSplastics | datasheet CELCON® M90™ https://www.campusplastics.com/campus/en/datasheet/CELCON®+M90™/Celanese/163/60965f98/SI?pos=37 (accessed Jul 6, 2021).

[186] Wang, Z.; Zhang, X.; Chen, J. An Effective Thermal-Mechanical Coupling Method for Simulating Friction Stir-Assisted Incremental Aluminum Alloy Sheet Forming. *Int. J. Adv. Manuf. Technol. 2020 1077*, **2020**, *107* (7), 3449–3458.

[187] Shaaban, A.; Elsabbagh, A. M. Optimization of AL6061-T6 Tube End Forming Process Using Response Surface Method. *Model. Simul. Eng.*, **2021**, *2021*.

[188] Song, F.; Yang, H.; Li, H.; Zhan, M.; Li, G. Springback Prediction of Thick-Walled High-Strength Titanium Tube Bending. *Chinese J. Aeronaut.*, **2013**, *26* (5), 1336–1345.

[189] Blok, H. Theoretical Study of Temperature Rise at Surfaces of Actual Contact under Oiliness Lubricating Conditions. *Proc. Instn. Mech. Engrs.(General Discuss. Lubr. Lubr.*, **1937**, *2*, 222.

[190] Jaeger, J. C. Moving Sources of Heat and the Temperature of Sliding Contacts. In *Proceedings of the royal society of New South Wales*; 1942; Vol. 76, pp 203–224.

[191] Ling, F. F.; Lai, W. M.; Lucca, D. A. *Fundamentals of Surface Mechanics: With Applications*; Springer Science & Business Media, 2002.

[192] Bos, J.; Moes, H. Frictional Heating of Tribological Contacts. *J. Tribol.*, **1995**, *117* (1), 171–177.

[193] Bansal, D. G.; Streator, J. L. On Estimations of Maximum and Average Interfacial Temperature Rise in Sliding Elliptical Contacts. *Wear*, **2012**, *278–279*, 18–27.

[194] Talati, F.; Jalalifar, S. Analysis of Heat Conduction in a Disk Brake System. *Heat Mass Transf. und Stoffuebertragung*, **2009**, *45* (8), 1047–1059.

[195] Federici, M.; Straffelini, G.; Gialanella, S. Pin-on-Disc Testing of Low-Metallic Friction Material Sliding Against HVOF Coated Cast Iron: Modelling of the

Contact Temperature Evolution. *Tribol. Lett.*, **2017**, *65* (4), 1–12.

[196] Kennedy, F. E.; Lu, Y.; Baker, I. Contact Temperatures and Their Influence on Wear during Pin-on-Disk Tribotesting. *Tribol. Int.*, **2015**, *82* (PB), 534–542.

[197] Ling, F. F. A Quasi-Iterative Method for Computing Interface Temperature Distributions. *Zeitschrift für Angew. Math. und Phys. 1959 105*, **1959**, *10* (5), 461–474.

[198] Komanduri, R.; Hou, Z. B. Analysis of Heat Partition and Temperature Distribution in Sliding Systems. *Wear*, **2001**, *251* (1–12), 925–938.

[199] Kennedy, F. E. Surface Temperatures in Sliding Systems—A Finite Element Analysis. *J. Lubr. Technol.*, **1981**, *103* (1), 90–96.

[200] Rowe, K. G.; Bennett, A. I.; Krick, B. A.; Gregory Sawyer, W. In Situ Thermal Measurements of Sliding Contacts. *Tribol. Int.*, **2013**, *62*, 208–214.

[201] Archard, J. F. The Temperature of Rubbing Surfaces. *wear*, **1959**, *2* (6), 438–455.

[202] Laraqi, N.; Alilat, N.; de Maria, J. M. G.; Baïri, A. Temperature and Division of Heat in a Pin-on-Disc Frictional Device—Exact Analytical Solution. *Wear*, **2009**, *266* (7–8), 765–770.

[203] Mirnia, M. J.; Shamsari, M. Numerical Prediction of Failure in Single Point Incremental Forming Using a Phenomenological Ductile Fracture Criterion. *J. Mater. Process. Technol.*, **2017**, *244*, 17–43.

[204] Bai, Y.; Wierzbicki, T. Application of Extended Mohr-Coulomb Criterion to Ductile Fracture. *Int. J. Fract.*, **2010**, *161* (1), 1–20.

[205] Bai, Y.; Wierzbicki, T. A Comparative Study of Three Groups of Ductile Fracture Loci in the 3D Space. *Eng. Fract. Mech.*, **2015**, *135*, 147–167.

[206] Johnson, G. R.; Cook, W. H. Fracture Characteristics of Three Metals Subjected to Various Strains, Strain Rates, Temperatures and Pressures. *Eng. Fract. Mech.*, **1985**, *21* (1), 31–48.